2011 NRL REVIEW

		Form Approved OMB No. 0704-0188

Report Documentation Page

1. REPORT DATE **2011**	2. REPORT TYPE	3. DATES COVERED **00-00-2011 to 00-00-2011**

4. TITLE AND SUBTITLE **2011 NRL REVIEW**	5a. CONTRACT NUMBER
	5b. GRANT NUMBER
	5c. PROGRAM ELEMENT NUMBER
6. AUTHOR(S)	5d. PROJECT NUMBER
	5e. TASK NUMBER
	5f. WORK UNIT NUMBER

7. PERFORMING ORGANIZATION NAME(S) AND ADDRESS(ES) **Naval Research Laboratory,,4555 Overlook Ave, S.W.,Washington,,DC,20375**	8. PERFORMING ORGANIZATION REPORT NUMBER

9. SPONSORING/MONITORING AGENCY NAME(S) AND ADDRESS(ES)	10. SPONSOR/MONITOR'S ACRONYM(S)
	11. SPONSOR/MONITOR'S REPORT NUMBER(S)

12. DISTRIBUTION/AVAILABILITY STATEMENT **Approved for public release; distribution unlimited**

13. SUPPLEMENTARY NOTES

14. ABSTRACT

15. SUBJECT TERMS

16. SECURITY CLASSIFICATION OF:			17. LIMITATION OF ABSTRACT	18. NUMBER OF PAGES	19a. NAME OF RESPONSIBLE PERSON
a. REPORT **unclassified**	b. ABSTRACT **unclassified**	c. THIS PAGE **unclassified**	**Same as Report (SAR)**	**240**	

NRL's MISSION

To conduct a broadly based multidisciplinary program of scientific research and advanced technological development directed toward maritime applications of new and improved materials, techniques, equipment, systems, and ocean, atmospheric, and space sciences and related technologies.

The Naval Research Laboratory provides primary in-house research for the physical, engineering, space, and environmental sciences; broadly based applied research and advanced technology development programs in response to identified and anticipated Navy and Marine Corps needs; broad multidisciplinary support to the Naval Warfare Centers; and space and space systems technology, development, and support.
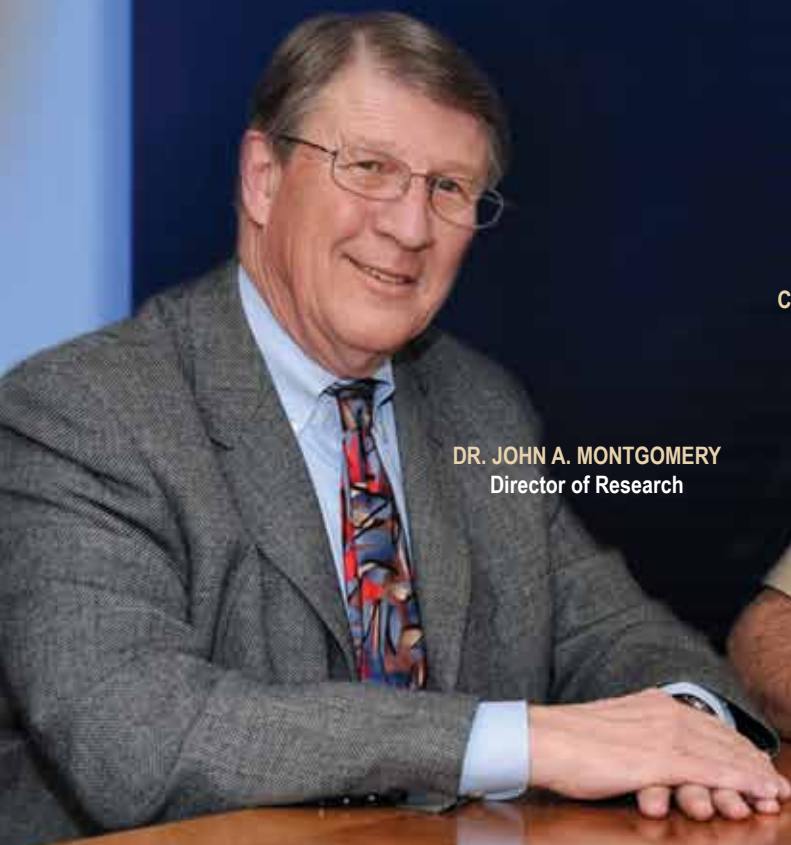
VIEW FROM THE TOP

Since its establishment on July 2, 1923, the Naval Research Laboratory has excelled in conducting a broadly based multidisciplinary program of scientific research and technological development focused on Navy and Marine Corps applications of new and improved materials, techniques, equipment, systems, and ocean, atmospheric, and space sciences. NRL's dedicated scientists, engineers, and support personnel — working in our world-class facilities — have developed a number of innovations that have revolutionized the capabilities of our Navy and Marine Corps, and of our Nation as a whole.

In keeping with our long-term focus on discovery and invention and the Navy of the future, NRL is completing construction of a major new facility called the Laboratory for Autonomous Systems Research (LASR). The 50,000 square foot facility, which will open in the Spring of 2012, will integrate science and technology components into research prototype systems and will become the nerve center for basic research that supports autonomous systems research for the Navy and Marine Corps.

While the Laboratory for Autonomous Systems Research is new, NRL's research into autonomous systems dates back to the founding of the Laboratory. In 1923, NRL devised a remote control system that was applied to a three-wheel cart. This led to the development of a control system for the first U.S. flight of a radio-controlled pilotless aircraft in 1924. Since that time, NRL has developed autonomous systems for underwater, surface, land, air, and space applications. With the opening of the LASR facility, NRL will further expand its science and technology capabilities in the development of new autonomous systems.

The idea behind the creation of NRL was to help build American sea power, protect national security through technological innovation, and make the U.S. Fleet the most formidable naval fighting force in the world. In the 88 years since its establishment, the Laboratory's record of technical excellence confirms that NRL has made a profound difference — in times of war and in times of peace, during times of economic austerity and international challenge — through the creative work of scientists and engineers who serve in the Nation's interest. Despite the current economic, technical, and military challenges faced by our Nation, NRL is expanding its capabilities and we remain very optimistic that our research will continue to have a significant impact on America's national security.

CAPT PAUL C. STEWART, USN
Commanding Officer

DR. JOHN A. MONTGOMERY
Director of Research

2011 NRL REVIEW
contents

ON THE COVER

Octavia is an MDS (Mobile/Dexterous/Social) robot that uses an integrated sensor suite to perceive the world and cognitive models to interact with people. See "A Timeline of NRL's Autonomous Systems Research," page 7.

NRL's Involved!

Electric Dog (1923) — NRL devised a control switch with a vertical handle, similar to the control stick of an aircraft, which could operate selective relays simultaneously to provide for the several controls necessary to the flight of aircraft. It was first applied to a three-wheel cart system, the "electric dog," which could be seen wandering about on NRL's driveways.

A Timeline of NRL's

AUTONOMOUS SYSTEMS
Research

The Naval Research Laboratory has been actively involved in research in unmanned and autonomous systems since its opening in 1923. From one of the first unmanned ground vehicles to the development of more than 200 prototype air, ground, underwater, and space platforms, and from smart sensors to smart batteries to robots that reason like humans, NRL's research has been at the forefront. In January 2012, NRL completed construction on its new Laboratory for Autonomous Systems Research. This Laboratory provides specialized facilities to support highly innovative research in autonomous systems, including intelligent autonomy, sensor systems, power and energy systems, human–system interaction, networking and communications, and platforms. The Laboratory capitalizes on the broad multidisciplinary character of NRL, bringing together scientists and engineers with disparate training and backgrounds to tackle common goals in autonomy research at the intersection of their respective fields. The Laboratory provides simulated environments (littoral, desert, tropical) and instrumented reconfigurable high bay spaces to support integration of science and technology components into research prototype systems. The objective of the Laboratory is to enable continued Navy and DoD scientific leadership in this complex, emerging area and to identify opportunities for advances in future defense technology. In the following pages, we present a timeline of NRL's research in unmanned and autonomous systems from 1923 to the present.

1923 Electric Dog

NRL devised a control switch with a vertical handle, similar to the control stick of an aircraft, which could operate selective relays simultaneously to provide for the several controls necessary to the flight of aircraft. It was first applied
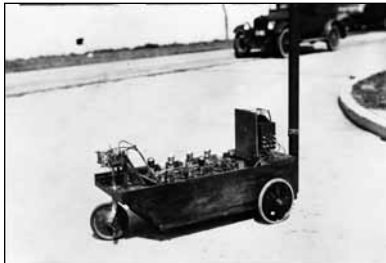
to a three-wheel cart system, the "electric dog," which could be seen wandering about on NRL's driveways.

1924 Remote-Controlled Pontoon Plane

NRL developed the control system for the first U.S. flight of a radio-controlled pilotless aircraft. Remotely controlled from the ground, the N-9 float plane took off from the Potomac River, followed a triangular course, executed

glides and climbs, and landed on the river.

1926 Joystick Remote Control Circuit Patent

NRL's C.B. Mirick patented his system for remote radio control of pilotless aircraft (or of "any circuits or objects which are to be controlled at a distance") using a "'joy stick' identical with the 'joy stick' provided in aircraft." U.S. Patent no. 1,597,416, "Electrical Distant-Control

System," Aug. 24, 1926. "My invention relates broadly to distant control systems, and more particularly to a control circuit for a radio transmitter, and a selectively responsive circuit for a radio apparatus whereby particular controls may be caused to function individually or simultaneously."

1930s Remote-Controlled Decoy Battleships

For exercises to test the vulnerability of ships to air bombing, NRL devised a radio remote control system to maneuver the warships USS *Stoddert* and USS *Utah,* which had been converted to target ships. The steering and throttle controls were operated through selector

switches based on the teletype mechanism using the Baudot code.

1936–WWII
Anti-Aircraft Target Drones

The Navy needed more realistic anti-aircraft practice targets than target sleeves towed by piloted aircraft, so NRL developed the radio-control system for an unmanned aircraft that, in demonstration, could be controlled by a "mother plane" 25 miles away. Target "drones" became widely used and led to rapid improvement in fire-control systems. Hundreds of F6F and other type aircraft were converted to drones for gunnery training, evaluation of defense procedures, and to carry out simulated "Japanese suicide" attacks.

1942 Assault/Guided Missile Drones

The first complete simulation of a guided missile was demonstrated using an unmanned type BG-1 aircraft equipped as an assault drone with NRL's radio-command guidance system and remote observation by television. The drone crashed through a towed battle raft, proving the capabilities as a weapon.

1945 Aircraft Carrier Traffic and Landing Control

NRL developed a radar carrier-controlled approach system that allowed aircraft to land on a carrier in complete darkness. It was first demonstrated on USS *Solomons* (CVE 67).

1946 Bikini Atoll Test Observation by Drones

Radio-guided drones collected data on nuclear explosions during the Bikini tests in the Pacific, telemetering it to safe observation points aboard ship.

1947 Loon Ship-to-Surface Guided Missile System

The Loon, with the guidance system developed by NRL, provided the first successful demonstration of a surface-to-surface guided missile and the first guided missile to be launched from a submarine, USS *Cusk*. NRL contributions included tracking by radar and steering by radio remote control.

1955 Polaris

NRL participated extensively in the conceptual planning and development of the submarine-launched Polaris missile.

1957 Blossom Point Satellite Tracking and Command Facility

NRL developed the first operational U.S. satellite tracking station at Blossom

Point, Maryland. Still in operation, Blossom Point pioneers automated ground commanding of satellites.

1958 Vanguard Solar Power System

Vanguard I proved that solar cells could be used for several years to power satellite radio transmitters. Vanguard's solar cells operated for about 7 years, while conventional batteries powering another onboard transmitter lasted only 20 days.

1960 GRAB

The Galactic Radiation and Background satellite was America's first electronic intelligence (ELINT) satellite. GRAB's ELINT antennas collected each pulse of a Soviet radar signal in a specified bandwidth, and a larger and separate

turnstile antenna transponded a corresponding signal to NRL receiving and control huts.

1964 Gravity Gradient Stabilization Experiment Satellites

NRL pioneered the gravity-gradient system for stabilizing the attitude of satellites with respect to Earth. This system is widely used in present-day satellites.

1976 MSD/Titan Launch Dispenser

NRL conceived and built the Multi-Satellite Dispenser (MSD), later modified

as the Titan Launch Dispenser (1990), a booster stage that goes through a

preprogrammed sequence of tasks to deposit multiple satellites from low shuttle orbits into their respective orbits, with or without real-time guidance from Earth.

1977 Nickel Hydrogen Battery on Navigation Technology Satellite-2

This was the first use of an NiH_2 battery as the primary energy source on a satellite, instead of nickel cadmium, for higher power and longer life.

1979 Unmanned Free-Swimming Submersible (UFSS)

NRL developed a long-range autonomous submersible to demonstrate (1) autonomy obtained by an OMEGA navi-

gator and a preprogrammed command and control microcomputer, and (2) high endurance (25 hr at 5 kt) attained with a low-drag hull and inexpensive battery energy source.

1981 NCARAI Established

Realizing the importance of artificial intelligence to the development of more intelligent autonomous and human-centered systems, NRL created the Navy Center for Applied Research in Artificial Intelligence.

1985 Cluster-based Routing

NRL conducted seminal work on distributed, self-organizing routing protocols for autonomous networking based upon clustering concepts. The novel concept of automated, dynamic structural formation amongst network nodes allowed improvements in mobile organization and wireless channel access coordination in self-forming networks.

1985 Fault Isolation Shell (FIS)

This tool captures device-specific knowledge to build expert systems to autonomously determine the causes of the breakdown of complex electro-mechanical-optical equipment, to aid maintenance and troubleshooting.

1986 Navy Message Understanding

This robust natural language processing system enabled automatic processing and summarizing of Navy Casualty Report (CASREP) messages, reducing the dependence on time-consuming human analysis.

1988 Low Altitude/Airspeed Unmanned Research Aircraft (LAURA)

This highly instrumented testbed aircraft was developed to address operational requirements of UAVs for Fleet EW missions. Its modular fuselage accepted the

installation of several wing/tail combinations for comparative aerodynamic testing. Other requirements driving UAV research included long flight endurance at ship-like speeds, flying in gusts, and storage in a protective canister prior to launch.

1990 Automated Weapon Assignment Algorithms for SDI Mid-Course Battle Management

NRL developed weapon allocation algorithms for the defense of selected assets against a MIRV ballistic missile threat based on a tracking and correlation algorithm. The software continually reassessed the threat and reassigned weapons to targets not previously engaged based on new situational assessment.

1990 NAUTILUS

The Navy Automated Intelligent Language Understanding System incorporates both robust natural language processing and semantic interpretation, providing greater ease of user interaction with autonomous systems. The system was used in the speech controller for the VIEWER immersive virtual reality tactical warfare simulation display system and an interface to a cartographic database with graphical map display.

1991 Tripod Operators for Recognizing Objects

NRL developed this class of feature extraction operators for range images which facilitate the automated recognition and localization of objects.

1992 Anytime Learning

NRL developed an "anytime learning" algorithm that allows a robot to adapt in near real time to a changing environment.

1993 Samuel: Evolutionary Approach to Learning in Robots

NRL developed Samuel, a learning system based on evolutionary algorithms, to explore alternative robot behaviors within a simulation model, as a way of reducing the overall knowledge engineering effort. Behaviors for collision avoidance navigation were learned and then successfully demonstrated on real ground robots.

1993 FLYRT

The FLYing Radar Target RF-distraction decoy flew at ship-like speeds following launch from a shipboard chaff launcher.

The fiber optic gyroscope provided highly accurate angle rate data.

1994 Clementine

NRL built and operated the first spacecraft known to conduct autonomous operations scheduling. The Spacecraft Command Language (SCL) became a widely used standard for automating spacecraft.

1995 Adaptive Testing

NRL developed a system that applies learning techniques to the general problem of evaluating an intelligent controller for an autonomous vehicle, searching for combinations of conditions and faults the controller is unable to handle. The system was successful in finding faults in two domains, an aircraft landing autopilot and an underwater autonomous vehicle controller.

1995 Heterogeneous Ad Hoc Network with Collaborative Data Streaming

In the Data and Voice Integration Advanced Technology Demonstration, NRL demonstrated one of the first working
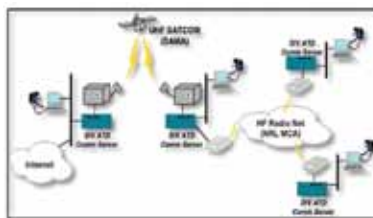
mobile ad hoc networking systems providing secure, mobile self-organization

and routing across heterogeneous radio technologies. The system also provided compressed and optimized Internet interoperability and demonstrated early forms of network-centric collaborative applications including compressed VoIP, reliable file dissemination, multicast situational awareness, and electronic whiteboarding.

1995 Multicast Dissemination Protocol (MDP)

The MDP framework was developed to provide reliable data transport improvements within autonomous collaborative groups that are often formed at the forward edge of a Navy or military communication network. This work introduced a novel information coding approach for network parity encoding and repairing in multicast networks.

1995 Non-Linear Discrete Event Tracking

NRL developed a multiple-target, multiple-sensor, automated data fusion algorithm based on ambiguous sensor reports to track land, sea, and undersea objects. The solution is provided in a unique set of probability maps and velocity probability wheels. The probability maps process both negative and positive information to create an area map of likely location of the object.

1996 Mobile Ad Hoc Networking (MANET)

NRL co-founded an Internet-standards working group to develop ad hoc routing technologies for self-organizing mobile Internet wireless infrastructures. This work stimulated extensive applied research activity and open standard designs that can be adapted and applied to military self-organizing wireless network technology.

1996 Robo-Shepherd

NRL demonstrated the ability for a robot to learn adversarial behaviors, in this case "herding" other robots into a "corral." This work showed that for tasks that are too expensive or dangerous to learn from experience, behaviors can be learned in simulation and then transferred into the real world.

1997 Hors d'Oeuvres, Anyone?

NRL's robot Coyote placed first in technical achievement at the 1997 AAAI Mobile Robot Competition. In developing a robot to serve hors d'oeuvres at

the conference reception, the research investigated several issues important to autonomous systems: navigating in a crowded space, being assertive without being intimidating or dangerous, human–robot interaction in noisy environments, and tracking of resources.

1998 Analyte 2000 Fiber Optic Biosensor

As payload on the Swallow UAV, NRL's biosensor provided one of the first demonstrations of the identification of

aerosolized bacteria by a sensor flown on a remotely piloted plane, with data transmitted to a ground station.

1998 ARIEL Frontier-based Exploration

For robotic mapping of unknown environments, it is useful for the robot to concentrate on areas at the edge of its knowledge, in order to expand that

knowledge. The ARIEL algorithm analyzes the robot's map, identifies frontier regions where known empty space borders unsensed space, and directs the robot to examine these areas in order to improve its ability to map unknown environments.

1998 Constrained Routing for Aircraft

NRL developed algorithms for computing least cost paths for multiple aircraft involved in strike missions. These included taking into account turn constraints, threat (no-fly) areas, goals, and efficient computing.

1998 Interbot

To reduce the warfighter's cognitive load, NRL developed natural interfaces that integrate the use of spoken natural language and hand/arm gestures for interacting with autonomous robots.

1998 Optical Flow for Control

NRL's novel sensor for detecting optical flow was mounted on a mobile robot and used to develop controls for steering the robot to avoid obstacles.

1998 DC-ARM: Damage Control Automation for Reduced Manning

Addressing the Navy's need to reduce manning aboard ships, the DC-ARM program shifts both routine and hazardous manpower-intensive manual damage control operations to survivable automation. The program reduces manning requirements while improving surface ship survivability. From 1998 to 2001, DC-ARM demonstrated Smart Valves, the Early Warning Fire Detection System, the Area-wide Water Mist Fire Protection System, the Smoke Ejection System, and a Supervisory Control System. DC-ARM combines a multi-criteria (sensor array) approach with sophisticated data analysis methods and improved organization and procedures.

1998 ORCA

NRL adapted the semi-submersible ORCA (Oceanographic Remotely Controlled Automaton), a diesel-powered, unmanned survey vehicle, to collect

oceanographic data at a fraction of the cost of a survey ship.

1998 SENDER

The man-portable Self-Navigating Drone, Expendable/Recoverable provided advanced technology in a

simple and affordable platform. Flown autonomously or under radio control, it featured electric propulsion, advanced composite structure, digital microprocessor autopilot, GPS navigator, and lithium propulsion batteries.

1999 Dynamic Autonomy

Intelligent mobile robots that interact with humans must be able to dynamically adjust their level of autonomy depending on the current situation. NRL demonstrated the ability for an autonomous robot to be able to interact with, or be interrupted by, a human, and then smoothly return to its earlier goals.

1999 Integrating Exploration, Localization, Navigation, and Planning with a Common Representation

This research demonstrated a novel approach to the common SLAM (simultaneous localization and mapping) problem that was able to work in dynamic environments, and also showed the utility of using a unifying representation. Experiments with indoor ground robots

showed only 13.6 cm of error over a half-mile traverse without the use of GPS.

2000 Adapting to Sensor Failures

NRL demonstrated the ability for a ground robot to adapt to failures in its sensors, learning to use its remaining sensors to perform its mission. This research explored autonomous systems that can continue to learn throughout their lives, adapting to changes in the environment and in their own capabili-

ties. While operating in the real world, the vehicle is always exploring different strategies via an internal simulation model; the simulation, in turn, is changing over time to better match the world.

2000 DarkHORSE/ WAR HORSE

The DarkHORSE project demonstrated that a hyperspectral sensor could be used for autonomous detection of air and ground targets. WAR HORSE demonstrated the first autonomous, real-time, visible hyperspectral target detection system flown aboard a Predator UAV. The system provides the ability to detect manmade objects in areas of natural background, for reconnaissance and surveillance.

2000 Extender

This 10-ft-wingspan, air-drop-deployable UAV for electronic warfare missions had

a battery-powered electric motor and 7.5-lb payload capacity. It could perform

an entirely autonomous mission or be directed in real time through an RF link. It was designed to glide for 77 miles from a 5-mile release altitude.

2000 Navy Smart Valve

As part of the DC-ARM program, NRL developed Smart Valves embedded with pressure sensors and processors that

allow the valve to identify fire main ruptures, and thereby automate opening or closing of the valve as appropriate.

2001 AN/WLD-1 RMS(O)

NRL developed and transitioned this oceanographic variant of the Remote

Minehunting System semi-submersible UUV by developing a swappable center section equipped with hydrographic survey sensors.

2001 Mobile Network System Emulation

NRL developed sophisticated mobile ad hoc network emulation systems and analysis tools to support the design, development, and testing of distributed autonomous networking protocols. This capability helped bridge the gap between simulation and expensive, limited field testing of self-organizing network systems.

2001 Hybrid Cognitive/ Reactive Autonomous System

To create more intelligent autonomous systems, NRL developed a hybrid control system that combined process models of human cognition for performing high-level reasoning, with evolved reactive behaviors for low-level control of an autonomous system.

2002 Coevolution of Form and Function

For an autonomous micro air vehicle, NRL developed a system that used simulation to evolve both an optimal minimum sensor suite, and reactive strategies for navigation and collision avoidance using data from the evolved sensor suite.

2002 CFD Simulations of UAVs

Aerodynamic characterization and performance assessment of micro air vehicles via computational fluid dynamics (CFD) led to the controller development for the MITE and Dragon Eye vehicles.

2002 FINDER

This long-endurance UAV (Flight Inserted Detector Expendable for Reconnaissance) can carry payloads including chemical sensors, high-resolution battle damage assessment imagers, GPS jammer homing sensors, and SIGINT sensors. Launched from a Predator UAV, it can report its findings in near real time


through the Predator to a ground control station for distribution to the warfighter, and can retrieve samples for laboratory testing.

2002 Flapping Foil Propulsion in Insects and Fishes

Computations at NRL have provided insights into unsteady force production in nature that guide the design of

insect-like autonomous air vehicles and fish-like autonomous undersea vehicles. Flapping foil propulsion has many applications, such as submersible propulsion, maneuvering and flow control, and aerodynamics of unconventional micro air vehicles (MAVs). The Biplane
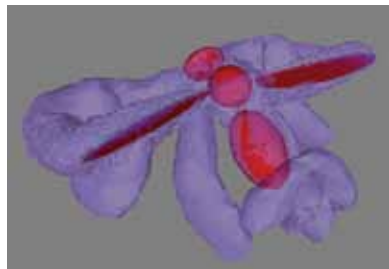
Insectoid Travel Engine (BITE) MAV and a pectoral fin–driven UUV make use of these bio-inspired mechanisms for propulsion.

2002 GRACE

A joint project with academic and corporate partners, GRACE was an autonomous robot system entered in the 2002 AAAI Robot Challenge. GRACE acted

autonomously to travel, without a map, from the front floor of a convention center to the registration desk by interacting with people and reading signs, then registered, made its way to an assigned location, presented a talk, and answered questions about itself.

2002 MITE

The Micro Tactical Expendable micro air vehicle is designed to be the smallest practical aircraft that can still perform useful Navy missions, such as over-the-hill reconnaissance, surveillance, and electronic warfare. Different wingspans (10–24 in.) are used depending on the payload and endurance required. Several very low cost autonomous flight control

systems have been demonstrated on the vehicle.
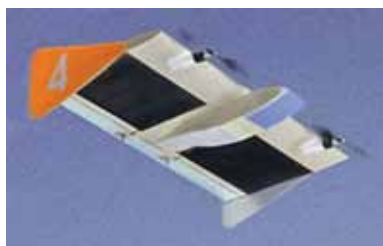
2003 Dragon Eye

This lightweight, backpackable UAV is an affordably expendable sensor platform launched with a "slingshot." It provides real-time reconnaissance, battle

damage assessment, and threat detection through a miniature ground control station. Dragon Eye has provided critical intelligence in the Iraq and Afghanistan conflicts.

2003 Finding Hidden People (Hide and Seek)

NRL scientists extended their models of visual perspective-taking to address the problem of searching for people who are trying to hide (e.g., snipers). Using a cognitive process model of how people hide, they developed a cognitive model for determining likely hiding places in the environment, and integrated this high-level reasoning with a reactive robot controller. The same model could be used to reason about what makes a good hiding place, and resulted in a robot that could play "hide and seek" with a human.

2003 Multicast Forwarding in Mobile Ad Hoc Networks

NRL produced the first draft Internet specification for simplified, self-organizing mobile multicast. Simplified Multicast Forwarding (SMF) is useful for autonomous group data forwarding since
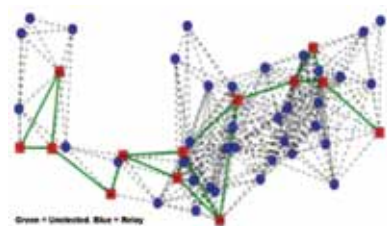
it is a highly distributed and resilient protocol approach that can adapt to change with minimized control signaling and can operate with a variety of optimized network relay set algorithms.

2004 Analogical Hypothesis Elaborator for Activity Detection (AHEAD)

NRL developed a software system that uses computational analogy to assess the support that a given hypothesis has in a given body of evidence. The system demonstrated its utility to perform this task for simulated terrorist activities, where the evidence would include facts such as specific actions by specific people who have known organizational, family, or other types of relationships.

2004 BUG

The Benthic Unattended Generator persistently generates electrical power in marine environments from oxidation of sediment organic matter with oxidants in overlying water. The BUG enables very long-term use of autonomous marine deployed scientific and surveillance instruments that are presently limited in duration by batteries.

2005 AutoSurvey®

NRL-patented AutoSurvey® autonomous line running software, originally developed for the ORCA unmanned vehicle,

was transitioned to all NAVOCEANO TAGS 60 class survey ships. AutoSurvey provides up to 60% reduction in survey time in areas with rough terrain.

2005 Dragon Warrior/ Vantage™

Originally developed with the Marine Corps Warfighting Laboratory for reconnaissance and communications relay

missions, this vertical take-off and landing UAV resembles a small helicopter and can be transported in a Humvee. It features fully autonomous flight operation, a 44-hp heavy-fuel engine, and a ducted electric tail rotor.

2005 Scalable Robust Self-Organizing Sensors (SRSS)

NRL designed multiple-function sensor devices capable of self-organizing, autonomous network formation and data routing. This capability enabled distributed sensors and other devices to form a distributed data network when deployed in an ad hoc manner with minimum planning and management. Both autonomous mobile and non-mobile devices (e.g., distributed cameras) could discover distributed sensor events, collaborate over the network, and take appropriate action with minimal human interaction.

2005 Visual–Spatial Perspective Taking

An important aspect of human–human interaction is visual-spatial perspective-taking, in which one participant is able

to interpret a scene from the other's point of view. NRL developed a computational cognitive process model for

perspective-taking and integrated it with a robot. The robot successfully solved a series of perspective-taking problems and was able to resolve different frames of reference to facilitate collaborative problem solving with a person.

2006 Control of a Team of Robots

NRL developed a sketch-based interface and algorithms that allow one operator, using a tablet PC, to manage a team of robots performing tasks such as surveillance, reconnaissance, damage assessment, and search and rescue. A precise map of the environment is not required. Rather, the user sketches a qualitative map of a live scene and directs the team using the interface.

2006 Swarm Control with Physicomimetics

Advantages of swarm intelligence include robustness to uncertainty and change, the ability to self-organize, and a decentralized nature which makes the population less vulnerable. One method of implementing swarm intelligence is the artificial physics representation of physicomimetics, in which agents behave as point-mass particles and respond to artificial forces generated by local interactions with nearby particles. NRL is taking a multitiered approach to the design and real-time control of physicomimetics swarms that includes machine learning techniques for the acquisition of swarm behavior modes and a human–swarm interface to dynamically influence swarm behavior.

2007 Cooperative Multi-Agent Systems in Mobile Ad Hoc Networks

This project developed and demonstrated various multi-agent systems that autonomously self-organized and communicated teamwork information using NRL-based ad hoc networking technology. The agents were capable of seamlessly fragmenting and coalescing topologically as network and mobility conditions varied. Agents could autonomously take on and optimize various mission roles but could also view their network function as a role and participate in sustaining the network by dynamically positioning themselves as relays within a distributed, mobile scenario.

2007 Coping with Information Overload

NRL developed methods to automatically accelerate multiple acoustic channels and prioritize message trafficking. This research allows watchstanders to process the ever-increasing amounts of information generated and exchanged in combat information centers aboard Navy ships, thereby reducing workloads and the errors resulting from the simultaneous transmission of aural messages.

2008 Embodied Cognition

NRL developed the first cognitively plausible robot architecture, ACT-R/E. Based on what is known about human reasoning and memory (from both psychological studies and fMRI data), ACT-R/E, using the robot's perceptual inputs, performs reasoning and decision making in a way that is similar to how people reason, and allows the robot to interact naturally with people.

2008 FREND: Autonomous Rendezvous and Docking

NRL developed and ground-demonstrated guidance and control algorithms

to allow a robotic servicing vehicle to autonomously rendezvous and dock with satellites not pre-designed for docking. The demonstration was completed in a realistic spaceflight environment under full autonomy with no human-in-the-loop assistance.

2008 Gaze Following

NRL developed a system that uses a combination of visual perception algorithms and computational cognitive models to allow a robot to track a person's head movements and understand that person's focus of attention. This allows the robot to work well in joint tasks with people.

2008 Gesture Recognition

NRL's system for learning and recognizing static and dynamic hand gestures (both one-handed and two-handed) allows autonomous systems to understand a person's communicative intent, improving human–robot interaction in joint tasks.

2008 Tracking Conversation with Vision and Audition

One of the goals of human–robot interaction research is to have natural dialog, which requires conversation tracking. NRL developed a system that uses sound localization to guide the robot's vision system to find the speaker. The audition and visual streams are integrated to form a coherent representation of the speaker. This system allowed a robot to correctly track conversations.

2008 UUV Mission Planner

Demonstrated during RIMPAC 08, the UUVMP provides automated planning and monitoring for fleets of unmanned underwater gliders on long-endurance (months) missions. An advanced vehicle motion model allows simulation using forecast currents to predict trajectory.

2009 XFC

The eXperimental Fuel Cell unmanned aerial system is a fully autonomous, affordably expendable surveillance plat-

form. The folding-wing UAV ejects from a transport tube, unfolds to its X-shaped configuration, and can fly for 6 hours. The hydrogen fuel cell provides power for electric propulsion, command and control, avionics, and payload operation. XFC is being modified for launch from a submarine.

## 2009 Automated Image Understanding for Maritime Threat Analysis

NRL developed an integrated video processing and learning system for object identification, maritime vessel behavior recognition, and threat analysis from land-based optical video cameras. Previous approaches were limited to perimeter defense penetration alerts.

2009 InterTrack

NRL collaborated to develop a user interface to a video surveillance system that permits easier natural interaction with the video output. InterTrack also provides an automatic inferencing capability that removes some of the burden of users' surveillance tasks and creates more autonomous or system-generated analyses.

2009 Optimization of ISR Platforms to Improve Signal Collection in Maritime Environments

NRL developed intelligence, surveillance, and reconnaissance (ISR) optimization algorithms for tracking targets of interest in the maritime domain. The algorithms simultaneously optimize over several measures of interest (e.g., suspicious vessel movements, cargo, ports, piracy areas), "difficulty" measures (e.g., meteorological conditions), and ISR
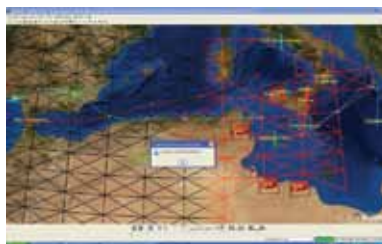
performance characteristics to improve signal collection for maritime domain awareness.

2009 Predicting and Preventing Procedural Errors

Using a combination of theories of human memory (memory for goals) and an eyetracker, NRL created a system that can predict when an operator is about to make a post-completion error before the error actually occurs, and give a just-in-time cue to prevent the error from being made.

2009 Self-Organizing Airborne Networking Backbones

NRL collaborated to develop and demonstrate technology for hybrid air/surface (ground) networks that self-organize and adapt to both gateway and legacy network infrastructures. NRL multicast routing and distributed applications were critical to the success of the field demonstration of multiple UAVs and surface nodes in the same mobile network.

2009 Ion Tiger

This UAV flew for 26+ hours with a 5-lb payload by using a high-energy hydrogen fuel cell system for electric propulsion, exceeding by 6× the endurance provided by batteries. With this demonstration, NRL created a new class

of stealthy, small, unmanned air vehicles capable of "big vehicle missions." A new liquid hydrogen fuel tank may extend the UAV's endurance to 72 hours.

2010 Assessing Translation Memory Technology

NRL teamed with the National Virtual Translation Center to evaluate the effectiveness of Translation Memory technology, which provides automated assistance to human translators for timely and cost-effective translations of documents related to military strategy and national security.

2010 Automatic Face Recognition

NRL developed an algorithm to perform automatic face recognition that has an extremely low false positive rate and that can work in a wide variety of environments with a minimal number of photos of the target subject.

2010 Bio-Inspired Deformable Fin UUV

This unmanned undersea vehicle is propelled and controlled using fish-like, biorobotic fins inspired by the bird wrasse, a coral reef fish. Actuation of individual ribs within each fin creates the curvatures necessary to generate the high-

magnitude, variable-direction forces that enable precise, low-speed maneuvering in highly dynamic environments such as nearshore and cluttered areas with currents and waves.

2010 Dynamic Goal Management

NRL developed methods for goal-driven autonomy that permit agents to automatically self-select their goals. These are particularly valuable for unmanned systems on long-duration deployments in complex environments.

2010 Flow Immunosensor Payload

NRL demonstrated its flow immunosensor payload on a Hydroid REMUS 100 AUV. Low parts-per-billion levels of

TNT were detected in a simulated plume while underway, and data acquisition was observed remotely in real time over a Web-based interface.

2010 Foundations of Collective Classification

NRL developed and evaluated methods for leveraging relations among instances in supervised learning (classification) tasks.

2010 Serverless Messaging Systems

NRL designed and developed serverless messaging systems that effectively operate in highly distributed and disruptive network environments. This system also supports proxy interfaces to standards-based clients and servers that cannot normally operate without server centralization. A serverless messaging system extension allows more autonomous operations by combining effective group discovery and collaboration among multiple communication nodes.

2010 Shibboleth

NRL developed automatic procedures for determining the native language of non-native speakers of English, lessening the burden on warfighters and security personnel in sensitive environments such as border patrols, VBSS (visit, board, search, and seizure) operations, and foreign countries.

2010 Theory of Mind

NRL developed a system that, when an anomaly is discovered, runs multiple simulations to determine the most likely reason for that anomaly. The anomaly can then be pointed out to a person along with a possible (most likely) solution.

2010 Volume Sensor

This multisensor shipboard detection system provides early warning detection of flames, smoke, thermally hot objects, pipe rupture, and gas leaks through improved situational awareness. Based on data fusion, the system combines video image detection and machine vision software with spectral sensors and acoustic data inputs to correctly identify damage

control events and discriminate against false positives.

2010 Unmanned Semi-Submersible (USS)

NRL demonstrated this vehicle for shallow-water (2 m to 200 m) bathymetry and sidescan surveying. It provides vastly superior coverage rates (2× or greater) compared to unmanned surface

or underwater vehicles, and is excellent for rapid response in hostile environments (combat, disasters).

2011 Low Frequency Broadband Sonar

NRL's AUV-based broadband active sonar system for the high-performance detection and identification of underwater mines was transitioned to production. The "squint capable" synthetic aperture sonar measures scattering cross-sections very precisely for identification based on
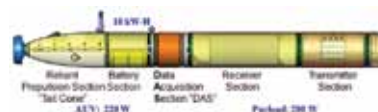
structural acoustic features. The sonar is configured on a long-endurance, quiet AUV that navigates using a fusion of Doppler velocity measurement, fiber-optic gyroscope inertial navigation, and GPS. Deployment is anticipated on the Littoral Combat Ship and other platforms of opportunity. NRL is extending the technology to longer ranges and exploring the applicability to antisubmarine warfare.

2011 Behavior Recognition and Threat Analysis for Unmanned Sea Surface Vehicles

NRL is developing and testing methods for automatically recognizing behaviors of maritime vessels and assessing their threat, using sensor data from unmanned sea surface vehicles.

2011 Evaluating Deep Learning Technology

NRL is evaluating novel methods for automatic feature extraction for event detection from optical videos, sentiment analysis from text documents, surveillance, and other complex classification tasks.

2011 Facilitating Resumption After an Interruption

NRL developed a computational cognitive model that can help people resume a task after being interrupted. The model can understand the effect of an interruption on a person, and offer help so the person can continue the task with less error.

2011 Highly Distributed Networked Services Discovery

NRL developed working prototypes of highly distributed network service discovery that operates across self-organizing networks in the absence of any hierarchy or server availability. This technology allows more distributed systems to be deployed hosting services and applications that can more effectively self-organize and adapt at the middleware and application layer.

2011 RAFT Robotic Boat Refueling

NRL demonstrated the first autonomous boat-to-boat refueling system, capable of mating a refueling fitting with an autonomous surface vehicle fuel tank in sea states exceeding 3 ft maximum wave height.

2011 Supervisory Control of Multiple Autonomous Vehicles

A single operator controlling multiple autonomous vehicles can experience cognitive overload. NRL built a model that predicts when human performance limits have been reached, in order to provide automatic alerts to direct the operator's attention to critical events.

2011 Autonomous Network Modeling Framework

NRL developed a framework for rapidly constructing distributed wireless network protocol test cases for controlled, repeatable, emulation- and simulation-based experimentation. The resulting capability is being used to plan and execute complex mobile network scenarios involving large numbers of heterogeneous wireless links and nodes operating in challenging environmental conditions. Instrumentation and visualization tools provide an observable and interactive experimentation environment in real time.

2011 Damage Control Technologies for the Twenty-First Century

The DC-21 program is developing humanoid robotic systems to support future shipboard firefighting operations. Advanced human–system interfaces will enable natural human–robot interactions and supervisory control. The program consists of four highly integrated elements: Shipboard Autonomous Firefighting Robot (SAFFiR), Human–Robot Interaction for Autonomous Firefighting Robots, Fire Suppression Methodologies and Real-Scale Demonstrations, and Robotic Firefighter Sensor Development.

2011 Sea Nimbus

With a goal of improving detection of the very quietest underwater threats in shallow water environments, NRL created an autonomous distributed sensing and identification technology for short- (<1 month) and long- (2 to 10 months) duration monitoring over a wide area. This approach deploys large numbers of small, inexpensive, power-efficient/harvesting, intercommunicating but otherwise unconnected underwater sensor nodes which through their own cooperative decision making rise to the surface and RF-link contact information and then re-submerge to continue monitoring. The principal focus is antisubmarine warfare in littoral ocean areas, with applications in other environments including rivers and harbors.
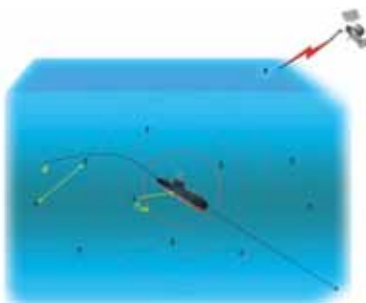
2011 Robotic Materials Testing System

NRL's robotic system provides high-rate, fully automated testing to generate large quantities of response data for characterizing the behavior of complex materials.
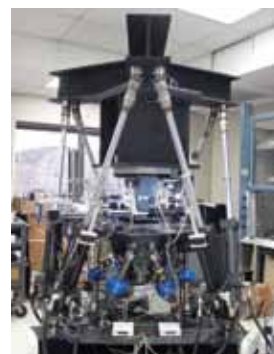
It features six-degree-of-freedom multiaxial loading, a wireless sensor network infrastructure, and a whole-field 3D optical method for measuring displacement and strain fields. Such a system is expected to influence the design, certification, and qualification methodologies used for sea and aerospace platforms built from high-performance composite and other anisotropic materials.

2012 Laboratory for Autonomous Systems Research

NRL opened the LASR to become a nerve center for autonomous systems research for the Navy and Marine Corps.

NRL Hosts Its First Annual

KARLES INVITATIONAL CONFERENCE

AUGUST 15-16, 2011

& MICROBIAL SYSTEMS SYNTHETIC BIOLOGY

The professional contributions of Dr. Jerome Karle, 1985 Nobel Laureate in Chemistry, and Dr. Isabella Karle, a 1993 Bower Award Laureate and 1995 recipient of the National Medal of Science, were critical in enabling the resolution of the molecular structure and function of complex macromolecules. While fundamental in nature, the Karles' contributions continue to have a significant impact on the basic and applied physical, chemical, metallurgical, geological, and biological sciences. In commemoration o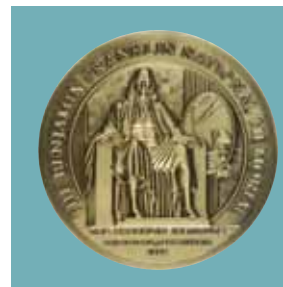f their achievements and broad scientific impact, the U.S. Naval Research Laboratory in Washington, DC, has initiated an annual invitational conference that will convene the leading authorities and innovators from scientific disciplines that are on the verge of producing contributions with similar reach and impact. In recognizing the rapid progress of two fields that are helping the research community realize the promise of the post-genomics era, we selected "Microbial Systems and Synthetic Biology" as the topic for the first annual Karles Invitational Conference.

The completion of the first decade of research in both fields has resulted in the development of the tools and methods necessary to make global cellular measurements, integrate these data to map, model, and predict cellular function, and use this systems-level understanding to guide the rational design, construction, and optimization of novel genetically engineered circuits and organisms. As a result of this considerable progress, both fields now lie on the verge of combining to develop transformative bioengineered solutions for recalcitrant problems in energy and biofuel synthesis, environmental remediation, chemical and biological sensing, pharmaceutical synthesis, and materials science. It is this potential that has elicited considerable interest and investment, and resulted in the prioritization of systems and synthetic biology research in academia, industry, and government.

The assembled two-day program embodied the diversity of ideas, research approaches, and microbial systems utilized in both of these fields and provided a forum for approximately 150 multidisciplinary scientists, sponsors, and policy makers to discuss the current state, challenges, and future of microbial systems and synthetic biology research.

| RADM Nevin P. Carr | John Montgomery | Bhakta B. Rath | David A. Honey | Subra Suresh | Leroy Hood |

John Montgomery welcomes participants to the Karles Invitational Conference.

Keynote speaker David A. Honey with Bhakta Rath and John Montgomery.

Keynote speaker Leroy Hood with Bhakta Rath and John Montgomery.

Bhakta Rath, Subra Suresh, RADM Nevin Carr, and John Montgomery.

Systems Biology speakers Gary Vora, Pamela Silver, Hiroaki Kitano, and Bernhard Palsson with Bhakta Rath and John Montgomery.

Synthetic Biology speakers Drew Endy, Christopher Voigt, John Glass, and Steven Benner with Bhakta Rath and John Montgomery.

Synthetic Biological Applications speakers Adam Arkin, Zach Serber, Arthur Grossman, and Andreas Schirmer with Bhakta Rath and John Montgomery.

Bhakta Rath presented a lunch seminar on the "Life and Times of Jerome and Isabella Karle."

Participants enjoyed a lunch seminar titled, "An Introduction and Brief History of the Naval Research Laboratory."

A few members of the organizing committee – Ashley Monie, Ena Barts, Jennifer Moran, and Denise Quinn.

Jerome and Isabella Karle with their daughters, Madeleine Tawney and Louise Hanson; their grandson Brian Tawney; John Montgomery, Bhakta Rath, and Lou Massa.

Participants enjoyed the reception at the end of Day 1.

The Karle Room

Drs. Jerome and Isabella Karle
Dedicated on June 24, 2008

This room is dedicated to Drs. Jerome and Isabella Karle, and their more than six decades of exemplary service to the Naval Research Laboratory, the Department of the Navy, the Department of Defense, and the Nation. Their combined research in diffraction theory and its application to the direct determination of complex atomic structures have been lauded throughout the world.

Awards

1985 • 1995 • 1993

1985 NOBEL CHEMISTRY

Reflections of an Era

EARLY DIFFRACTION STUDIES

THE NON-NEGATIVITY CRITERION

THE "UNSOLVABLE" PHASE PROBLEM SOLVED

THE SYMBOLIC ADDITION PROCEDURE

THE NOBEL PRIZE

NRL Karle Room Display

NRL completed its display commemorating the lives and research of Drs. Jerome and Isabella Karle in Building 226 at NRL's Washington, DC campus. The panels describe the Karles' molecular structure research from the time they came to NRL in 1946 to their retirement in 2009, including the research that led to the 1985 Nobel Prize in Chemistry.

The display includes the many congratulatory letters the Karles received upon their retirement, from President Barack Obama, Secretary of Defense Robert Gates, Secretary of the Navy Ray Mabus, and other dignitaries.

Other panels describe the Karles' colleagues in the Laboratory for the Structure of Matter, some applications of the research conducted by their group, and the many awards and honors the Karles received throughout their long and successful careers.

The Naval Research Laboratory

SENDER (1998) — The man-portable Self-Navigating Drone, Expendable/Recoverable provided advanced technology in a simple and affordable platform. Flown autonomously or under radio control, it featured electric propulsion, advanced composite structure, digital microprocessor autopilot, GPS navigator, and lithium propulsion batteries.

NRL — OUR HERITAGE

The Naval Research Laboratory's early 20th-century founders knew the importance of science and technology in building naval power and protecting national security. They equally knew that success depended on taking the long view, focusing on the long-term needs of the Navy through fundamental research. NRL began operations on July 2, 1923, as the United States Navy's first modern research institution.

Thomas Edison's Vision: The first step came in May 1915, a time when Americans were deeply worried about the great European war. Thomas Edison, when asked by a *New York Times* correspondent to comment on the conflict, argued that the Nation should look to science. "The Government," he proposed in a published interview, "should maintain a great research laboratory....In this could be developed...all the technique of military and naval progression without any vast expense." Secretary of the Navy Josephus Daniels seized the opportunity created by Edison's public comments to enlist Edison's support. He agreed to serve as the head of a new body of civilian experts — the Naval Consulting Board — to advise the Navy on science and technology. The Board's most ambitious plan was the creation of a modern research facility for the Navy. Congress allocated $1.5 million for the institution in 1916, but wartime delays and disagreements within the Naval Consulting Board postponed construction until 1920.

The Laboratory's two original divisions — Radio and Sound — pioneered in the fields of high-frequency radio and underwater sound propagation. They produced communications equipment, direction-finding devices, sonar sets, and perhaps most significant of all, the first practical radar equipment built in this country. They also performed basic research, participating, for example, in the discovery and early exploration of the ionosphere. Moreover, the Laboratory was able to work gradually toward its goal of becoming a broadly based research facility. By the beginning of World War II, five new divisions had been added: Physical Optics, Chemistry, Metallurgy, Mechanics and Electricity, and Internal Communications.

World War II Years and Growth: Total employment at the Laboratory jumped from 396 in 1941 to 4400 in 1946, expenditures from $1.7 million to $13.7 million, the number of buildings from 23 to 67, and the number of projects from 200 to about 900. During WWII, scientific activities necessarily were concentrated almost entirely on applied research. New electronics equipment — radio, radar, sonar — was developed. Countermeasures were devised. New lubricants were produced, as were antifouling paints, luminous identification tapes, and a sea marker to help save survivors of disasters at sea. A thermal diffusion process was conceived and used to supply some of the ^{235}U isotope needed for one of the first atomic bombs. Also, many new devices that developed from booming wartime industry were type tested and then certified as reliable for the Fleet.

Post-WWII Reorganization: The United States emerged into the postwar era determined to consolidate its significant wartime gains in science and technology and to preserve the working relationship between its armed forces and the scientific community. While the Navy was establishing its Office of Naval Research (ONR) as a liaison with and supporter of basic and applied scientific research, it was also encouraging NRL to broaden its scope and become, in effect, its corporate research laboratory. There was a transfer of NRL to the administrative oversight of ONR and a parallel shift of the Laboratory's research emphasis to one of long-range basic and applied investigation in a broad range of the physical sciences.

However, rapid expansion during WWII had left NRL improperly structured to address long-term Navy requirements. One major task — neither easily nor rapidly accomplished — was that of reshaping and coordinating research. This was achieved by transforming a group of largely autonomous scientific divisions into a unified institution with a clear mission and a fully coordinated research program. The first attempt at reorganization vested power in an executive committee composed of all the division superintendents. This committee was impractically large, so in 1949, a civilian director of research was named and given full authority over the program. Positions for associate directors were added in 1954, and the laboratory's 13 divisions were grouped into three directorates: Electronics, Materials, and Nucleonics.

The Breadth of NRL: During the years since World War II, the Laboratory has conducted basic and applied research pertaining to the Navy's environments of Earth, sea, sky, space, and cyberspace. Investigations have ranged widely — from monitoring the Sun's behavior, to analyzing marine atmospheric conditions, to measuring parameters of the deep oceans. Detection and communication capabilities have benefitted by research that has exploited new portions of the electromagnetic spectrum, extended ranges to outer space, and provided a means of transferring information

reliably and securely, even through massive jamming. Submarine habitability, lubricants, shipbuilding materials, firefighting, and the study of sound in the sea have remained steadfast concerns, to which have been added recent explorations within the fields of virtual reality, superconductivity, biomolecular science and engineering, and nanotechnology.

The Laboratory has pioneered naval research into space — from atmospheric probes with captured V-2 rockets, through direction of the Vanguard project (America's first satellite program), to inventing and developing the first satellite prototypes of the Global Positioning System (GPS). Today, NRL is the Navy's lead laboratory in space systems research, as well as in fire research, tactical electronic warfare, microelectronic devices, and artificial intelligence.

The consolidation of NRL and the Naval Oceanographic and Atmospheric Research Laboratory, with centers at Bay St. Louis, Mississippi, and Monterey, California, added critical new strengths to the Laboratory. NRL now is additionally the lead Navy center for research in ocean and atmospheric sciences, with special strengths in physical oceanography, marine geosciences, ocean acoustics, marine meteorology, and remote oceanic and atmospheric sensing.

The Twenty-First Century: The Laboratory is focusing its research efforts on new Navy strategic interests in the 21st century, a period marked by global terrorism, shifting power balances, and irregular and asymmetric warfare. NRL scientists and engineers are working to give the Navy the special knowledge, capabilities, and flexibility to succeed in this dynamic environment. While continuing its programs of basic research that help the Navy anticipate and meet future needs, NRL also moves technology rapidly from concept to operational use when high-priority, short-term needs arise — for pathogen detection, lightweight body armor, contaminant transport modeling, and communications interoperability, for example. The interdisciplinary and wide-ranging nature of NRL's work keeps this "great research laboratory" at the forefront of discovery and innovation, solving naval challenges and benefiting the nation as a whole.

HIGHLIGHTS OF NRL RESEARCH IN 2010

The scientific community at NRL conducts innovative research across a wide spectrum of technical areas, much of it detailed in the *NRL Review* chapters ahead. The following is a selection of the many projects pursued during 2010.
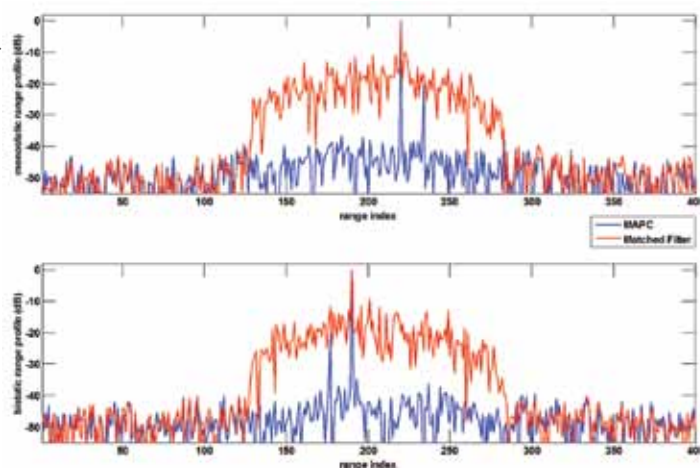

Plots of the received signal power at a radar subjected to EMI from a second radar. At the receiver, filtering is performed to attempt to separate the radar signal of interest (top plot, "monostatic") from the interfering signal (bottom plot, "bistatic"). The use of standard matched filter pulse compression (red) does little to suppress the EMI that can obscure low radar cross section (RCS) targets. The MAPC (blue) algorithm suppresses the EMI, thus unmasking the low RCS targets at range indices 235 (top) and 175 (bottom).

Shared-Spectrum Radar: The operation of proximate, concurrently transmitting radars typically requires that the transmissions of each radar be separated in frequency (i.e., frequency multiplexed) such that the radars are not sources of electromagnetic interference (EMI) to one another. As RF spectral crowding becomes more severe, frequency multiplexing alone may not be able to support the number of systems that desire to operate in a given portion of the spectrum, thus motivating the development of shared-spectrum radar. NRL's Multistatic Adaptive Pulse Compression (MAPC) algorithm has been shown, via simulation, to mitigate interference successfully in a shared-spectrum radar scenario. The MAPC algorithm is a waveform diversity technique, wherein each radar transmits a unique waveform, and signal processing in the receiver is used to separate the individual waveforms, perform pulse compression, and mitigate interference. Experiments conducted under the Adaptive Pulse Compressor program using a dual-channel X-band multistatic radar test bed demonstrated greater than 25 dB sensitivity improvement relative to the Standard Pulse Compressor whose performance is dictated by the cross correlation of the radar waveforms.

Examples of two different views (two sets of vessel track data) presented to users based on users' privileges (e.g., need-to-know).

Federated Authentication and Authorization System: Security architectures and mechanisms are essential enablers for data sharing because data stewards are more willing to share when they feel secure with the data protection mechanisms of the host system. Maritime Domain Awareness (MDA) enterprise applications require the fusion and analysis of many types of data (e.g., vessel, cargo, people, infrastructure) from multiple data stewards, and thus require such security services. A federated authentication and authorization system based on bilateral agreements has been developed to manage users from multiple organizations, or coalition partners, that have different need-to-know. An attribute-based access control (ABAC) mechanism that works with Oracle label security (OLS) has also been developed to satisfy different data handling requirements. The technology provides secure information sharing through data labeling, federated identity management, single sign-on and logout, and ABAC. These capabilities have been seamlessly integrated into the MDA Enterprise Node that will support joint users globally.
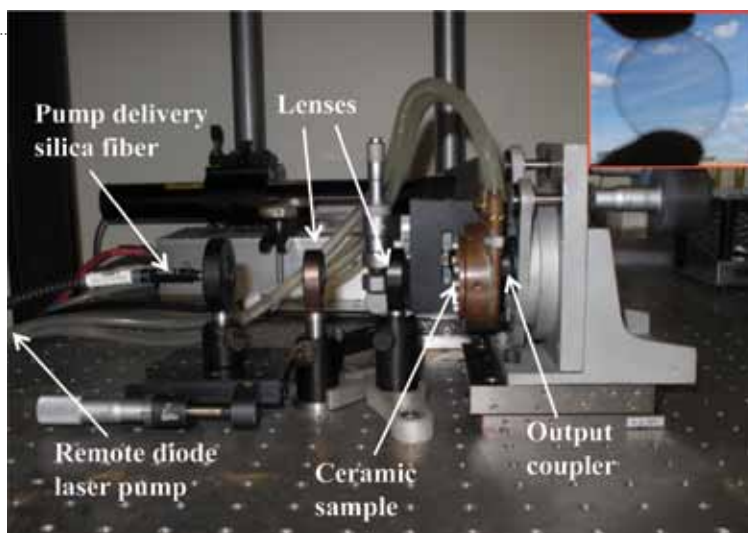
Ceramic laser demonstration test bed. The inset shows the transparent 10% Yb^{3+}:Lu_2O_3 ceramic.

Ceramic Laser Demonstrates 74% Efficiency: Lightweight and compact high-power lasers will enable integration of directed energy weapons systems on tactical platforms. Solid-state crystalline lasers would be ideal for these applications, but are difficult to grow due to high-temperature growth issues that limit size and quality. However, NRL's Optical Sciences Division has overcome these challenges by developing a low-temperature ceramization process to fabricate hard-to-grow materials with high optical quality. This was exemplified by fabrication of ultra-high-purity Yb^{3+}-doped Lu_2O_3 nanopowders and then hot pressing to make a highly transparent 10% Yb^{3+}:Lu_2O_3 ceramic. The ceramic demonstrated lasing at 1080 nm with a world-record efficiency of 74%. This is a remarkable result considering the high doping level of 10% Yb^{3+}. This result paves the way forward for scaling to beyond 100 kW class laser systems.
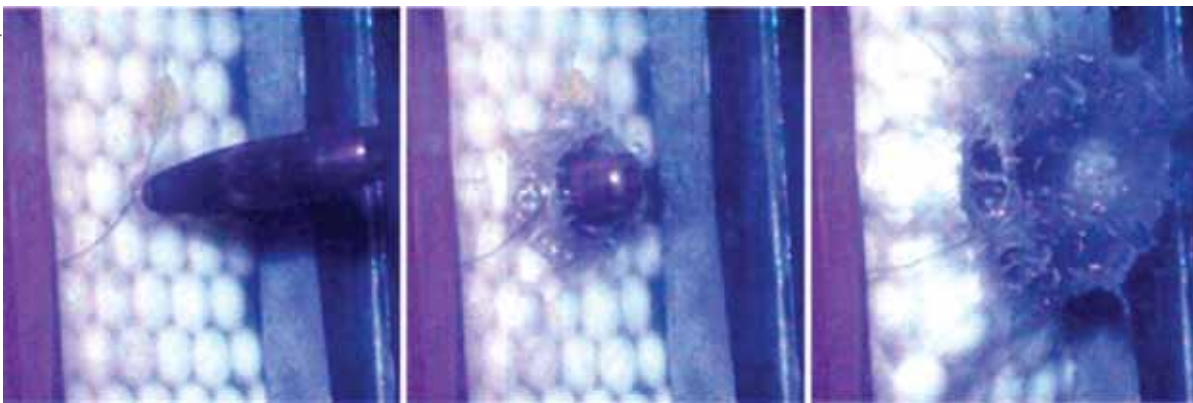
Series showing a 50 cal armor-piercing bullet arriving at the front face of the armor. The impact granulates the ceramic balls; however, the particles are constrained by the surrounding elastomer, retaining their effectiveness.

Infrastructure Protection – Munitions Transport: New legislation requires that "sensitive" munitions be protected over their life cycle. NRL has developed shielding that protects missiles during transport on trucks across public roads from attack by .50 caliber armor-piercing and other ammunition. The technology can be readily extended to other "insensitive munitions" applications.
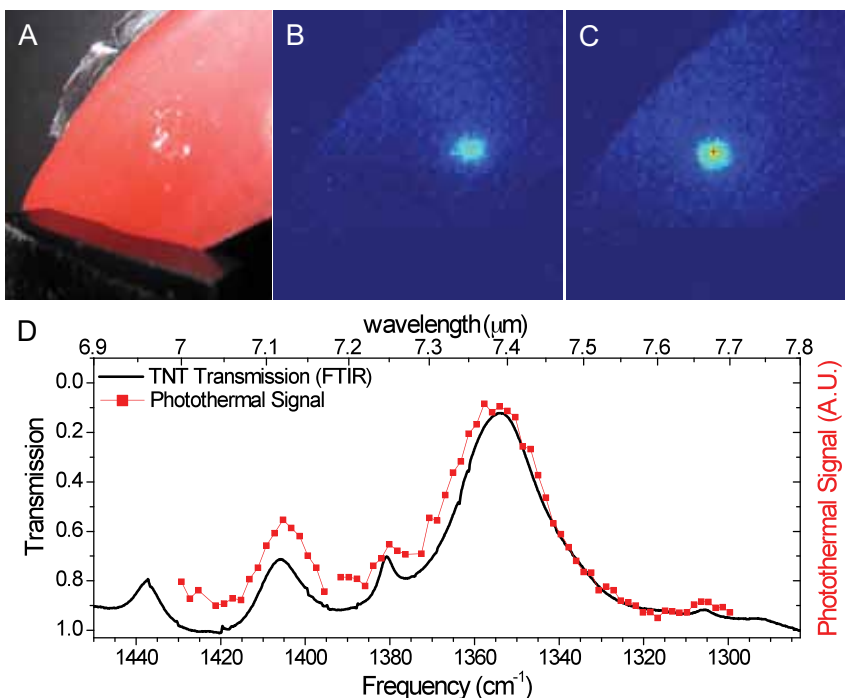

Experimental results from the Remote Explosives Detection (RED) system. (A) Traces of RDX deposited onto a plate cut from an automobile. (B) Infrared camera image shows the heating effect of the laser (light blue area) is minimal where no RDX is present. (C) Where RDX is present, the thermal image clearly reveals the heating due to the laser (bright red dot within the light blue area). (D) High selectivity: the measured intensity of the photothermal signal (red) closely matches the signature infrared absorption spectrum of the analyte (black), which in this example is TNT.

Standoff Spectroscopic Detection of Trace Explosive Residues Using Infrared Photothermal Imaging: Developing technology that can detect explosives without the need for swabbing surfaces is a major thrust for the Departments of Defense and Homeland Security. The ultimate goal is real-time detection from significant standoff distance using techniques that are safe to people and nondamaging to objects. At NRL, we have developed and field tested a technique that meets these goals. Our approach, based on infrared lasers and a thermal imaging array, has been demonstrated at the Yuma Proving Ground to detect TNT, RDX, PETN, C4, Tetryl, Comp B, PBX4, and PE4 explosives residues from at least 10 meters away. Light from an infrared laser tuned to a wavelength that is selectively absorbed by analytes of interest is directed toward the surface to be interrogated. Thermal imaging of the surface reveals the resultant localized laser-induced heating. Advantages of this technique relative to competing optical approaches include eye-safety, stealth, sensitivity, selectivity, and imaging capability. In 2010, we expanded the approach to include multiwavelength excitation for enhanced sensitivity and selectivity.
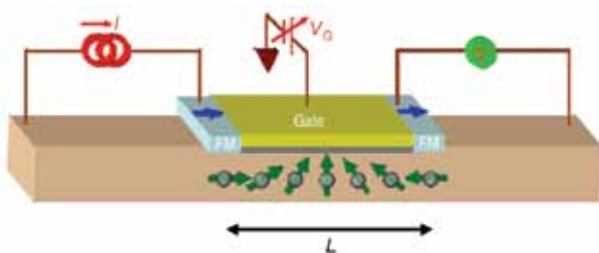
Top: Perspective sketch of the spin-injected field effect transistor. Bottom: Examples of data showing oscillatory channel conductance. The wavelength of the oscillation is predicted to scale inversely with the distance L between the two FM electrodes, as confirmed by the data.
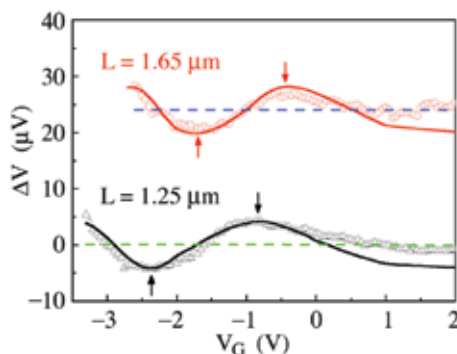
Electric Field Control of Spin Precession in a Spin-Injected Field Effect Transistor: Two decades ago, Datta and Das proposed an experiment involving spin injection, detection, and spin precession caused by a gate voltage and special relativistic effects on ballistic electrons in the two-dimensional electron gas (2DEG) channel of a field effect transistor. In their famous proposal, spin-polarized electrons are injected into the channel from the left ferromagnetic electrode (FM), with their spin orientation perpendicular to their velocity vector. In the rest frame of the electrons, the gate electric field transforms as an effective magnetic (Rashba) field that causes a torque-driven spin precession. The rate of spin precession is proportional to the gate voltage (V_G), and the voltage recorded at the second FM is high (low) when the spins are parallel (anti-parallel) with the magnetization of the electrode. The result is a channel conductance that oscillates as a function of gate voltage. NRL has made the first experimental confirmation of their predictions using an InAs single quantum well (SQW) with a spin-orbit interaction so large that a gate voltage of a few volts can modulate the Rashba field by several tesla. The importance to the field of spintronics, which proposes the use of both spin and charge as state variables in next-generation digital electronics, is the demonstration that spin orientation can be modulated by voltage, a parameter that also can modulate charge transport.
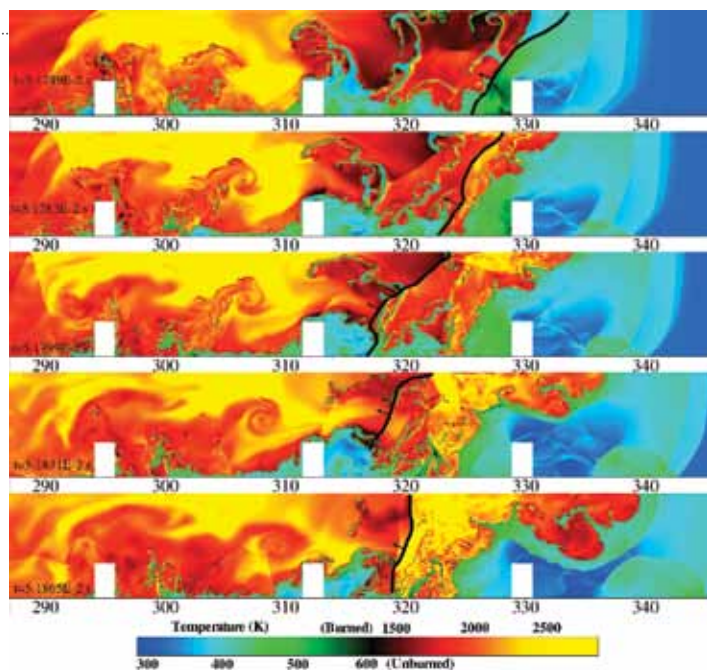
Snapshots of temperature from a simulation of an explosion in an obstructed channel filled with a mixture of methane and air as a shock wave (represented by the heavy black line) collides with and passes through the flame front, causing the speed and strength of the reaction to increase drastically.

Deflagration-to-Detonation Transitions in Large-Scale Methane-Air Mixtures: In light of several recent tragic explosions in underground coal mines in the United States and abroad, NRL has been working to understand how low-speed, low-pressure flames can accelerate to high-speed deflagrations that then transition into violent, supersonic, high-pressure detonation waves that can cause significant losses of life and property. Our research has resulted in the development of computationally efficient models for the chemical energy release and diffusive processes in methane-air mixtures that often form in coal mines and other industrial areas. This improved modeling capability opens the possibility of simulating explosions in large, confined spaces similar to what may be found in underground mining operations, industrial buildings, or ships. In conjunction with a team of experimentalists from the National Institute for Occupational Safety and Health (NIOSH), we have been exploring the limits of detonability of methane-air mixtures. Detailed simulations and concurrent large-scale experiments at NIOSH have shed new light on the ability of detonations to form in systems previously thought to be undetonable.
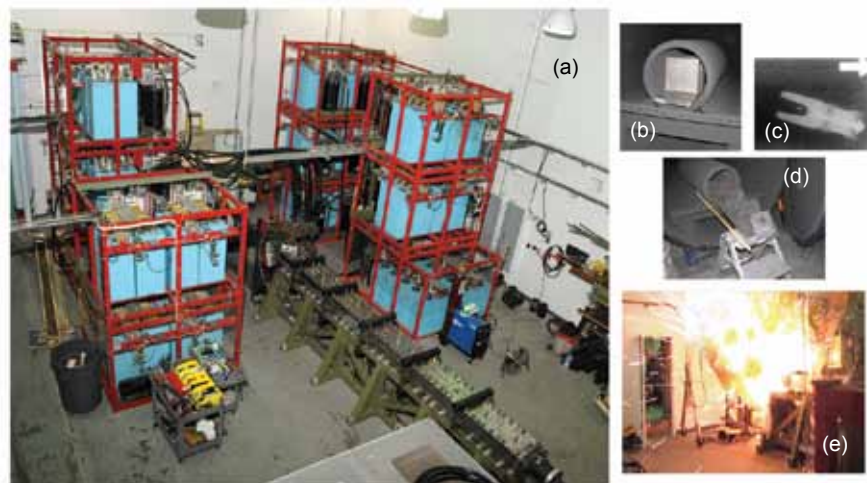
NRL Railgun Experiments: NRL researchers have developed advanced techniques to launch hypersonic projectiles using electrical energy. The NRL Materials Testing Facility (a) contains an 11 MJ capacitive energy store, a 6-m-long railgun, and a target chamber. Energy stored in the capacitor banks is discharged into the railgun using a series of high-current, solid-state switches. Currents of up to 1.5 million amperes driven in parallel metal rails magnetically accelerate 500-gram projectiles to 2.5 km/s (Mach 7) velocities in the barrel. An arc is generated at the muzzle as the projectile leaves the barrel (e). The projectile travels several meters through a steel transport tube into a shielded target chamber where it impacts a multilayer steel target (b). This target contained in a steel tube absorbs and contains the projectile energy. A flash X-ray image of the projectile (c) is taken just before it strikes the target. The projectile impacts the target and penetrates up to six half-inch-thick target plates before coming to a stop (d). The NRL group has investigated advanced rail, projectile, and insulator designs, as well as high-strength materials and advanced concepts in an effort to optimize launch dynamics and minimize bore damage generated during launch. Detailed analysis of bore materials coupled with in situ and ex situ diagnostics and modeling of the launch dynamics have provided insight into the conditions in the bore during launch. Reproducible, high-power launch of hypervelocity projectiles with minimal damage has been demonstrated. The research program is part of the Navy's Electromagnetic Railgun program developing electric weapons for a future naval platform.
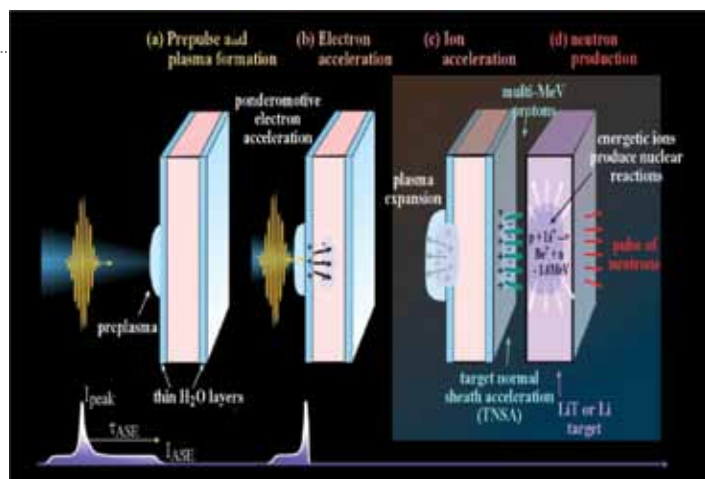

The main ion acceleration mechanisms in the interaction of a high-intensity laser pulse with a thin foil target. (a) The ASE-pedestal arriving at the target surface, prior to the peak of the laser pulse, creates a plasma. (b) The peak intensity of the laser pulse interacts with the preformed plasma, ponderomotively accelerating electrons into the target. (c) The accelerated electrons emerge from the target rear surface, forming an electron sheath due to charge separation with microscale Debye length. The resulting quasi-static electric field, of the order of TV/m, leads to ionization and ion acceleration to multi-MeV energies. (d) Energetic ions (protons or deuterons) induce nuclear reactions in the target, producing neutrons.

Ultrashort Laser Target Production of Directed Neutrons: NRL is investigating multi-MeV ion acceleration from the interaction of an intense ultrashort laser pulse with a thin planar foil target, to exploit the feasibility of producing directional energetic neutrons (protons) for detection of Special Nuclear Materials (SNM). When an intense ($>10^{18}$ W cm^{-2}) ultrashort laser pulse irradiates a thin foil target, protons are generated from hydrogenated contamination layers on the surfaces of the foil and are accelerated as a result of electric-field formation. Protons with energies up to 60 MeV have been measured. The proton beams have a number of unique properties including high brightness and ultralow emittance. This laser-based source of ions is ideal for a number of military and civilian applications because of its compactness, excellent beam quality (highly directional beam), and reduced angular spread, making it unique for beam target production of neutrons/protons. The neutrons/protons can be used directly to probe nuclear materials, as is already done in radiographing nuclear materials, or as a beam source irradiating a selected target to produce energetic gammas. These two options provide the basis for using neutrons and/or protons as a diagnostic tool to interrogate hidden nuclear materials.
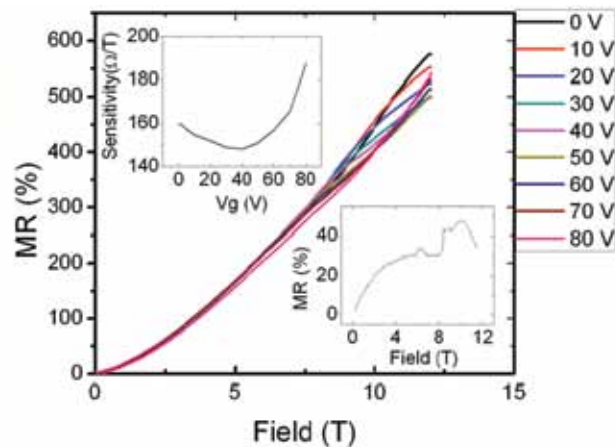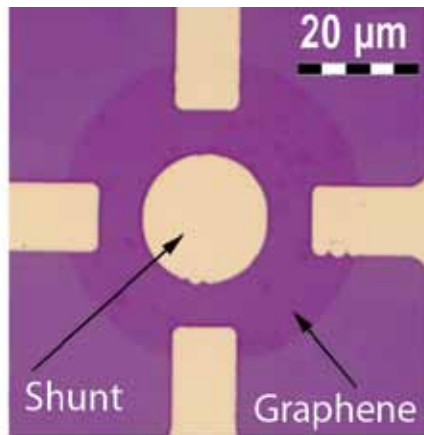
A Ti/Au-shunted van der Pauw disc (left) produces a linear magnetoresistance of ~600% at 12 T (right). The sensitivity of the device as a function of gate voltage is directly proportional to the Dirac point (top inset), and small Shubnikov–de Haas oscillations are observed (bottom inset) indicating the quality of the material.

Anomalously Large Linear Magnetoresistance Effects in Graphene: NRL scientists in the Electronics Science and Technology Division have demonstrated that by fabricating graphene devices with intentional inhomogeneities such as metallic shunts that change the paths of charge carriers as an applied magnetic field is varied, large linear magnetoresistances can be observed. The devices have the largest magnetoresistances ever observed in graphene, and because the magnetoresistance is proportional to the square of the mobility, the devices have the potential to become some of the most sensitive magnetic sensors ever made, which suggests a rare and important application for as-grown, unmodified graphene.
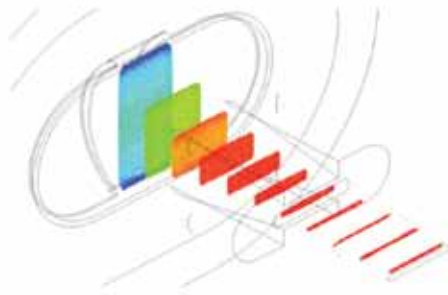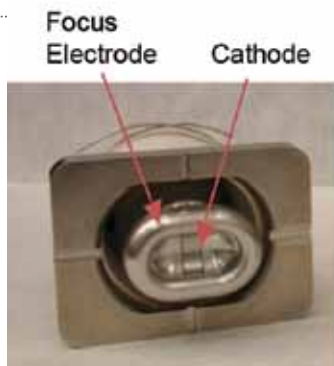
Electron gun (left), MICHELLE simulation of beam formation showing beam slices at successive axial positions (center), and assembled beam generation and transport system (right). MICHELLE is an NRL-developed electron beam simulation tool, which was essential to this successful development effort.

Development of a Sheet Electron Beam for Millimeter-Wave Amplifiers: NRL researchers recently developed a 100 kW sheet electron beam that will be used to power a new class of compact, high-power, millimeter-wave amplifiers (frequencies from 35 to 220 GHz). The sheet beam, up to 4.5 A at 22 kV, is produced by a unique electron gun, which focuses the beam down to a narrow 0.3 mm × 4 mm ribbon. A permanent magnet that was developed for this device produces the 8.5 kG uniform field needed to transport the beam through the amplifier circuit. At the nominal 19.5 kV operating voltage, 98.5% of the emitted current was transported through a 0.4 mm × 5 mm beam tunnel over a distance of 20 mm, which is sufficient for a 10 kW amplifier at 94 GHz. This is the first multi-ampere sheet beam that has been produced at such a low beam voltage and high current density. This new capability makes possible an order-of-magnitude increase in the power level of millimeter-wave amplifiers, with no corresponding increase in operating voltage. The ability to generate high power at modest voltages (<20 kV) is critical for several emerging DoD requirements in areas such as electronic warfare, millimeter-wave radar, and high-data-rate and/or covert communications.
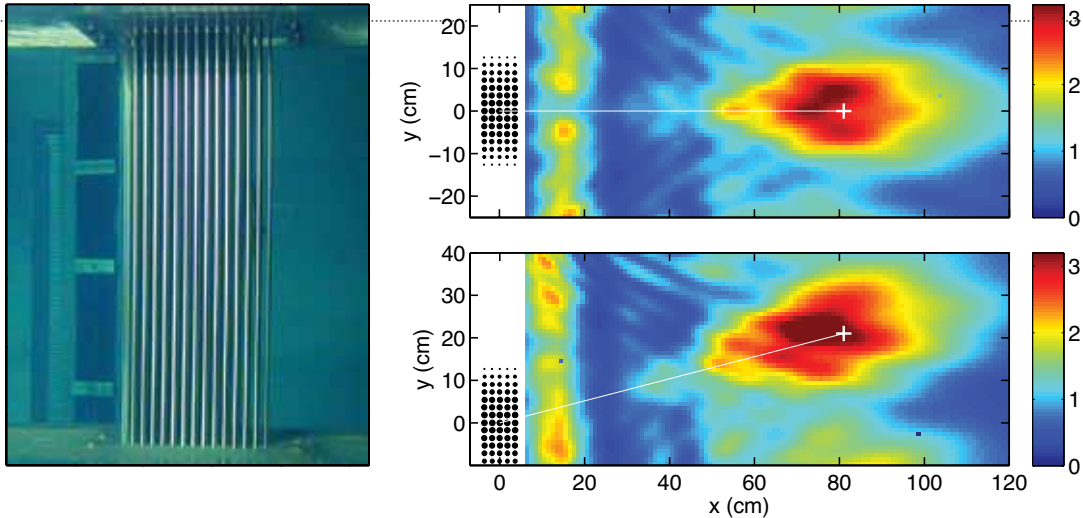
Left: The phononic crystal. Right: Measured intensity maps of a 20 kHz acoustic pulse transmitted through the lens. Focusing peaks are observed at the expected positions (marked with a +) based on a point-source transducer located 196 cm to the left of the lens, and at angles of 0° (upper) and 15° (lower) with respect to the horizontal.

Gradient Index Lens for Aqueous Applications: Scientists from the NRL Acoustics Division have designed a phononic crystal that behaves as an acoustic lens at sonic frequencies in water. The lens is an example of an acoustic metamaterial, a new class of materials designed to have special properties that typically do not exist in nature. The phononic crystal is composed of a regular array of stainless steel cylinders that act together through sub-wavelength scattering as a homogenized composite medium. The cylinder diameters are varied along one axis of the crystal, producing a graded index of refraction. The Acoustic Division's graded index design has been experimentally demonstrated to focus sound in the same manner as an ideal, graded optical lens focuses light.

The module containing HICO™ is shown docked to the Japanese Kibo facility on the International Space Station. HICO™ images through a slot in the nadir-facing panel of the payload module, with the ability to point the line of sight in the direction perpendicular to the Space Station's motion to image scenes that are not directly under the Space Station's orbital path. (Photograph courtesy NASA)

HICO™ Completes Its First Year of Imaging Operations from the International Space Station: The NRL Hyperspectral Imager for the Coastal Ocean (HICO™) completed its first year of operation on the International Space Station in September 2010, collecting during that time approximately 2000 hyperspectral images of littoral environments worldwide. Sponsored by the Office of Naval Research as an Innovative Naval Prototype and designed and built by the NRL Remote Sensing Division, HICO™ images the Sun-illuminated coastal ocean and adjacent land at 92 m ground sample distance in as many as 128 wavelength bands, and records a contiguous spectrum of the light from each pixel in the scene. This spectral data is exploited to extract significantly more information from the image than is possible with conventional imagery. For the ocean component of the image scene, the hyperspectral data is used to produce maps of in-water dissolved and suspended matter, coastal bathymetry, bottom type, and underwater visibility. For the land component of the scene, the spectral information is used to classify onshore vegetation and terrain. The HICO™ imager and product retrieval algorithms are based on the heritage of more than 20 years of airborne littoral hyperspectral imaging at NRL and other laboratories. The launch of HICO™ to the Space Station, provided by the DoD Space Test Program, extends this capability to the diversity of coastal environments worldwide, providing an exciting new view of the coastal ocean.
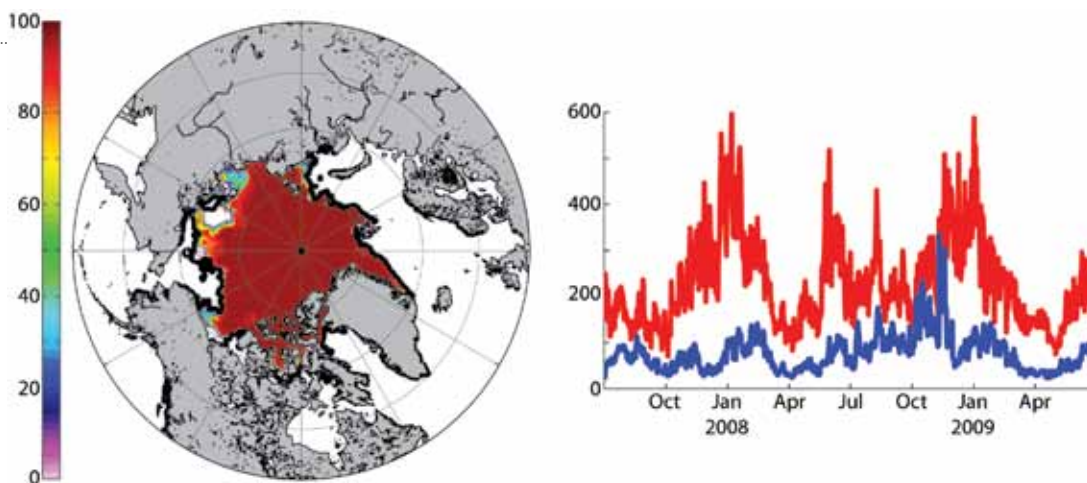
Left: An ACNFS snapshot of ice concentration (%) for 15 October 2008, with the independent ice edge (thick black line) from the NIC. Right: Daily mean ice edge distance (km) between the independent NIC observed ice edge and the ice edge predicted using the 24 hr forecasts from two forecast systems, ACNFS (blue) and PIPS 2.0 (red), for the period July 2007 to June 2009.

Validation of the Arctic Cap Nowcast/Forecast System (ACNFS): The ACNFS is a coupled sea ice and ocean data assimilative system that nowcasts and forecasts ice conditions in the sea ice covered areas in the northern hemisphere. ACNFS nowcasts/forecasts were compared to independent observations of ice thickness, ice drift, and ice edge location from the National Ice Center (NIC). The average ice edge error was 76 km as compared to 210 km for the Navy's existing operational sea ice forecast system, the Polar Ice Prediction System (PIPS 2.0). The improved physics of the sea ice model and the significant increase in horizontal resolution of the ACNFS (~3.5 km vs 27 km) has led to improved nowcasts and forecasts of Arctic ice conditions. The ACNFS will lead to improved knowledge of the ice environment that will be valuable not only to the warfighter but also to the increased ship traffic that may result from the summer opening of passages that historically have been closed with ice.

(a) Natural Run

(b) Satellite Data

(c) Assimilation Run

0   0.2   0.4   0.8
Aerosol Optical Thickness (550 nm)
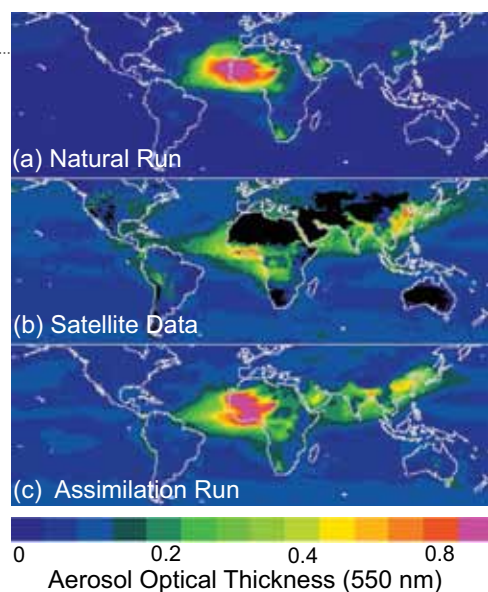
Comparison of mean AOD for 2007 for (a) the natural NAAPS model run; (b) the NASA MODIS satellite data after NRL post-processing; and (c) the final model analysis with satellite data assimilation. Note the significant increase in model particle concentrations (i.e., lower visibility) for South and East Asia.

Aerosol Data Assimilation Development and Transition: NRL's Marine Meteorology Division has developed and delivered the world's first operational system for the assimilation of aerosol optical depth (AOD) data from satellite sensors into an aerosol forecast model. This system, the NRL Atmospheric Variational Data Assimilation System–Aerosol Optical Depth (NAVDAS-AOD), is used to improve the Navy Aerosol Analysis and Prediction System (NAAPS). NAAPS is used by Department of Defense and civilian users to forecast severe visibility reduction events caused by dust, smoke, and pollution. Implementation of NAVDAS-AOD at the Fleet Numerical Meteorology and Oceanography Center (FNMOC), assimilating quasi-operational NASA Moderate Resolution Imaging Spectroradiometer (MODIS) data, has nearly halved errors in Navy aerosol forecasts. New breakthrough technologies developed for this system in 2010 include a data-assimilation-grade over-land AOD product, CALIOP (Cloud-Aerosol Lidar with Orthogonal Polarization) space-based lidar capabilities, and a 3D variational analysis (3DVAR) component.

Intense laser radiation is focused onto a gold target and generates relativistic electrons, positrons, and gamma rays.

Gamma-Ray and Positron Generation in High Energy Density Laboratory Plasmas: NRL Space Science Division (SSD) scientists have recorded for the first time mega-electron volt (MeV) gamma-ray spectra that are generated inside solid-density targets irradiated by intense picosecond lasers. The strong electric field of the laser beam accelerates electrons to MeV energies which produce slowing-down (Bremsstrahlung) gammas and positrons. The Bremsstrahlung gammas were recorded by two solid-state electronic detectors, and the 0.511 MeV gammas resulting from positron annihilation inside the target were observed for the first time using an SSD spectrometer. These experiments simulate in a controlled laboratory setting the production and propagation of energetic radiation and particles in dense astrophysical objects and the extreme conditions of thermonuclear fusion weapons and are therefore representative of the most energetic phenomena in the Universe.

Map of the sky in Galactic coordinates as seen by the Fermi Gamma-Ray Space Telescope in its first two years of operation. The color image shows the intensity of gamma rays above an energy of 500 million electron volts. More than 1500 point sources are detectable in the image, along with diffuse emission associated with the Milky Way. The circles mark gamma-ray point sources where radio searches uncovered new millisecond pulsars.

NASA's Fermi Gamma-Ray Space Telescope Points the Way to New Millisecond Pulsars: Since August 2008, the Fermi Large Area Telescope, in which NRL is a major partner, has been scanning the sky in the gamma-ray band, pinpointing more than 1500 new gamma-ray sources in the first year alone. More than 600 of these sources were not coincident in position with any known cosmic source that could be powering the gamma-ray emission. Over the past year, an international team of radio astronomers, led by NRL, has made deep searches of many of these sources with radio telescopes around the world. These searches have resulted in the discovery of more than 30 new millisecond pulsars, increasing the known population of these rapidly rotating neutron stars in our Galaxy by 30%! Millisecond pulsars are neutron stars weighing more than our Sun that spin on their axis hundreds of times per second, making them nature's most precise clocks. In addition to identifying the sources powering the gamma rays, these new discoveries provide stellar laboratories where the physics of extreme density, gravitation, and magnetic field can be studied in regimes inaccessible to Earth-bound experiments.
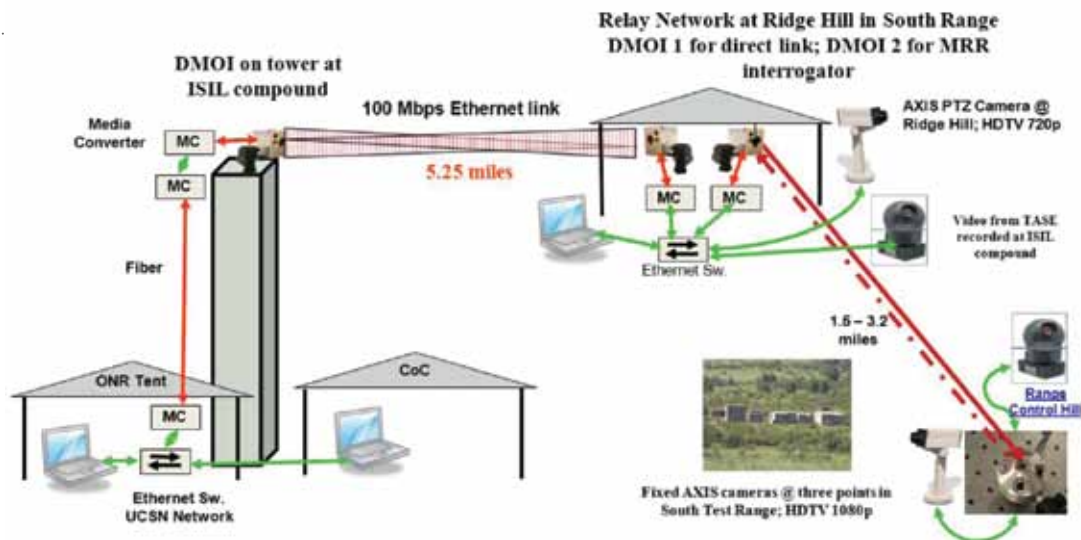
Diagram of the free-space lasercomm tactical network demonstration at Empire Challenge 2010. Video and pan/tilt/zoom (PTZ) control of an AXIS P3344 HD camera at Ridge Hill and video from fixed AXIS P1346 HD cameras equipped with MRR communication devices were passed to the command center over the 100 Mbps lasercomm link.

Free-Space Lasercomm Successfully Demonstrated at Empire Challenge 2010: During Empire Challenge 2010 (an annual intelligence, surveillance, and reconnaissance demonstration) at Fort Huachuca, Arizona, NRL demonstrated a 5.25-mile, direct free-space optical (FSO) lasercomm link operating full duplex at 100 Mbps from Ridge Hill in the South Test Range back to the main command center at the Intelligence Systems Integration Laboratory (ISIL) compound. NRL also demonstrated three different modulating retroreflector (MRR) links to transfer streaming video from Office of Naval Research (ONR)-sponsored sensors at ranges of ~1.5 miles to ~3.2 miles. The MRR-equipped sensors were interrogated from Ridge Hill and the video was passed over the 100 Mbps FSO link to the command center.
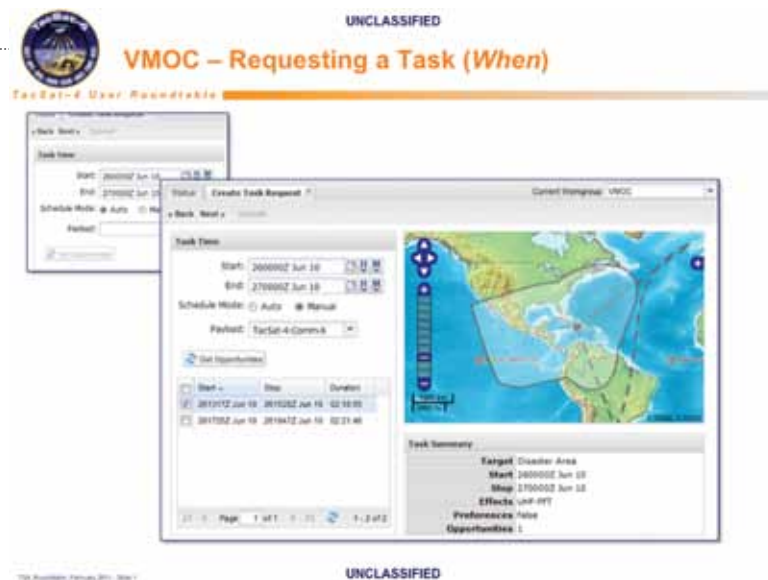
The "Tactical Application" of VMOC allows for automatic or manual scheduling of payload resources. The user is able to browse for available opportunities and make one or more requests. For each coverage opportunity, VMOC calculates and displays the coverage.

Virtual Mission Operations Center (VMOC) Deployed: NRL has deployed a remarkable capability that has been the focus of a six-year project developed in concert with numerous government and industry partners. Developed by NRL's Spacecraft Engineering Department, the Virtual Mission Operations Center (VMOC) is a Web-enabled multi-application service that ushers in a new era for globally dispersed military users of DoD, commercial, and civilian satellite payloads. Approved users can submit requests for satellite services, and these will be automatically prioritized, evaluated, and if approved, autonomously loaded into a Satellite Operations Center upload buffer. This new capability will dramatically improve satellite utilization and speed of command, critical in today's dynamic battlefield.

NRL TODAY

ORGANIZATION AND ADMINISTRATION

The Naval Research Laboratory is a field command under the Chief of Naval Research, who reports to the Secretary of the Navy via the Assistant Secretary of the Navy for Research, Development and Acquisition.

Heading the Laboratory with joint responsibilities are CAPT Paul C. Stewart, USN, Commanding Officer, and Dr. John A. Montgomery, Director of Research. Line authority passes from the Commanding Officer and the Director of Research to three Associate Directors of Research, the Director of the Naval Center for Space Technology, and the Associate Director for Business Operations. Research divisions are organized under the following functional directorates:

- Systems
- Materials Science and Component Technology
- Ocean and Atmospheric Science and Technology
- Naval Center for Space Technology

The *NRL Fact Book*, published every two years, contains information on the structure and functions of the directorates and divisions.

NRL operates as a Navy Working Capital Fund (NWCF) Activity. All costs, including overhead, are charged to various research projects. Funding in FY10 came from the Chief of Naval Research, the Naval Systems Commands, and other Navy sources; government agencies such as the U.S. Air Force, the Defense Advanced Research Projects Agency, the Department of Energy, and the National Aeronautics and Space Administration; and several nongovernment activities.

PERSONNEL DEVELOPMENT

At the end of FY10, NRL employed 2706 persons — 36 officers, 58 enlisted, and 2612 civilians. In the research staff, there are 813 employees with doctorate degrees, 325 with master's degrees, and 449 with bachelor's degrees. The support staff assists the research staff by providing administrative support, computer-aided design, machining, fabrication, electronic construction, publication and imaging, personnel development, information retrieval, large mainframe computer support, and contracting and supply management services.

Opportunities for higher education and other professional training for NRL employees are available through several programs offered by the Employee Relations Branch. These programs provide for graduate work leading to advanced degrees, advanced training, college course work, short courses, continuing education, and career counseling. Graduate students, in certain cases, may use their NRL research for thesis material.

For non-NRL employees, several postdoctoral research programs exist. There are also agreements with several universities for student opportunities under the Student Career Experience Program (formerly known as Cooperative Education), as well as summer and part-time employment programs. Summer and interchange programs for college faculty members, professional consultants, and employees of other government agencies are also available. These programs are described in the *NRL Review* chapter "Programs for Professional Development."

NRL has active chapters of Women in Science and Engineering (WISE), Sigma Xi, Toastmasters International, and the Federal Executive and Professional Association. An amateur radio club, a drama group, and several sports clubs are also active. NRL has a Recreation Club that provides gymnasium and weight-room facilities. NRL also has an award-winning Community Outreach Program. See "Programs for Professional Development" for details on all these programs and activities.

NRL has its very own credit union. Established in 1946, NRL Federal Credit Union (NRLFCU) is a sound financial institution that serves about 20,000 NRL employees, contractors, select employee groups, and their families. Focusing on its mission of *Trusted Partners for Life*, NRLFCU provides many free and low-cost products and services including free bill payer, great rates on deposits, credit cards, auto loans, mortgages and more. It offers direct deposit, online access, three local branches (one of them located in Bldg. 222) and nationwide access via the National Shared Branching Network. NRLFCU also offers full-service investment and brokerage services. For more information, call 301-839-8400 or log onto www.nrlfcu.org.

Public transportation to NRL is provided by Metrobus. Metrorail service is three miles away.

SITES AND FACILITIES

NRL's main campus in Washington, D.C., consists of 87 main buildings on about 130 acres. NRL also maintains 11 other research sites, including a vessel for fire research and a Flight Support Detachment. The many diverse scientific and technological research and support facilities are described here. More details can be found in the *NRL Major Facilities* publication at www.nrl.navy.mil.

Institute for Nanoscience

NRL researchers working in the Institute for Nanoscience clean room.

The revolutionary opportunities available in nanoscience and nanotechnology led to a National Nanotechnology Initiative in 2001. The NRL Institute for Nanoscience was established in that same year with a current annual budget of $11 million in core research funds. The prospect for nanoscience to provide a dramatic change in the performance of materials and devices was the rationale for identifying this emerging field as one of the DoD strategic research areas for basic research funding on a long-term basis.

The mission of the NRL Institute for Nanoscience is to conduct highly innovative, interdisciplinary research at the intersections of the fields of materials, electronics, and biology in the nanometer size domain. The Institute exploits the broad multidisciplinary character of the Naval Research Laboratory to bring together scientists with disparate training and backgrounds to pursue common goals at the intersection of their respective fields in systems at this length scale. The Institute provides the Navy and DoD with scientific leadership in this complex, emerging area and identifies opportunities for advances in future defense technology. NRL's nanoscience research programs and accomplishments directly impact nearly all Naval S&T focus areas.

The Institute's current research program emphasizes multidisciplinary, cross-division efforts in a wide range of science and technology applications:

- Ultra-low-power electronics
- Quantum information processing
- Chem/bio/explosive sensing
- Energy conversion/storage
- Photonics/plasmonics
- Multifunctional materials
- Biomimetics
- Biologically based complex assembly

The Institute for Nanoscience building, opened in October 2003, provides NRL scientists access to state-of-the-art laboratory space and fabrication facilities. The building has 5000 ft^2 of Class 100 clean room space for device fabrication, 4000 ft^2 of "quiet" space with temperature controlled to ±0.5 °C, acoustic isolation at the NC35 standard (35 dB at 1 kHz), floor vibration isolation to <150 μm/s rms at 10 to 100 Hz and <0.3

mOe magnetic noise at 60 Hz, and 1000 ft^2 of "ultra-quiet" laboratory space with temperature controlled to ±0.1 °C and acoustic isolation at the NC25 standard (25 dB at 1 kHz). Clean room equipment includes a wide range of deposition and etch systems; optical mask aligners; an electron beam writer; a focused ion beam writer; an optical pattern generator for mask making; a plasma-enhanced atomic layer deposition system; a laser machining tool; a wide variety of characterization tools; and more. ✦

Transmission electron microscopy.

Metrology.

The Institute for Nanoscience research building.

Radar
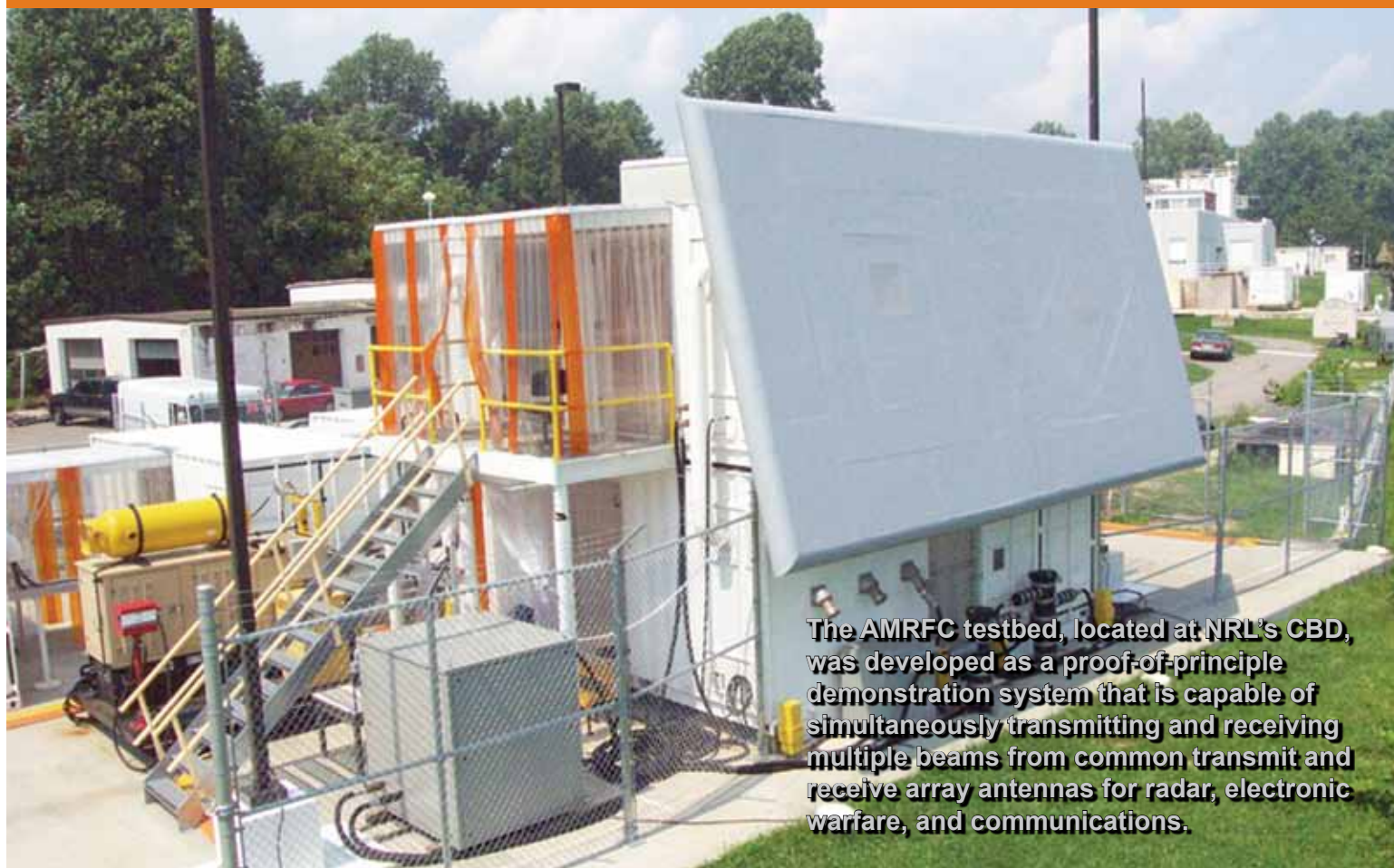
The AMRFC testbed, located at NRL's CBD, was developed as a proof-of-principle demonstration system that is capable of simultaneously transmitting and receiving multiple beams from common transmit and receive array antennas for radar, electronic warfare, and communications.

NRL has gained worldwide renown as the "birthplace of U.S. radar," and for more than half a century has maintained its reputation as a leading center for radar-related research and development. A number of facilities managed by NRL's Radar Division continue to contribute to this reputation.

A widely used major facility is the Compact Antenna Range (operated jointly with the Space Systems Development Department) for antenna design and development and radar cross section measurements. The range is capable of simulating far-field conditions from 1 to 110 GHz, with a quiet zone approximately 7 ft in diameter and 8 ft in length. Instrumentation covers from 1 to 95 GHz. Another strong division capability is in the Computational Electromagnetics (CEM) Facility, which has capabilities for complex electromagnetic modeling, including radar target and antenna structures. The Radar Signature Calculation Facility produces detailed computations of radar cross sections of various targets, primarily ships. The CEM facility includes multiple-CPU supercomputers that are also used to design phased array radar antennas.

The tremendous synergism between the CEM group and the Compact Antenna Range Facility provides the ability to design in the CEM environment, to test in the compact range, and to have immediate feedback between the theoretical and experimental aspects to shorten the development cycle for new designs.

In connection with airborne radar, the division operates a supercomputer-based Radar Imaging Facility and an inverse synthetic aperture radar (ISAR) deployed either in the air, on the ground, or aboard ship for radar imaging data collection. A P-3 aircraft equipped with the AN/APS-145 radar and cooperative engagement capability is also available for deploying experiments.

In connection with ship-based radar, the division operates the Radar Testbed Facility at the Chesapeake

Bay Detachment (CBD) near Chesapeake Beach, Maryland. The site has radars for long-range air search and surface search functions and features the newly developed W-band Advanced Radar for Low Observable Control (WARLOC), a fully operational high-power coherent millimeter-wave radar operating at 94 GHz. The WARLOC transmitter is capable of producing 10 kW average power with a variety of waveforms suitable for precision tracking and imaging of targets at long range. Waveforms with a bandwidth of 600 MHz can be transmitted at full power. A 6-ft Cassegrain antenna is mounted on a precision pedestal and achieves 62 dB of gain.

The Advanced Multifunction Radio Frequency Concept (AMRFC) testbed is a new installation at CBD operated by the Radar Division, with joint participation of several other NRL divisions as well. The goal of the AMRFC program is to demonstrate the integration of many sorts of shipboard RF functions, including radar, electronic warfare (EW), and communications, by utilizing a common set of broadband array antennas, signal and data processing, and signal generation and display hardware. The testbed consists of separate active transmit and receive arrays that operate over the 6 to 18 GHz band (nominally). Current functionality of the testbed includes a multimode navigation/surface surveillance Doppler radar, multiple communication links (line-of-sight and satellite), and passive and active EW capabilities. Testbed electronics are housed in seven converted 20-ft shipping containers and trailers. The arrays are mounted on a 15° tilt-back in the ends of two of the trailers overlooking the Chesapeake Bay, simulating a possible shipboard installation.

The division also has access to other radar systems: the Microwave Microscope (MWM); the Navy's relocatable over-the-horizon radar (AN/TPS-71); and an experimental Cooperative Aircraft Identification system. The internally developed MWM has a high-resolution (2 cm) ultrawideband capability that is used to investigate backscatter from surface and volumetric clutter, has through-wall detection capability, and characterizes the impulse responses of scattering objects. The division provides direct technical support for AN/TPS-71 and has direct access to data. The Cooperative Aircraft Identification system is used to explore system concepts and engineering developments in connection with target identification. ✦

Compact Range Facility.

Radar antennas in front of and on the roof of the Radar Test Facility.

Information Technology

The Information Management and Decision Architectures Branch includes research on the structure, transmission, analysis, and visual presentation of large data sets. The 246-million pixel display wall enables users to focus on one region of the data while maintaining the global context and offers a facility for collaborative data exploration.

NRL's Information Technology Division (ITD) conducts basic research, exploratory development, and advanced technology demonstrations in the collection, transmission, processing, dissemination, and presentation of information. ITD's research program spans the areas of artificial intelligence, autonomous systems, high assurance systems, tactical and strategic computer networks, large data systems, modeling and simulation, virtual and augmented reality, visual analytics, human/computer interaction, communication systems, transmission technology, and high performance computing.

NRL's RF Communications laboratory conducts research in satellite communications systems and modulation techniques, develops advanced systems for line-of-sight communications links, and conducts designs for the next generation of airborne relays. A Voice Communication Laboratory supports the development of tactical voice technology, a Wireless Networking Testbed supports the development of Mobile Ad Hoc Networking (MANET) technology, and an Integrated Communications Technology Test Lab provides the capability to perform analysis, testing, and prototype development of high-speed wired and wireless networked data communication systems. A Freespace Laser Communications Laboratory supports the design and development of prototype technical solutions for Naval laser communications requirements. ITD research networks connect internal NRL networks via high-speed links to the Defense Research and Engineering Network (DREN) and to a multi-agency Washington-metro all-optical research network that provides a development and testing venue for Global Information Grid (GIG) technology. ITD's High Performance Computing Facilities and the Laboratory for Large Data provide an OC-192c based environment for experimentation and proof-of-concept development in high performance networking and the use and sharing of extremely large (petabytes and larger) data sets.

The Cryptographic Technology Laboratory supports the development of certifiable Communications Security (COMSEC) and Information Assurance (IA) products, including programmable cryptographic devices, cryptographic applications, and high assurance cross-domain solutions. The Naval Key Management Laboratory investigates electronic key management and networked key distribution technologies for the Navy and DoD. The Cyber Defense Development Laboratory provides direct support to the Fleet in the areas of computer network defense and visualization, cross-domain solutions, and reverse code analysis.

The Autonomous Systems and Robotics Laboratory provides the ability to develop and evaluate intelligent software and interfaces for autonomous vehicles. The Immersive Simulation Laboratory utilizes a collection of commercial off-the-shelf and specially developed components to support R&D in interfaces for virtual simulators, ranging from fully immersive to desktop simulations. The Warfighter Human System Integration Laboratory maintains a range of Virtual Environment interface technologies as well as wearable, Wi-Fi physiological monitors and associated real-time processing algorithms for use in adaptive operational and training support technologies. The core of the new Visual Analytics Laboratory is a display wall composed of LCD tiles, which enable teams of analysts to explore massive, diverse streams of data, supporting research into the science of analytical reasoning facilitated by visual interfaces. The Service Oriented Architecture Laboratory is used to investigate, prototype, and evaluate flexible, loosely coupled Web services that can be rapidly combined to meet dynamically changing warfighter needs. The Behavioral Detection Laboratory supports the development of algorithms, processes, and sensor suites associated with behavioral indicators of deception. ✦
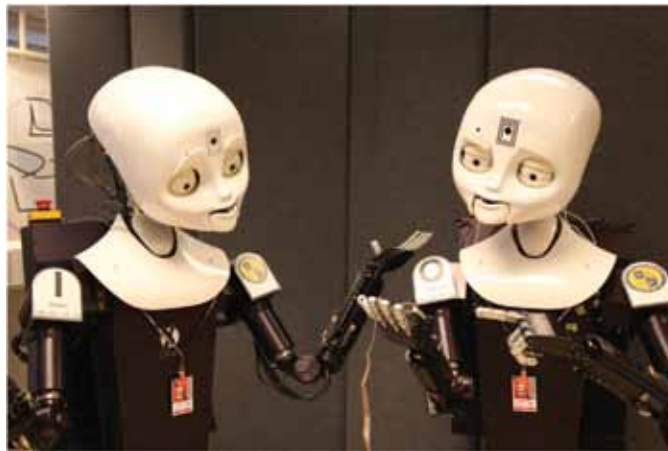
The Navy Center for Applied Research in Artificial Intelligence uses Mobile, Dexterous, Social robots Octavia and Isaac to support research in human–robot interaction and autonomy.

Prototype of the Navy's future multitask, multimodal watchstation, known as the Common Display System, located inside the NRL Audio Lab's 48-element spherical loudspeaker array. The Audio Lab's facilities are used for a wide variety of applied auditory research purposes, including simulations of aural environments in real-world settings, such as Navy combat information centers and open spaces.

Optical Sciences

The Advanced Optical Materials Fabrication Laboratory, a state-of-the-art high vacuum cluster system, consists of a series of interconnected chambers allowing vacuum deposition of complex, multilayer films to be deposited and patterned without breaking vacuum during processing.

T he Optical Sciences Division has a broad program of basic and applied research in optics and electro-optics. Areas of concentration include fiber optics and fiber-optic sensing, materials and sensors for the visible and infrared (IR) spectral regions, integrated optical devices, signal processing, optical information processing, panchromatic and hyperspectral imaging for surveillance and reconnaissance, and laser development.

The division occupies some of the most modern optical facilities in the country. The newest facility in Optical Sciences is the Advanced Optical Materials Fabrication Laboratory, a state-of-the-art cluster system for vacuum deposition of thin films. The facility consists of a series of interconnected high vacuum chambers, allowing complex, multilayer films to be

deposited without breaking vacuum during processing. The system includes a glove box, sample distribution robot, sputtering chambers for chalcogenide materials and oxides, evaporators for metals and dielectrics, and a mask changing module to enable layers to be patterned in situ while eliminating interface effects that result from exposure to air. Three other recently added facilities include the Optical Fiber Preform Fabrication Facility for making doped and undoped, multimode, single-mode, multi-core, and photonic crystal glass preforms at temperatures as high as 2300 °C; the Surface Characterization Facility for ultraviolet and X-ray photoemission spectroscopy, atomic force and scanning tunneling microscopy (STM), and STM-induced light emission measurements; and the molecular beam epitaxial growth system dedicated to infrared lasers and detectors based on GaSb/InAs/AlSb quantum well and superlattice structures. In addition, an extensive set of laboratories

exists to develop and test new laser and nonlinear frequency conversion concepts and to evaluate non-destructive test and evaluation techniques. Fiber-optic sensor testing stations include acoustic test cells and a three-axis magnetic sensor test cell. There is also an Ultralow-loss Infrared Fiber-Optic Waveguide Facility using high-temperature IR glass technology. The facilities for ceramic optical materials include powder preparation, vacuum presses, and a 50-ton hot press

for sintering. The Focal Plane Array Evaluation Facility allows measurement of the optical and electrical characteristics of infrared focal plane arrays being developed for advanced Navy sensors. The IR Missile-Seeker Evaluation Facility performs open-loop measurements of the susceptibilities of IR tracking sensors to optical counter-measures. A UHV multichamber deposition apparatus is used for fabrication of electro-optical devices and can be interlocked with the Surface Characterization Facility.

The Optical Fiber Preform Fabrication Facility includes computer control of the glass composition and standard fiber-optic dopants as well as rare earths, aluminum, and other components for specialty fibers.

The Optical Sciences Surface Characterization Facility includes instrumentation for ultraviolet and X-ray photo-emission spectroscopy (UPS and XPS), atomic force and scanning tunneling microscopy (AFM and STM), and STM-induced light emission (STM-LE) measurements.

Molecular beam epitaxy (MBE) system dedicated to quantum confined GaSb/InAs/AlSb structures for mid-wave infrared laser development.
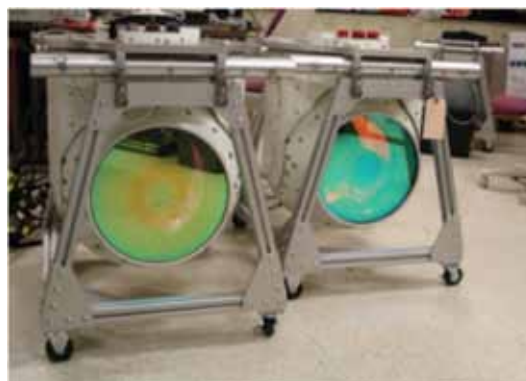
MX-20SW hyperspectral sensors.

Tactical Electronic Warfare

Learjet with simulators during RIMPAC exercises.

The Tactical Electronic Warfare (TEW) Division's program for electronic warfare (EW) research and development covers the entire electromagnetic spectrum. The program includes basic technology research and advanced developments and their applicability to producing EW products. The range of ongoing activities includes components, techniques, and subsystems development as well as system conceptualization, design, and effectiveness evaluation. The focus of the research activities extends across the entire breadth of the battlespace. These activities emphasize providing the methods and means to detect and counter enemy hostile actions — from the beginning, when enemy forces are being mobilized for an attack, through to the final stages of the engagement. In conducting this program, the TEW Division has an extensive array of special research and development laboratories, anechoic chambers, and modern computer systems for modeling and simulation work. Dedicated field sites, an NP-3D EW flying laboratory, and Learjets allow for the conduct of field experiments and operational trials. This assemblage of scientists, engineers, and specialized facilities also supports the innovative use of all Fleet defensive and offensive EW resources now available to operational forces. ✦
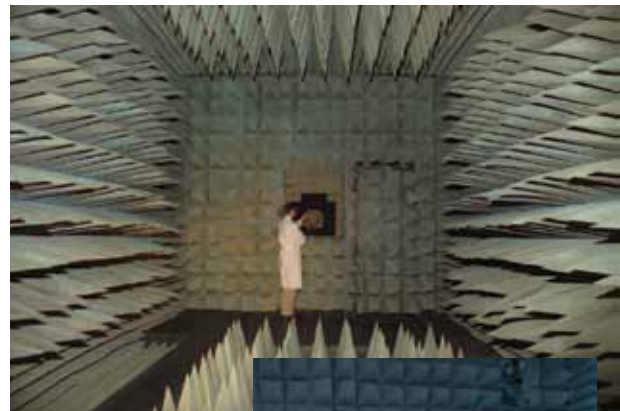
Radio Frequency Countermeasures anechoic chamber for EW testing.
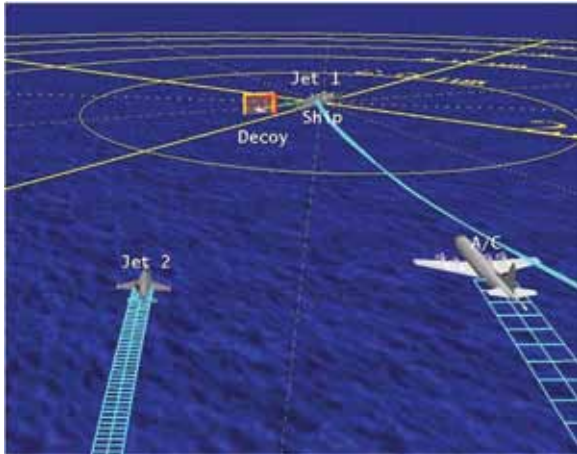
TEWD develops and implements advanced visualization tools to support EW systems development and analysis.
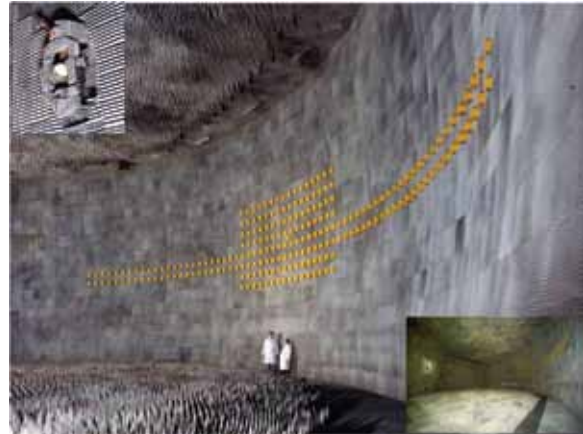
A high-performance, hardware-in-the-loop simulator for real-time closed-loop testing and evaluation of electronic warfare systems and techniques to counter the antiship missile threats.

EATES — Electronic Attack Technique Evaluation System, a stand-alone portable EA testing system.

Deployed EW subsystem to improve emitter detection and classification based on conceptualization and development performed in TEW.

Dragon Eye

FINDER

NRL's Vehicle Research Section (VRS) in the TEW Division develops technologies for autonomous, affordably expendable, unmanned systems that carry a wide variety of payloads for numerous mission scenarios. The VRS has developed more than 50 unmanned flying machines since the mid-1970s: fixed and rotary wing vehicles, ground, ship, and air deployed vehicles, EW decoys, reconnaissance aircraft, electric vehicles powered by fuel cells, unpowered vehicles, vehicles designed for planetary exploration, and more.

Chemistry

NRL has designed and constructed a state-of-the-art trace explosives detection testbed system that will facilitate the development and evaluation of new materials, sensors, and instrumentation for explosives detection.

NRL has been a major center for chemical research in support of naval operational requirements since the late 1920s. The Chemistry Division continues this tradition. The Chemistry Division conducts basic research, applied research, and development studies in the broad fields of diagnostics, dynamics, synthesis, materials, surface/interfaces, environment, corrosion, combustion, and fuels. Specialized programs currently within these fields include the synthesis and characterization of organic and inorganic materials, coatings, composites, nondestructive evaluation, surface/interface modification and characterization, nanometer structure science/technology, chemical vapor processing, tribology, solution and electrochemistry, mechanisms and kinetics of chemical processes, analytical chemistry, theoretical chemistry, decoy materials, radar-absorbing materials/radar-absorbing structures (RAM/RAS) technology, chemical/biological warfare defense, atmosphere analysis and control,

environmental remediation and protection, corrosion science and engineering, marine coatings, personnel protection, and safety and survivability. The Division has several research facilities.

Chemical analysis facilities include a wide range of modern photonic, phononic, magnetic, electronic, and ionic based spectroscopic/microscopic techniques for bulk and surface analysis.

The Magnetic Resonance Facility includes advanced high-resolution solid-state nuclear magnetic resonance (NMR) spectroscopy techniques to observe nuclei across much of the periodic table and provides detailed structural and dynamical information.

The Synchrotron Radiation Facility has intense, monochromatic X-ray photon beams tunable from 10 eV to 35 KeV available from four beam lines developed by NRL at the National Synchrotron Light Source at the Brookhaven National Laboratory.

The Nanometer Characterization/Manipulation Facility includes fabrication and characterization capability based on scanning tunneling microscopy/

spectroscopy, atomic force microscopy, and related techniques.

The Materials Synthesis/Property Measurement Facility has special emphasis on polymers, surface-film processing, and directed self-assembly.

The Chemical Vapor and Plasma Deposition Facility is designed to study and fabricate materials such as diamond using in situ diagnostics, laser machining, and plasma deposition reactors.

The Navy Fuel Research Facility performs basic and applied research to understand the underlying chemistry that impacts the use, handling, and storage of current and future Navy mobility fuels.

Fire research facilities include a 11,400 ft^3 fire-research chamber (Fire I) and the 457-ft ex–USS *Shadwell* (LSD 15) advanced fire research ship. Commensurate support has been devoted to survivability of the new classes of ships, DDX, LPD 17, LCS, CVNX, and LHA(R).

The Marine Corrosion and Coatings Facility located on Fleming Key at Key West, Florida, offers a "blue" ocean environment and unpolluted, flowing seawater for studies of environmental effects on materials. Equipment is available for experiments involving accelerated corrosion and weathering, general corrosion, long-term immersion and alternate immersion, fouling, electrochemical phenomena, coatings application and characterization, cathodic protection design, ballast water treatment, marine biology, and corrosion monitoring.

The Chemistry Division has focused on force protection/homeland defense (FP/HD) since September 11, 2001, especially on the development of improved detection techniques for chemical, biological, and explosive threats. As part of a multidivisional program to develop new technology systems, the Chemistry Division is a major contributor to the NRL Institute for Nanoscience. Nanoscience complements FP/HD in that nanoscience is expected to provide dramatic improvements to chemical/biological detection, protection, and neutralization. Chemistry will approach the nanoscale from the bottom up — building smaller atoms and molecules into nanostructures with new properties and developing the directed assembly of nanostructures into hierarchical systems. The NRL Nanoscience building is linked directly into the Chemistry building to provide controlled access and auxiliary space for work not requiring a "low noise" environment. ✦

Optical image (left), scanning electron micrograph (middle), and transmission electron micrograph (right) of an FeO*x*−carbon nanofoam used potentially as negative electrodes in next-generation aqueous-based electrochemical capacitors and nonaqueous Li-ion batteries.
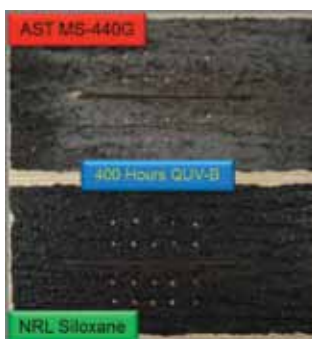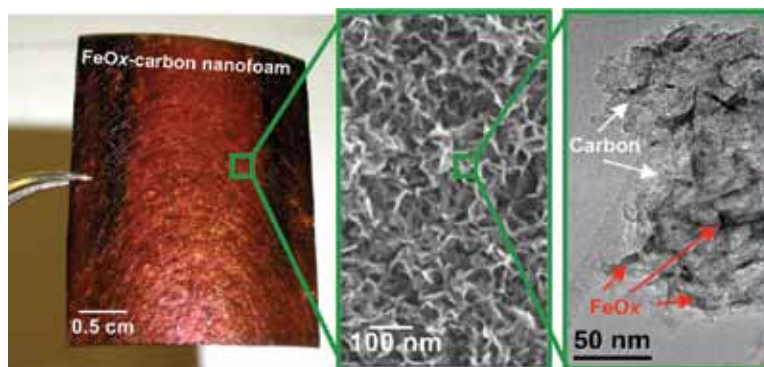
Comparison of a legacy nonskid coating to an NRL-developed organosiloxane nonskid coating. Left: Five-month service comparing legacy nonskid to NRL organosiloxane applied to the USS *Ponce* LPD 15. The NRL system holds its deck gray color while the legacy nonskid systems degrade to an ocean gray from solar radiation. Right: Two 6-in. x 12-in. x 1/4-in. steel plates. The lower plate is coated with the NRL organosiloxane, while the upper plate is coated with the legacy nonskid. 400 hours of accelerated UV testing show the improved color stability of the NRL system over the legacy system.

Materials Science and Technology

The Magnetoelectronics Fabrication Facility consists of a Class 1000 clean room equipped with tools for lithographic construction of magnetoelectronic and spintronic devices.

The Materials Science and Technology Division at NRL provides expertise and facilities to foster materials innovation. The Division houses many specialized and unique facilities for carrying out basic and applied materials synthesis and characterization research.

The Magnetoelectronics Fabrication Facility consists of a Class 1000 clean room equipped with tools for lithographic construction of magnetoelectronic and spintronic devices. It provides pattern definition, metallization, dielectric layer deposition, and both reactive and Ar^+ ion etching of wafers and small pieces.

The Electrical, Magnetic, and Optical Measurement Facility contains several complementary instruments that allow for the magnetic, electrical, optical, and heat capacity characterization of materials and devices. SQUID (superconducting quantum interference device) magnetometry and vibrating sample magnetometry are used to determine important properties of superconducting, paramagnetic, diamagnetic, and ferromagnetic materials. The transport properties of materials, namely the temperature- and magnetic-field-

dependent resistivity combined with heat-capacity measurements, allow for a fundamental physical understanding of electronic properties.

The Materials Processing Facility includes apparatuses for powder production by fluid atomization, thermal evaporation, and arc erosion, and a physical vapor deposition system designed to produce and coat submicron powders in situ. Facilities to process powder into bulk specimens by hot and cold isostatic pressing permit a variety of consolidation possibilities. The isothermal heat treatment facility and quenching dilatometer permit alloy synthesis and single crystal growth. Bulk alloys can be prepared by induction melting, while rapid solidified metals of thin cross section can be made by splat quenching and melt spinning. Ceramic and ceramic-matrix composites processing facilities include a wide variety of conventional, controlled atmospheric furnaces, hot presses, a ball milling apparatus, particle size determination capability, and sol-gel and organometallic coating processing capabilities.

The Mechanical Characterization Facility consists of various testing systems, many with automated computer control and data acquisition, for determining the mechanical response of materials under controlled

NRL GelMan human surrogate technology is used to record and analyze dynamic responses to blast pressure and impacts. GelMan torso measurement systems assess pressure transmission directly into the body, and through body armor into the body. GelMan-Brain systems quantify headborne protective equipment performance with the aim of reducing traumatic brain injury.

loading/deformation and environmental conditions. Basic capabilities include quasi-static tensile and fracture testing, dynamic storage and loss moduli as a function of frequency and temperature, cyclic fatigue crack growth and corrosion fatigue testing, and stress-corrosion cracking testing.

The Thin-Film Materials Synthesis and Processing Facility provides users a wide variety of techniques for growth and processing of thin films (thickness 1 μm or less). Sputter deposition offers a versatile method of depositing metallic and dielectric films and is a primary tool of this facility. Thermal evaporation of metals is implemented in both high-vacuum and ultra-high-vacuum systems. Pulsed laser deposition (PLD) with variable stage temperature and controlled atmosphere allows growth of oxides. Electrolytic deposition offers efficient growth of gold and silver films. Laser direct-write ablation and deposition processes provide unique methods for imposing CAD-defined features via ablation of a substrate film and ablative mass transfer to a substrate.

The Micro/Nanostructure Characterization Facility is capable of performing transmission electron microscopy (TEM), scanning transmission electron microscopy (STEM), atomic resolution transmission electron microscopy (ARTEM), electron energy loss spectroscopy (EELS), Z-contrast imaging, and spectral imaging through the use of a JEOL 2010F transmission electron microscope, an FEI Tecnai G^2 30 analytical transmission electron microscope, and a JEOL JSM-7001F Variable Pressure scanning electron microscope

with secondary and backscattered electron imaging capabilities, as well as energy dispersive spectrometry (EDS) and electron backscatter diffraction (EBSD). In addition, this field-emission microscope operates in low-vacuum mode, which allows for high-resolution imaging of nonconductive materials without coatings or any additional preparation. Other standard microstructure characterization instruments are also available. ✦

The JEOL JSM 7001FLV Variable Pressure Field Emission Scanning Electron Microscope, outfitted with EDS and EBSD capabilities.

Laboratory for Computational Physics and Fluid Dynamics
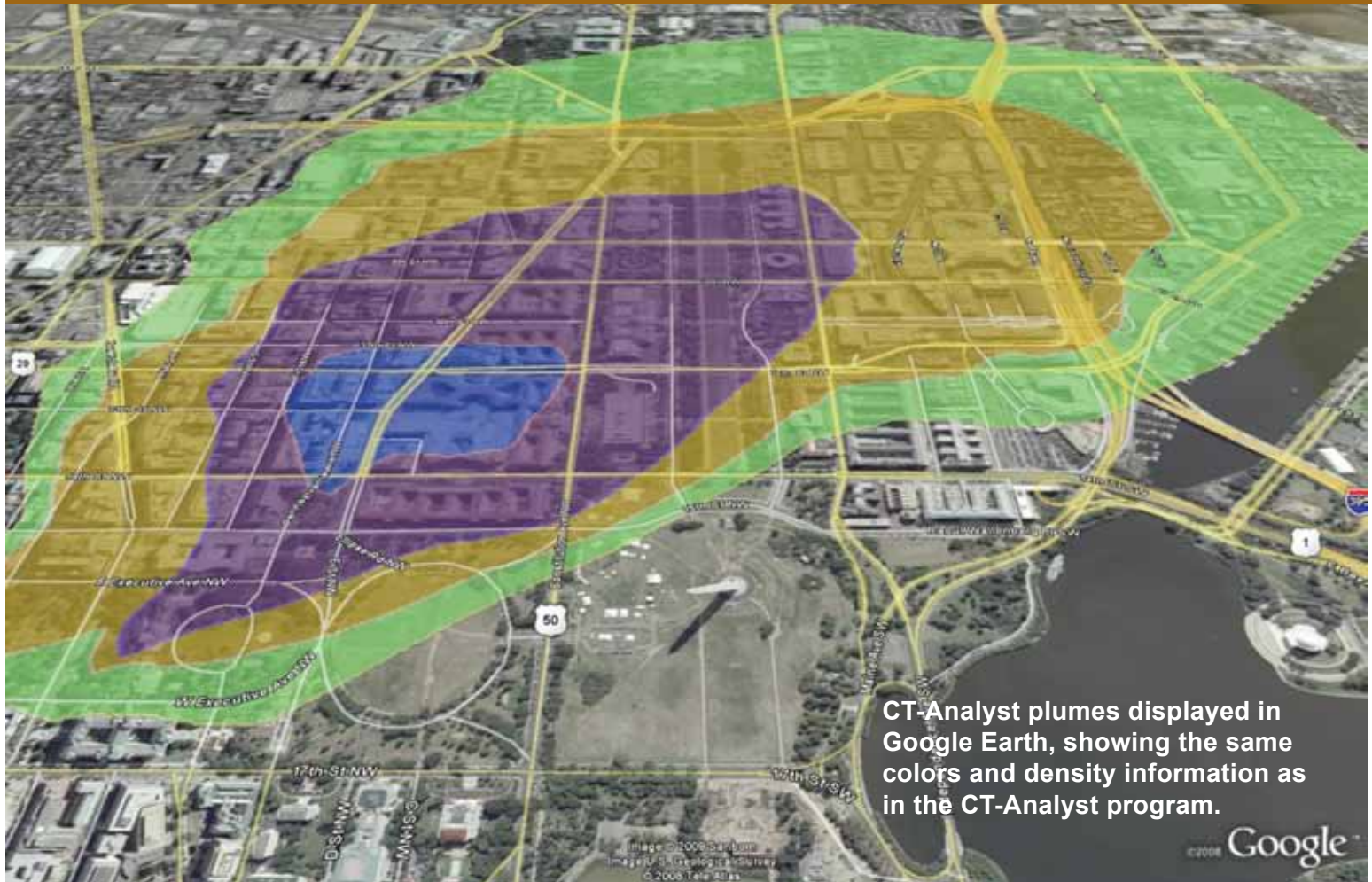
CT-Analyst plumes displayed in Google Earth, showing the same colors and density information as in the CT-Analyst program.

The Laboratory for Computational Physics and Fluid Dynamics (LCP&FD) is a division of physicists, engineers, and computer scientists who use high-performance computers to solve priority problems for the Navy, the DoD, and the nation when existing capabilities and readily available commercial software prove inadequate to the application. For example, the LCP&FD developed the CT-Analyst crisis management software (figure above) so first responders can have instant predictions of an airborne contaminant plume in a city.

The LCP&FD maintains a very powerful collection of computer systems applied to a broad collection of work. There is currently a total of 320 shared memory Itanium processors, 2548 clustered x86_64 cores, and their associated support systems. In addition, there are more than 50 Macintoshes in the group, most of which are capable of large calculations both independently and in parallel ad hoc clusters.

The shared memory computer systems are comprised of three 64-core and one 128-core Itanium 2 SGI Altix machines. There are four 64-bit x86 multi-core distributed memory clusters, each well coupled with Infiniband high speed switched interconnect. The GPU cluster is comprised of 48 NVIDIA Fermi GPUs tightly coupled to 24 x86 multi-core processor nodes connected with Infiniband.

Each system has on the order of 72 terabytes of disk for storage during a simulation, and at least one gigabyte of memory per processor core. All unclassified systems share a common disk space for home directories as well as 1.4 terabytes of AFS space which can be used from any AFS-capable system throughout the allowed internet.

Each system is connected to NRL's network via 10Gb ethernet as well as an internal Infiniband intranet.
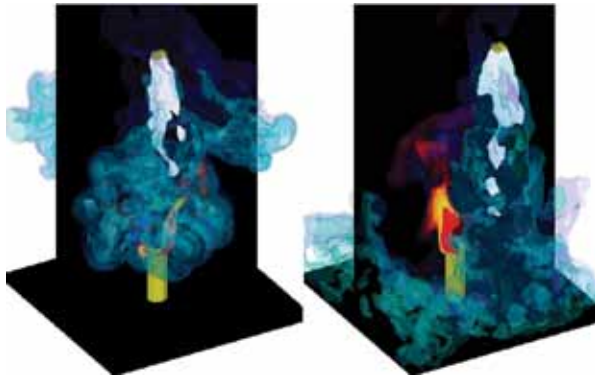
Simulations of fire suppression with different sprinkler locations, fuel flow rates, and under different gravitational environments allow us to understand the interaction of several different physical processes such as vaporization and buoyancy that are important for fast suppression of flames. The current Fire-Blast-Mitigation code uses parallel adaptive mesh refinement to handle detailed physics in large domains efficiently.
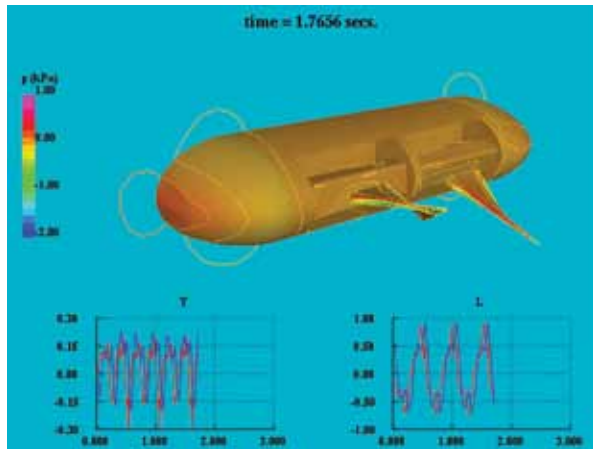
Flow past an unmanned underwater vehicle (UUV) propelled by flapping fins with controlled deformation.
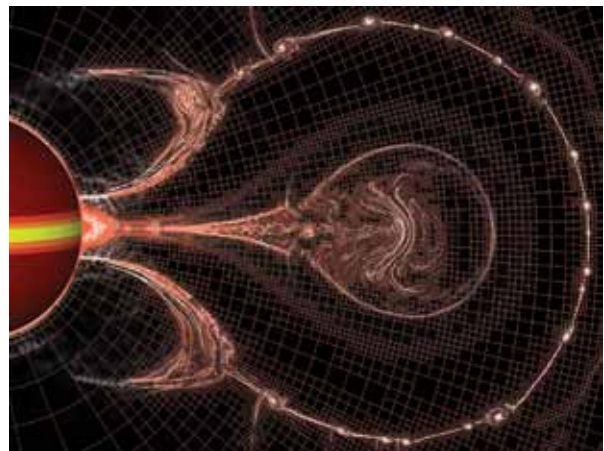
Numerical simulation of an eruptive solar flare and coronal mass ejection using the Adaptively Refined Magnetohydrodynamics Solver (ARMS). The gradual accumulation of a strong longitudinal magnetic field concentrated near the Sun's equator (yellow band on sphere at left) powers the explosive eruption. Electric current sheets (white shading against the sky) separate regions of oppositely directed fields and highlight regions permeated by magnetohydrodynamic shock waves and strong magnetic forces. The computational grid (red lines against the sky) adaptively refines to capture all of this fine-scale structure.
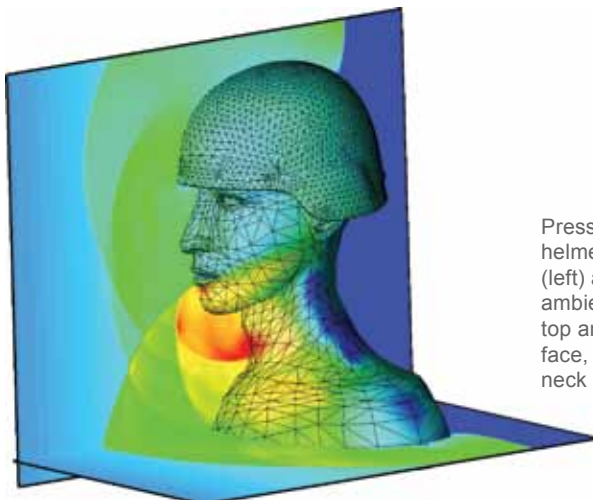
Pressure contours resulting from blast interaction with a helmeted head. The shock wave approaches from the front (left) and envelopes the geometry; the boundary between ambient (dark blue) and post-shock (green) air is seen at the top and bottom right. Interacting shock reflections from the face, helmet, and torso generate high pressures (red) on the neck below the chin.

Plasma Physics

NRL's Materials Testing Facility railgun. This system is designed to perform experiments on bore materials under high-power launch conditions.

The Plasma Physics Division is the major center for in-house Navy and DoD plasma physics research. The Division conducts a broad program in laboratory and space plasma physics and related disciplines, including high power lasers, pulsed-power sources, intense particle beams, advanced radiation sources, materials processing, and nonlinear dynamics.

The two largest of the Division's lasers, Nike and Electra, are krypton fluoride (KrF) lasers operating at 0.25-micron wavelengths and are used for inertial confinement fusion (ICF) energy studies. Nike provides a single, 3-kJ pulse and is used primarily for ICF target physics. Electra is used to develop repetitively pulsed KrF technology. Three ultrashort-pulse, high-intensity lasers, the Table-Top Terawatt (T3) laser, the Ti:Sapphire Femtosecond Laser (TFL), and the new Kilohertz Ti:Sapphire Femtosecond Laser (KTFL) investigate intense laser-target interactions, laser-

driven accelerators, laser-triggered discharges, and laser propagation in air, plasmas, and water. The High Energy Laser Laboratory includes four multi-kilowatt, continuous-wave (CW) fiber lasers and investigates laser propagation in the atmosphere and incoherent beam combining for directed energy and power beaming applications. The SWOrRD facility uses resonant Raman spectroscopy based on illuminating a target at many wavelengths using a rapidly tunable laser, thus generating two-dimensional signatures of explosives and biological/chemical/nuclear threats.

The Division also has a number of pulsed-power, microwave, and laboratory plasma facilities. The Railgun Materials Testing Facility railgun focuses on materials issues for a major Navy effort to develop a long-range, electromagnetic launcher for a future electric ship. Two large, high-voltage, pulsed-power devices, Gamble II and Mercury, are used to produce intense electron and ion beams, flash X-ray sources,

and high-density plasmas. The microwave materials processing laboratory includes a 20-kW, CW, 83-GHz gyrotron. Laboratory plasma experiments include the Space Physics Simulation Chamber (SPSC), an 11 m³ space chamber capable of reproducing the near-Earth space plasma environment, and the Large Area Plasma Processing System (LAPPS), designed to study modification of polymers, graphene, and other sensitive materials. ✦
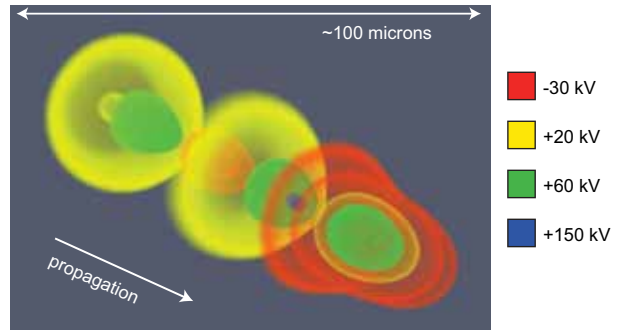

The scalar potential in a laser wakefield accelerator as computed by turboWAVE, a set of software modules used for simulating a wide range of phenomena involving plasmas.

Space Physics Simulation Chamber.
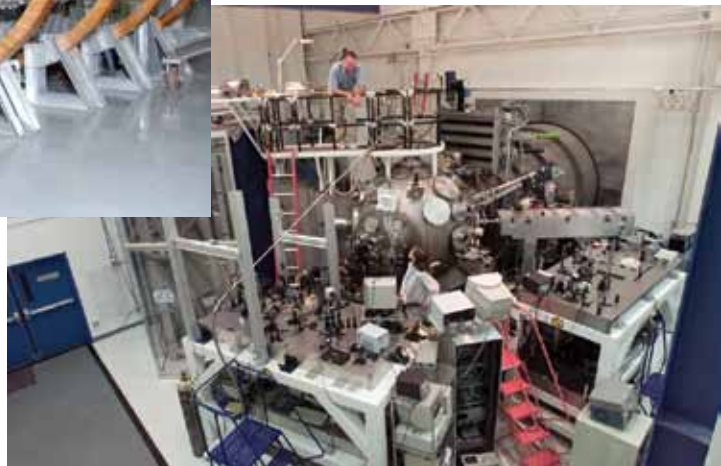
NRL's Nike target chamber, the largest krypton fluoride (KrF) laser facility in the world, where targets are accelerated to the velocities needed for fusion implosions.
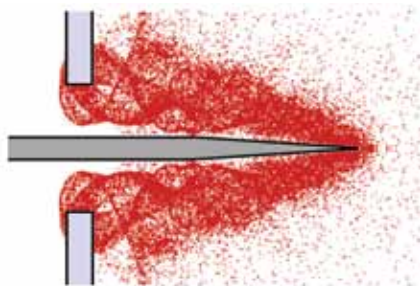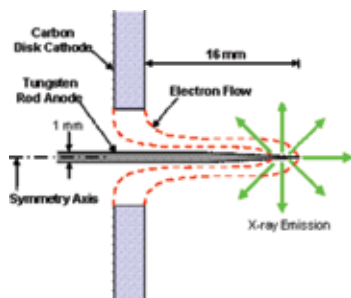
Electron distribution at the tip of a rod-pinch diode.

Electronics Science and Technology

The Electronics Science and Technology Division's Advanced Silicon Carbide Epitaxial Research Laboratory (ASCERL).

The Electronics Science and Technology Division conducts a multidisciplinary basic and applied research program in solid-state electronics; electronic materials including growth, theory, and characterization of semiconductors and heterostructures; surface and interface science; microwave and millimeter-wave components and techniques; microelectronic device research and fabrication; nanoelectronics science and technologies; vacuum electronics; power electronics; photovoltaics and optoelectronics; and process modeling and simulation.

The Division operates seven major facilities: the Compound Semiconductor Processing Facility (CSPF), the Laboratory for Advanced Materials Synthesis (LAMS), the Ultrafast Laser Facility (ULF), the Epicenter, the Advanced Silicon Carbide Epitaxial Research Laboratory (ASCERL), the Space Solar Cell Characterization Facility (SSCCF), and the Millimeter-Wave Vacuum Electronics Synthesis Facility (MWVESF).

The CSPF processes compound semiconductor structures on a service basis, especially if advanced fabrication equipment such as electron beam lithography or reactive ion etching is required. But most fabrication can be hands-on by NRL scientists to assure personal process control and history. The LAMS uses metallorganic chemical vapor deposition to synthesize a wide range of thin films, particularly wide bandgap semiconductors such as gallium nitride (GaN) and related alloys. The Epicenter (a joint activity of the Electronics Science and Technology, Materials Science and Technology, Optical Sciences, and Chemistry Divisions) is dedicated to the growth of multilayer nanostructures by molecular beam epitaxy (MBE). Current research involves the growth and etching of conventional III-V semiconductors, ferromagnetic semiconductor materials, 6.1Å III-V semiconductors, and II-VI semiconductors. The structures grown in this facility are analyzed via in situ scanning tunneling microscopy and angle resolved electron microscopy.

The ASCERL is the focal point of NRL efforts to develop thin film heterostructure materials needed for high-voltage, high-power silicon carbide (SiC) power electronic components in future naval systems. ASCERL employs an EPIGRESS reactor capable of growing thick, low-defect, ultra-high-purity SiC epitaxial layers. The SSCCF studies the effects of particle irradiation on new and emerging solar cell technologies for space applications. The ULF is optimized for the characterization of photophysical and photochemi-
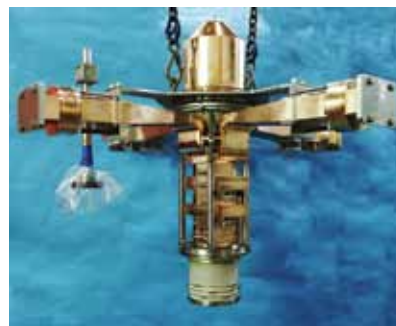
The MISSE7 experiment (upper center of photo) on the International Space Station, photographed by a space-walking STS-129 astronaut. MISSE7 is the latest in a series of experiments that expose materials to space for several months before they are returned for analysis. The results provide a better understanding of the durability of advanced materials and electronics when they are exposed to vacuum, solar radiation, atomic oxygen, and extremes of heat and cold. The project is a collaboration between the Electronics Science and Technology Division, Naval Center for Space Technology, and outside organizations. (Photo Credit: NASA, ISS021-E-031746, 23 Nov. 2009).

The NRL eight-beam (45 kV, 30 A), 600-kW output power S-band multiple-beam klystron (MBK). MBKs produce coherent, broadband microwave radiation in a compact package. This promising device technology has the potential to provide the low-noise, high average power transmitter performance required by shipboard radar systems to keep pace with evolving ballistic missile and anti-ship cruise missile threats in high clutter environments.


A microfabricated grating circuit made using deep reactive ion etching (DRIE) at NRL for a vacuum electronic traveling-wave amplifier driven by a sheet electron beam. The device is designed to generate up to 50 W at a center frequency of 220 GHz and has potential applications in extremely high data rate communication systems and high-resolution radar, with the added benefit of a drastically reduced antenna footprint.

Acetone molecule and single-walled carbon nanotube over an array of nanotube transistor structures.

cal processes on a timescale of tens of femtoseconds. It includes a synchronously pumped dye laser system for simulating the effects of charge deposited in semiconductors characteristic of space radiation.

The MWVESF contains a computer numerically controlled (CNC) milling machine and a CNC precision lathe capable of fabricating intricate millimeter-wave vacuum electronic components and a wire electric discharge machining (EDM) tool for fabrication of submillimeter-wave components that cannot be fabricated by conventional rotary cutting tools. EDM offers a non-contact process for both hard and soft metals as well as SiC and doped silicon. ✦

Center for Bio/Molecular Science and Engineering
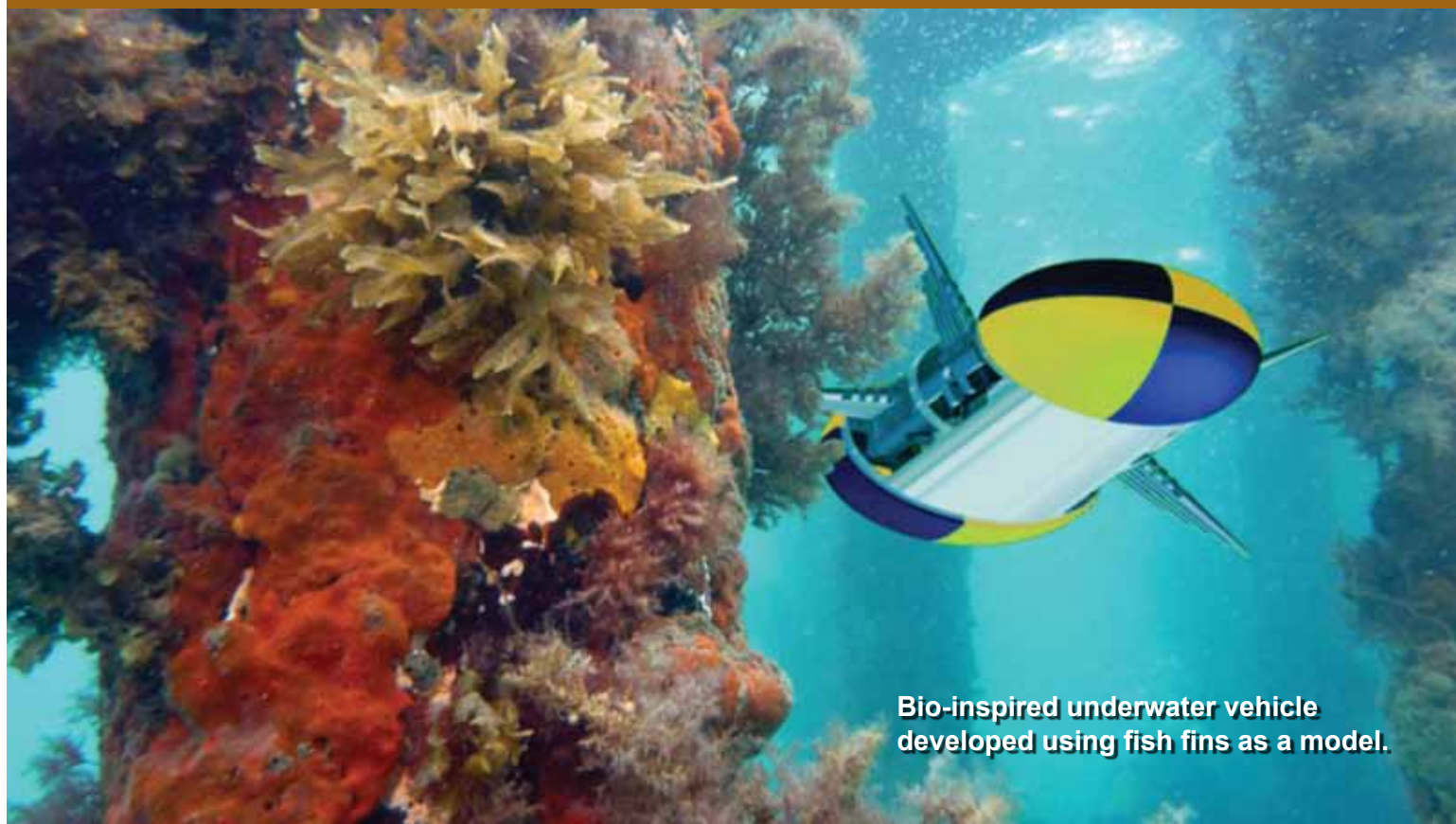
Bio-inspired underwater vehicle developed using fish fins as a model.

The Center for Bio/Molecular Science and Engineering conducts cross-disciplinary, bio-inspired research and development to address problems relevant to the Navy and the DoD by exploiting biology's well-known ability for developing effective materials and sensing systems. The primary goal is to translate cutting-edge, bio-based discoveries into useful materials, sensors, and prototypes that can be scaled up, are robust, and lead to enhanced capabilities in the field. The challenges include identifying biological approaches with the greatest potential to solve Navy problems and provide new capabilities while focusing on bio-inspired solutions that have not otherwise been solved by conventional means.

Studies involve biomaterial development for chemical/biological warfare defense, structural and functional applications, and environmental quality/cleanup. Program areas include optical biosensors, nanoscale manipulations, genomics and proteomics, bio/molecular and cellular arrays, surface modification,

energy harvesting, systems biology, viral particles as scaffolds, and bioorganic materials from self-assembly.

The staff of the Center is an interdisciplinary team with expertise in biochemistry, surface chemistry, biophysics, molecular and cell biology, organic synthesis, materials science, and engineering. The Center also collaborates throughout NRL and with other government laboratories, universities, and industry.

The Center's modern facilities include laboratories for research in chemistry, biochemistry, systems biology, and physics. Specialized areas include controlled-access laboratories for cell culture and molecular biology, an electron microscope facility, a scanning probe microscope laboratory, instrument rooms with access to a variety of spectrophotometers, a multichannel surface plasmon resonance (SPR) sensor, and an optical microscope facility including polarization, fluorescence, and confocal microscopes. Additional laboratories accommodate nuclear magnetic resonance (NMR) spectroscopy, liquid chromatography–mass spectrometry (LCMS), and fabrication of microfluidic and micro-optical systems in polymers. The Center maintains a state-of-the-art X-ray diffraction system including a MicroSTAR-H X-ray generator. In com-

bination with new detectors and components, the system is ideal for data collection on proteins or very small single crystals of organic compounds and is also capable of collecting data on films and powders. Addi-

tional core facilities have recently been established for Fluorescence Activated Cell Sorting (FACS), micro-array analysis and Circular Dichroism (CD) spectros-copy. ✦
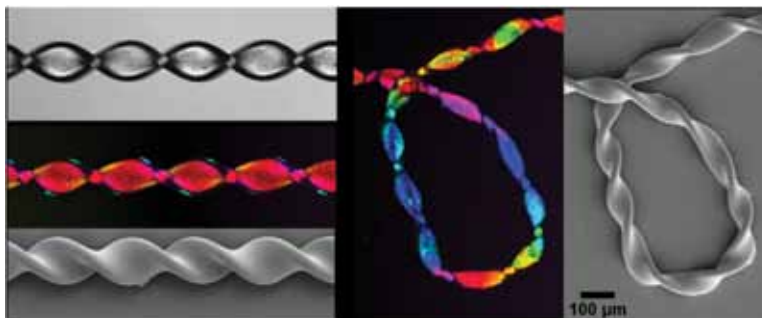

Liquid crystal structures controlled on the nano-, micro-, and milli-meter scale using hydrodynamic focusing. Shown are oriented liquid crystal acrylate fibers following post-fabrication manipulations.
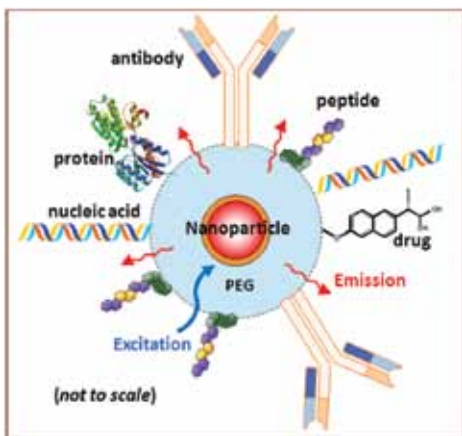
A Nanotoolbox has been developed to attach proteins and peptides to nanoparticles. Use of these methods is leading to new biologically active "smart" nanomaterials.

Test apparatus used to evaluate the performance of Benthic Microbial Fuel Cells (BMFCs) deployed worldwide at sites with different sediment types; shown here deployed in the Adriatic Sea off the coast of Slovenia.
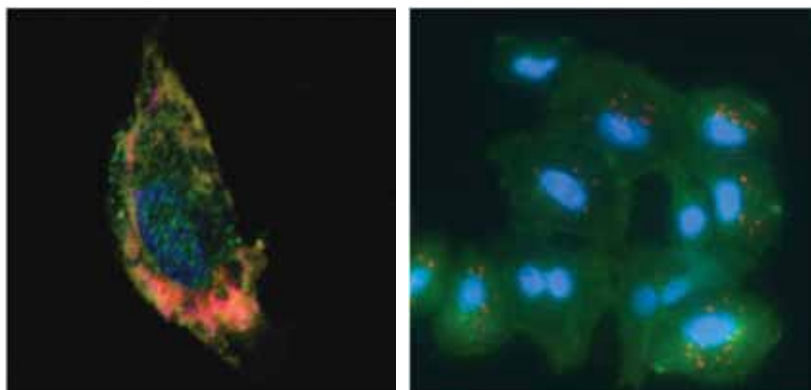
Simultaneous monitoring of signaling events within cells using quantum dots.

Acoustics

A 21-inch-diameter AUV is used for detection and classification in mine hunting and antisubmarine warfare applications.

The Acoustics Division conducts a broad research and development program in underwater acoustics, atmospheric acoustics, and physical acoustics requiring laboratory and at-sea measurements.

Laboratory Facilities: The Division has three integrated structural acoustic facilities — two pools (one with a sandy bottom) and a large, in-air, semi-anechoic laboratory. These facilities support research in areas including mine detection and identification, antisubmarine warfare, and detection of improvised explosive devices (IEDs). These facilities have a number of measurement capabilities including compact range scattering, nearfield holography, and scanning laser Doppler vibrometry. The major pool facility is cylindrical (17 m dia. × 15 m deep) and filled with approximately 1 million gallons of deionized water. Features include vibration and temperature control and anechoic interior walls to reduce reverberation.

The Salt Water Tank Facility provides a controlled environment for studying complex ocean processes under saline conditions, especially the acoustics of bubbly media. This 6 × 6 × 3 m pool facility has large plexiglass windows on all four sides to permit imaging of processes inside the tank. Instrumentation includes acoustic sources, amplifiers, hydrophones, environmental sensors, a digital holographic imaging system, high-speed digital cameras, and a LabVIEW-based data acquisition system.

The Geoacoustic Model Fabrication Laboratory enables fabrication of rough topographical surfaces in various materials (usually plastics) for acoustic scattering and propagation measurements in the tank facilities. The facility consists of a three-axis computer-controlled milling machine capable of cutting with 100-µm accuracy over a 1.37 × 1.27 m region.

The SOnoMAgnetic LABoratory (SOMALAB) is used to study magnetic fields produced by acoustic motions in electrically conducting media, such as seawater. Two nested skins of HY-80 steel plate magneti-

cally shield this facility. Inside is a 3 × 6 × 3 ft plexiglass experimental water tank on a vibration-insulating optical table equipped with three sets of mutually perpendicular Helmholtz coils to control the magnetic field. The tank is instrumented with a three-axis magnetometer, and acoustic signals are generated from an external transducer.

The Division also operates laboratories to study the structural dynamics and performance of high-Q oscillators and other micromechanical and nanomechanical systems. A super-resolution nearfield scanning optical microscope permits spatial mapping of the complex vibratory motion at resolutions of 100 nm. These laboratories can also measure the mechanical and electrical properties of micro-oscillators, and thin films applied to them.

At-Sea Research: The Division operates several systems to generate and receive sound in at-sea experiments. Sound sources include two XF-4 units, one ITC 2077 source with tow body, two battery-operated organ-pipes that can project single tones from off-board moorings, and a towable, vertically directional source array consisting of 10 individually controllable elements at frequencies of 1.5 to 9.5 kHz. In addition, the Division has several battery-operated, rubidium-clock controlled, programmable sound source moorings that can transmit sounds with arbitrary waveforms. The division has a 64-channel broadband source-receiver array with time reversal mirror functionality operating over 500–3500 Hz. The division operates high-frequency (up to 600 kHz) measurement systems to obtain scattering, target strength, and propagation data using bottom-moored instrumentation towers and a remotely operated vehicle.

The Division performs research to relate acoustic array gain variability to fluid dynamic variability and bottom heterogeneity in the littorals. Measurements are made with an autonomous acoustic data acquisition suite. Three independent, autonomous, 32-channel vertical arrays receive and store 24-bit data at 4 kHz for 22 days. Two autonomous sources operate at center frequencies of 300 and 500 Hz and generate programmable waveforms at 50% duty cycle for 22 days. The division also has seven Environmental Acoustic Recording Systems (EARS) buoys. The buoys are autonomous, self-recording, bottom-mounted acoustic acquisition systems. Each buoy can record four channels simultaneously at 25 kHz bandwidth per channel and has a storage capacity of 480 Gbyte. Each buoy has four hydrophones on a 22 m array.

Narrowbeam 200 and 350 kHz acoustic backscattering (flow visualization) systems are used to study

fine structure, internal wave, and larger-scale fluid dynamic perturbation of the density and sound speed field in the ocean. A 25 kW radar system is used in conjunction with the flow visualization system to record the surface expression of internal waves.

The Structural Acoustics In-Air Facility is instrumented with acoustic and vibration measurement systems for conducting ultra-high-precision, highly spatially sampled measurements on scaled submarine structures, satellite payload fairings, active and passive material systems for sound control, and new transducer and sensor systems.

The Division conducts research addressing the channel capacity of multi-node underwater acoustic communications networks. Two 8-channel acoustic communications data acquisition systems or modems, which can be moored or towed and remotely controlled, provide measurements in the 2–5 kHz, 6–14 kHz, and 10–14 kHz frequency bands.

NRL is developing and deploying AUV-based and rail-based systems for acquiring signature data at sea. The rail-based system has a 100 m horizontal robotic scanner used to collect synthetic aperture (SA) scattering data from proud and buried targets. The receiver system is used in conjunction with impulsive broadband projectors mounted on the scanner. The AUV-based system uses acoustic SA techniques to recover high-fidelity, quantitative broadband data over a large range of target aspect angles. ✦

Remote Sensing

The NRL HREP (HICO/RAIDS Experiment Payload) being deployed for operations on the Japanese Experiment Module of the International Space Station.
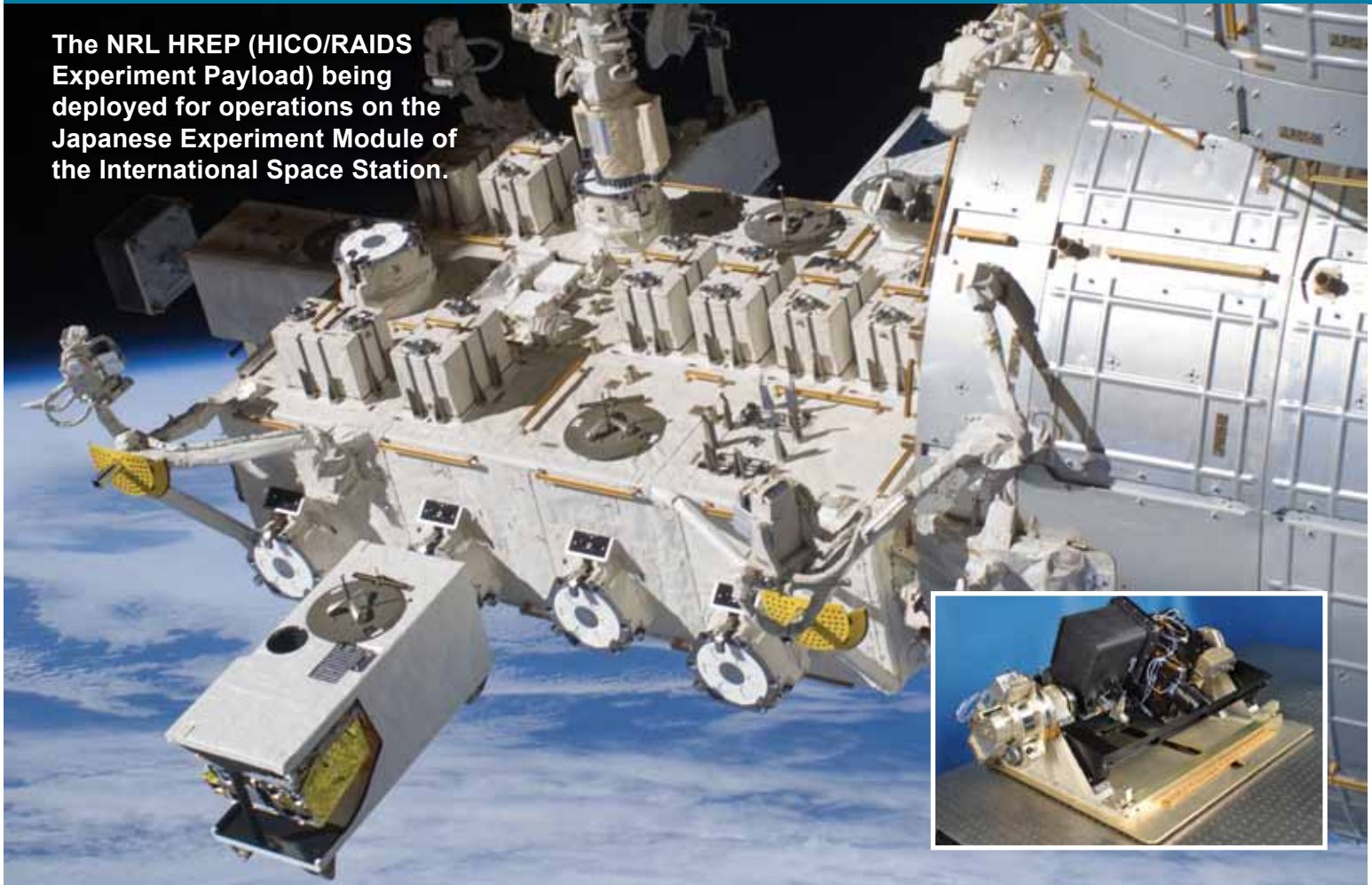
The Remote Sensing Division is the Navy's center of excellence for remote sensing research and development, conducting a broad program of basic and applied research across the full electromagnetic spectrum using active and passive techniques from ground-, air-, and space-based platforms. Current applications include earth, ocean, atmospheric, astronomy, astrometry, and astrophysical science, and surveillance/reconnaissance activities including maritime domain awareness, antisubmarine warfare, and mine warfare. Special emphasis is given to developing space-based platforms and exploiting existing space systems.

Research in ocean and earth science includes maritime hyperspectral imaging, radar measurements of the ocean surface for the remote sensing of waves and currents, model- and laboratory-based hydrodynamics, and land-based trafficability studies.

Current airborne sensors used for characterization of the littoral environment include visible/near-IR and shortwave hyperspectral imagers, a broadband, visible polarimetric sensor, long- and midwave IR thermal cameras, and an X-band, 2-channel interferometric synthetic aperture radar. As an outgrowth of our airborne sensing program, the Division developed the Hyperspectral Imager for the Coastal Ocean (HICO), the world's first spaceborne hyperspectral sensor specifically designed for coastal maritime environmental observations. HICO was launched to the International Space Station in September 2009 and is currently providing scientific imagery of varied coastal types worldwide. Ground-based instruments for maritime sensing include the NRL Focused Phased Array Imaging Radar (NRL FOPAIR), an X-band, high-frame-rate polarimetric radar system.

For radiometric and spectral calibration of the visible and IR imaging sensors, the Division operates a Calibration Facility that includes a NIST-traceable integrating sphere and a set of gas emission standards for wavelength calibration.

The Division's Free Surface Hydrodynamics Laboratory (FSHL) supports ocean remote sensing research. The lab consists of a 10 m wave tank equipped with a computer-controlled wave generator and a comprehensive set of diagnostic tools. Recent work focuses on
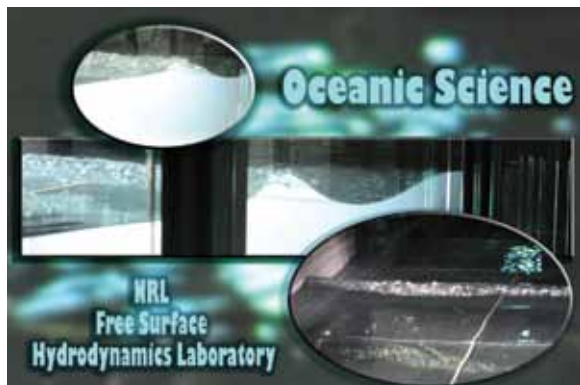
Snapshots of breakers generated in the Free Surface Hydrodynamics Laboratory. At lower right, a wave traveling toward the viewer is seen breaking across the width (approx. 3 m) of the tank. In the upper images, waves traveling from left to right are breaking and forming surface turbulence.

the physics of breaking waves, their infrared signature, and their role in producing aerosols. Experiments conducted in the FSHL are also used to test and validate numerical results and analytical theories dealing with the physics of the ocean's free surface.

Current atmospheric science research areas include the remote sensing of aerosols, measurement of ocean surface winds, and middle atmospheric research. The Division has developed a unique eye-safe volume-imaging lidar system to remotely characterize aerosol backscatter. NRL also developed the first spaceborne polarimetric microwave radiometer, WindSat, launched in January 2003 and still operational. Its primary mission was to demonstrate the capability to remotely sense the ocean surface wind vector with a passive system. WindSat provides major risk reduction for development of the microwave imager for the next-generation DoD operational environmental satellite program. WindSat data are processed at the Navy Fleet Numerical Meteorology and Oceanography Center (FNMOC), and operationally assimilated into the Navy global weather model, NOGAPS. In addition, the Remote Sensing Division is exploiting WindSat's unique data set for other environmental parameters such as sea surface temperature, soil moisture, and sea ice concentration.

The Water Vapor Millimeter-wave Spectrometer (WVMS) is a ground-based instrument designed to measure water vapor in the middle atmosphere. It

is part of the international ground-based Network for Detection of Atmospheric Composition Change (NDACC), with sensors based in Lauder, New Zealand, Mauna Loa, Hawaii, and Table Mountain, California.

The Division has research programs in astronomy and astrophysics ranging in wavelength from the optical to longwave radio, with an emphasis on interferometric imaging. Facilities include the Navy Prototype Optical Interferometer (NPOI), located near Flagstaff, Arizona, a joint project between the U.S. Naval Observatory and the NRL Remote Sensing Division. The NPOI is used for optical astrometry, to investigate unfilled aperture imaging technologies, and to conduct astrophysical research. When completed,

The NRL WindSat polarimetric radiometer prior to spacecraft integration.

it will be the highest-resolution ground-based optical telescope in the world. The Division is also at the forefront of research in low-frequency (<100 MHz) radio astronomy and associated instrumentation and interferometric imaging techniques. The Division developed and installed VHF receivers on the National Radio Astronomy Observatory's Very Large Array (VLA), and developed the imaging techniques to correct for ionospheric phase disturbances which had heretofore severely limited observational baselines and, thus, the utility of low-frequency astronomical imaging. The Division is also collaborating with the University of New Mexico and New Mexico Tech on the Long Wavelength Array, a prototype, next-generation, low-frequency imaging array with 200–300 km baselines. ✦

Oceanography

Profiling the SEPTR instrument in the Oceanography Division test pool.

The Oceanography Division is the major center for in-house Navy research and development in oceanography. It is known nationally and internationally for its unique combination of theoretical, numerical, experimental, and remotely sensed approaches to oceanographic problems. The Division's modeling focus is on a truly integrated global-to-coastal modeling strategy, from deep water up to the coast including straits, harbors, bays, inlets, and rivers. This requires emphasis on both ocean circulation and wave/surf prediction, with additional emphasis on coupling the ocean models to atmospheric, biological, optical, and sediment models. This includes processing and analysis of satellite and in-water observations, development of numerical model systems, and assimilation for predicting the ocean environment. This modeling is conducted on the Navy's and DoD's most powerful vector and parallel processing machines. The Division's in-house Ocean Dynamics and Prediction Computational Network Facility provides computer services to scientists for program development, graphics, data processing, storage, and backup. To study the results of this intense modeling effort, the Division operates a number of highly sophisticated graphic systems to visualize ocean and coastal dynamic processes. Problems addressed cover a wide scope of physics including parameterization of oceanic processes, construction and analysis of ocean models and forecast systems, basic and applied research of ocean dynamics, surface waves, thermohaline circulation, nearshore circulation, estuarine and riverine modeling, Arctic ice modeling, internal waves, and ocean/atmosphere coupling. Additional emphasis is on optimization of underwater, airborne, and satellite observing systems, representation of ocean processes affecting temperature, salinity, and mixed-layer depth, uncertainty analysis in coupled systems, ensemble and probabilistic ocean forecasting, targeting ocean observations, representing probability in ocean/acoustic systems, and satellite-observed surface heat fluxes. The end goal is to build cutting-edge technology systems that transition to operational forecast centers.

The Division's Ocean Sciences Branch conducts basic and applied research in ocean physics, air-sea interaction, ocean optics, and marine microbially influenced corrosion. Emphasis of this research is

on understanding the oceans' physical processes and their interactions with the atmosphere and biological/chemical systems at scales ranging from basin-scale to microscale. Numerical and analytical models are developed and tested in laboratory and field experiments. The results of this research support the Navy's operational capability for predictions of oceanic atmospheric exchanges, acoustic propagation/detection, light transmission/emission, and influences of microbes on marine corrosion. The seagoing experimental programs of the Division range worldwide. Unique measurement systems include a wave measurement system to acquire in situ spatial properties of water waves; a salinity mapper that acquires images of spatial and temporal sea surface salinity variabilities in littoral regions; an integrated absorption cavity and optical profiler system, and towed optical hyperspectral array for studying ocean optical characteristics; self-contained, bottom-mounted, upward-looking acoustic Doppler current profilers (ADCPs) for measuring ocean variability; and an in situ volume scattering function measurement system to support remote sensing and in-water optical programs. NRL worked jointly with the NATO Undersea Research Center (NURC) for development and deployment of the SEPTR instrument, a trawl-resistant, bottom-mounted ADCP system that includes a pop-up profiling float for real-time observation and reporting. A new capability is the addition of an optical sensor on the profiling float.

The Oceanography Division has acquired new capabilities for sensing the littoral environment. These include a Vertical Microstructure Profiler (VMP), a Scanfish, four Slocum Gliders, and an instrument test pool. The turbulent dissipation rate can be quickly obtained with very high accuracy from measurements collected by the VMP. The Scanfish allows efficient and rapid three-dimensional mapping of mesoscale oceanic features. The Gliders rely on a low-powered battery-induced change of buoyancy to glide autonomously through the coastal ocean collecting both physical and optical data that are uplinked to satellite and then relayed to the laboratory or ship in near real time. In the laboratory, the Division operates an environmental scanning electron microscope and a newly acquired dual beam environmental scanning electron focused ion beam microscope for detailed studies of biocorrosion in naval materials.

The Division's remote sensing research focuses on radiative transfer theory, optical ocean instrumentation, lasers and underwater imaging and vision, satellite and aircraft remote sensing, remote sensing of bio-optical signatures, and coupled physical bio-optical

modeling. The research includes applying aircraft and satellite ocean color and thermal infrared signatures for understanding the bio-geo-chemical cycles in the surface ocean. Additional emphasis is on algorithm and model development using satellite (SeaWifs, MODIS, MERIS, NPOESS, OCM, HICO, GEOCAPE, ACE) and aircraft (CASI, AVIRIS, PHILLS) sensors to address the spatial and temporal variability of coastal optical properties. The Division has the capability to download MODIS data directly using an X-band receiving system and is a national leader in the development and analysis of MODIS ocean color data for oceanographic processes and naval applications in littoral areas. The Division conducts optical field experiments using advanced in situ and remote sensing instrumentation (ship-towed sensors, sea gliders, and bio-optical/physical moorings) to understand remotely sensed signatures for calibration, validation, and refinement of algorithms. The Division also conducts research addressing how remote sensing optical and biological signatures can be fused with in-water bio-optical profiles and assimilated into ocean process models, and includes developing methods and techniques to understand and forecast the ocean optical environment through the combined use of remote sensing products and models. ✦

The X&L Band Antenna adjacent to the Oceanography Division building.

Marine Geosciences

Sand ripples are studied in a small oscillatory flow tunnel where fluid and sediment are imaged with high-speed video cameras. The inset images illustrate the formation of sedimentary strata resulting from sorting processes between smaller (blue) and larger (natural) sands.
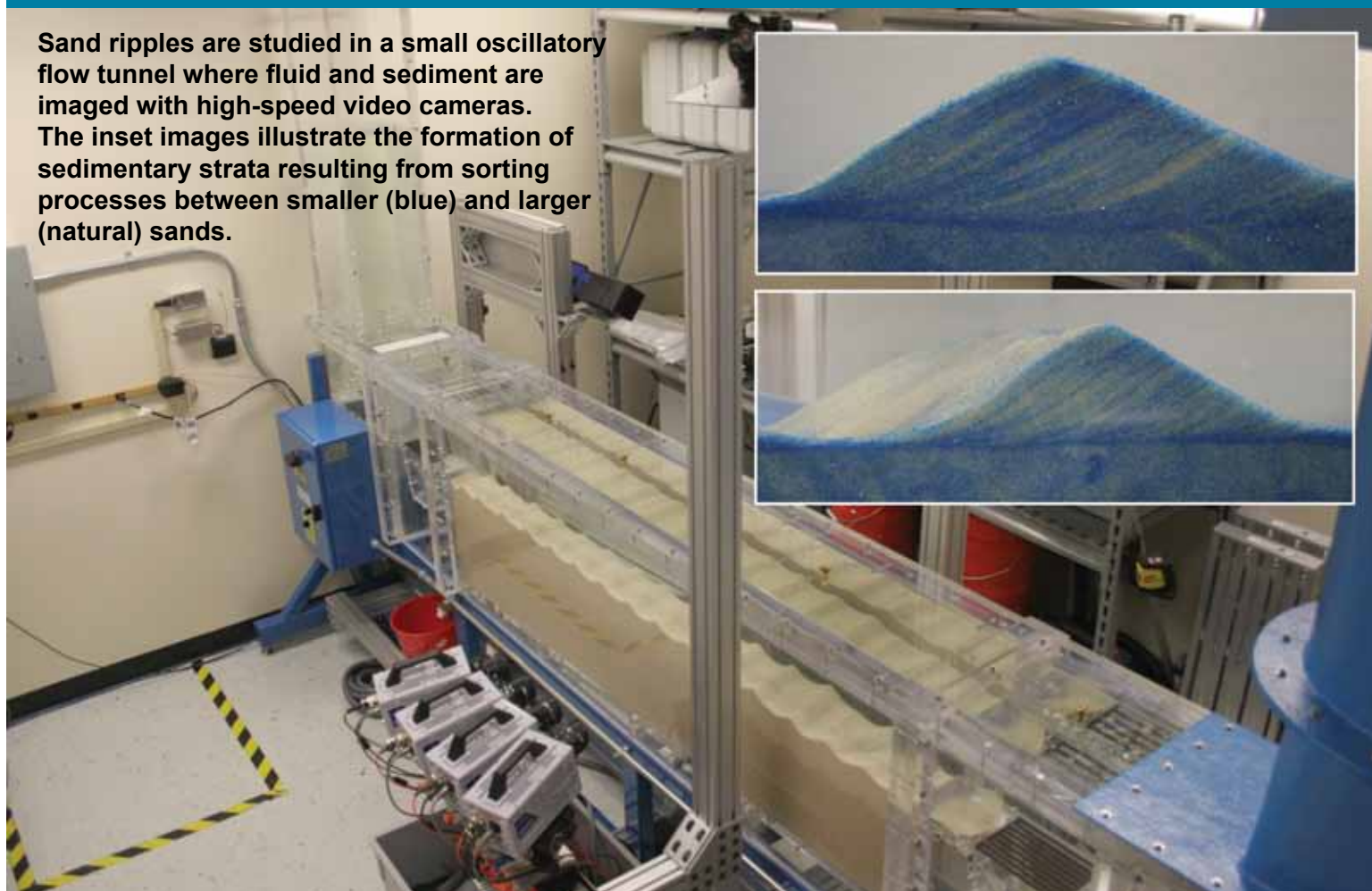
The Marine Geosciences Division is the major Navy in-house center for research and development in marine geology, geophysics, geodesy, geoacoustics, geotechnology, and geospatial information and systems.

Instrumentation used in the field is deployable from aircraft, ships, submarines, remotely operated and unmanned vehicles, undersea platforms, and by divers. Instrumentation includes an integrated airborne geophysical sensor suite with gravity, magnetic, and sea/ice/land topographic profiling sensors, all based on centimeter-level KGPS aircraft positioning. Seafloor and subseafloor research uses the Deep-Towed Acoustics/Geophysics System (220 to 1000 Hz); a chirp sub-bottom profiler; high-resolution sidescan sonars (100 and 500 kHz); the Acoustic Seafloor Characterization System (15, 30, and 50 kHz); the In Situ Sediment Acoustic Measurement System, measuring compressional and shear wave velocities and attenuation; a heat flow probe system; and underwater stereo photography and nearshore video imaging systems. Five instrumented, 8-ft-long, 2220-lb, mine-like cylinders are used to gather impact burial data (one system) and scour and sand wave burial data (four systems) for testing and validation of mine burial prediction models.

Laboratory facilities allow measurement of sediment physical, geochemical, and geotechnical properties. Equipment includes a photon correlation spectrometer and a laser Doppler velocimeter to measure size and electrostatic properties of submicrometer-size sediment particles. The Transmission Electron Microscopy Facility includes a 300 kVa transmission electron microscope with environmental cell enabling real-time observations of hydrated and gaseous experiments for research in microscale biological, chemical, and geological processes. A high-resolution industrial computed-tomography scanner provides capability for investigating volumetric heterogeneity of sediments.

The Geospatial Services Laboratory provides for advanced geospatial service development and hosting of content on its 36 racks of computer hardware, 250 servers, and 1 petabyte of storage in a new 1400 ft^2 facility. The Geospatial Hub (GHub) is a geospatial content management system that allows: (1) a collab-orative environment for organizing/searching disparate DoD content, (2) full access and control over the system and content using Web Services, and (3) automatic syn-chronization of content among multiple GHub systems from initial production to field usage. ✦
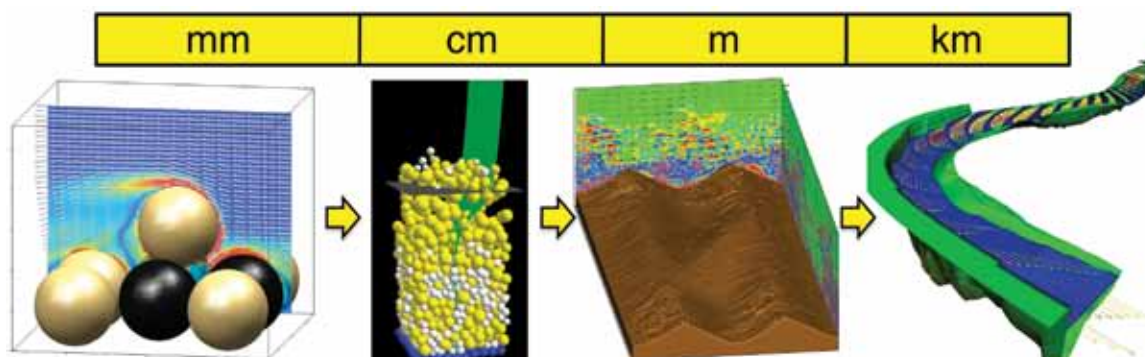
In the Marine Geosciences Division, scientists model sediment transport phenomena that span many orders of magnitude, from the discrete particle scale (far left) where individual grains are simulated, up to the continuum scale (far right) where the flow in rivers is resolved. The goal is to develop reliable forecasting models for operational length and time scales. Consequently, we must simulate the relevant physics of the problem at each scale and identify links between adjacent scales (arrows). Pictures from left to right: a fully resolved simulation of the entrainment of an individual particle into a turbulent boundary layer; simulation of sheet flow transport using a discrete particle model; simulation of sand ripple evolution using mixture theory (SedMix3D); and simulation of flow in a reach of the Kootenai River, Idaho.
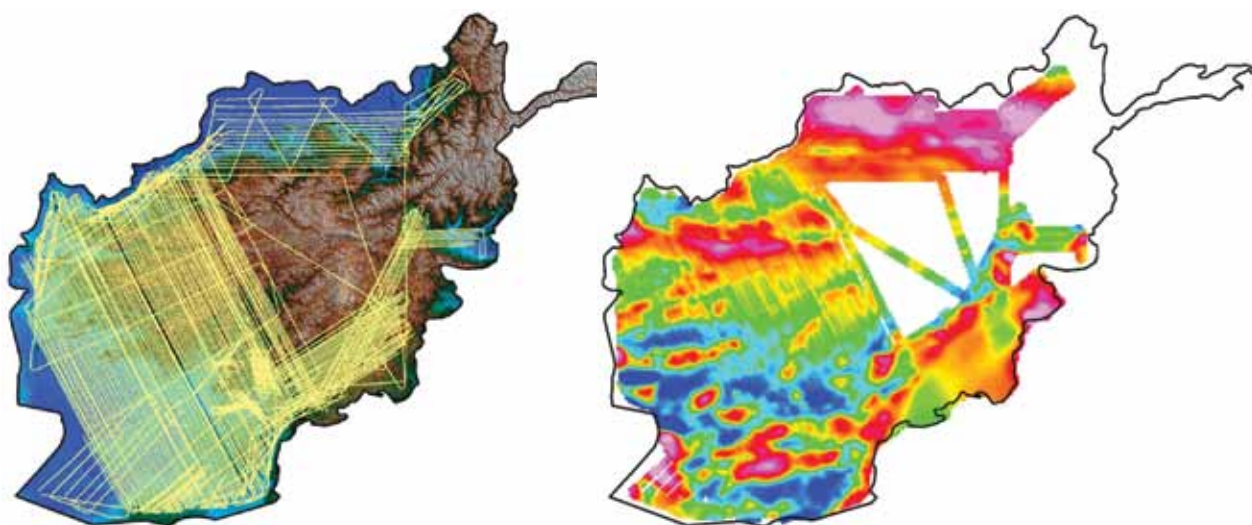
Rampant Lion I and II were multisensor aerogeophysical surveys of Afghanistan conducted in 2006 and 2008 by NRL and the U.S. Geological Survey to advance geospatial techniques, support military planners, and aid in economic infrastructure develop-ment. During Rampant Lion I, 40 mission flights produced more than 125,000 line-km of airborne survey tracks (left) and 330,000 km^2 of imagery. The magnetic anomaly map (right) provides data for oil, gas, and mineral exploration.

Marine Meteorology
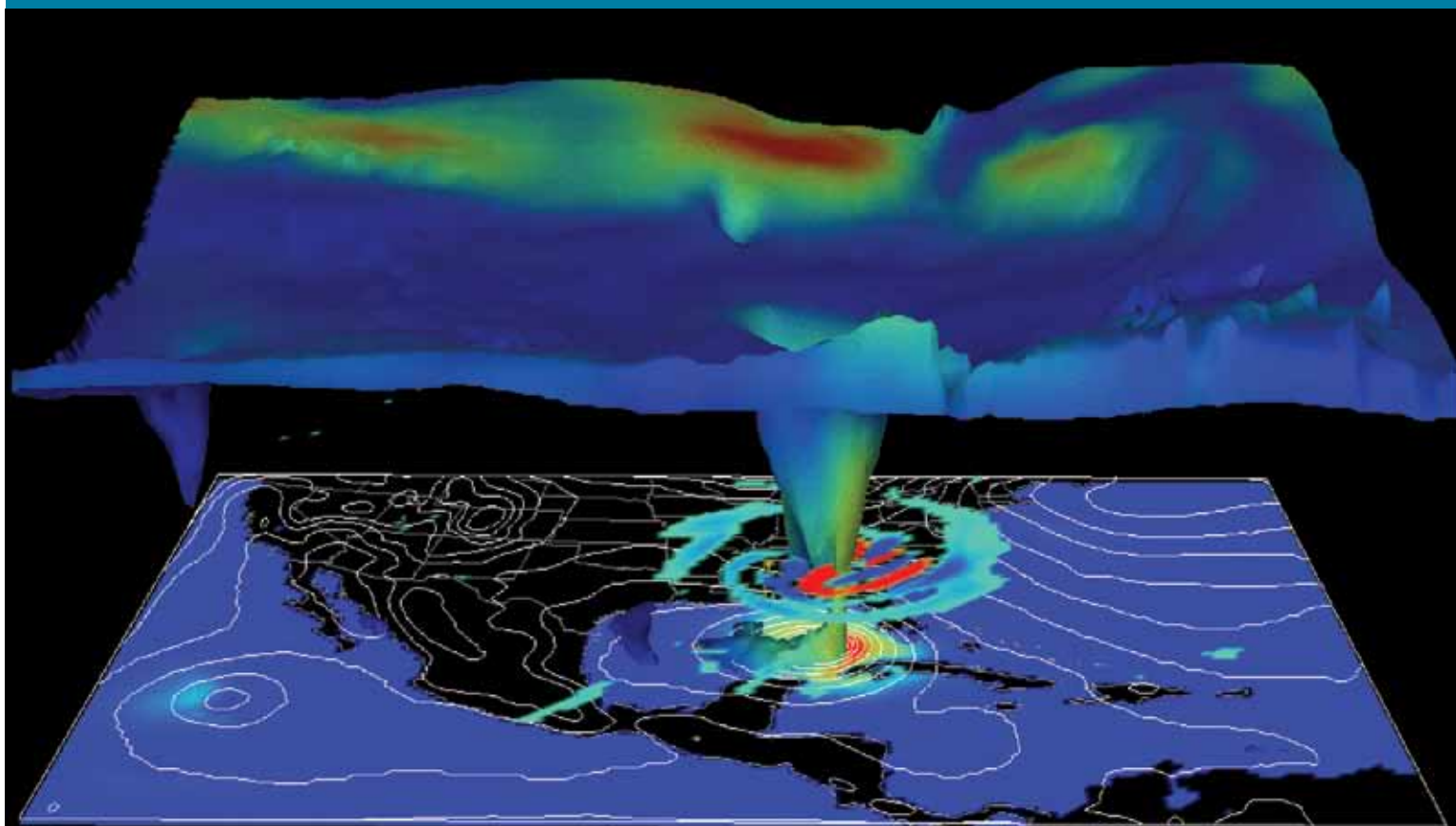
3D depiction of Hurricane Katrina 2005 by NRL's high-resolution operational mesoscale model, COAMPS®-TC (Coupled Ocean/Atmosphere Prediction System–Tropical Cyclone)

The Marine Meteorology Division, located in Monterey, California, conducts basic and applied research in atmospheric sciences and develops meteorological analysis and prediction systems and other products to support Navy and other customers at the theater, operational, and tactical levels. The Division is collocated with the Fleet Numerical Meteorology and Oceanography Center (FNMOC), the Navy's operational production center for numerical weather prediction (NWP) and satellite imagery interpretation.

The Division's Environmental Prediction System Development Laboratory is built around several LINUX clusters (currently up to 176 processors and a planned upgrade to over 5000 processors) supported by an approximately 800 TB RAID storage system and a tape library capable of expansion to about 10 PB. The Division also maintains over 100 LINUX servers, including a unique Global Ocean Data Assimilation Experiment (GODAE) server hosting data sets suitable for research and development of ocean and atmospheric data assimilation capabilities. These systems, in combination with DoD Supercomputing Resource Centers (DSRC) and FNMOC assets, enable the Division to efficiently develop, improve, and transition numerical weather analysis and prediction systems and coupled air/ocean systems to operational use, producing guidance which is used by Fleet forces around the globe. These systems also support basic research in atmospheric processes such as air-sea-ice interaction, atmospheric dynamics, and cloud/aerosol physics, as well as development of environmental applications, decision aids, and probabilistic prediction products.

The Division's state-of-the-art Satellite Data Processing Laboratory allows direct downlink of real-time NOAA geostationary (GEO) data and data relays from

five other geostationary satellites. Data from numerous low Earth orbiting (LEO) platforms is also received in near real time via extensive interagency agreements. In total, NRL-Monterey processes satellite data from 26 LEO sensors and seven GEO platforms and uses that data to conduct research and development of multisensor data fusion products to support a variety of DoD operations. These activities range from monitoring and analyzing tropical cyclone characteristics to providing special meteorological products in support of combat operations in Southwest Asia.

The Mobile Atmospheric Aerosol and Radiation Characterization Observatories (MAARCO) are a pair of mobile laboratories housed in climate-controlled shipping containers with integrated suites of meteorological, aerosol, gas, and radiation instruments that can be deployed to operate in strategic areas around the globe, including remote regions, overseas locales, and aboard ships at sea. The modular instruments can also be removed and mounted on aircraft for added flexibility in field data collection, and are used to investigate boundary layer meteorology, aerosol microphysics, and electro-optical propagation. ✦

MAARCO is designed as a stand-alone facility for basic atmospheric research and the collection of data to assist in validating aerosol and weather models. Its purpose is to enable research on atmospheric aerosols, gases, and radiation (visible and IR light) in areas of key interest, including remote areas, overseas locales, and aboard ships. This complete mobile laboratory facilitates deployment in areas with limited facilities, and provides maximum flexibility for integration of additional instrumentation.

NRL's Marine Meteorology Division processes satellite data from 26 low-Earth-orbit sensors and seven geostationary platforms and uses that data to conduct research and development of multisensor data fusion products to support a variety of DoD operations.
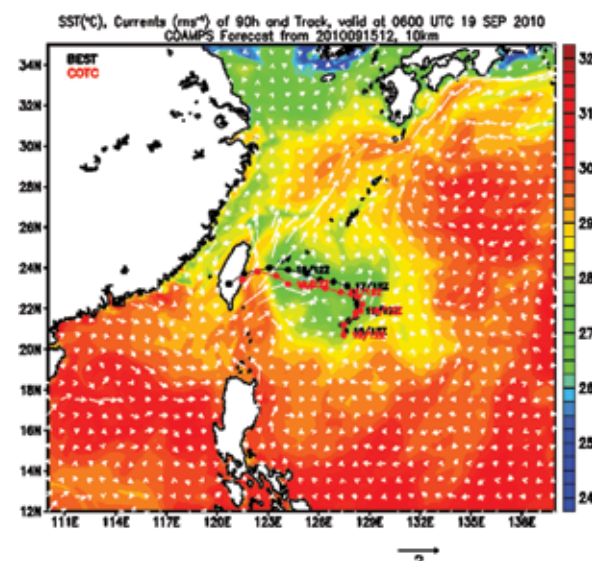
The sea surface temperature (shaded, in °C) and surface currents (vectors, ms⁻¹) at 90 hour of the coupled COAMPS®-TC forecast starting at 1200 UTC 15 Sept. 2010, overlaid with the model track (red dots) and the BEST track (black dots).

Space Science
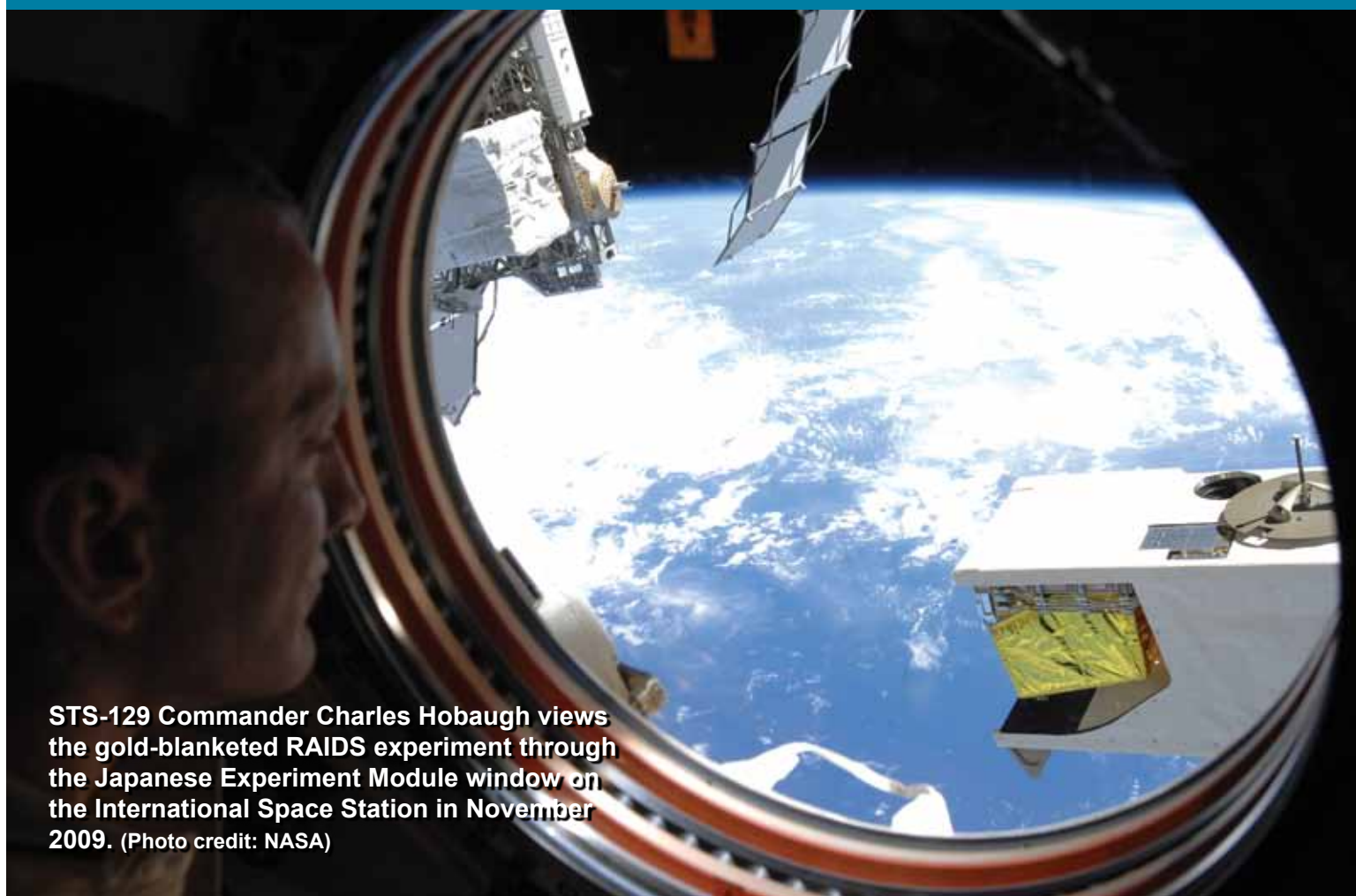
STS-129 Commander Charles Hobaugh views the gold-blanketed RAIDS experiment through the Japanese Experiment Module window on the International Space Station in November 2009. (Photo credit: NASA)

The Space Science Division conducts a broad-spectrum RDT&E program in solar-terrestrial physics, astrophysics, upper/middle atmospheric science, and astronomy. Division researchers conceive, plan, and execute scientific research and development programs and transition the results to operational use. They develop instruments to be flown on satellites, sounding rockets and balloons; and ground-based facilities and mathematical models. Division major research thrusts include remote sensing of the upper and middle atmospheres, studies of solar activity and effects on the Earth's ionosphere, and studies of high-energy natural radiation and particles, for applications ranging from astrophysics through force protection.

The Division's Vacuum Ultraviolet Solar Instrument Test (SIT) facility is an ultra-clean solar instru-ment test facility designed to satisfy the rigorous contamination requirements of state-of-the-art solar spaceflight instruments. The facility has a 400 ft^2 Class 10 clean room and a large Solar Coronagraph Optical Test Chamber (SCOTCH). The SIT clean room is ideally suited for assembly and test of contamination-sensitive spaceflight instrumentation. It contains a large vibration-isolated optical bench and a 1-ton capacity overhead crane. The SCOTCH consists of a large vacuum tank and a precision instrument-pointing table. The division also maintains extensive facilities for supporting ultraviolet (UV) spectroscopy sounding rocket programs. These facilities include a dedicated Class 1000 instrument clean room, and a gray room area for assembling and testing the rocket payloads that incorporates all of the fixtures required for safe handling of payloads. The Division rocket facilities also include a large UV optical test chamber that is additionally equipped with a large vibration- and

thermal-isolated optical bench for telescope testing, which allows the laboratory area to be turned into a Schlieren facility. The Division also has a unique facility for developing Doppler Asymmetric Spatial Heterodyne (DASH) thermospheric wind sensors, which are currently being evaluated and tested in support of potential future space flight missions.

The division has a wide range of new satellite, rocket, balloon, and ground-based instruments under development. These include the SoloHI heliospheric imager that will image both the quasi-steady flow and transient disturbances in the solar wind when aloft on-board the Solar Orbiter mission; the Compact CORonagraph (CCOR), an elegant, externally occulted instrument that uses a single-stage optical design with two lens groups, a polarization analyzer, and a spectral filter to achieve performance comparable to the traditional three-stage Lyot coronagraph but with significantly lower mass and volume than the traditional design; and the NRL-led Large Area Scintillation Array (LASA), intended to demonstrate standoff detection of radiation/nuclear weapons of mass destruction (WMD) in maritime environments in support of the Office of Naval Research's Maritime WMD Detection program. Division scientists are also designing innovative high-resolution spectrometers for a possible flight on the Japanese Solar-C mission that will provide unprecedented views of the solar atmosphere.

Two Division experiments are measuring the Earth's thermosphere and ionosphere to improve Space Weather forecasting for these near-space atmospheric regions which significantly influence the performance of important operational systems such as GPS navigation, communication, and space debris tracking. The Remote Atmospheric and Ionospheric Detection System (RAIDS) is a new NRL experiment studying the Earth's upper atmosphere from a vantage point on the International Space Station (ISS). The RAIDS suite of eight optical sensors passively measures naturally occurring airglow from extreme ultraviolet to near infrared to derive atmospheric composition, density, and temperature. Demonstrating new remote sensing techniques, RAIDS is serving as a pathfinder experiment for atmospheric remote sensing from the ISS platform, and has provided the first globally sampled temperature measurements in the 120 to 165 km altitude range. The Special Sensor Ultraviolet Limb Imager (SSULI) developed by NRL's Space Science Division and Spacecraft Engineering Department offers a first-of-its-kind technique for remote sensing of the ionosphere and thermosphere from space. Flying on the U.S. Air Force Defense Meteorological Satellite

Program (DMSP) F18 (flight 18) satellite, SSULI's characterization of the Earth's upper atmosphere and ionosphere provides the necessary scientific data to support military and civil systems. Offering global observations that yield near-real-time altitude profiles of the ionosphere and neutral atmosphere over an extended period of time, SSULI makes measurements from the extreme ultraviolet (EUV) to the far ultraviolet (FUV).

Division scientists, using the Division network of computers and workstations and other connected high performance computing assets, develop and maintain physical models in support of their research. These include NOGAPS-ALPHA, the Advanced Level Physics High Altitude middle atmosphere extension of the Navy Operational Global Atmospheric Prediction System; HiFi, a user-friendly, highly parallel, fully implicit adaptive spectral element code framework designed for model development, magnetohydrodynamics, and multi-fluid numerical modeling in two- and three-dimensional geometries; and GAIM (Global Assimilation of Ionospheric Measurements), a physics-based assimilative model of the ionosphere now operational at the Air Force Weather Agency. ✦

The Hyperspectral Imager for Coastal Ocean (HICO) and Remote Atmospheric and Ionospheric Detection System (RAIDS) Experiment Payload (HREP) installed on the Japanese Experiment Module Exposed Facility on the ISS. In this view from the Japanese Experiment Module window, the gold-blanketed RAIDS scan head is tipped down to make extreme ultraviolet measurements of the Earth's daytime ionosphere below the ISS. (Photo credit: NASA)

Space Systems Development Department

Space Systems Development Department Optical Test Facility transmits laser light at both 1064 nm and 1550 nm for both satellite laser ranging and free space optical communication signals.

The Space Systems Development Department (SSDD) is responsible for the end-to-end definition, design, development, integration, test, and operation of space systems that satisfy naval and national defense requirements.

The total system engineering philosophy employed by the SSDD enables seamless sensor-to-shooter capabilities to be deployed that optimize the interfaces between command and control, on-orbit satellite collection, and onboard and ground processing functions; the dissemination of data to tactical and national users; and the design of tools that provide for the automated correlation and fusion of collected information with other sources.

Research and development is conducted in the areas of space system architectures; advanced mission data processing and data analysis techniques; advanced information systems concepts, including enterprise and cloud computing and networking of space, air, ground, and subsurface sensors; and mission simulation techniques. Intelligence collection, advanced RF, optical, and laser communication, satellite laser ranging, digital signal processing, data management, and space navigation systems are constantly improved upon to satisfy evolving requirements. These systems are engineered for maximum reuse and interoperability.

Having conceived of and developed the payload for the first Global Positioning System (GPS) satellite, the SSDD continues to be the world's center of excellence in the research and development of advanced GPS technology. Advanced theoretical and experimental investigations are applied to expanding the design and interoperability of systems used for a wide range of military, space, geodetic, and time dissemination applications. These investigations involve critical precise time generation and measurement technology

for passive and active ranging techniques incorporating advanced data transmission and signal design. Precise time and time interval research conducted involves theoretical and experimental development of atomic time/frequency standards, instrumentation, and time-keeping to support highly precise and accurate time-scale systems in scientific and military use. Net-centric systems are critically dependent on highly accurate and stable time/frequency standards coordinated to a common timescale through the diverse dissemination comparison techniques developed within the SSDD.

The PCEF (Precision Clock Evaluation Facility) is one of the major facilities within NRL's Naval Center for Space Technology. The PCEF was developed to support development of high precision clocks for GPS spacecraft and ground applications, primarily atomic standards. Space atomic clocks are evaluated, qualified, and acceptance tested for space flight using the assets of this facility. Testing performed includes long- and short-term performance evaluation, and environmental testing (including shock and vibration). Investigations

system development and deployment. The ability to evaluate and test highly precise atomic clocks, especially in a space environment, requires unique facilities, precise time and frequency references, and precise instrumentation not available anywhere else. The primary time and frequency reference for the PCEF is a specially designed environmental chamber housing a number of hydrogen masers combined with measurement equipment permitting a realization of Universal Coordinated Time (UTC) to be maintained as UTC (NRL) in cooperation with the International Bureau of Weights and Measures (BIPM) for reference and research purposes.

In addition to a wide array of test tools and facilities, the Department operates several field sites including the Midway Research Center satellite calibration facility in Stafford, Virginia; the Blossom Point Satellite Tracking and Command Facility in Welcome, Maryland; and the Chesapeake Bay Detachment Radar Range in Chesapeake Beach, Maryland. ✦

The Naval Center for Space Technology's Precision Clock Evaluation Facility (PCEF).

of on-orbit anomalies are performed within the PCEF to attempt to duplicate similar effects in space-qualified hardware under controlled conditions. The facility was originally developed to evaluate developments in the Global Positioning System concept development program (Block I) and expanded for the dedicated space clock development conducted during operational

Spacecraft Engineering Department
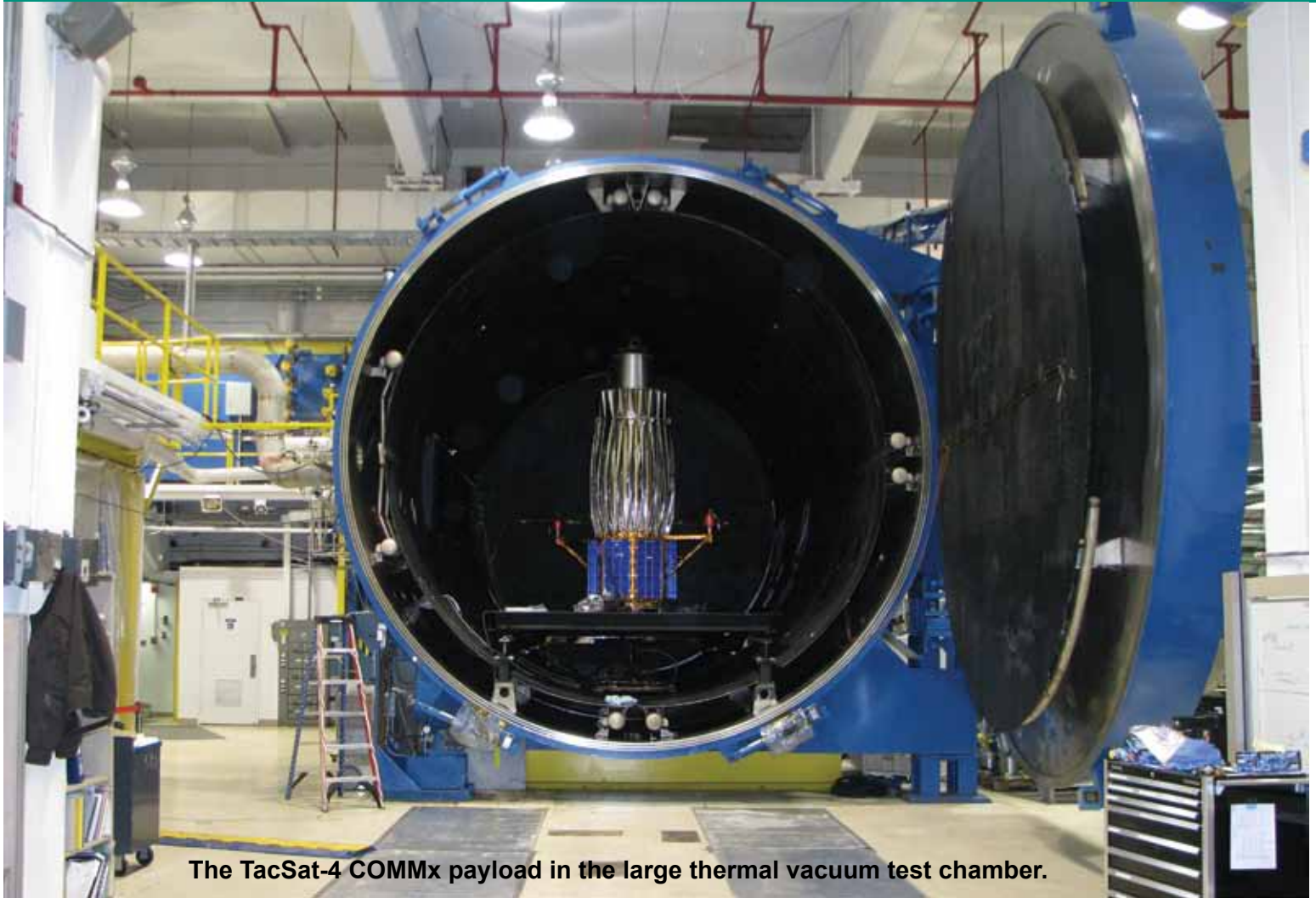
The TacSat-4 COMMx payload in the large thermal vacuum test chamber.

The Spacecraft Engineering Department (SED) and the Space Systems Development Department, together comprising NRL's Naval Center for Space Technology (NCST), cooperatively develop space systems to respond to Navy, DoD, and national mission requirements with improved performance, capacity, reliability, efficiency, and life cycle cost.

The SED facilities that support this work include integration and test highbays, large and small anechoic radio frequency chambers, varying levels of clean rooms, shock and vibration tables, an acoustic reverberation chamber, large and small thermal/vacuum test chambers, a thermal systems integration and test laboratory, a spin test facility, a static loads test facility, and a spacecraft robotics engineering and control system interaction laboratory.

Integration and Test Facilities

The Radio Frequency Anechoic Chamber supports electromagnetic compatibility/radio frequency interference (EMC/RFI) testing of flight hardware. It is also used to support custom RF testing up to 40 GHz. The facility consists of a 23 × 23 ft semi-anechoic main chamber with a 23 × 20 ft antechamber. It is a completely welded steel structure which provides a minimum of 120 dB of shielding effectiveness at 18 GHz and 100 dB up to 50 GHz. The main chamber uses a hybrid anechoic material consisting of wideband pyramidal absorbers and ferrite tiles for performance from

20 MHz to 50 GHz. A 10 ft high × 11 ft wide sliding bladder type door allows easy access of large test items to the main chamber.

The Laminar Flow Clean Room provides a Class 100 ultraclean environment for the cleaning, assembly, and acceptance testing of contamination-sensitive spacecraft components, and integration of complete spacecraft subsystems. The facility is used primarily to support spacecraft propulsion systems but has been used to support all spacecraft electrical, electronic, and mechanical subsystems.

The Vibration Test Facility, which simulates the various vibration loading environments present during flight operations and demonstrates compliance to design specifications, consists of the following shakers: Unholtz-Dickie T5000 50K Flb random 2-in. DA stroke, Ling 4022 30K Flb random 2-in. DA stroke, Ling 2022 16K Flb random 2-in. DA stroke, and a Ling 335 16K Flb random 1-in. DA stroke.

The Acoustic Reverberation Simulation Facility is a 10,000 ft^3 reverberation chamber that simulates the acoustic environment that spacecraft will experience during launch. The maximum capable sound pressure level is approximately 152 dB.

The Thermal Fabrication and Test Facility supports the design, fabrication, installation, and verification of spacecraft thermal control systems. It also provides for the analytical thermal design and analysis of any spacecraft. This includes conceptual design, analytical thermal model development, definition of requirements, worst-case environments and design conditions, and temperature predictions for all cases. The facility

provides the means to go from design and analysis to hardware qualification and acceptance testing and then to orbit.

The Spin Test Facility contains two spin balancing machines (one horizontal and one vertical) to handle various types of balancing requirements. Both machines are provided with a plane separation network to obtain correction readings directly in the plane of correction. Moment of inertia (MOI) tables of various capacities are used to verify MOI and center of gravity for units under test.

The Static Loads Test Facility provides the capability to perform modal survey testing on a wide variety of spacecraft and structures. It consists of two 6-ft × 12-ft × 6-in.-thick, ~15,500-lb steel plates (attachable) with floating base, six 75-Flb stinger shakers (1/2-in. DA stroke), two 250-Flb stinger shakers (4-in. DA stroke), and a ~300-channel data acquisition system (expandable).

Spacecraft Robotics Engineering and Controls Laboratory

This facility, which is the largest dual-platform motion simulator of its kind, is operated by NCST in collaboration with NRL's Naval Center for Applied Research in Artificial Intelligence. It supports research in the emerging field of space robotics including autonomous rendezvous and capture, remote assembly operations, and machine learning. It allows full-scale, hardware-in-the-loop testing of flight mechanisms, sensors, and logic of space robotic systems.
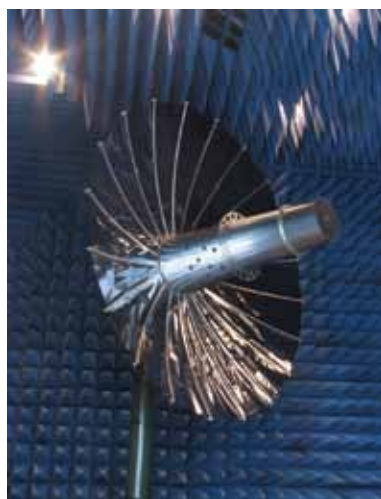
The TacSat-4 COMMx reflector being tested in the anechoic chamber.
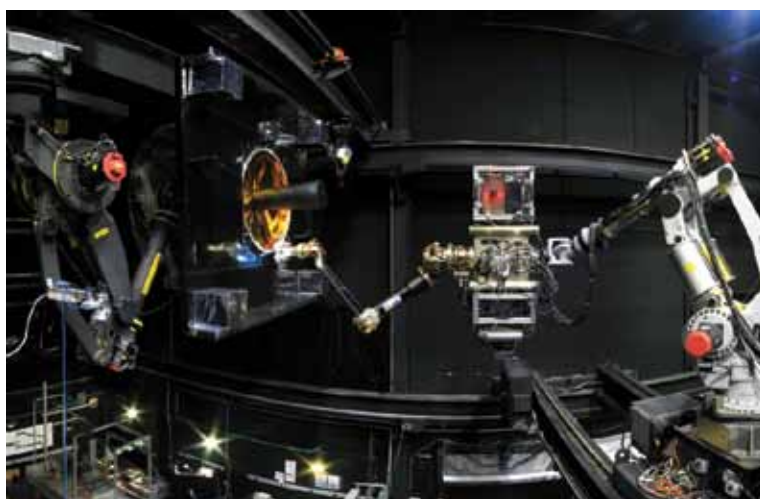
The Spacecraft Robotics Engineering and Controls Laboratory.

RESEARCH SUPPORT FACILITIES

Technology Transfer Office

The NRL Technology Transfer Office (TTO) is responsible for NRL's implementation of the Federal Technology Transfer Act. It facilitates the transfer of NRL's innovative technologies for public benefit by marketing NRL technologies and by negotiating patent license agreements and Cooperative Research and Development Agreements (CRADAs).

TTO markets NRL technologies through its Web site, by the preparation of Fact Sheets to be distributed at trade shows and scientific conferences, and through DoD-contracted Partnership Intermediaries such as TechLink.

A license grants a company the right to make, use, and sell NRL technologies commercially in exchange for equitable licensing fees and royalties. Revenue is distributed among the inventors and NRL's general fund. Prior to granting a license, TTO reviews the commercialization plan submitted by the licensee in support of its application for license. The plan must provide information on the licensee's capabilities, proposed development expenditures, milestones, a time line to commercialization, and an assessment of the intended market.

A license may be exclusive, partially exclusive (exclusive for a particular field of use or geographic area), or non-exclusive. Once a license is executed, TTO monitors the licensee for timely payments and for its diligence in commercializing the licensed invention.

TTO also negotiates Government Purpose Licenses to transition NRL technologies for manufacture and sale solely for Navy and other U.S. Government purposes.

CRADAs provide a vehicle for NRL scientists and engineers to collaborate with their counterparts in industry, academia, and state and local governments. Under a CRADA, a company may provide funding for collaborative work between it and NRL and is granted an exclusive option to license technologies developed under that CRADA's Statement of Work (SOW). TTO works with the NRL scientist to develop a SOW that has sufficient detail to define the scope of the CRADA partner's rights.

Technical Information Services

The Technical Information Services (TIS) Branch combines publication, printing and duplication, graphics, photographic, multimedia, exhibit, and video services into an integrated organization. Publication services include writing, editing, composition, publications consultation and production, and printing management. Quick turnaround digital black-and-white and color copying/printing/CD duplicating services are provided. TIS uses digital publishing technology to produce scientific and technical reports that can be used for either print or Web. Graphics support includes technical and scientific illustrations, computer graphics, design services, photographic composites, display posters, and framing. The HP large format printers offer exceptional color print quality up to 1200 dpi and produce indoor posters and signs with 56 inches being the limitation on one side. Lamination and mounting are available.

Photographic services include digital still camera coverage for data documentation, both at NRL and in the field. Photographic images are captured with state-of-the-art digital cameras and can be output to a variety of archival media. Photofinishing services provide custom printing and quick service color prints from digital files.

Visual information specialist printing an exhibit on one of the large-format printers.

Video services include producing video reports and technical videos, and capturing presentations of scientific and technical programs. TIS digital video editing equipment allows in-studio and on-location editing. The TIS Exhibits Program works with NRL's scientists and engineers to develop exhibits that best represent a broad spectrum of NRL's technologies, and promotes these technologies to scientific and nonscientific communities at conferences throughout the United States.

Administrative Services

The Administrative Services Branch is responsible for collecting and preserving the documents that comprise NRL's corporate memory. Archival documents include personal papers and correspondence, laboratory notebooks, and work project files — documents that are appraised for their historical or informational value and considered to be permanently valuable. The

Employees of the Administrative Services Branch working in the mail room.

Branch provides records management services, training, and support for the maintenance of active records, including electronic records, as an important information resource. The Branch is responsible for processing NRL's incoming and outgoing correspondence and provides training and support on correct correspondence formats and practices. The Branch is responsible for NRL's Forms and Reports Management Programs (including designing electronic forms and maintaining a Web site for Lab-wide use of electronic forms), compiles and publishes the NRL Code Directory and Organizational Index, and is responsible for providing NRL postal mail services for first class and accountable mail and for mail pickup and delivery throughout NRL. The Branch also provides NRL Locator Service.

Ruth H. Hooker Research Library

NRL's Ruth H. Hooker Research Library continues to support NRL and ONR scientists in conducting their research by making a comprehensive collection of the most relevant scholarly information available and useable; by providing direct reference and research support; by capturing and organizing the NRL research portfolio; and by creating, customizing, and deploying a state-of-the-art digital library.

Traditional library resources include extensive technical report, book, and journal collections dating back to the 1800s housed within a centrally located research facility that is staffed by subject special-

ists and information professionals. The collections include 44,000 books; 80,000 bound historical journal volumes; more than 3,500 current journal subscriptions; and approximately 2 million technical reports in paper, microfiche, or digital format (classified and unclassified). Research Library staff members provide advanced information consulting; literature searches against all major online databases including classified databases; circulation of materials from the collection including classified literature up to the SECRET level; and retrieval of articles, reports, proceedings, or documents from almost any source around the world. Staff members provide scheduled and on-demand training to help researchers improve productivity through effective use of the library's resources and services.

The Research Library staff has developed and is continuing to expand the NRL Digital Library. The Digital Library currently provides desktop access to thousands of journals, books, and reference sources to NRL-DC; NRL-Stennis; NRL-Monterey; and the Office of Naval Research.

Library systems provide immediate access to scholarly information, including current issues of journals and conference proceedings that are fully searchable at the researcher's desktop (more than 4,000 titles). Extensive journal archives from all the major scientific publishers and scholarly societies are now available online. The breadth and depth of content available

Librarians working in the Ruth H. Hooker Research Library.

through TORPEDO, NRL's locally loaded digital repository, continues to grow and provides a single point of access to scholarly information by providing full text search against journals, books, conference proceedings, and technical reports from 19 publishers (12.7 million items by June 17, 2011). The NRL Online Bibliography, a Web-based publications information system, is ensuring that the entire research portfolio of written knowledge from all NRL scientists and engineers since the 1920s will be captured, retained, measured, and shared with current and future generations.

OTHER RESEARCH SITES

NRL has acquired or made arrangements over the years to use a number of major sites and facilities outside of Washington, D.C., for research. The largest facility is located at the Stennis Space Center (NRL-SSC) in Bay St. Louis, Mississippi. Others include a facility near the Naval Postgraduate School in Monterey, California (NRL-MRY), and the Chesapeake Bay Detachment (CBD) and Scientific Development Squadron One (VXS-1) in Maryland. Additional sites are located in Virginia, Alabama, and Florida.

Stennis Space Center (NRL-SSC)

The NRL Detachment at Stennis Space Center, Mississippi (NRL-SSC), consists of NRL's Oceanography Division and portions of the Acoustics and Marine Geosciences Divisions. NRL-SSC, a tenant activity at NASA's John C. Stennis Space Center (SSC), is located in the southwest corner of Mississippi, about 50 miles northeast of New Orleans, Louisiana, and 20 miles from the Mississippi Gulf Coast. Other Navy tenants at SSC include the Naval Meteorology and Oceanography Command, the Naval Oceanographic Office, the Navy Small Craft Instruction and Training Center, the Special Boat Team-Twenty-two, and the Human Resources Service Center Southeast. Other Federal and State agencies at SSC involved in marine-related science and technology are the National Coastal Data Development Center, the National Data Buoy Center, the U.S. Geological Survey, the Environmental Protection Agency's Gulf of Mexico Program and Environmental Chemistry Laboratory, the Center of Higher Learning, University of Southern Mississippi, and Mississippi State University.

Slocum gliders, autonomous underwater vehicles, are equipped with temperature/salinity/pressure sensors and with real-time satellite connection to the Iridium network.

The Naval Meteorology and Oceanography Command and the Naval Oceanographic Office are major operational users of the oceanographic, acoustic, and geosciences technology developed by NRL researchers. The Naval Oceanographic Office operates the Navy DoD Supercomputing Resource Center, one of the nation's High Performance Computing Centers, which provides operational support to the warfighter and access to NRL for ocean and atmospheric science and technology.

The Acoustics, Marine Geosciences, and Oceanography Divisions occupy more than 175,000 ft^2 of research, computation, laboratory, administrative, and warehouse space. Facilities include the sediment core laboratory, transmission electron microscope,

The JEOL JEM-3010 transmission electron microscope.

moving-map composer facility, underwater navigation control laboratory, computed tomography scanning laboratory, real-time ocean observations and forecast facility, ocean color data receipt and processing facility, environmental microscopy facility, maintenance and calibration systems, Ocean Dynamics & Prediction Computational Network Facility, and numerous laboratories for acoustic, geosciences, and oceanographic computation, instrumentation, analysis, and testing. Special areas are available for constructing, staging, refurbishing, and storing seagoing equipment.

Monterey (NRL-MRY)

NRL's Marine Meteorology Division (NRL-MRY) is located in Monterey, California, on a 5-acre Navy Annex about one mile from the Naval Postgraduate School (NPS) campus. This group has occupied this site since the early 1970s, when the U.S. Navy collocated the

Artist's rendering of the entrance to NRL Monterey's new 15,000 ft^2 Marine Meteorology Center. Now under construction through the MILCON program, Project P-174 is scheduled for completion and occupancy in Summer 2012.

meteorological research facility with the operational center, now known as Fleet Numerical Meteorology and Oceanography Center (FNMOC). FNMOC was stood up in Monterey around 1960 to be able to share resources and expertise with NPS. This collocation of

research, education, and operations continues to be a winning formula, as FNMOC remains the primary customer for the numerical weather prediction and satellite product systems developed by NRL-MRY. NRL scientists have direct access to FNMOC's large classified supercomputers, allowing advanced development to take place using the real-time, on-site, global atmospheric and oceanographic databases, set in the same computational environment as operations. Such access offers unique advantages for successfully implementing new systems and system upgrades, and allows for rapid integration of new research results into the operational systems. Proximity to NPS also offers unique opportunities for collaborative research, as well as educational and teaching/mentoring opportunities for NRL staff.

The Monterey Navy Annex is now comprised of four primary buildings — one dedicated to FNMOC supercomputer operations (B-700); two large shared buildings dedicated to NRL-MRY and FNMOC office spaces (B-702 and 704), computer laboratories, and conference facilities; and a fourth building (B-712) now occupied by NOAA's local National Weather Service Forecast Office, which offers additional opportunities for interagency collaboration and data sharing. NRL-MRY also occupies two modular office buildings and a warehouse. Altogether, NRL-MRY occupies approximately 1500 ft^2 of storage space and 26,500 ft^2 of office/laboratory/conference space, which includes a research library, a computer center that supports the Atmospheric Prediction System Development Laboratory, the Atmospheric Composition Monitoring Station, and a small classified data processing facility.

The NRL/FNMOC compound is currently in transition. A $10.2M MILCON project for NRL-MRY was begun in Spring 2011 will give the Division a new, state-of-the-art, "green" LEED Silver building that will include an atmospheric aerosol laboratory, classified computing facilities, and a Division Front Office Suite. Upon completion in Spring FY12, NRL-MRY and FNMOC plan a building reorganization with NRL-MRY vacating B-702 and the two modular trailers, and relocating into B-704 and the as yet un-numbered new 15,000 ft^2 building.

Chesapeake Bay Detachment (CBD)

NRL's Chesapeake Bay Detachment (CBD) occupies a 168-acre site near Chesapeake Beach, Maryland, and provides facilities and support services for research in radar, electronic warfare, optical devices, materials, communications, and fire research.

Because of its location high above the western shore of the Chesapeake Bay, unique experiments can be performed in conjunction with the Tilghman Island site, 16 km across the bay from CBD. Some of these experiments include low-clutter and generally low-background radar measurements. Using CBD's support vessels, experiments are performed that involve dispensing chaff over water and characterizing aircraft and ship radar targets. Basic research is also conducted in radar antenna properties, testing of radar remote sensing concepts, use of radar to sense ocean waves, and laser propagation. A ship-motion simulator (SMS) that can handle up to 12,000 lb of electronic systems is used to test and evaluate radar, satellite communications, and line-of-sight RF communications

Aerial view of the Chesapeake Bay Detachment at Randle Cliff (Chesapeake Beach), Maryland.

systems under dynamic conditions (various sea states). CBD also hosts facilities of the Navy Technology Center for Safety and Survivability, which conducts fire research on simulated carrier, surface, and submarine platforms.

The Radar Range facility at CBD, together with the Maritime Navigation Radar (MNR) Test Range at Tilghman Island, provide the emitters and analysis tools for developing comprehensive Maritime Domain Awareness capabilities. The MNR consists of dozens of radars that represent a precise cross-section of today's actual MNR environment. An

CBD's LCM-8 providing test support for electronic warfare research.

integrated suite of advanced sensors has been developed for data collection and processing to identify and classify vessels. A suite of similar sensors and processors has been integrated into a transportable shelter, the Modular Sensor System (MSS), that can be rapidly deployed to ports or other sites for enhanced maritime awareness reporting.

Scientific Development Squadron One (VXS-1)

Scientific Development Squadron ONE (VXS-1) located at Naval Air Station Patuxent River, Maryland, is manned by approximately 13 officers, 52 enlisted and 8 civilians. VXS-1 is currently responsible for three

uniquely configured NP-3D Orion aircraft, two RC-12 Beech King Air research aircraft, four Scan Eagle Unmanned Aerial Systems (UAS), and one MZ-3A Airship. The squadron conducts numerous worldwide detachments in support of a wide range of scientific research projects. In FY09/10, VXS-1 provided flight support for several diverse research programs: Operation Rampant Lion V utilized new technology Multi-Band Synthetic Aperture Radar (SAR) and Commercial

Project Perseus, Iraq, July–October 2010.

Off The Shelf (COTS) optics to conduct ongoing research in Counter-IED technologies and Concepts of Operations (CONOPS) in US Central Command Area of Responsibility (AOR); Persistent Autonomous Surveillance System (PASS) was a multiple VXS-1 aircraft endeavor which supported systems integration, technology risk mitigation, and performance testing of P-8A Poseidon and BAMS UAS sensors for data fusion and exploitation programs; Communications Airborne Layer Expansion (CABLE) demonstrated

Scientific Development Squadron ONE personnel.

information exchange at the tactical edge by using a backbone network for IP-based, high capacity data transfer, secure gateways to interconnect data links, voice systems, and net-centric IP-based networks that bridged air, ground, and space networks carried on manned and unmanned aircraft; Tactical Electronic Warfare (TEW) testing included Surface Electronic Warfare Improvement Program (SEWIP) Block II Electronic Support Systems (ESM) and Anti-Surface Cruise Missile (ASCM) Early Warning performance evalu-

ations; Missile Defense Agency (MDA) testing and experimentation vital to the success of global defense efforts included multinational land- and surface-based missile tracking and interceptor tests. In July 2010 while operating over the Gulf of Mexico, the MZ-3A Airship provided support to US Coast Guard responders during a 30-day Proof of Concept Operations conducting Incident Awareness and Assessments (IAA) flights which detected recoverable oil and directed surface assets performing skimming operations in response to Deep Water Horizon. VXS-1 surpassed 48 years and 70,000 hours of Class "A" mishap-free operations in FY10.

Midway Research Center

The Midway Research Center (MRC) is a worldwide test range that provides accurate, known signals as standards for performance verification, validation, calibration, and anomaly resolution. In this role, the MRC ensures the availability of responsive and coordinated scheduling, transmission, measurement, and reporting of accurate and repeatable signals. The MRC, under the auspices

Midway Research Center satellite calibration facility in Stafford, Virginia.

of NRL's Naval Center for Space Technology, provides NRL with state-of-the-art facilities dedicated to Naval communications, navigation, and basic research. The headquarters and primary site is located on 162 acres in Stafford County, Virginia. The main site consists of three 18.2-m, radome-enclosed precision tracking antennas and a variety of smaller antennas. The MRC has the capability to transmit precision test signals with multiple modulation types. Its normal configuration is transmit but can be configured to receive as required. The MRC also provides cross-mission and cross-platform services from worldwide locations using a combination of fixed and transportable resources and a quick-reaction, unique signals capability. Assets include Pulstar Systems (several worldwide locations), a 45-m tracking antenna in Palo Alto, California, and a 25-m tracking antenna system on Guam. The MRC instrumentation suite includes nanosecond-level time reference to the U.S. Naval Observatory, precision frequency standards, accurate RF and microwave power measurement instrumentation, and precision tracking methodologies. The MRC also contains an Optical

Test Facility with two specialized suites of equipment: a multipurpose Transportable Research Telescope (TRTEL) used for air-to-ground optical communications and for passive satellite tracking operations, and a Satellite Laser Ranging (SLR) system built around a 1-meter telescope as a tool for improving customer ephemeris validation processes.

Pomonkey Facility

The Naval Research Laboratory's Pomonkey Facility is a field laboratory with a variety of ground-based antenna systems designed to support research and development of space-based platforms. Located 25 miles south of Washington, D.C., the facility sits on approximately 140 acres of NRL-owned land, which protect its systems from encroaching ground-based interferers. Among its various precision tracking antennae, the facility hosts the largest high-speed tracking antenna in the United States. Boasting a diameter of 30 meters, its range of trackable platforms includes those in low Earth orbit through those designed for deep space missions. The facility's antenna systems are capable of supporting missions at radio frequencies from 50 MHz through 20 GHz and can be easily configured to meet a variety of mission requirements. The ease of system configuration is due to the

The NRL Pomonkey Facility.

facility's stock of multiple antenna feeds, amplifiers, and downconverters. Other facility assets include an in-house ability to design, fabricate, test, and implement a variety of radio frequency components and systems. The facility also hosts a suite of spectrum analysis instrumentation that when coupled to its antenna systems, provides a unique platform for a variety of research and development missions.

Blossom Point Satellite Tracking and Command Facility

The Blossom Point Satellite Tracking and Command Facility (BP) provides engineering and operational support to several complex space systems for the Navy and other sponsors. BP provides direct

line-of-sight, two-way communications services with spacecraft in multiple bands and multiple orbits including LEO, HEO, GEO, and Lunar. Additionally, with BP as a node on the Air Force Satellite Control Network (AFSCN), it has the capability to provide coverage worldwide. BP consists of a satellite mission operations center, multiple antennas, and an infrastructure capable of providing space system command, control, and management. Specific BP resources include the following:

Common Ground Architecture (CGA): CGA is government-owned software that provides infrastructure and reusable components facilitating construction of command, control, and monitoring systems for space vehicle development, integration, test, and operations. CGA with Auto-

Blossom Point Satellite Tracking and Command Facility.

mated Ground Operations (AGO) software allows for 5×8 (lights out) operations or 24×7 operations. Current missions include 13 satellites with 186 worldwide contacts per day. The GAO-10-55 report dated October 2009, titled *Challenges in Aligning Space Systems Components*, lauds BP with CGA as one facility that can control a variety of satellites.

Hardware Architecture: Based on RF, video, and matrix switching with net-centric control and processing, virtually any hardware asset can be "switched" into a path to create the correct capability required for any mission. This architecture supports both classified and unclassified operations and missions, and internal LANs support multiple simultaneous mission operations. Salient resources include antennas; receivers; telemetry, tracking, and command (TT&C); command encoder; front-end processors; operations automatic data processing (ADP) resources; and satellite health and monitoring/engineering evaluation and maintenance (SHM/EEM).

Marine Corrosion and Marine Coatings Facilities

The Chemistry Division's Marine Corrosion and Coatings Facility located in Key West, Florida, offers a "blue" ocean environment with natural seawater characterized by historically small compositional variation and a stable biomass. This continuous source of stable, natural seawater provides a site ideally suited

for studies of marine environment effects on materials, including accelerated and long-term exposure testing and materials evaluation. The site maintains capabili-

Demonstration of the removal of non-skid coating by heat induction at NRL Key West.

ties for extensive RDT&E of marine engineering and coatings technologies and supports a wide array of Navy and industrial sponsors. Equipment is available for experiments involving accelerated corrosion and weathering, general corrosion, long-term immersion and alternate immersion, fouling, electrochemical phenomena, coatings application and characterization, cathodic protection design, ballast water treatment, marine biology, and corrosion monitoring. In 2009, the facility received a comprehensive refurbishment due to hurricane damage.

Research Platforms

Mobile research platforms contribute greatly to NRL's research. These include six P-3 Orion turbo-

Moored in Mobile Bay, Alabama, the ex–USS *Shadwell* is regularly set ablaze in a controlled environment to further the safety of operational Navy and civilian firefighting measures.

prop aircraft and one ship, the ex–USS *Shadwell* (LSD 15), berthed in Mobile Bay, Alabama. The *Shadwell* is used for research on aboard-ship fire suppression techniques.

Featured Research

AutoSurvey® (2005) — NRL-patented AutoSurvey autonomous line running software, originally developed for the ORCA unmanned vehicle, was transitioned to all NAVOCEANO TAGS 60 class survey ships. AutoSurvey provides up to 60% reduction in survey time in areas with rough terrain.

Up, up, and away…

UAV's Endurance Gets a Lift by Latching onto Thermals

By using the naturally occurring air currents known as thermals, unmanned aerial vehicles (UAVs) can dramatically extend their operational endurance. NRL researchers demonstrated autonomous soaring using an unpowered, winch-launched unmanned sailplane, which soared within thermals to fly a notional road-monitoring mission for 5.3 hours beyond its nominal 3-minute capability. Since the autonomous soaring technology can be implemented as a software upgrade to existing UAV autopilots, NRL's Tactical Electronic Warfare Division expects that other UAVs such as the hydrogen-powered Ion Tiger will soar to new heights and longer flight times.

Caption: Using autonomous soaring algorithms, an unpowered sailplane flew a 113.5 km course in 4.5 hours.

Autonomous Soaring for Unmanned Aerial Vehicles

D.J. Edwards and M. Hazard
Tactical Electronic Warfare Division

N RL researchers have developed a way to extend the endurance of unmanned aerial vehicles (UAVs) by exploiting the naturally occurring rising air currents known as thermals. Unlike a typical UAV autopilot, which naively attempts to reject these atmospheric "disturbances," the new system adapts its flight path to maximize energy extraction. The system detects the presence of rising air using onboard sensors, finds the center of the thermal, and redirects the guidance system to circle in the thermal. These algorithms were incorporated into an unmanned sailplane, a winch-launched aircraft with a nominal endurance of only 3 min. With autonomous soaring engaged, the unpowered vehicle was able to fly for more than 5.3 h. Because implementing autonomous soaring might be as simple as a software upgrade — UAVs already carry the necessary sensors for thermal detection — this enabling technology could be widely deployed at low cost. Our current research focuses on extending these benefits to powered UAVs such as the hydrogen fuel cell powered Ion Tiger. This article presents an overview of the autonomous soaring algorithms, flight test results, and potential directions for continued research.

INTRODUCTION

The increasing use of small unmanned aerial vehicles (UAVs) in military and civilian applications has been accompanied by a growing demand for improved endurance and range. These demands have been typically addressed by improvements in aerodynamic and structural efficiency, improved fuel-efficient propulsion systems, and the ongoing miniaturization of onboard computer and payload systems. Recently, more attention has been given to the extraction of energy from the atmosphere. Aircraft can make use of atmospheric updrafts, or thermals, to gain altitude without expenditure of onboard fuel stores. By intelligently tracking thermals, an unmanned aircraft can extend its range or endurance without carrying additional fuel or specialized sensors.

However, current UAV autopilots attempt to reject thermals and other atmospheric perturbations. Enabling autonomous soaring required the development of a thermal identification framework that could efficiently compare autopilot sensor data to a thermal model, allowing the autopilot to determine when it is flying in a thermal and choose the best flight path to maximize energy extraction. This basic soaring functionality was wrapped with a mission management algorithm that maintained the balance between soaring and timely arrival at the required destination. Finally, the thermal identification and mission management algorithms were implemented on a UAV sailplane for

flight testing. This article gives an overview of thermal sensing and identification, soaring guidance, and flight testing results.

THERMAL UPDRAFTS

Thermal updrafts are naturally occurring atmospheric convection currents that are created by uneven heating of the Earth's surface. Radiant solar energy is absorbed by terrain and transferred to the air. If a parcel of air becomes warmer than its surroundings, it will rise like a bubble in a boiling pot of water, creating a thermal. Each parcel of warm air in the thermal continues ascending (and expanding) until it cools to the temperature of the surrounding air and is no longer buoyant. Depending on atmospheric conditions, the top of the thermal may be hundreds or thousands of meters above the surface. Thermal formation and evolution are influenced by terrain texture and albedo, time of day, and ambient meteorological conditions. These factors make accurately modeling thermal activity a difficult task. Computational fluid dynamics (CFD) tools such as large-eddy simulation could be used to model thermals with high fidelity, but their computational cost makes them ill-suited for real-time simulation or control.

Instead, a simpler model that approximates the vertical wind profile of a single thermal is used. To reduce the complexity of the model, several assumptions are made: a thermal is radially symmetric about

a center point, does not create horizontal winds, drifts with the ambient wind velocity, and is invariant with altitude and time. Figure 1 shows the modified three-dimensional Gaussian distribution chosen to represent vertical wind speeds in a thermal. Its main features are the characteristic "core" region of rising air and a ring of sinking air around the core. This reduced-order model is based on four parameters: the two-dimensional center location, peak updraft strength, and characteristic radius.

The simplified model is one component of the autonomous soaring framework. We also need some way to measure the instantaneous vertical wind speed, and a systematic way to update the estimated thermal location based on vertical wind speed measurements.
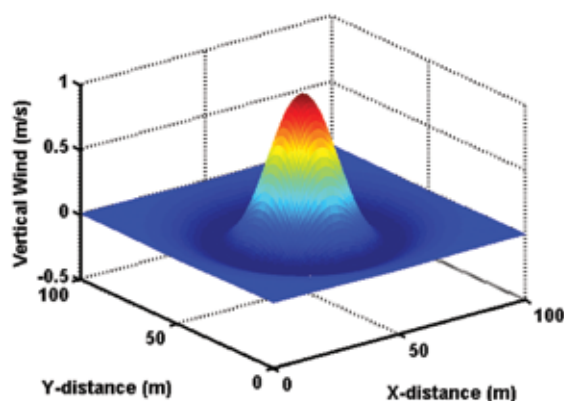
FIGURE 1
Modified Gaussian distribution updraft cross-section.

SENSING THERMALS

The updraft model represents a distribution of vertical wind motion, which is not easy to measure directly from a moving aircraft. Instead, we examined the problem from an energy/power perspective. In general, the total energy of the aircraft system is conserved aside from work done on the aircraft by external forces: thrust, drag, and any atmospheric contributions. Known contributors such as thrust and drag can be directly compensated based on wind tunnel and flight test data, leaving an "atmospheric power" signal. If thermals are the only atmospheric contribution, this power measurement is equivalent to vertical wind speed measurement and is compatible with our low-order model.

Accurate measurement of the aircraft's specific power state can be achieved using the same suite of sensors carried in a typical autopilot. Initial investigations computed total energy based on altitude and airspeed measurements, and then numerically differentiated this signal to estimate the instantaneous power. The differentiation step reduced the quality of the data, especially with the low-resolution sensors typical of

small UAVs. In our improved system, the power state is computed directly using the onboard three-axis accelerometer, GPS velocity, and GPS position measurements. This alleviates the need to differentiate and significantly improves the data quality. The power signal is then compensated for drag effects using experimental sink polar data and for thrust effects using wind tunnel propeller efficiency data. Any remaining power contribution, whether positive or negative, is assumed to come from the atmosphere. Figure 2 shows the compensated specific power signal for a representative flight path that intersects a thermal.

In Fig. 2, warmer colors show faster vertical air motion and cooler colors show little or no vertical air motion. Qualitatively, we can see a specific power distribution that matches key components of the updraft model, including a circular shape around a local peak. These measurements can be correlated with the low-order updraft model to estimate the thermal parameters that best fit the flight data.
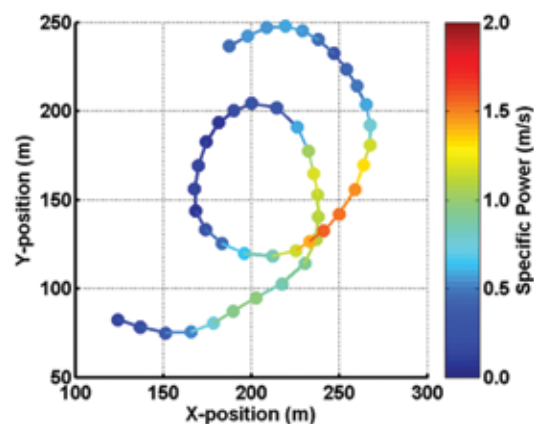
FIGURE 2
Measurement of specific power distribution of a thermal.

THERMAL PARAMETER IDENTIFICATION

Given vertical wind speed measurements, the next component is an algorithm to reduce the flight data into parameters that can be used to guide the aircraft. Our research investigated two options: batch methods, which accumulate sensor time history and iteratively solve for the model parameters; and recursive methods, which only use the most recent data to quickly update a previous parameter estimate. In general, recursive methods trade absolute accuracy for lower computational burden. Reducing computational burden is important to stay within the weight and power requirements of a small UAV.

The batch method is based on a similar approach developed by John Wharington that used an adaptive neural network.[1] To reduce computational workload

for real-time use, the full method was reduced to an iterative nonlinear regression. In short, the method begins with a candidate center location node and computes the residual error associated with a two-dimensional fit in the remaining parameters (strength and radius) at that location. The residual is similarly evaluated at nearby locations and the candidate location with the smallest error is chosen as the winner. A new set of candidate locations is drawn in a smaller ring around the winner, and the process repeats until the algorithm converges on a location with stronger correlation to the model. While relatively computationally time consuming, this method of searching provides a robust means of multiparameter nonlinear curve fitting. In Fig. 3, several steps of the process are shown, starting from an initial location within the flight path and moving down the error surface toward the global minimum where the model best fits the measured data. The step sizes were purposely limited to serve as a low-pass filter on the center estimation.
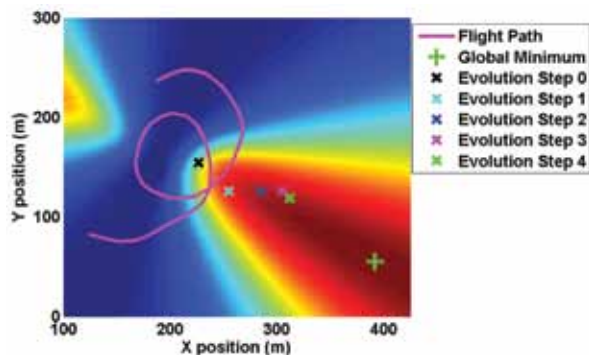
FIGURE 3
Evolutionary search method moving toward the global minimum.

A recursive unscented Kalman filter (UKF) method was also investigated to reduce the computational burden of the batch method. Kalman filters are a class of algorithms that track a set of parameters along with a covariance matrix that describes the filter's confidence in its parameter estimate. As each new measurement is received, the accuracy of the new measurement is weighed against the covariance matrix to compute the optimal balance between old data already fused into the parameter estimate and new measurements. In this work, we used the UKF, an extension of the classic linear Kalman filter, to allow using a fully nonlinear measurement model. The UKF takes a fixed time to complete at each time step, while the execution time of the batch method varies on the conditioning of the data set. The estimation accuracy of each algorithm is compared in Fig. 4, using the mean squared error in all four thermal model parameters as the metric. The batch method generally showed slightly lower error than the

UKF, but both provide sufficient accuracy for autonomous soaring.[2] Simulations comparing the batch and recursive thermal identification algorithms showed the recursive method was between one and two orders of magnitude faster than the batch method.
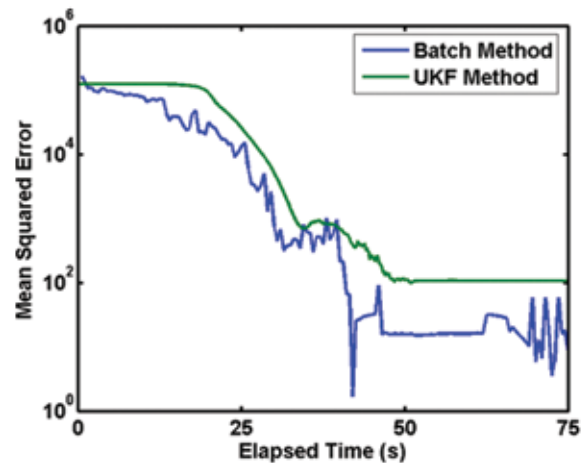
FIGURE 4
Comparison of mean squared error for batch and recursive methods.

SOARING GUIDANCE

Once a thermal is detected and located, the aircraft needs to be steered to fly inside the updraft core. Fortunately, many commercial autopilots include the ability to "orbit" around a GPS waypoint. The autonomous soaring algorithm uses this existing controller instead of interacting with the sensors and control surfaces directly. In other words, the autopilot (inner feedback loop) is nested inside the soaring controller (outer feedback loop), as shown in Fig. 5. This form of decoupled control is common to many aircraft control systems. Chief among the advantages of this architecture is the ability of the inner loop to run at high rates, typically
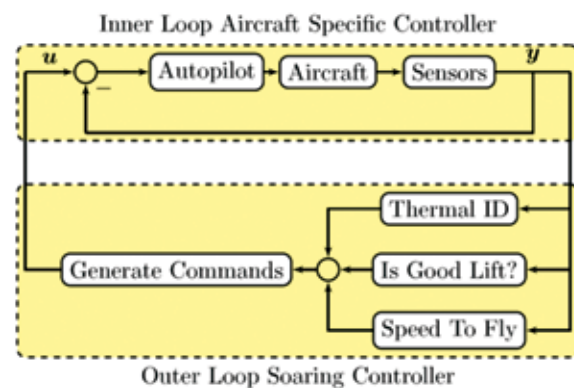
FIGURE 5
High-level autonomous soaring controller diagram.

50 Hz, while the outer loop may update more slowly — in the developed system, the orbit waypoint is updated at 2 Hz. The outer loop soaring controller also becomes autopilot and vehicle agnostic, making it easier and less expensive to adapt the soaring algorithms to a different unmanned vehicle.

MISSION MANAGEMENT

For an aircraft capable of autonomous soaring to be able to complete a useful mission, it must be able to balance progress along its commanded course with the possible endurance or range gains presented by thermals. At a very basic level, this requires flying efficiently along a course, stopping to investigate a thermal when it is encountered (latching), finding and soaring in the thermal, and returning to course (unlatching) if the energy gains are no longer worthwhile. An example of these behaviors in action is shown in Fig. 6. The system latches into soaring mode if the average vertical wind speed (thermal strength) exceeds a threshold, the thermal identification algorithm shows a good fit, and the vehicle is within mission limits and airspace boundaries. In soaring mode, the aircraft is commanded to fly an orbit around the thermal center as described in the previous section. The system unlatches if the average thermal strength drops below the threshold, with sufficient hysteresis to allow the system enough time to find and track the thermal after its initial engagement.

The thermal strength threshold for latching into soaring mode is determined by MacCready speed-ring theory. The speed ring is a manned sailplane instrument developed by the late Paul MacCready. It uses an

estimate of local average thermal strength to provide two pieces of information: the optimal cross-country speed to fly and the minimum thermal strength required to make stopping to soar worthwhile. In the test system, the speed ring setting is coupled with altitude. This ensures the aircraft flies conservatively at low altitudes, latching onto weaker thermals when

gathering energy is crucial; as the vehicle gains altitude, thermals must get progressively stronger for latching to occur. Similarly, the aircraft flies faster at high altitudes to maximize its cross-country speed; the vehicle has sufficient altitude reserves, and the chance of intercepting a strong thermal improves with the distance traveled. At lower altitudes, the vehicle is commanded to fly slowly to conserve energy reserves (altitude) and maximize flight time to give a chance of finding even a weak thermal. Recently, this behavior has compared favorably with that of birds.[3]

IMPLEMENTATION

An off-the-shelf fiberglass composite sailplane served as a host vehicle for testing the soaring algorithms (Fig. 7). The Autonomous Locator of Updrafts (ALOFT) has a 4.2 m wingspan, a 5 kg takeoff weight, and a best glide slope of about about 24 m forward for every 1 m of descent. The aircraft is launched using a winch that hoists the vehicle like a kite to approximately 200 m altitude, giving a 3 min gliding descent when no thermals can be found.

In addition to the airframe and six electric control surface actuators, a few other items are needed to facilitate autonomous soaring. An off-the-shelf Piccolo II miniature autopilot from Cloud Cap Technologies provides the primary navigation solution and vehicle guidance. The autopilot communicates with a remote ground station via a 900 MHz spread-spectrum modem, giving operators the ability to monitor and retask the vehicle as necessary. A separate manual override circuit allows a safety pilot to completely circumvent the autopilot and fly the aircraft in remote control mode, providing a measure of redundancy in case of autopilot failure. An 87 Wh lithium-ion battery located in the aircraft nose provides power to the avionics and actuators for 8 h of continuous operation. ALOFT has no motor; therefore, any endurance beyond the nominal 3 min of flight time comes from the atmosphere.

FLIGHT TESTING

With the autonomous soaring algorithms installed on a UAV, the soaring algorithms were tested in a cross-country (XC) soaring scenario.[4] Cross-country soaring typically involves a "distance task" where the goal is to travel as far as possible on a single launch, or a "speed task" where the goal is to complete a predetermined course with the highest average speed. Satisfying these soaring tasks is a challenge for unmanned systems which, unlike a human pilot, do not have a priori knowledge of local thermal hotspots. Both tasks are similar to road-monitoring or communications relay missions.

FIGURE 7
ALOFT vehicle and internal hardware.

After completing a short in-air controls check following a manual launch, the autopilot followed a preprogrammed series of waypoints with the outer loop soaring controller managing the behavior of the vehicle. ALOFT soared in nearby thermals to reach a starting altitude of approximately 500 m, and then the mission task waypoints were activated to send the vehicle traveling on course. Along the way, the mission manager balanced its desire for altitude with the mission task of distance or speed. Once the task was complete or the vehicle breached a preset lower altitude limit, manual control was activated and the vehicle was landed to complete the test.

RESULTS

Over 170 flights were performed with the ALOFT glider, accounting for more than 70 h of flight time and 20 h of time spent actively soaring. Several milestones were reached over the course of the research program:

- September 30, 2007: First demonstration of autonomous cross-country soaring.

- October 5, 2008: Unofficially beat the world record for goal-and-return cross-country soaring (5 kg class), flying 48.6 km each way.
- May 23, 2009: Longest autonomous cross-country flight to date of 113.5 km over 4.5 h, for an average cross-country speed of 25.2 km/h.
- June 12, 2009: Highest endurance cross-country flight to date of 5.3 h.

Figure 8 shows the altitude time history from a distance task flight, showing how the algorithm moves in and out of soaring mode and operates in the altitude band of 500 m to 1500 m.

FUTURE RESEARCH DIRECTIONS

The success of the autonomous soaring algorithms has opened up a number of different research avenues. An ongoing effort supported by an NRL Karle Fellowship seeks to implement soaring algorithms on other existing unmanned aircraft systems with complementary endurance technology. Ion Tiger, the NRL-devel-
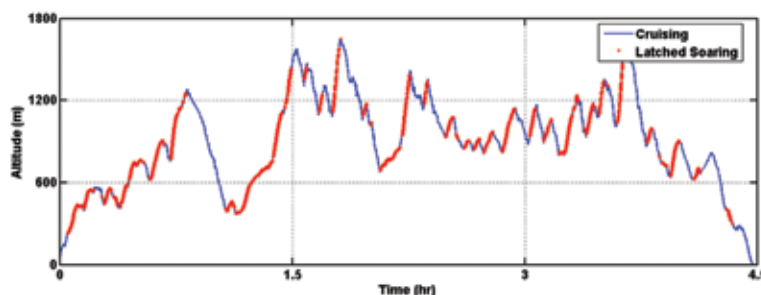
FIGURE 8
Altitude trace of a distance task flight.

oped ultralong-endurance hydrogen fuel cell powered aircraft, has demonstrated 26 h of endurance using gaseous hydrogen alone. Adding autonomous soaring capability to the system could entirely offset fuel consumption during times of convective activity, leading to further gains in endurance. Other research interests include improving the fidelity of thermal models and implementing the algorithms on micro-UAVs.

CONCLUSION

This project has culminated in the development of a system for autonomously locating and actively guiding a UAV to soar in thermals. In flight tests, an unpowered glider with a 3 min nominal endurance flew for more than 5 h in a realistic cross-country scenario, extending its flight time by autonomously extracting energy from ambient air motion. Any endurance improvement is of direct tactical benefit to many UAV missions. Because no additional hardware is required to enable autonomous soaring, the technique could be applied to many existing unmanned aircraft systems.

References
[1] J. Wharington, "Autonomous Control of Soaring Aircraft by Reinforcement Learning," Ph.D. thesis, Royal Melbourne Institute of Technology, Melbourne, Australia (1998).
[2] M. Hazard, "Unscented Kalman Filtering for Real-Time Atmospheric Thermal Tracking," M.S. thesis, Mechanical and Aerospace Engineering Dept., North Carolina State University, Raleigh, NC (2010), http://www.lib.ncsu.edu/resolver/1840.16/6353.
[3] Z. Ákos, M. Nagy, and T. Vicsek, "Thermal Soaring Flight of Birds and Unmanned Aerial Vehicles," *IOP Journal of Bioinspiration and Biomimetics* **5**(4), 045003 (2010).
[4] D. Edwards and L. Silverberg, "Autonomous Soaring: The Montague Cross Country Challenge," *AIAA Journal of Aircraft* **47**(5), 1763–1769 (2010).

"I need more power, Scotty"...

Might be the demand of a future Naval commander, and that is exactly what he or she will get if NRL researchers can more fully comprehend the complex physics of rotating detonation engines (RDEs), which offer exciting possibilities for improved specific fuel consumption in gas-turbine engines.

The heck with building a better mousetrap…build a better gas-turbine engine and you've really got something. Even the all-electric ships of tomorrow's Navy will use gas-turbine engines to generate electricity for both the propulsion system and critical onboard systems, so improving their specific fuel consumption is critical.

NRL has applied its experience in developing and simulating pulse detonation engines (PDEs), which use the detonation cycle rather than the Brayton thermodynamic cycle used in previous gas-turbine engines, to the even more attractive RDEs. Use of the detonation cycle eliminates the need for compressors to generate the high pressures required by the engines. Controlling detonations, however, is the key to maximizing efficiency. RDEs will do this by allowing the detonation to propagate azimuthally at phenomenal speed around the combustion chamber, thereby holding the inflow kinetic energy to a relatively low value and using most of the compression for better efficiency.

Using models to study the detonation processes and dynamics allows the researchers to understand more fully the flow field, wave structure, the basic thermodynamic cycle, and the key role that pressure change plays in engine performance. These simulations also allow researchers to study performance under a wide array of conditions and how it is affected by engine and sizing parameters.

A functioning RDE gas-turbine engine might not appear tomorrow (and it won't use dilithium crystals), but when it does emerge, we'll have NRL research to thank for the benefits it will offer.

Rotating Detonation-Wave Engines

D.A. Schwer and K. Kailasanath

Laboratory for Computational Physics and Fluid Dynamics

All Navy aircraft and missiles use gas-turbine engines for propulsion. Many ships are also dependent on gas-turbine engines to generate both propulsive power and electricity. These engines are fundamentally similar to engines used to power commercial airplanes. Future ships moving to an "all electric" paradigm for the propulsion system will still require these gas-turbine engines to generate electricity for the propulsion system and also for other critical onboard systems. Because of the amount of power required by modern warfighting ships and the prospect that this power requirement will only increase, there is a strong interest in improving the specific fuel consumption of these engines.

Gas-turbine engines are attractive because they scale nicely to large powers, are relatively small and self-contained, and are relatively easy to maintain. Current gas-turbines are based on the Brayton thermodynamic cycle, in which air is compressed and mixed with fuel, combusted at a constant pressure, and expanded to do work for either generating electricity or for propulsion. Since gas-turbines have been heavily used both for commercial flight engines, such as turbofans and turbojets, and for electrical power generation, this cycle has been highly optimized. Further improvements in increasing the efficiency of these engines will provide only a few percent increase in efficiency over current capabilities.

To make significant improvements to the performance of gas-turbine engines, we need to look at different and possibly more innovative cycles rather than the Brayton cycle. An attractive possibility is to use the detonation cycle instead of the Brayton cycle for powering a gas-turbine.[1] NRL has been on the forefront of this research for the last decade and has been a major player in the development of pulse detonation engines (PDEs). The rotating detonation engine (RDE) is a different strategy for using the detonation cycle for obtaining better fuel efficiency. Like PDEs, RDEs have the potential to be a disruptive technology that can significantly alter the fuel efficiency of ships and planes; however, there are several challenges that must be overcome before their benefits are realized. The objective of our current research is to get a better understanding of how the RDE works and the type of performance that can be expected.

WHY A DETONATION ENGINE?

Detonations have long been associated with explosions (and explosives), not with engines. There are many reasons for this; however, the most important is that detonations produce extremely high pressures, shock waves, and high velocities. Another difficulty for engine applications is repeatedly generating detonations consistently and efficiently. Research over the last several decades on materials that are able to withstand the high pressures, temperatures, and heat fluxes associated with detonations, and on initiators that are efficient, fast, and reliable, have made detonation engines a possibility.

A comparison of the basic detonation cycle with the Brayton cycle is shown in Fig. 1 on a pressure–specific volume (*P-v*) diagram. Thermodynamic cycles show how properties vary for a fluid particle as it travels through an engine, and can be used to determine the efficiency or the amount of work that can be done by the engine. There are quite a few interesting aspects to the detonation cycle that make it an attrac-
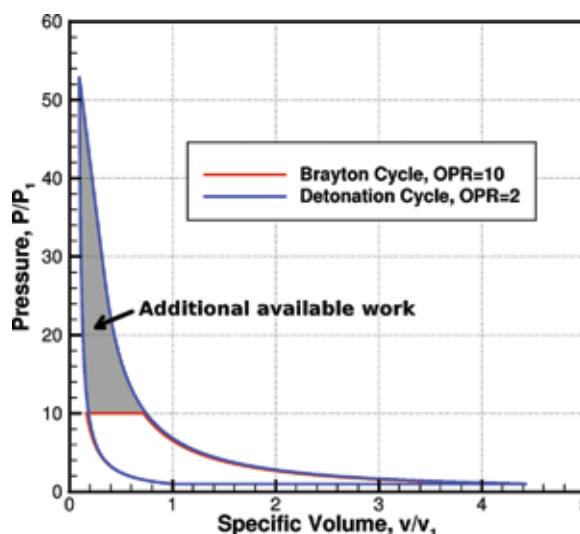
FIGURE 1
Comparison of Brayton and detonation cycles on a *P-v* diagram, with an operating pressure ratio (OPR) of 2 for the detonation cycle, and 10 for the Brayton cycle.

tive alternative to the typical Brayton cycle. A Brayton cycle relies on a multistage compressor in order to increase the pressure of the air from atmospheric to a higher pressure. Without this compression, no work can be obtained from the gas-turbine engine. Typical compressor ratios vary from 10 to 30 and are easily the most complex machinery in a gas-turbine engine. Detonations, on the other hand, are close to a constant volume reaction process, and naturally generate high pressures that can then be expanded to do work without any compressor at all. Without a compressor, an engine based on the detonation cycle provides a cycle efficiency of about 30% (compared to 0% for the Brayton cycle).[1] This means that much simpler compressors can be used to generate the equivalent efficiency. Adding a compressor to a detonation engine increases the efficiency further, and so technology developed for Brayton cycle engines can still be used for detonation engines.

The challenge with detonation engines is realizing the efficiency of the detonation cycle. Concepts such as oblique detonation-wave engines have failed to be able to recover the efficiency of this detonation cycle, because much of the energy of the inflow is bound up in kinetic energy, which does not increase the pressure and thus does not improve the efficiency. Pulse detonation engines have taken a different approach by creating an unsteady process that removes the requirement of having high velocity inflow. This creates a whole new set of issues, such as rapid initiation of detonations and the requirement of efficient detonators.

The rotating detonation engine takes a different approach toward realizing the efficiency of the detonation cycle. By allowing the detonation to propagate azimuthally around an annular combustion chamber, the kinetic energy of the inflow can be held to a relatively low value, and thus the RDE can use most of the compression for gains in efficiency, while the flow field matches the steady detonation cycle closely.

ROTATING DETONATION ENGINES

A schematic of a rotating detonation engine[2] is given in Fig. 2. Current basic studies done at the Naval Research Laboratory are focused on a much simpler annular combustion chamber, also shown in Fig. 2. The combustion chamber is an annular ring, in which the mean direction of flow is from the injection end (bottom in figure) to the exit plane (top). A series of micro-nozzle injectors flow in a premixture of fuel and air or oxygen axially from a high pressure plenum, and a detonation propagates circumferentially around the combustion chamber, consuming the freshly injected mixture. The gas then expands azimuthally and axially, and can be either subsonic or supersonic (or both),

depending on the back pressure at the outlet plane. The flow has a very strong circumferential aspect due to the detonation wave propagation. Because the radial dimension is typically small compared to the azimuthal and axial dimensions, there is generally little variation radially within the flow. Because of this, the RDE is usually "unrolled" into two dimensions, and we do this for many of our simulations with small thickness-to-diameter ratios.

At the Naval Research Laboratory, we have constructed a model for simulating RDEs based on our previous work done on general detonations, and in particular on pulse detonation engines.[3] RDEs present a challenge to model because they are strongly multidimensional and have both strong axial and circumferential components. As mentioned, the detonation wave itself propagates azimuthally around the combustion chamber, while the exhaust and injection systems both operate axially. A large part of the early work was to show how the strong azimuthal flow is transferred to axial flow that will produce thrust, and to account for any excess swirl that may remain within the combustion chamber. Once the basic flow field and performance were demonstrated, we conducted a number of studies to show how the performance varies as different parameters are varied.

FLOW FIELD AND PERFORMANCE OF RDEs

Our first set of simulations examines a baseline RDE. This RDE corresponds with experimental work done outside of NRL. The diameter of the annular combustion chamber is 140 mm (inner) and 160 mm (outer) (giving a 10 mm thickness), the axial length of the chamber is 177 mm, and stoichiometric hydrogen-air is injected from a plenum at a stagnation pressure and temperature of 10 atm and 300 K.

Basic Flow-Field and Wave Structure

We have found that by examining the gradient magnitude of temperature and pressure for an example RDE, finer details of the flow field can be easily seen. This is shown for one of our baseline RDE calculations in Fig. 3, with many of the relevant flow features labeled in the figure. Micro-nozzles inject the fuel-air premixture from a high pressure plenum chamber below the RDE. Although the detonation wave in an RDE is considered a continuous detonation wave, it is not stationary as in some continuous detonation-wave engine concepts, and propagates in the azimuthal direction from left to right through the chamber near the injection wall, and the detonated products expand azimuthally and axially to the exit plane at the top of the domain. Weak secondary shock waves form in the combustion
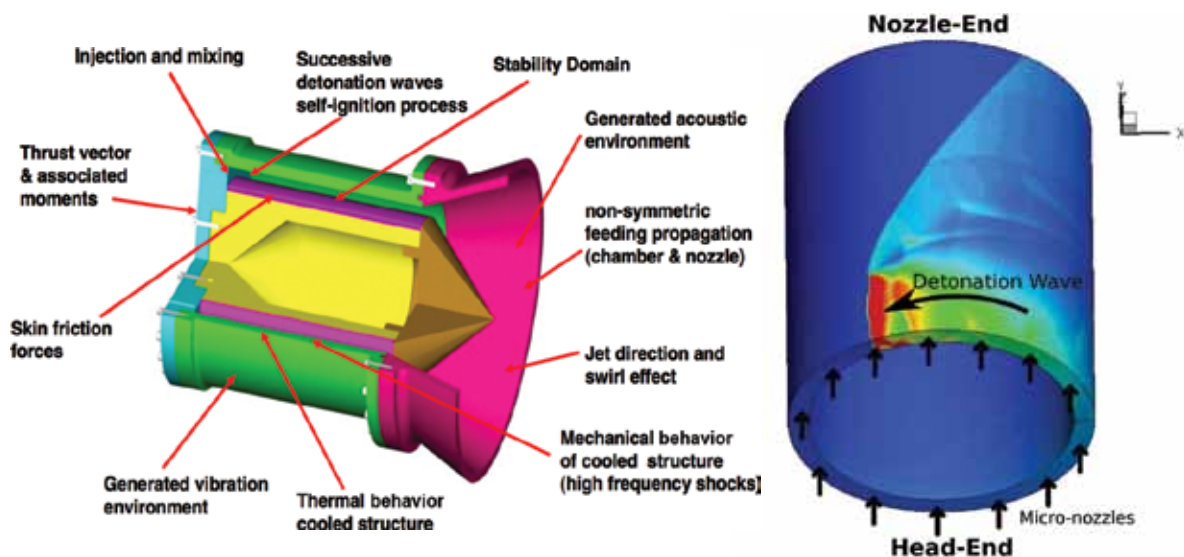
FIGURE 2
Example of an RDE (left) from Ref. 2 and simulation of the combustion chamber (right) for an RDE.
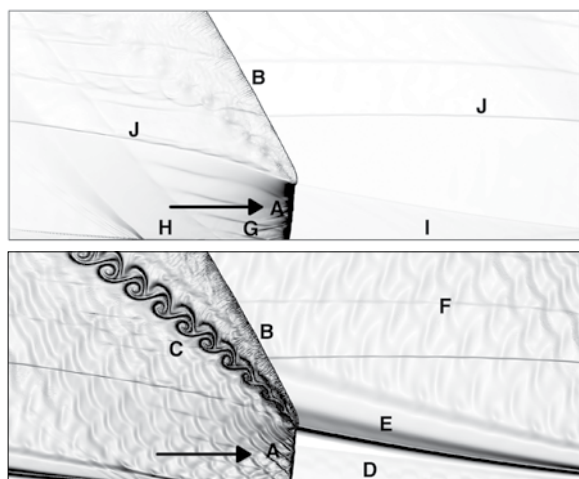
FIGURE 3
Temperature (top) and pressure (bottom) gradient solution of an "unrolled" hydrogen-air RDE solution, showing different relevant features of the flow. A) detonation wave, B) trailing edge shock wave, C) slip line between freshly detonated products and older products, D) fill region, E) nondetonated burned gas region, F) expansion region with detonated products, G) inlet region with blocked injector micro-nozzles, H) inlet region with partial filling micro-nozzles, I) inlet region with choked micro-nozzles, and J) secondary shock wave. Detonation wave moves azimuthally from left to right.

chamber (J) and can become quite strong depending on the plenum pressure and the back pressure at the exit plane. Directly behind the detonation wave, the pressure is high enough that the injection micro-nozzles are blocked (G). Experimentally, this can potentially lead to backflow into the premixture plenum, which can be problematic. Further behind the detonation front, the fuel-air mixture begins to penetrate into the chamber

(H), and for most of the region, the micro-nozzles are choked (I), which is why the premixture region expands almost linearly. Also of interest is the region where the premixture and reacted gases meet (E). Here the RDE experiences nondetonative burning, which results in a loss in performance. In this computation, about 14% of the premixture undergoes nondetonative burning, which is similar to experimental findings.

Basic Thermodynamic Cycle

Our approach to obtaining information on the effective thermodynamic cycle is to take streamline information from an average of the detailed simulation of the flow field and plot the results on conventional *P-v* or enthalpy–entropy (*h-s*) diagrams and compare this directly with the detonation cycle. To do this, we fix the detonation wave location at the center of the domain and average the solution over 100 RDE cycles, one cycle being the time it takes the detonation wave to do a complete revolution around the combustion chamber. We can then take this average solution in the reference frame of the detonation wave, and follow streamlines from near the inlet plane through the engine to the exit plane. Figure 4 shows the enthalpy and entropy along several streamlines through the entire engine. Thermodynamically, we see a close correlation between the ideal detonation cycle and the RDE cycle. The largest difference between the two results is seen near the so-called von Neumann point, which is an ideal representation of a detonation wave and does not correspond to real detonation waves, and does not have an effect on the overall performance of the detonation cycle. There is a small amount of variability in the simulation

results, which is due to some variation in the pressure ahead of the detonation wave, which is not present in the simple detonation cycle analysis. Nevertheless, because of the close correlation between the RDE and ideal thermodynamic cycle results, we expect better performance than a PDE or "intermittent" detonation engine, where all fluid elements do not lie on the detonation cycle in a *P-v* diagram framework.
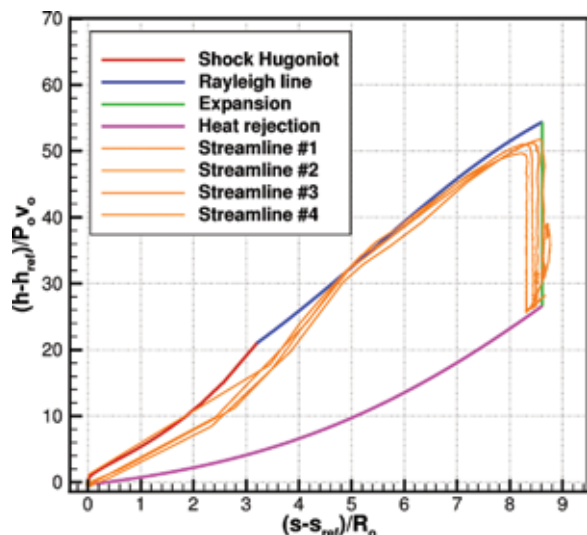
FIGURE 4
Thermodynamic cycle of the RDE simulation compared with an ideal detonation cycle on an *h-s* diagram.

A Key Parameter

At the Naval Research Laboratory, several two- and three-dimensional simulations of RDE combustion chambers have been conducted to understand the effect of different relevant parameters on the performance and flow field of RDEs. Pressure change is one of the important factors for determining the performance of detonation-based engines since these are examples of "pressure-gain" combustion systems. There are two key pressures to be considered in the generic RDE discussed above. The first key pressure is the plenum pressure for the injector micro-nozzles, P_o, and the second is the back pressure at the exit of the combustion chamber, P_b. To highlight the impact of these pressures, the pressure ratio, P_o/P_b, was varied in two ways. First, the plenum pressure was set to 10 atm, and the back pressure was varied from 0.5 to 4 atm. Second, the back pressure was held constant at 1 atm, and the plenum pressure was varied from 2.5 atm to 20 atm. In both cases, the pressure ratio varied from 2.5 to 20. As shown in Figs. 5 and 6, although the mass flow rate and thrust force varied considerably between all cases, the specific impulse (the basic measure of performance of a propulsion device) was only dependent on the pressure

ratio, P_o/P_b. Further parametric studies done at NRL have also helped to better understand engine sizing parameters on performance and the flow field of RDEs.
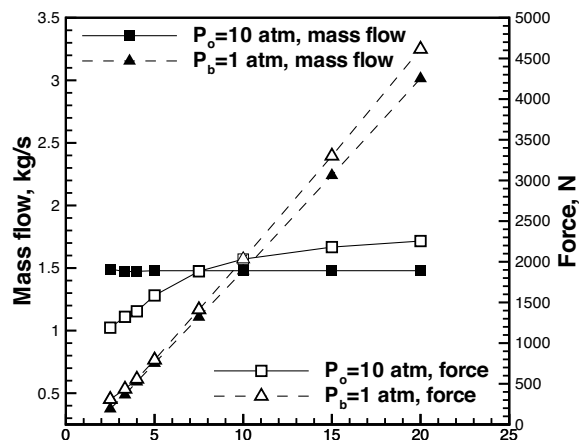
FIGURE 5
Impact of stagnation pressure and back pressure on the mass flow rate and computed thrust for an RDE.
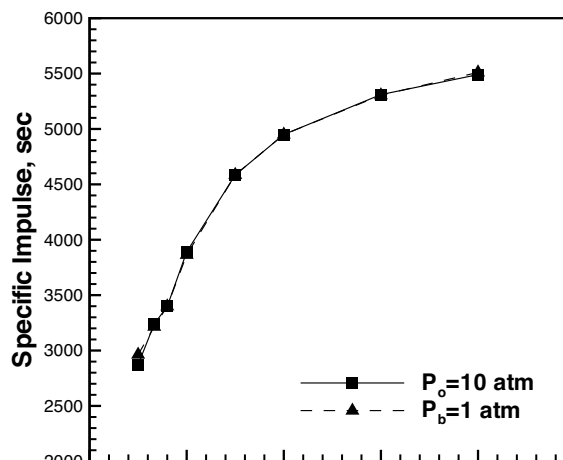
FIGURE 6
Dependence of the specific impulse on the stagnation and back pressures.

Overall Performance

Specific impulse is the ratio of thrust or output force to fuel mass flow rate, and provides a good indication of the efficiency of an engine. It is useful to put the computed overall specific impulse of an RDE in the context of other high-speed and advanced engine concepts. The comparable specific impulse for a multi-tube PDE operating on a stoichiometric hydrogen-air mixture is around 4100 s. For the RDE, under the same conditions, we compute a specific impulse from

the baseline case of around 4950 s, which represents an increase in performance for the RDE over the PDE of about 33%. The ideal detonation cycle performance estimate under the same conditions is around 5500 s. For a ramjet, the specific impulse is zero at sea-level static conditions but increases to about 4400 s at Mach 2.1. Losses for the RDE include swirl losses (due to the flow being partially azimuthal at the exit plane), in addition to the nondetonation losses mentioned above. Through simulations being conducted at the Naval Research Laboratory, and through collaborations at the Air Force Research Laboratory at Wright-Patterson Air Force Base and at the University of Connecticut, we are exploring more completely where these losses occur and how performance can be improved even further.

CONCLUSION

Rotating detonation engines, a form of continuous detonation-wave engine, are shown to have the potential to further increase the performance of air-breathing propulsion devices above pulsed or intermittent detonation-wave engines. At the Naval Research Laboratory, we have been able to extend our leadership in simulation of pulse detonation engines to show many of the significant flow-field features of RDEs and to explain how the performance of these engines relates to the ideal thermodynamic detonation cycle. In addition, through extensive simulations over a wide range of conditions, we have been able to form a picture of how performance is affected by different common engine parameters and sizing parameters. Continued work in this area will help to further understand the performance envelope of these engines and to develop experimental rigs and eventually functioning engines.

[Sponsored by NRL]

References
[1] W.H. Heiser and D.T. Pratt, "Thermodynamic Cycle Analysis of Pulse Detonation Engines," *J. Propulsion and Power* **18**(1), 68–76 (2002).
[2] F. Falempin, "Continuous Detonation Wave Engine," in *Advances on Propulsion Technology for High-Speed Aircraft*, RTO-EN-AVT-150, Paper 8, NATO (2008).
[3] D.A. Schwer and K. Kailasanath, "Numerical Investigation of the Physics of Rotating Detonation Engines," *Proceedings of the Combustion Institute* **33**, 2195–2202 (2011).

Testing the Waters: NRL Puts TNT-Contaminated Seawater in HARM's Way

During this time of vigilance against terrorist activity, in situ detection and testing of seawater for trace levels of explosives is a high priority of the Navy and the DoD, both for protection of U.S. personnel and assets and for environmental monitoring of Navy-patrolled littoral waters. NRL has immersed itself in this project and surfaced with a solution: the use of Hydroid REMUS100 autonomous underwater vehicles (AUVs) equipped with high throughput microfluidic immunosensors (HTMIs) and high aspect ratio microstructures (HARM) containing immobilized antibodies.

As the AUV glides through the marine environment, its high throughput microfluidic sensors collect, detect, and quantify trace levels of trinitrotoluene (TNT) at a flow rate of 2 ml/min; this yields a 30 s lag time, but at the 9 ml/min possible flow rate, nearly instantaneous detection is eventually expected. In initial tests, the REMUS100 operated at 6 to 9 ft depth for 2-h deployments, successfully analyzing seawater contaminated with ~20 to 200 ppb of TNT without sample pretreatment and without HTMI failures due to clogging from biomass infiltration or device leaks.

This technology represents a significant time savings over offsite chemical analysis and brings laboratory-level sensitivity to a field-deployable system that can be used to assess the environmental safety of marine environments for dispatched medical personnel and other first responders and to monitor levels of contaminants leached by unidentified unexploded ordnance (UXO) in defunct munitions testing grounds and military installations.

This is just another demonstration of NRL's willingness to go deep to defuse potentially explosive situations.

REMUS100 AUV with an Integrated Microfluidic System for Explosives Detection

A.A. Adams
National Academy of Sciences, National Research Council,
Postdoctoral Research Associate

P.T. Charles, J.R. Deschamps, and A.W. Kusterbeck
Center for Bio/Molecular Science and Engineering

Detecting explosive materials at trace concentrations in the marine environment is critical to protecting U.S. citizens, waterways, and military personnel during this era of potential domestic terroristic activity. Presented here are results from recent field trials that demonstrate detection and quantitation of nitroaromatic materials using novel high-throughput microfluidic immunosensors (HTMIs) to perform displacement-based immunoassays onboard a Hydroid® REMUS100® autonomous underwater vehicle (AUV). Antibodies were immobilized on high aspect ratio microstructures (HARM) incorporated into high-throughput microfluidic devices, thereby creating larger surface-area-to-volume ratios that facilitated more efficient analyte extraction. Missions were conducted 6 to 9 ft below sea level, and no HTMI failures were observed due to clogging from biomass infiltration or device leaks. HTMIs maintained immunoassay functionality during 2-h deployments while continuously sampling seawater at a flow rate of 2 ml/min, which resulted in reduced lag time (10^1). Contaminated seawater with ~20 to 200 ppb trinitrotoluene (TNT) was successfully analyzed in situ without sample pretreatment.

INTRODUCTION

Monitoring the composition of waterways about the continental United States, its territories, and its allies is an ongoing concern for the Navy and the Department of Defense. Highly energetic small molecules classified as explosives and their associated degradation products pose major security and environmental concerns during this era of imminent domestic terroristic activity.[1] In addition to being a major cause for concern relative to security, the leaching of explosives in the vicinity of various operational/defunct military installations and munitions testing grounds throughout the U.S. indicates the need for autonomous environmental monitoring of unidentified unexploded ordnance (UXO) and the associated degradation products of these materials. Finally, forensic investigations, as they pertain to domestic terroristic activities, also dictate that field-deployable assessment tools be readily available for untrained field technicians in order to rapidly determine the safety of dispatched emergency medical personnel and other first responders.

Traditionally, offsite chemical analysis has been performed using conventional analytical instrumentation including high performance liquid chromatography, gas chromatography coupled to mass spectrometers, surface-enhanced Raman spectroscopy, ion mobility spectrometry, cyclic voltammetry, and energy dispersive X-ray diffraction in the analysis of explosives. These methods have successfully delivered high sensitivity and selectivity for the analytes, yet these methods offer limited amenability to portability, which detracts from their potential field readiness. Size notwithstanding, these instruments require significant expertise to employ. Real-time reporting from remote analysis of trace levels of explosives has been an elusive target.

The most prolific field-deployable detection system has been the extensively trained canine. These animals are expensive to train, require continuous maintenance, and are subject to fatigue and injury. Further, the canine's strong sense of smell is rendered ineffective when the analyte or target exists in a submerged plume within a body of seawater such as those that exist in the U.S. coastal waters.

The nature of explosives and concern for the safety of the analyst and first responders demonstrate the need for sensing these dangerous and potentially toxic (≥ 0.002 µg/mL as reported by the Environmental Protection Agency) environmental contaminants remotely.[2] For underwater operations, there is a significant threat posed by UXO, both to maritime traffic and to

divers. A new breed of highly sensitive immunosensors embedded into autonomous underwater vehicles (AUVs) such as the commercially available Hydroid® REMUS100® offers distinct advantages such as (1) enabling on-site in situ assessment that eliminates the low bias due to sample storage, degradation, and transport; (2) remote sensing capability that minimizes putting people in harm's way; and (3) programmable vehicles that can survey the area of interest for the targets. Sensors for explosive nitroaromatic compounds that offer better approaches to the rapid, highly sensitive and selective remote detection of trace levels of various explosives are undeniably warranted. Presented herein is a novel approach with application of high-throughput microstructures designed to meet three primary requirements: (1) reducing false positive and false negative responses in complex marine matrices; (2) providing for rapid analysis; (3) increasing sensitivity by more efficient extraction.

AUTONOMOUS UNDERWATER VEHICLE, IMMUNOSENSOR, AND PLUME GENERATOR

The vehicle used in these field trials was the Hydroid REMUS100 AUV, which has been widely employed for port and harbor surveillance by the U.S. Navy as well as by NATO countries. The standard REMUS100 is 7.5 in. in diameter, 63 in. long, and weighs approximately 80 lb (see Fig. 1). The expandability of the REMUS100 is provided by an interface connector on the front of the REMUS100 vehicle supplying operational commands, communications, and power

FIGURE 1
Hydroid® REMUS100® autonomous underwater vehicle.

to the sensor payloads. The first part of the REMUS100 augmentation systems is the adapter collar. The collar provides access to the electrical connector on the front of the REMUS100 and provides a mechanical attachment for the additional sensors. This collar has access ports for the programming connector; conductivity, temperature, and depth (CTD) sensor; the acoustic transponder; and EcoPuck Triplet for optical measurements. The external CPU section (ECPU) of REMUS100 was custom designed by SubChem Systems (Narragansett, RI) to provide an external controller for adaptive missions with the REMUS100. The section consists of a single-board computer, power conditioning, and an acoustic modem (Benthos ATM-885 board

set). For each mission, once transponders (underwater navigational aids) are positioned within the operational area, the REMUS100 can be programmed to navigate a specified path while continuously assaying the contents of its environment and reporting the results over the acoustic modem to the main controller. Results can also be broadcast to a secure IP address for visualization by offsite individuals over the Internet.

The immunosensor was fitted with a pump capable of delivering flow rates of 9 ml/min that can be controlled independent of the rest of the system via acoustic modem commands. Once directed, the pump turned on at the requested flow rate and pushed the trinitrotoluene (TNT) sample through the sample injector shown in Fig. 2. The REMUS's forward velocity moved fluid through the sample injector and TNT sample was mixed into that flow, producing the final concentration that was assessed by the immunosensor. The flow rate through the manifold was determined by the vehicle's forward velocity. The REMUS velocity for this trial was programmed to be 1 m/s throughout the mission. The corresponding flow rate through the manifold was approximately 1.9 L/min through the 0.25-in.-diameter flow path. As configured, with the high flow pump set to 1 ml/min, the corresponding TNT concentration of the plume was 20 ppb. Plume concentration was linearly controlled with the high flow pump flow rate, and a 9 ml/min setting yielded a TNT concentration of 175 ppb. The immunosensor's filtered intake was positioned at the aft end of the manifold flow path (see Fig. 2).

FIGURE 2
Nose of REMUS100 with plume generator and the filter capped inlet for the immunosensor.

The immunosensor is shown in Fig. 3. The unit was optimized for TNT detection in seawater matrices during bench scale experiments.[3] The system was designed to be submersible in order to be used in chemical sensing for submerged UXO. In the REMUS100
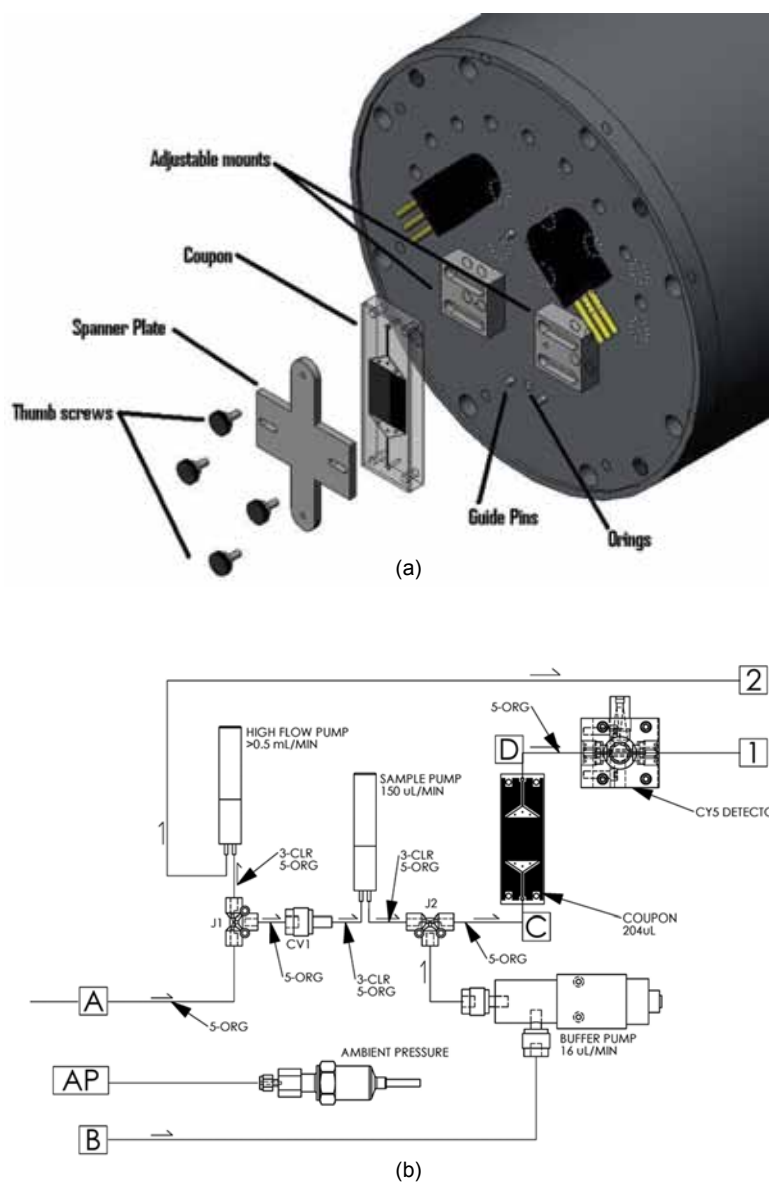
FIGURE 3
(a) Immunosensor payload with an exploded view of the high throughput microfluidic device interface. (b) Schematic of REMUS100 payload internals with high-throughput microfluidic immunosensor.

framework, the immunosensor was poised immediately aft of the nose. The free flooded REMUS100 nose housed the sample intake and buffer solution. The sample intake filter was located bottom dead-center just outside the nose within the REMUS100's free flow boundary layer. On the forward bulkhead of the immunosensor was the high-throughput microfluidic immunosensor (HTMI) or coupon interface. In the face sealing design, as coupons were exhausted, they were exchanged by removing the nose and replacing the spent coupon with a charged coupon. This was accomplished by removing the mounting bracket and sliding

the coupon off the alignment pegs between the ~2-h REMUS100 deployments. The quick coupon removal interface of the immunosensor is illustrated in Fig. 3(a).

HIGH-THROUGHPUT MICROFLUIDIC IMMUNOSENSOR (HTMI)

The high-throughput microfluidic immunosensor was created via a high-precision micromilling process whereby a molding tool was cut from brass feedstock with a positive impression of the desired microarchitectures. The molding tool was used in a

hot embossing process that transferred the positive features of the molding tool into poly(methylmethacrylate) (PMMA) blanks. PMMA was chosen due to its well-characterized surface chemistry, high impact resistance, durability, and resistance to biofouling. Next, the substrate was coupled to PMMA coverslips via a trisolvent-assisted thermal bonding process, resulting in the production of high-throughput microfluidic devices. The microchannels were then treated to provide a scaffold that was later used to covalently immobilize antibodies directed against TNT. After the antibody immobilization was complete, the devices were saturated with a solution containing fluorescently labeled analogues of TNT. The devices were sealed with a plastic film and encased in aluminum foil to prevent leaks and photodegradation of the bound fluorophores. All devices were refrigerated or stored on ice in a cooler until used. A representation of the HTMI (labeled "coupon") is shown in Fig. 3(a). The HTMI uses 39 parallel 1-in.-long centrally located microchannels. The high aspect ratio microstructures (HARM) increased the surface-area-to-volume ratio of the HTMI, thereby enabling more efficient analyte extraction, subsequently resulting in improving overall assay sensitivity. The highly parallelized microchannels enabled unequalled throughput by reducing the pressure drop across the device to a negligible amount, allowing for operational flow rates of up to 9 ml/min, which is 90× greater than previous reports while maintaining favorable kinetic conditions for the displacement-based immunoassay.

FIELD DEMONSTRATION

All tests were performed in Narragansett Bay, Rhode Island, within the Greenwich Bay. Tests were conducted August 9 and 10, 2010. A topographical representation of the Greenwich Bay is shown in Fig. 4(a). The green diamonds show the position of the transponders and a green plus symbol represents the ship location. The REMUS100 assay path is shown in purple while the location of the REMUS100 at the time of the image is illustrated by a white plus symbol. A prelaunch photo of the REMUS100 is shown in Fig. 4(b) during the ballasting procedure in which the unit's buoyancy was optimized for the mission.
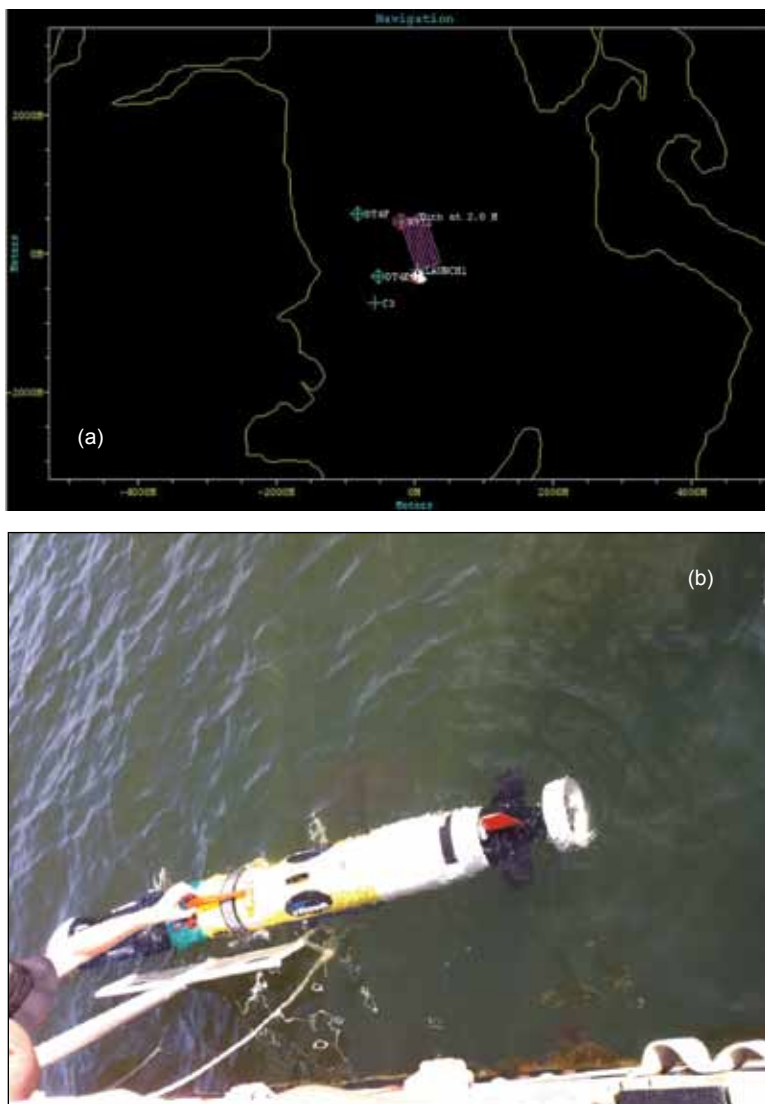
FIGURE 4
(a) Topographical representation of Narragansett Bay, RI, region, with green diamonds representing transponder locations and a green plus sign representing the ship, with the REMUS100 assay path in purple. (b) Photograph of the REMUS100 with the payload mounted during prelaunch ballasting.

REMUS100 IMMUNOSENSOR PERFORMANCE

Prior to the mission, the immunosensor was calibrated against matrix-matched TNT standards as shown in Fig. 5. Triplicate analyses of TNT standards of 0.01, 0.1, 1, and 10 ppb prepared from a TNT stock solution were performed. An analysis of TNT samples at 1 and 10 ppb prepared using nonhazardous explosive for security training and testing (NESTT) material was also done in triplicate to compare the sensor response for other available TNT variants. Peak-to-peak reproducibility was in excellent agreement with %RSD (relative standard deviation) values of less than 8%. Figure 6(a) shows the sensor response over time as a black trace and the plume activation as a blue trace.
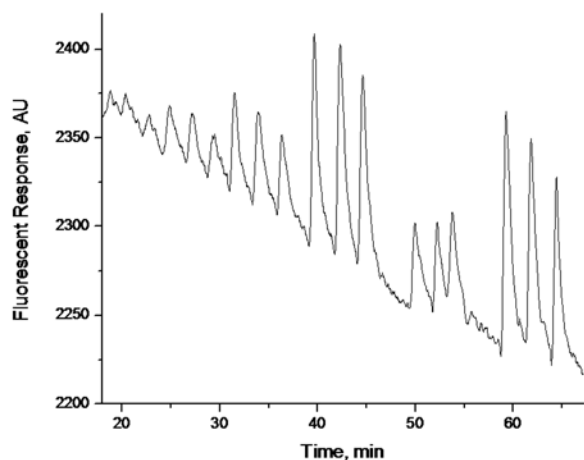
FIGURE 5
Immunosensor optimization for NESTT and TNT in seawater.

In agreement with bench testing, lag times during the field trial of approximately 30 s from plume initiation to signal production were observed during the trials. The operational flow rate for the TNT assay was 2 ml/min, which was 20× higher than previously reported. The inset in Fig. 6(b) shows the path of the REMUS100 during the mission, and the contour plot shows the response at the given position. Although the plume was simulated as detailed earlier, the contour plot is in excellent agreement with the TNT releases as time correlated with Fig. 6(a). The deviation peak symmetry in the field trial was expected. In the bench assays, a finite volume was injected into the column for quantitation; however, in the field, the volume injected was dependent upon crossing currents as well as other environmental effects.
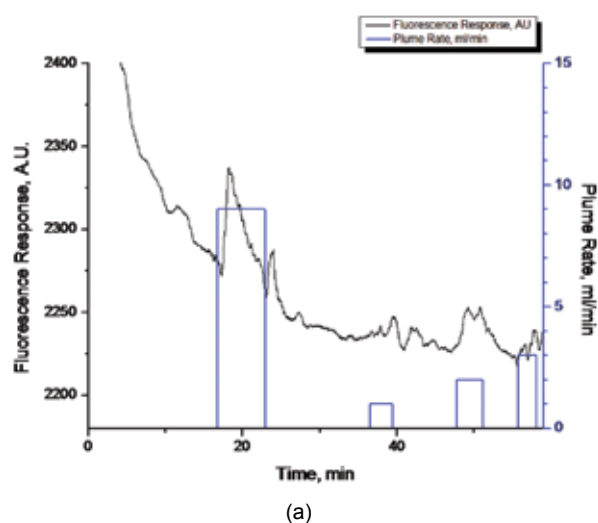
SUMMARY

We have demonstrated the potential for low ppb detection of TNT at significantly higher flow than previously demonstrated. The monoclonal antibodies used here were demonstrated to function in the harsh aquatic environment of the Narragansett Bay. The trial was conducted with an operational flow rate of 2 ml/min, yielding nearly 30 s lag times, but the immunosensor is capable of operating at flow rates as high as 9 ml/min. At that flow rate, lag time would be negligible, providing nearly instantaneous results. The immunosensor as configured for these trials successfully detected TNT from a simulated plume at 20 ppb in seawater while underway. Experiments are continuing to further extend the sensitivity of the assay by increasing the density and bioavailability of the receptors. In addition, small molecules that are toxic to indigenous species are also being evaluated as possible analytes for future versions of the immunosensor.

ACKNOWLEDGMENTS

(a)

(b)
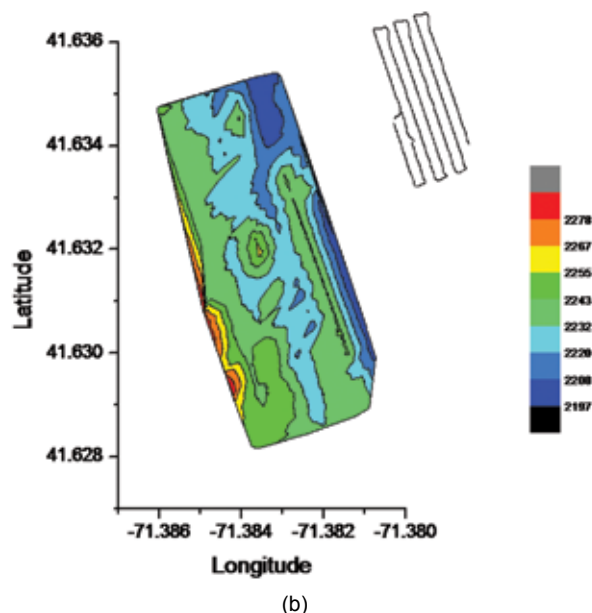
FIGURE 6
TNT response and plume rate data collected by REMUS100 payload underway. (a) Immunosensor response (Y1) and plume release rate (Y2) vs time. (b) Corresponding contour plot produced from the data in (a).

References
[1] S.Y. Rabbany, W.J. Lane, W.A. Marganski, A.W. Kusterbeck, and F.S. Ligler, "Trace Detection of Explosives Using a Membrane-based Displacement Immunoassay," *J. Immunolog. Methods* **246**(1-2), 69–77 (2000).

[2] F.S. Ligler, C.R. Taitt, L.C. Shriver-Lake, K.E. Sapsford, Y. Shubin, and J.P. Golden, "Array Biosensor for Detection of Toxins," *Anal. Bioanal. Chem.* **377**(3), 469–477 (2003).

[3] P.T. Charles, A.A. Adams, P.B. Howell, S.A. Trammell, J.R. Deschamps, and A.W. Kusterbeck, "Fluorescence-based Sensing of 2,4,6-Trinitrotoluene (TNT) Using a Multi-channeled Poly(methyl methacrylate) (PMMA) Microimmunosensor," *Sensors* **10**(1), 876–889 (2010).

■

Shedding Light on Dark Matter

can't actually be done – while these particles make up 82% of the matter in the Universe, they don't interact with light. So how do we know anything about these invisible particles? While the mere existence of dark matter particles is inferred from their gravitational pull on matter that we can see, we can go further and learn about the properties of these subatomic particles. The properties of subatomic particles have important effects on the formation of the first galaxies and present-day dwarf galaxies. Dark matter has been described as massive "cold" particles that decoupled from other particle species with little thermal velocity; however, if dark matter is composed of lighter "warm" particles, their thermal velocities allow them to stream out of the smallest over-dense regions in the early Universe thereby decreasing the density and preventing the collapse and formation of small galaxies. Using N-body simulations of the gravitational interaction of 200 million bodies, we can model Milky Way–sized galaxies with various particle masses. The number of small satellite galaxies in the simulated Milky Ways decreases with decreasing mass of the dark matter particle. Comparing the simulations to the number of satellite galaxies observed around the Milky Way sets a lower limit on the mass of the dark matter particle. Determining just how cold "cold dark matter" really is helps us to determine the composition of dark matter and thus understand galaxy formation. We still can't see dark matter, but we're finding out how to take its temperature.

Constraining the Very Small with the Very Large: Particle Physics and the Milky Way

E. Polisensky
Remote Sensing Division

M. Ricotti
University of Maryland

The majority of matter in the universe likely consists of one or more undiscovered particles that do not interact with light. The properties of this dark matter can be deduced from its gravitational interaction with visible matter. The early universe contained regions where the matter density was higher than average. These regions collapsed gravitationally to form galaxies. The velocities of dark matter particles in the early universe depend on the particle mass — less massive particles move faster and can stream out of the smallest dense regions, thereby decreasing their density and preventing gravitational collapse. In this way, the number of small satellite galaxies in massive galaxies can probe the unseen particle's mass. We have conducted N-body simulations of the gravitational interactions between 200 million bodies to model Milky Way–sized galaxies with various particle masses. Such simulations are computationally challenging because gravity is a long-range force and, in a direct approach, the complexity of the computation scales as N^2 for N bodies. We compare our simulations to the observed number of Milky Way satellites to derive a lower limit on the particle mass comparable to, and independent of, complementary astronomical methods.

INTRODUCTION

Cosmology has entered an age of precision where the major parameters such as the amount of matter and energy in the universe are known to within just a few percent. Of the matter in the universe, less than 18% is composed of the familiar protons and neutrons that make up the elements. The rest consists of an undiscovered particle that neither emits, absorbs, nor reflects light at a detectable level and is called "dark matter." The presence of dark matter is deduced from its gravitational interaction with the visible matter in galaxies and clusters. Simulations show the stars and gas of galaxies and clusters reside in extended spheroidal shaped halos of dark matter.

In the standard paradigm, the dark matter particle is "cold": it decoupled from the other particle species in the early universe with negligible thermal velocities. A cold particle would have a large mass, on the order of giga-electron volts (GeV) or more. Cold dark matter (CDM) is extremely successful at describing the large-scale features of matter distribution in the universe but has problems on small scales. Below the mega-parsec scale (Mpc = 3.3 million light years) CDM predicts numbers of satellite galaxies for Milky Way–sized hosts about an order of magnitude more than the number observed.

One proposed solution is the dark matter may be "warm" with a particle mass on the order of kilo-electron volts (keV). Warm dark matter (WDM) particles decouple in the early universe with relativistic velocities, enabling them to stream out of regions of higher density and erase density fluctuations on sub-Galactic scales. WDM thereby reduces the numbers of satellites. In this way, the satellite galaxies of the Milky Way can be used to probe the unseen particle's mass. Since the number of dark matter halos must be greater than or equal to the number of observed satellites, a census of observed Milky Way satellites combined with simulations of the satellite population of Milky Way–sized dark matter halos can set a lower limit on the particle mass.[1]

WARM DARK MATTER

The WDM particle is often assumed to be a thermal particle, meaning it was in thermal equilibrium with the other particle species at the time of its decoupling in the early universe. A candidate for a thermal WDM particle is the gravitino from supersymmetry theories of particle physics. In general, the dark matter particle may not have been in thermal equilibrium when it decoupled. This is the case for a sterile neutrino, a theoretical particle proposed as an explanation for

the anomalous excess of oscillations observed between neutrinos and antineutrinos. Figure 1 shows the effects of WDM on the power spectrum of density fluctuations for several thermal particle masses and an 11 keV sterile neutrino. As the particle mass decreases, structures are erased on larger scales.
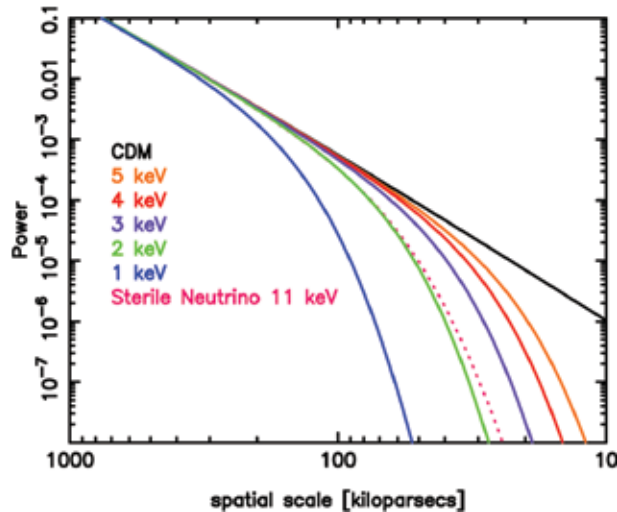
FIGURE 1
Power spectra of density fluctuations for CDM and WDM. As the particle mass decreases, the number of structures (power) decreases on larger scales.

SIMULATIONS

Dark matter can be treated as a collisionless gas. In the N-body method, the phase-space density of this gas is sampled with a finite number, N, of tracer particles. Solving the evolution of this gas from the early universe to the present requires calculating the gravitational force on every tracer particle and calculating its new position after a small time step from its acceleration and velocity. Since gravity is long ranged, the force on each particle is influenced by every other particle. A direct integration of forces would require N-1 force calculation for each particle, or on the order of N^2 computations for each time step. As the number of particles grows large, a direct approach to force calculation quickly becomes intractable. Algorithms have been developed requiring less computational resources and below we describe the methods used by the N-body code GADGET-2.

GADGET-2 separates the force on each particle into a short-range and a long-range term. A "particle mesh" method is used for calculating the long range force. The force is treated as a field quantity and approximated on a mesh. Densities are computed for each mesh cell and the gravitational potential and forces on

the grid are calculated. Gravitational potentials and forces at the particle positions are obtained by interpolating the mesh values.

The short range force is calculated with a "tree" method. This method uses the principle that the individual forces from distant groups of particles can be treated as a single force from a massive particle. This reduces the number of force computations for a single particle from N-1 in the direct approach to on the order of log N. The particles are grouped hierarchically with a recursive subdivision of space. A "root" node is formed encompassing the whole simulation volume. The root node is subdivided into smaller daughter nodes. These daughter nodes are recursively subdivided, like branches of a tree, until all particles are in "leaf" nodes of no more than one particle per leaf. To calculate the force on a particle, the tree is "walked"; starting at the root node, it is decided if the node is small enough and far enough away to provide an accurate force estimate. If so, the walk is stopped along this branch; if not, the node is opened and the procedure repeated at the next level of branches. This is repeated until the forces from all other particles in the short range region have been accounted for.

GADGET-2 is also a massively parallel simulation code flexible for use on an arbitrary number of processors. The computational volume is decomposed into a set of domains, each assigned to one processor with each processor running a separate instance of the GADGET-2 code. Each domain is compact with a small surface-area-to-volume ratio that reduces communication times between processors necessary when calculating the forces on domain-bordering particles.

OUR SIMULATIONS

We employ a "zoom" technique in which we run a simulation of a 90 Mpc^3 cubic box with coarse mass resolution and identify dark matter halos with properties similar to the Milky Way. We chose a halo for resimulation at higher resolution by placing a smaller refinement region over the volume containing the halo's particles in the initial conditions, a box within a box. The refinement region has many more particles with much lower mass resolution than the original simulation. Our highest resolution simulations have over 200 million particles with a resolution of 9×10^4 solar masses. We ran high-resolution simulations for two separate Milky Way halos in CDM and WDM cosmologies with dark matter particle masses of 1, 2, and 4 keV. We ran each high-resolution simulation using 128 processor cores on the "Deepthought" parallel computing cluster at the University of Maryland, College Park. Each simulation took about 13 days to run, or about 4.5 years total CPU time per simulation.
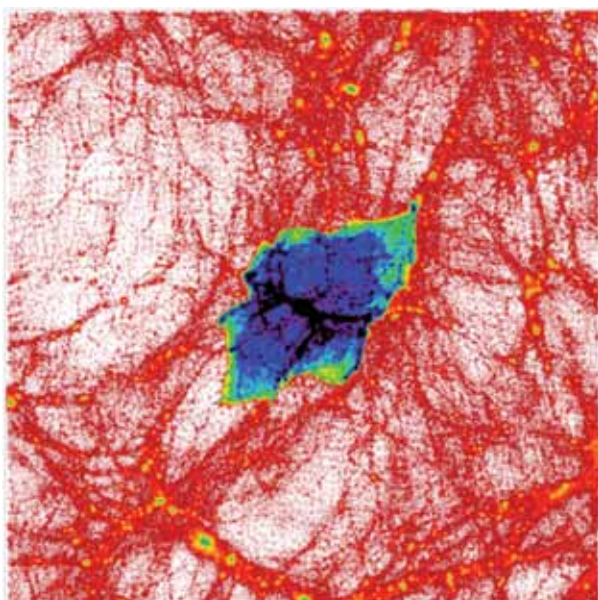
FIGURE 2
A 40 Mpc^3 cubic box centered on one of our simulated Milky Way halos. The image is color-coded by particle density showing the high mass resolution region embedded in the lower resolution simulation volume.

Figure 2 shows a 40 Mpc^3 region centered on one of our high-resolution halos at the end of the CDM simulation. The image is color-coded by particle density and shows the refinement region embedded in the larger, lower resolution simulation box. The Milky Way halo is at the center of the refinement region. Figure 3 shows portraits at 6 Mpc and 600 kpc of the same halo

in the high-resolution CDM and WDM simulations. The number of small-scale halos decreases as the dark matter particle mass decreases, while the large-scale features remain generally unchanged.

Finding the gravitationally bound dark matter halos in large N-body simulations is also a nontrivial computational problem. For our simulations, we used the AHF halo finding software. AHF constructs a hierarchy of grids and calculates the particle density in each cell. If the cell density is higher than a threshold value, the cell is divided into a refined subgrid and the procedure repeated. A tree of nested grids is thus constructed that traces the density field. Halos are followed by stepping in density contours from high values to the background density. Substructures are identified by recursively walking the tree from coarse grids to fine. Like GADGET-2, AHF supports parallel computing through domain decomposition techniques, allowing it to run quickly even on large N simulations.

COMPARISON TO OBSERVATIONS

Before the Sloane Digital Sky Survey (SDSS), there were only 12 classically known satellite galaxies of the Milky Way. Sixteen new satellites have been discovered in the SDSS. We correct for the primary incompleteness of the SDSS, its sky coverage of 28.3%, and combined with the classic Milky Way satellites, this forms our observed data set.

The SDSS is a magnitude-limited survey, meaning satellites of a given luminosity and surface brightness are preferentially detected at closer distances. The num-
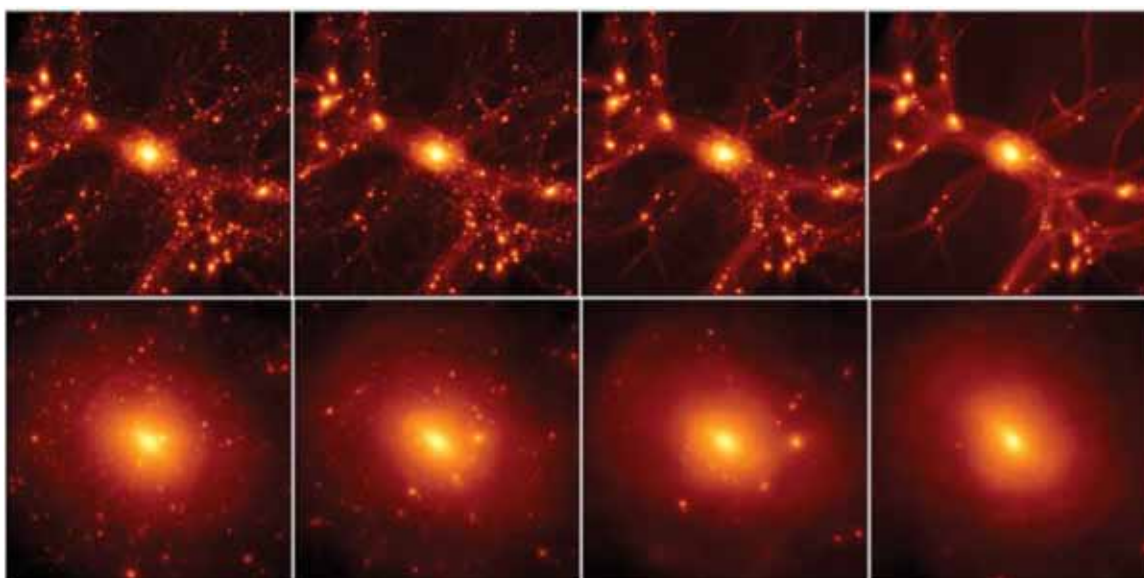
FIGURE 3
Portraits of the Milky Way halo at 6 Mpc (upper row) and 600 kpc (bottom row) for different cosmologies. From left to right the cosmologies are CDM, 4 keV WDM, 2 keV WDM, 1 keV WDM. As the dark matter particle mass decreases, the number of Milky Way satellites decreases.

ber of satellites within 50 kpc of the Milky Way center is most important for constraining the dark matter particle mass because the observations are most complete to this distance. Unfortunately, this is also the distance range where numerical destruction effects become important for the simulations. Satellites in simulations are destroyed artificially by extraneous tidal fields due to limitations of the simulation technique. This numerical destruction becomes dominant for satellites in the inner halo region. We calculate and correct the effects of numerical destruction using results of published high-resolution simulations found in the literature.

We count the number of satellites from 0 to 50 kpc in our high-resolution simulations. We consider the uncertainty in the simulated halo abundances due to halo-to-halo variation and, using the results of other published simulations, we conservatively set the scatter to 30% and interpolate the simulation results over the range $m_{WDM} = 1-5$ keV. We also consider an uncertainty in the number of observed satellites due to the incomplete sky coverage of the SDSS. In Fig. 4 we plot the difference in the number of observed and simu-
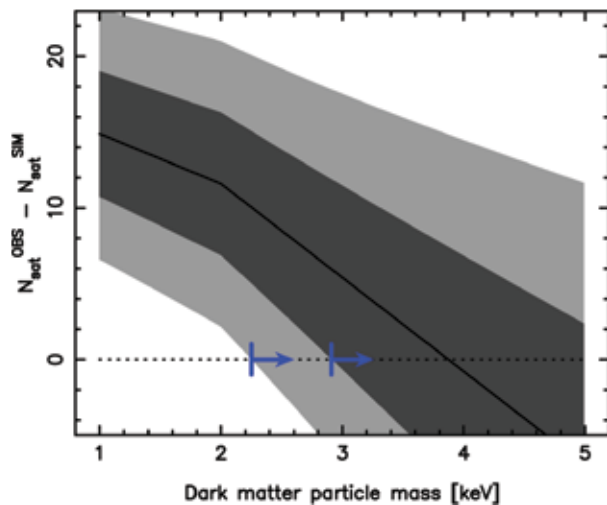
FIGURE 4
Number of observed Milky Way satellites minus the number of satellites in our simulations interpolated over WDM cosmologies with particle masses 1–5 keV. The dark and light shaded regions show the 1σ and 2σ ranges considering uncertainties in both the observed and simulated data sets. The arrowed lines show our lower limits on the dark matter particle mass at 1σ and 2σ confidence.

lated satellites with 1σ and 2σ limits (shaded regions) from combining the uncertainties of the observed and simulated data sets. The number of satellites in simulation must be at least equal to the number of observed satellites; therefore, where this quantity equals zero, a lower limit on the dark matter particle mass is defined.

The arrowed lines indicate the lower limits at 1σ and 2σ, and we adopt $m_{WDM} > 2.3$ keV at 95% confidence.

COMPARISON TO OTHER METHODS

Our result can be compared to limits on the particle mass from modeling the Lyman-α absorption by neutral hydrogen along the line of sight in the spectra of distant quasars. Work using low-resolution spectra for SDSS quasars finds a limit of > 2 keV for a thermal WDM particle. Adding high-resolution spectra for a subset of quasars raises the limit to > 4 keV; however, the derived temperature of the intergalactic medium is higher than expected and also higher than that derived from high-resolution spectra taken with other instruments and from the widths of thermally broadened absorption lines. This could be explained by an unaccounted-for systematic error in the data that may also affect the derived mass limits.

Using a scaling relation for sterile neutrinos, we find a lower limit $m_s > 13.3$ keV. Sterile neutrinos are expected to radiatively decay to a lighter mass neutrino and an X-ray photon. X-ray observations of the diffuse X-ray background and dark matter halos in clusters, the Andromeda galaxy, dwarf spheroidal galaxies, and the halo of the Milky Way have all been used to set constraints on the sterile neutrino mass in the range $m_s < 2.5-9.3$ keV. These upper limits are well below the lower limits derived in this work and from Lyman-α observations and seem to rule out the standard production mechanisms. However, these mass limits, including the constraints set in this work, are model dependent and make assumptions about the dependence of the sterile neutrino mass on the mixing angle with active neutrinos, their cosmic density, and the initial conditions in the early universe when they were created. Depending on the assumptions made and the adopted production model, the relationship between mass, mixing angle, and cosmic density changes so that robust constraints cannot be placed on any one parameter.

SUMMARY

We conducted N-body simulations of the satellite populations of Milky Way–sized dark matter halos in CDM and WDM cosmologies. These simulations would not be possible with direct calculation techniques but are made possible by the use of algorithms that reduce the number of computations by many orders of magnitude, and by parallel programming methods that allow a problem requiring large numbers of calculations to be divided into smaller pieces and distributed to many processors running simultaneously. We have demonstrated how N-body simulations of the

Milky Way and its satellites can set limits on the dark matter particle mass comparable to complementary methods, but the methods are independent and almost certainly are subject to different systematic errors if any exist. Our limits are helped greatly by the discovery of many new satellites in the SDSS. Future surveys have the potential to discover many more satellites. Better constraints will result from the smaller uncertainty in the number of observed satellites achieved by improving the sky coverage and reducing luminosity corrections. In addition, there may exist a yet unknown population of even fainter satellites with luminosities and surface brightnesses that have been so far undetectable.

Reference
[1] E. Polisensky and M. Ricotti, "Constraints on the Dark Matter Particle Mass from the Number of Milky Way Satellites," *Phys. Rev. D* **83**, 043506 (2011), arXiv:1004.1459.

■

A Pirate is Neither a Thug of the Past nor a Laughing Matter...

…and a multidisciplinary effort by NRL is addressing piracy head-on. The degree and severity of piracy around the Horn of Africa (HOA), in particular, is costing the U.S. maritime industry up to $16 billion dollars per year, hampers humanitarian aid efforts, and poses a threat to lives. In addition, money paid to the pirates to ransom ships might be used to finance HOA regional conflicts and to fund terrorism.

To stop them, however, you must first find them, which is harder than finding the proverbial needle in a haystack. This is where NRL expertise steps in. Using a combination of real-time intelligence information and meteorological and information technology tools and techniques, NRL researchers are predicting where the pirates will be and when they are most likely to strike. Since pirates primarily use small, fast watercraft that are highly vulnerable to high winds and rough seas, predicting their movements and effectiveness relies on quickly and accurately predicting the weather. NRL is improving and making operational a NAVOCEANO product that dynamically couples intelligence and environmental information to predict when and where pirates are likely to strike, and then communicate that information to interdiction forces.

Hearkening back to the earliest missions of the U.S. Navy, when fighting piracy required that the U.S. Navy assert its domination of the high seas to stop the plundering of U.S. merchant vessels, today's Navy again seeks to enforce its domination of the seas, but now through information domination as much as through military might.

Information Domination: Dynamically Coupling METOC and INTEL for Improved Guidance for Piracy Interdiction

J. Hansen
Marine Meteorology Division

G. Jacobs, L. Hsu, J. Dykes, J. Dastugue, R. Allard, and C. Barron
Oceanography Division

D. Lalejini
Marine Geosciences Division

M. Abramson, S. Russell, and R. Mittu
Information Technology Division

Global piracy activity is on the rise. The region around the Horn of Africa (HOA) experienced a tenfold increase in piracy in 2009 and 2010 relative to 2008 despite increased effort by European Union (EU), NATO, and U.S. Naval forces.[1] The U.S. Department of Transportation Maritime Administration outlines several economic impacts associated with enhanced piracy activity around the HOA.[2] These include the fuel and personnel costs associated with rerouting ships via the Cape of Good Hope, as well as the opportunity costs associated with increased transit times. For ships that choose to transit through high-risk areas, there are increased insurance costs for operating in an area with high piracy activity, costs of additional security, and costs of nonlethal deterrent equipment. In addition, there are national costs associated with increased naval activity to protect shipping in high-risk areas. It is estimated that piracy costs the U.S. maritime industry between $1 billion and $16 billion per year.[3] In addition to national and international economic impacts, piracy also threatens humanitarian aid efforts around the HOA. For example, the U.S.-flagged and crewed *MV Maersk Alabama* was en route to Somalia to deliver food aid when it was boarded by pirates. There is also concern that the money being paid in ransom for hijacked ships is being used to finance regional conflicts around the HOA and potentially to finance terrorist activities.

Because pirates tend to operate in small vessels, they are particularly vulnerable to adverse winds and seas. Several divisions at NRL are helping to operationalize and improve a product created and disseminated through the Naval Oceanographic Office (NAVOCEANO) in an effort to communicate the risk of pirate attack to commercial shipping taking into account environmental, intelligence, and behavioral information. Before describing the process of dynamically coupling environmental and intelligence information, the impact of the environment on pirate activity is quantified based on analysis of the historical record of pirate attacks. The novel approach of dynamic coupling of environmental and intelligence information is then described. Finally, a description of efforts associated with the use of autonomous intelligent agents for the elucidation of emergent pirate behavior is provided.

THE IMPACT OF METOC ON PIRATE ACTIVITY

Analysis by NRL of the meteorological and oceanographic (METOC) conditions associated with pirate attacks off the HOA indicates that meteorology and oceanography strongly modulate pirate activity. The NRL Oceanography Division constructed a re-analysis of the winds, waves, and currents in the region of the HOA during the period of January 2007 through July 2010. The reanalysis provides the best estimates possible of environmental conditions by blending information from observations and operational numerical models. Pirate events over the same period were collected and filtered to exclude events that occurred in ports.

In Fig. 1, the black curves plot the number of pirate events as a function of significant wave height (panel a), wind speed (panel b), and shipping density (panel c). The red solid curves plot the predicted number of pirate events under the assumption that the environment has no impact on pirate activity. The red dashed curves are the one standard deviation bounds. Insofar as the black curves are different from the red curves, the environment (and shipping density) impact pirate

behavior. Note that waves (panel a) have the largest impact on pirate activity, there is a small impact due to winds (b), and that pirates tend to attack in regions of relatively higher shipping density (c). These results tell us that it is important to account for the environment and shipping when building a product to provide guidance for piracy interdiction.

THE PIRACY PERFORMANCE SURFACE

NAVOCEANO currently disseminates a daily forecast product that fuses wave and ocean current information with historic and recent pirate activity.

The resulting index communicates the suitability of pirate activity as a function of location and time and is used operationally by U.S., EU, and NATO interdiction forces. An example of the product, called the Piracy Performance Surface (PPS), is shown in Fig. 2. The PPS is constructed by modifying wave forecasts to account for the effects of currents, mapping from waves to an index bounded by 0 and 1, and performing a weighted sum between the environmental field and an index associated with historical pirate attacks (90% of weight is given to environmental conditions). Recent piracy attempts are included with higher weights that decay over time.

(a)

(b)

(c)
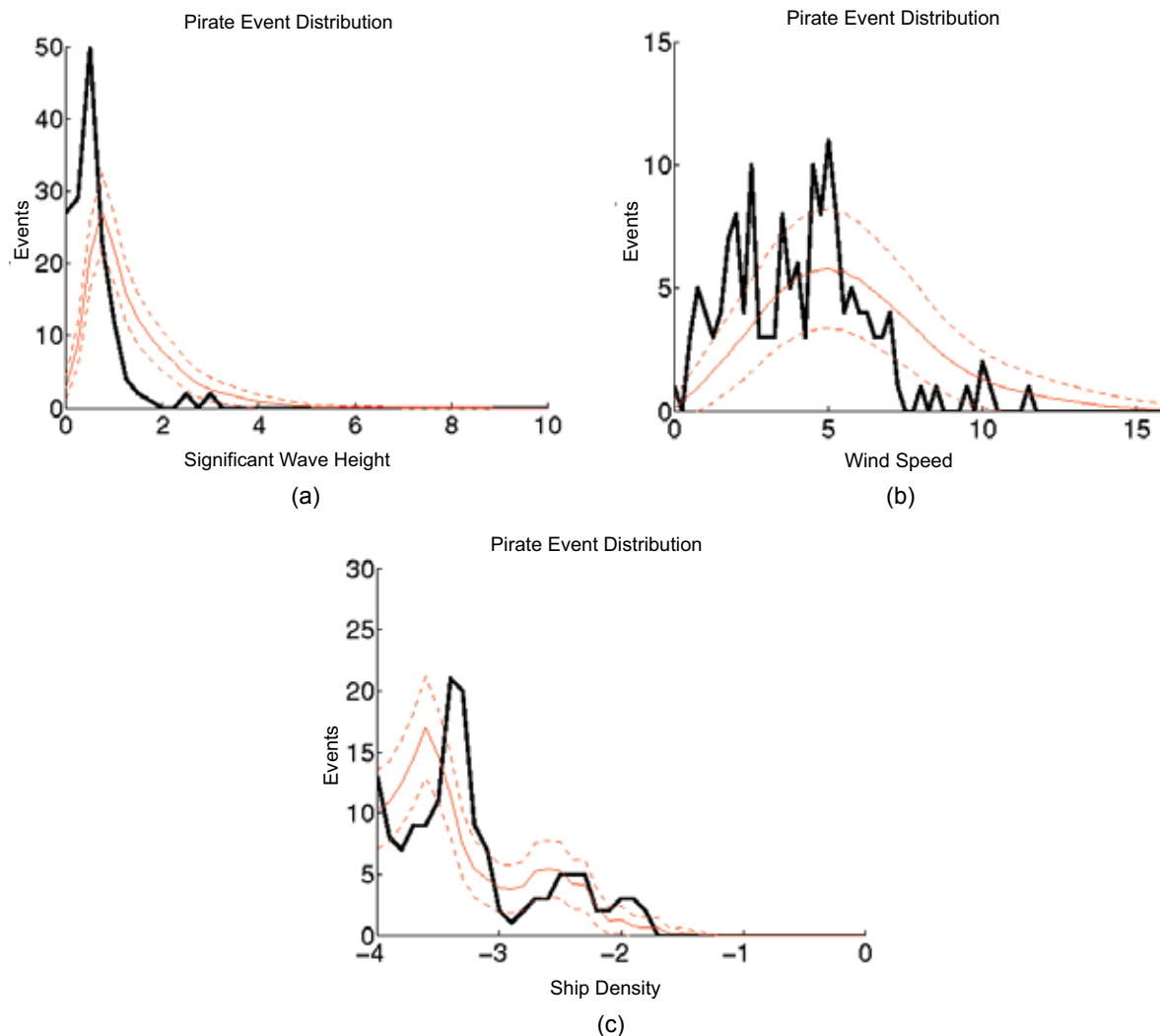
FIGURE 1
The black curves are the distribution of pirate events as a function of (a) significant wave height, (b) surface wind speed, and (c) commercial shipping density over the period January 2007 through July 2010. The red curves are the expected pirate event distributions under the assumption that the environment has no impact on pirate activity (dashed lines provide the one standard deviation bounds). Waves strongly impact pirate events; winds also impact pirate events, but to a much smaller degree. Pirates tend to operate in areas of relatively higher shipping density.
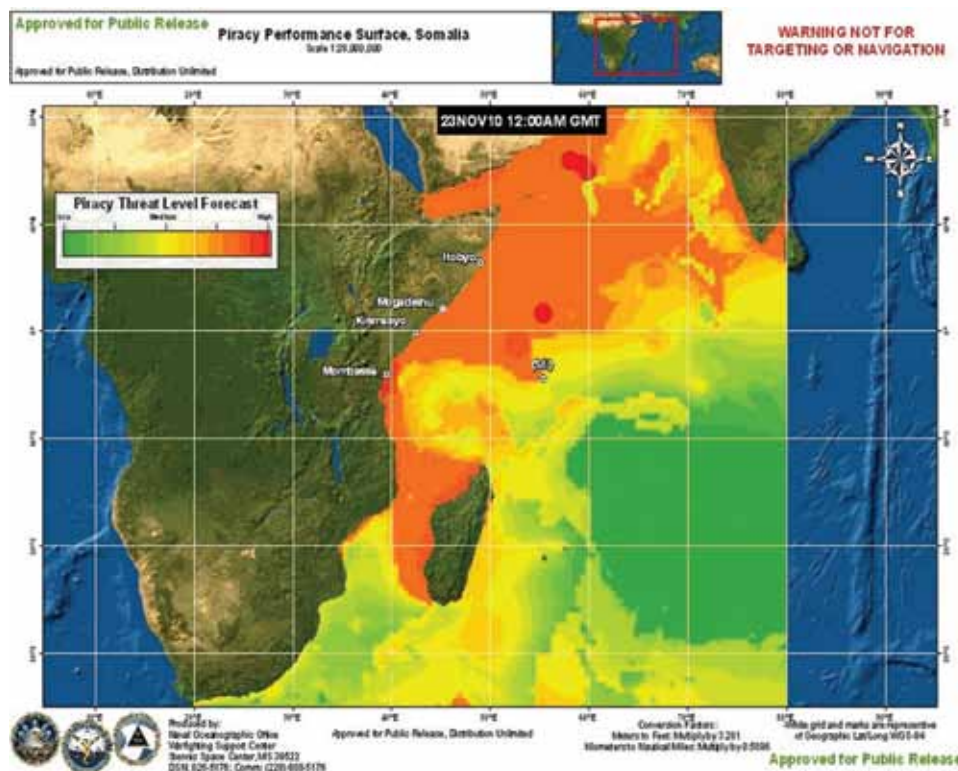
FIGURE 2
An example of the operational Piracy Performance Surface (PPS), which is created and disseminated once per day by NAVOCEANO for use by U.S., EU, and NATO pirate interdiction forces. The PPS thresholds wave height forecasts and merges with information about recent pirate activity.

EXPLICITLY PREDICTING PIRATE PROBABILITIES

A limitation of the PPS is that it uses only a small amount of intelligence information (historical attacks) and treats the environment separately from the intelligence information. Scientists at the NRL Marine Meteorology Division have developed a product that takes into account additional sources of intelligence information, such as pirate base locations and activity, details about pirate skiffs, and observations of likely pirate vessels. Instead of treating the environmental data and these additional sources of intelligence separately, this new product explicitly and dynamically couples the two.

The heart of the approach is the construction of a dynamic model of pirate tactics, techniques, and procedures that takes into account intelligence information (e.g., pirate CONOPS, equipment performance, base locations, numbers, and location of interdiction forces) and environmental information (e.g., forecasts of winds, waves, and currents). The pirate model predicts the track of a single pirate skiff as a function of time under the impact of the intelligence and environmental constraints (see Fig. 3(a)). The uncertainty associated with the intelligence and environmental information

is accounted for by running the pirate behavior model not once, but tens of thousands of times, sampling from all available sources of uncertainty, whether they be subjective distributions (such as pirate base locations) or objective distributions (such as wave ensembles). This generates millions of possible pirate locations (see Fig. 3(b)), and these millions of points can be interpreted as draws from a pirate distribution function (see Fig. 3(c)). The distribution of pirate locations changes over a forecast period as the environment impacts skiff motion. The resulting pirate distribution function can be updated in real time when observations of pirate activity become available by transforming the distribution of pirate trajectories in a Bayesian manner.

Although this is useful, interdiction forces are less interested in where pirates are likely to be and more interested in where an attack is likely to occur. The ingredients necessary for an attack at a given location are (a) the presence of a pirate, (b) a vulnerable commercial ship within line of sight, and (c) environmental conditions that are conducive to an attack. The probability of condition (a) is provided by the pirate probability product described above. The probability of (b) is obtainable from various unclassified and classified sources, and the probability of (c) is obtainable from available environmental forecasts and the information

(a)

(b)

(c)
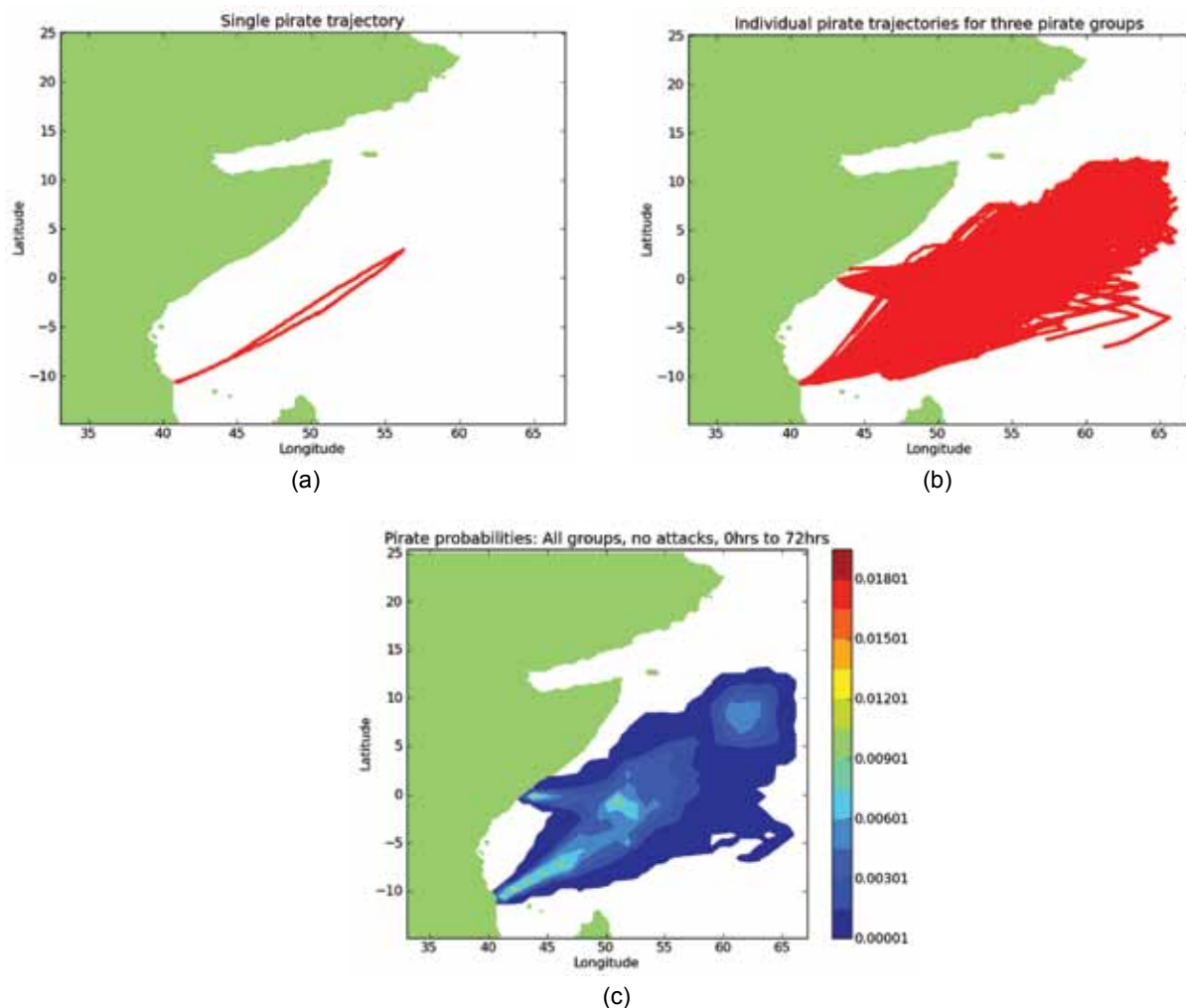
FIGURE 3
Example showing the construction of a pirate distribution. Panel (a) shows a single pirate trajectory. The pirate leaves base, transits at a set speed to a waypoint, hunts for commercial shipping, and then returns to base. Panel (b) shows the result of many thousands of pirate trajectories that sample from uncertainties in base location, skiff speed, environmental impact limits, hunting areas, hunting tactics, etc. Panel (c) plots the pirate distribution function for a 72-hr period. In this example, there are three active pirate groups: two operating from land bases and one from a sea-based mother ship.

in Fig. 1. We define the probability of attack to be the joint probability of (a), (b), and (c), which is given by the convolution of those three distributions.

Note that the probability of attack as defined above is conditioned upon the intelligence information that went into the construction of the pirate probabilities. If the intelligence information is incorrect or incomplete (which it most likely is), then so too will be the attack probabilities. To account for inaccuracies in intelligence information, "intelligence inadequacy" terms are added to the pirate distribution (based on long-term historical attack information) and the shipping distribution (based on long-term historical shipping distributions). This introduces a loss of theoretical rigor, but enables the communication of useful information to the decision maker.

An example of the product (now denoted Pirate Attack Risk Surface, PARS) is shown in Fig. 4. Figure 4(a) plots the pirate distribution, Fig. 4(b) plots the shipping distribution, and Fig. 4(c) plots the probability of an environment conducive to an attack. Note that if one simply plotted the probability of attack as created by the product of the distributions in Figs. 4(a-c), there would be large areas in which there was zero probability of attack. The inclusion of the "intelligence inadequacy" term fills the space. Note also that the color scale in Fig. 4(d) is not linear in probability. The probabilities in locations far from areas where pirates are expected to be located based on intelligence are orders of magnitude smaller than those in areas where intelligence indicates pirate activity. A nonlinear transformation is applied to the probability field to communicate the risk of pirate attack.

(a)   (b)   (c)

(d)
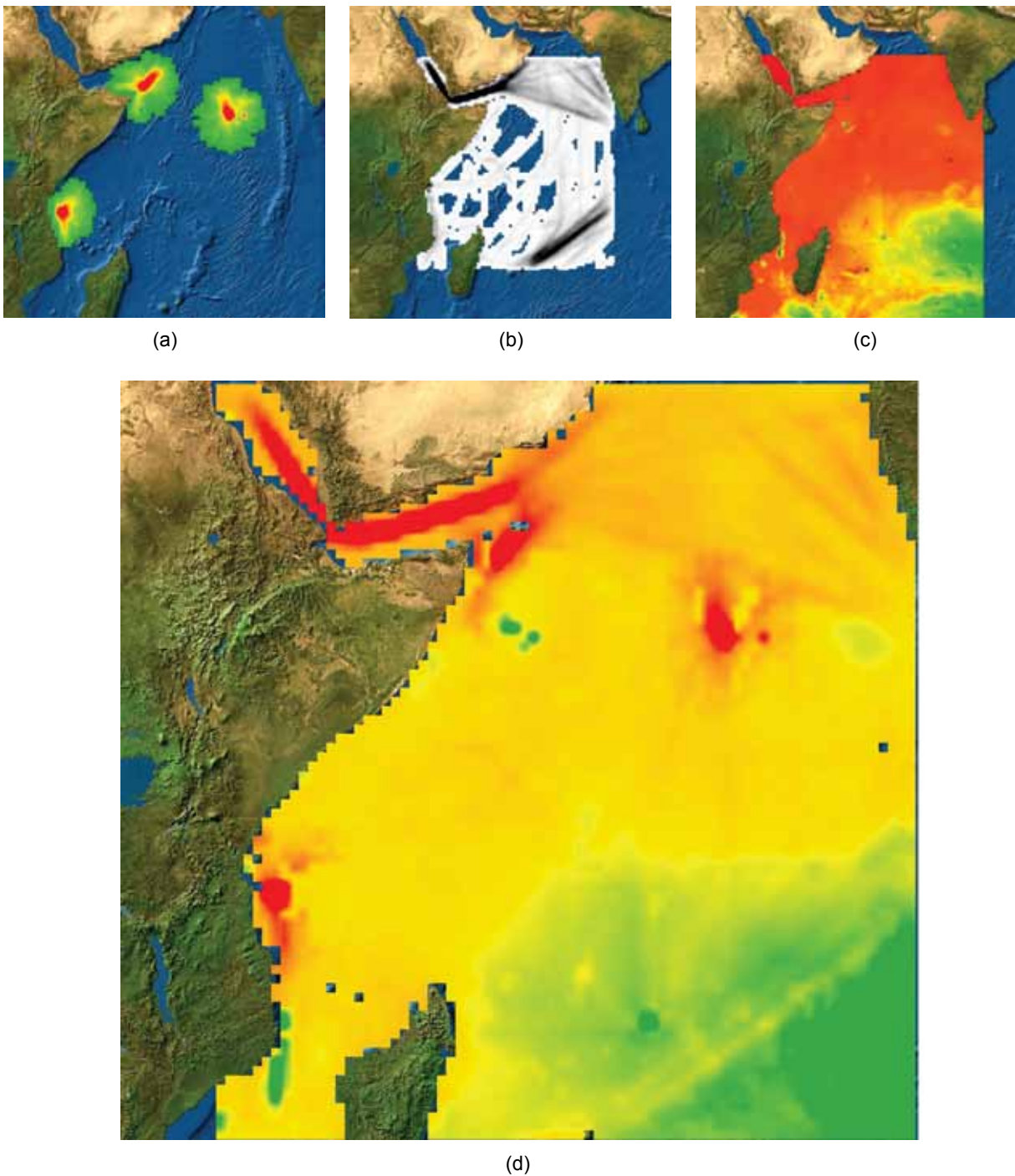
FIGURE 4
An example of the PARS product. The pirate probabilities in panel (a) are convolved with the shipping distribution in panel (b) and the probability of encountering a favorable environment in panel (c). An additional "intelligence inadequacy" term in the form of the environmental probability of panel (c) is added to account for the situation in which pirates are operating in areas unknown to intelligence agencies. The resulting risk of attack in panel (d) nonlinearly maps the probability of pirate attack to risk space so that very low probability areas can still be highlighted.

The PARS product is being operationalized at NAVOCEANO with the help of NRL's Marine Meteorology and Marine Geosciences divisions. NAVOCEANO will disseminate the product to U.S., EU, and NATO forces off the HOA to aid in pirate interdiction efforts.

INTELLIGENT PIRATES

A significant limitation of the PARS is that the pirate entities used to construct the pirate probability field do not directly interact with commercial shipping.

An attack is assumed to take place if a pirate, a vulnerable ship, and favorable environmental conditions are all present at a particular location. It would be preferable if commercial shipping, naval ships, and perhaps neutral fishermen were included in the pirate simulation and allowed to interact. Such modeling is naturally carried out in the context of agent-based modeling, but a limitation of existing agent-based modeling frameworks is that none have been developed in which the movements and actions of the agents is influenced by spatio-temporally varying boundary conditions such as those provided by environmental forecasts. The NRL Information Technology Division is performing research to address this limitation and examine the environment's impact on piracy in the agent framework.

Agent-based modeling and simulation is a powerful paradigm to explore complex interactions of goal-driven entities in order to support decision-making. The model used for the pirate problem is based on a prey/predator game with a learned hunting model for a pirate group as predator. Unlike prey/predator games where the population oscillates based on evolutionary dynamics, the presence of pirates at sea fluctuates depending on intelligence information as well as current and past meteorological conditions.

Research in agent-based modeling and simulation of pirate attacks involves (1) learning pirate hunting skills from past history and PARS' predictive analysis, (2) modeling the dynamics of risk-taking behavior, (3) optimizing the allocation of naval forces in a given area to minimize piracy attacks, and (4) developing adversarial strategies for commercial ships. Figure 5 illustrates our approach.

We are exploring agent-based behavior in Repast,[4] a grid-based framework where asynchronous agents act concurrently in a decentralized manner. The basic sense-think-act pirate agent loop leverages existing piracy efforts by calling PARS at each time step to obtain next state probabilities based on environmental and intelligence characteristics (such as skiff speed and environmental thresholds).

CONCLUSION

The generation of pirate distributions by dynamically coupling environmental, intelligence, and behavioral information is a new paradigm for product generation by the Navy Meteorology and Oceanography community. Four NRL divisions are working together to provide this novel capability through official operational dissemination channels to decision makers associated with piracy interdiction. The intelligent agent effort is anticipated to reveal emergent pirate behavior that can be compared against previously observed pirate behavior to reveal changes in or inadequate
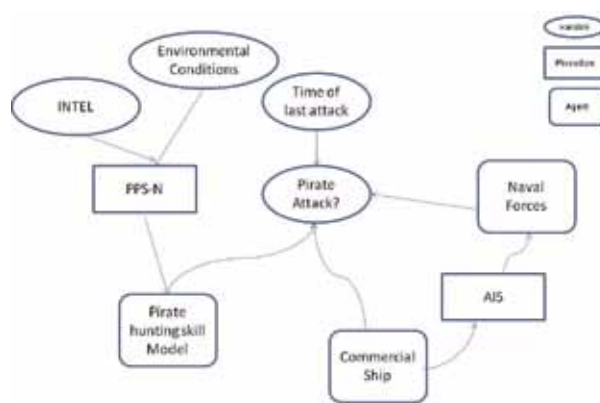
FIGURE 5
Conceptual framework for the agent-based modeling effort where pirates' risk-taking behavior is modulated by the time of last attack, and commercial ships alert Naval forces by broadcasting their location over AIS.[5]

representations of pirate behavior or its environmental dependencies. Such changes have been evident in the past as attack patterns have shifted in response to anti-piracy efforts, changing shipping patterns, and changes in pirate capabilities. Adapting the system to address these changes or deficiencies will ultimately improve the operational product. Similar approaches to product generation can be applied to any environmentally sensitive mission where the timescale of the event is similar to the timescale of impactful weather phenomena. We anticipate applying the approach to the drug interdiction problem where additional enhancements will be necessary to incorporate game theoretic aspects of the problem.

References
[1] International Maritime Bureau Piracy Reporting Centre, http://www.icc-ccs.org/piracy-reporting-centre.
[2] Economic Impact of Piracy in the Gulf of Aden on Global Trade, http://www.marad.dot.gov/documents/HOA_Economic Impact of Piracy.pdf, n.d.
[3] Peter Chalk, senior policy analyst, Rand Corporation. February 4, 2009, testimony to the House Committee on Transportation and Infrastructure, Subcommittee on Coast Guard and Maritime Transportation.
[4] N. Collier, "Repast, The Recursive Porous Agent Simulation Toolkit," retrieved from http://repast.sourceforge.net, 2001.
[5] Best Management Practice 3, Piracy Off the Coast of Somalia and Arabian Sea Area, http://www.marad.dot.gov/documents/Piracy_Best_Management_Practices_3.pdf, June 2010.

Unmanned Semi-Submersible (2010) — NRL demonstrated this vehicle for shallow-water (2 m to 200 m) bathymetry and sidescan surveying. It provides vastly superior coverage rates (2× or greater) compared to unmanned surface or underwater vehicles, and is excellent for rapid response in hostile environments (combat, disasters).

Three-Axis Fiber Laser Magnetometer

G.A. Cranch, G.A. Miller, C.G. Askins, R.E. Bartolo, and C.K. Kirkendall
Optical Sciences Division

Introduction: Acoustic detection of targets in shallow water environments is difficult due to high levels of anisotropic acoustic background noise. Detection range can be improved by simultaneously measuring non-acoustic signatures such as electromagnetic fields. A fiber laser vector magnetometer has been developed for seabed-mounted surveillance arrays. Three orthogonally mounted sensors measure each component of the Earth's field. Perturbations within these signals enable detection and tracking of remote targets.

Sensor Operating Principle: The sensor operates by converting a magnetic field into mechanical strain in a fiber laser sensor through the Lorentzian force.[1,2] A single-frequency, distributed-feedback (DFB) fiber laser is attached to a conducting ribbon carrying an AC current, i. In the presence of a magnetic induction, B, the ribbon experiences the Lorentzian force given by $F = B \bullet i$, causing it to oscillate at the AC frequency, thereby inducing strain in the fiber laser. The concept is illustrated in Fig. 1. Here, a gold-coated fiber laser is soldered to an aluminum ribbon, which is fixed in place, under tension, by aluminum clamps. Setting the AC frequency to a mechanical resonance of the ribbon
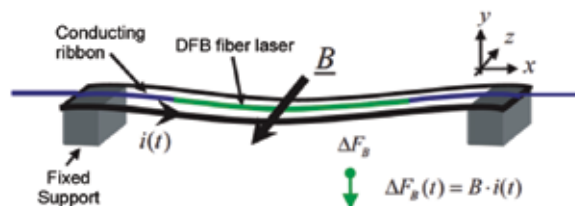
FIGURE 1
Operating principle of the sensor.

provides greater than 40 dB of signal amplification. The response of the sensor, expressed in terms of the component of the laser frequency modulation amplitude at the dither frequency, is given by

$$\Delta v \propto i \bullet B \bullet Q, \qquad (1)$$

where Q is the mechanical quality factor of the resonant sensor. The laser frequency shifts are measured interferometrically.[1] The dither frequency is actively adjusted to track the mechanical resonance, which may shift slightly due to changes in ambient temperature. A miniature induction coil in the sensor provides a means

of applying a bias field to compensate for the Earth's field, alleviating the dynamic range requirements of the interrogation system when attempting to measure nanotesla (nT) perturbations on a field that may exceed 10^5 nT. The resolution of the sensor, limited by thermomechanical noise in the oscillator, is currently 1 nT/Hz$^{1/2}$ at 1 Hz for an rms-current of 75 mA. Further improvement in the sensitivity can be achieved by increasing the mechanical-Q. A prototype magnetometer is shown in Fig. 2 (top right).

Three-Axis Magnetometer Node: This sensor has been developed into a remotely deployable, 3-axis magnetometer for undersea deployment. A sensing node incorporates three orthogonally mounted magnetometers and an optically powered microelectromechanical systems (MEMS)-based inclinometer. The deployed orientation of the node can be determined from a bearing obtained by the 3-axis magnetometer and inclinometer. The node is pressure tolerant to greater than 100 m depth and comprises an anodized aluminum base and acrylic dome. The instrumentation is mounted onto an additional aluminum plate and secured to the base. The instrumented node is shown in Fig. 2. The MEMS inclinometer is powered by a capacitor bank trickle-charged from a photonic power converter (PPC). The dither current for the magnetometers is supplied by a second PPC configured for high current generation into a low impedance load. A 2-W, 810-nm laser diode provides the MEMS power through a multimode fiber, and two 1480-nm laser diodes provide power for the dither current. As this system is optically powered, no additional electrical power is delivered to the node. A 1-km fiber-optic cable separates the node and electronics, which can be increased to several kilometers. The total separation distance is limited by the transmission loss of the 810-nm signal. A parallel effort has developed an all-optical inclinometer based on multicore fiber,[3] shown in Fig. 2 (far right). This would replace the MEMS inclinometer and enable an increase in the standoff distance to greater than 10 km.

Magnetic Field Measurements: Figure 3 shows the output of two orthogonal magnetometer axes aligned in a plane approximately parallel to the Earth's surface. The absolute measured levels reflect the local field experienced in the laboratory. The observed perturbations on this field correspond to a permanent magnet passing by the node. The characteristics of a moving dipole, resolved onto two orthogonal axes, are clearly visible in the measured data.

Summary: Fiber-optic sensors offer the benefits of remote interrogation and ease of multiplexing. A fiber laser-based sensor system has several advantages over

FIGURE 3
Output of two sensors showing magnetic perturbations.

previous fiber-optic magnetic field sensors. The Lorentzian force is a highly linear transduction mechanism, and the sensor exhibits no measurable hysteresis. This permits open loop operation, dramatically simplifying the sensor head. Increasing the dither current yields a proportional increase in responsivity and hence sensitivity. This novel technique further reduces the amount of electronics required in the sensor head, increases the permissible distance between the sensor and optoelectronics unit, and reduces the power requirement. Furthermore, the sensor contains no magnetic material, enabling its use in high field environments. Additionally, the system can be integrated with existing seabed-mounted fiber-optic hydrophone arrays[4] to form

multiparameter sensing arrays, increasing effectiveness in noisy acoustic environments.

[Sponsored by ONR and the Navy International Programs Office]

References
[1] G.A. Cranch, G.M.H. Flockhart, and C.K. Kirkendall, "High-resolution Distributed Feedback Fiber Laser DC Magnetometer Based on the Lorentzian Force," *Meas. Sci. Tech.* **20**, 034023 (2009).
[2] G.A. Cranch, G.M.H. Flockhart, and C.K. Kirkendall, "Distributed Feedback Fiber Laser Strain Sensors," *IEEE Sensors Journal* **8**(7), 1161–1172 (2008).
[3] G.A. Miller, C.G. Askins, and G.A. Cranch, "Interferometric Interrogation of a Multicore Fiber, Two-axis Inclinometer," *Proc. SPIE* **7503**, 75032R (2009).
[4] C.K. Kirkendall and G.A. Cranch, "Fiber-optic Bottom-Mounted Array," *2003 NRL Review*, pp. 189–191 (2003).

Navigating Using Spiral Sound

B.R. Dzikowicz[1] and B.T. Hefner[2]
[1]Acoustics Division
[2]Applied Physics Laboratory, University of Washington

Introduction: With the increased use of underwater robotics in both Navy and commercial applications, underwater navigation becomes more and more important. As researchers attempt to make these vehicles smaller and less expensive, simple systems for the navigation of multiple vehicles become important. A research team from the Naval Research Laboratory

in collaboration with the Applied Physics Laboratory at the University of Washington in Seattle, Washington, and the Naval Surface Warfare Center in Panama City, Florida, are developing and testing an underwater navigation system that uses a spiral-shaped acoustic wave to determine aspect. The single, stationary beacon can provide a navigation signal for any number of underwater vehicles.

Navigating with Spirals: Navigation by the satellite Global Positioning System (GPS) has become ubiquitous in modern life. Receivers are available for cars, boats, and even cell phones. These systems can be accurate to within a few meters. Differential GPS (DGPS), which uses a fixed antenna as a reference, can be accurate to within a centimeter. Unfortunately, GPS signals cannot penetrate the water's surface. Thus, various acoustic and inertial techniques have been developed for underwater navigation. Inertial techniques include accelerometers, like those popular in gaming consoles, and gyroscopic compasses that can determine position by judging how the vehicle is moving relative to the Earth. One acoustic technique available, known as "long-baseline," uses the distances to fixed sound sources, determined from the time it takes the sound to reach the receiver, to triangulate to the receiver's position. Another popular acoustic technique, called "ultra-short baseline" navigation, measures the arrival of a single incoming signal using several hydrophones (underwater microphones) positioned on the same vehicle.

The research team's navigation technique differs from the baseline techniques because the signal coming out of the beacon itself varies with aspect, thus only a single hydrophone is required. Consider the pattern of concentric circles made on the surface of a pond after a pebble is tossed in. These peaks and troughs are known as wave fronts and they travel out from a central source at a fixed speed. Under the water's surface, sound waves can easily be made to form circular wave fronts, analogous to the pebble in the pond. The research team developed another type of wave front, a spiral wave front, where, instead of concentric circles, there is one continuous spiral-shaped front emanating from the source. Figure 4 shows a spiral wave front and its source collocated with a circular wave front. Note in this figure that the distance between the circular and spiral wave fronts does not change along a particular direction. Thus, if a hydrophone is placed at some position around the beacon, the aspect angle relative to the beacon can be determined by comparing the arrival of the different wave fronts. This navigation technique is also used by aircraft navigation and is called VHF Omnidirectional Range (VOR). However, VOR uses radio signals rather than sound waves.
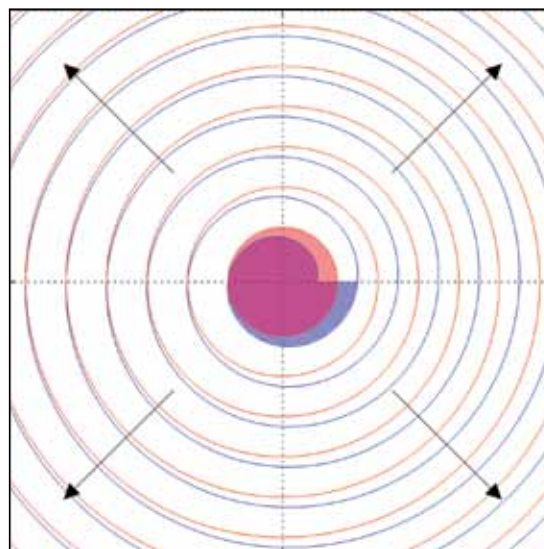
FIGURE 4
Spiral wave front beacon generating circular wave fronts in blue and a spiral wave front in red.

Testing on a Radio-Controlled Boat: Thomas Howarth at the Naval Undersea Warfare Center in Newport, Rhode Island, built a beacon based on this concept. To test the accuracy of the beacon, it is attached to a dock on a pond about 3 m below the water's surface at the Naval Surface Warfare Center in Panama City, Florida. A remote-controlled (RC) pontoon boat is equipped with a hydrophone below the water's surface to determine aspect from the spiral wave front beacon, and a GPS antenna above the surface deter-
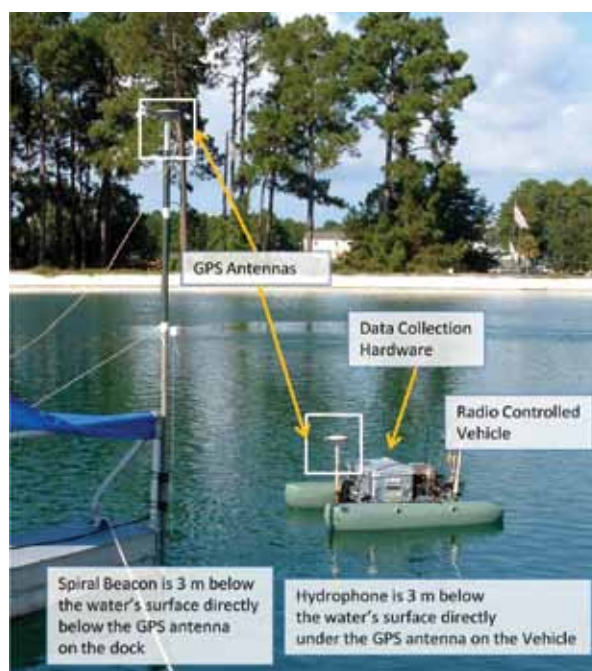
FIGURE 5
Photo of the experimental setup.

Green Line and Circle: path and current position of RC boat
Red Arrow: true aspect from DGPS
Blue Arrow: aspect from spiral beacon

FIGURE 6
Plot showing the position of the RC boat with aspect determination from both the spiral wave front beacon and differential GPS. The green line indicates earlier vehicle positions.
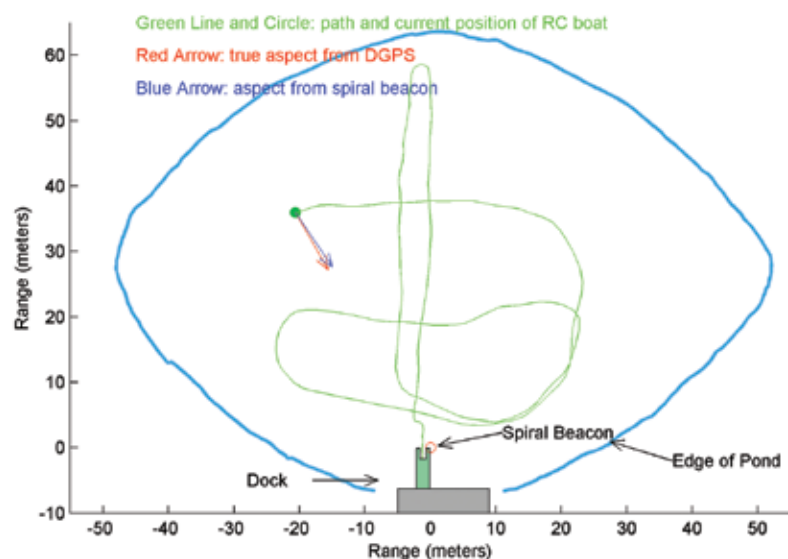
mines aspect using DGPS (see Fig. 5). The RC boat is piloted around a pond and aspect determination from the spiral wave front beacon is compared to the DGPS result. The system takes data from both systems every 2 s. A single measurement is plotted in Fig. 6. The result shows the position of the RC boat and arrows to depict the aspect to the beacon using both the spiral wave front beacon results and the DGPS results. Although not as good as the DGPS results, the beacon is quite accurate, giving an error between 5 and 15 degrees across all of the data. Several different signal processing schemes were tested, some of which worked better in different conditions than others.

The biggest advantage of this system over more traditional baseline techniques is simplicity. A single stationary beacon can be used to navigate any number of remote underwater vehicles. The remote vehicles need only have a single hydrophone available, and can even repurpose one from its sonar or acoustic communications system. With future visions of swarms of underwater vehicles, this can be a huge advantage.

[Sponsored by ONR]

■

Analysis of the Elasticity of Fibrous Brain Structures Using Sound

A.J. Romano and B.H. Houston
Acoustics Division

Background: The noninvasive evaluation of the elastic properties of the human brain is a very active area of research. This is a promising method of analysis in the sense that if the material properties of the brain can be determined with accuracy, they may provide a valuable metric for the evaluation of its state of health. It has been demonstrated that sound can be used to noninvasively interrogate biological tissues, since the wavelengths of the sound waves in the tissues are directly related to local elastic stiffness values.[1] This method has previously been applied to the brain; however, efforts to date tend to homogenize the brain structures to provide "effective" stiffness and viscoelastic parameters. Here we apply a method that attempts to track waves traveling along white matter pathways such as the cortico-spinal tracts (CST) and the corpus callosum. These structures differ from grey matter in that they are comprised of fiber bundles and can act as waveguides for wave propagation.

Two recent technological breakthroughs enabled the creation of our approach. The first was the development of diffusion tensor imaging (DTI),[2] which provides a mapping of the pathways of fibrous structures based on water perfusion. The second was the development of magnetic resonance elastography (MRE),[1] which provides a measurement of sound waves throughout biological media. Using the fusion of these two measurement methods, we developed an approach called Waveguide Constrained MRE[3] to investigate the elasticity of fibrous structures. Here, we apply this method to the CST of a healthy, 38-year-old male volunteer.

Methods: Waveguide Constrained MRE requires a knowledge of the pathways along which elastic waves may travel and a measurement of the dynamic displacements within the volume surrounding the pathways. Given a knowledge of the position vectors of the pathways, a spatial-spectral filter, in the form of a spatially dependent Radon transform, is applied to the measured displacements in an attempt to identify only
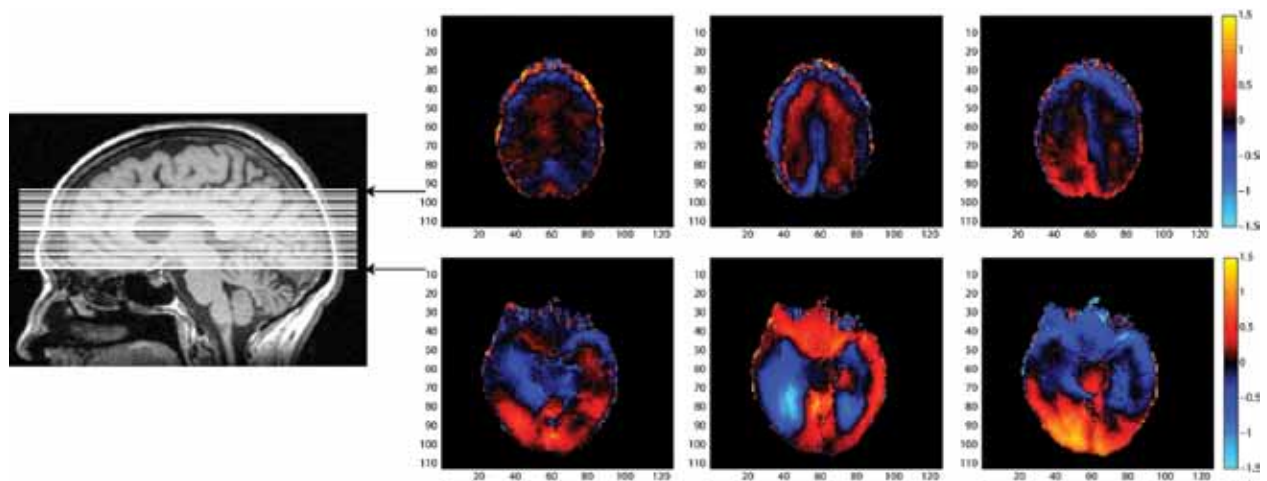
FIGURE 7
MRI of the head and X, Y, and Z displacements at the top and bottom of the field of view.

(a)   (b)   (c)
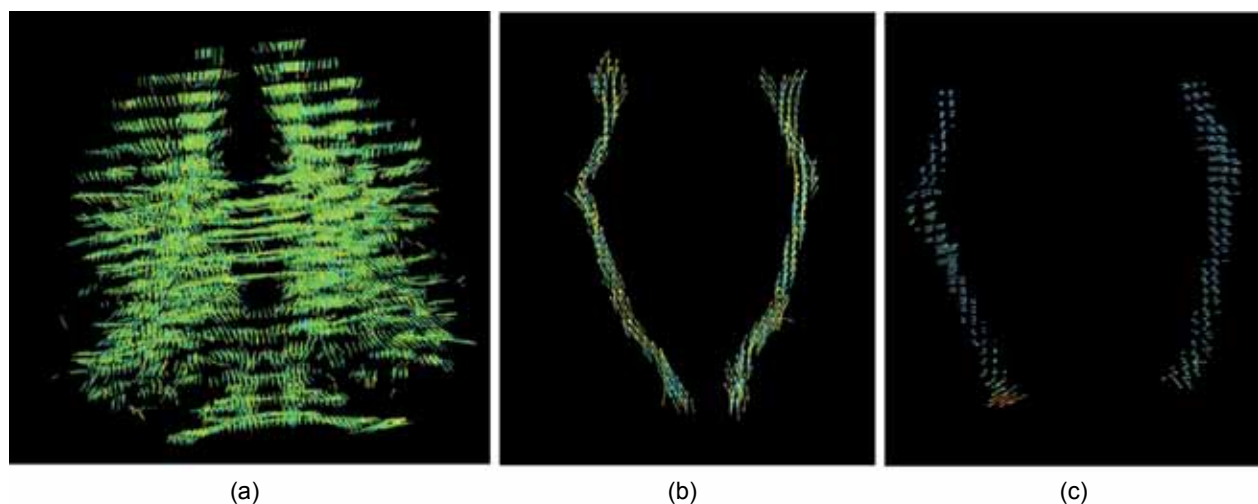
FIGURE 8
(a) DTI of the brain, (b) pathways comprising the CST, and (c) the corresponding filtered shear waves along the CST.

those waves that are traveling parallel along the fiber at every point as if it were a zero-order waveguide mode. Further, a Helmholtz decomposition is performed, which separates the total field into its longitudinal and transverse components. Finally, a sliding window spatial Fourier transform is then applied to these filtered displacements for dispersion analysis, yielding local stiffness values.

For the MRE measurement, the experiment was made using a standard 1.5-T clinical MRI scanner (Siemens, Erlangen, Germany). A head-cradle extended-piston driver was used for 50-Hz harmonic head stimulation. A single-shot spin-echo Echo Planar Imaging (EPI) sequence was used for acquiring three Cartesian components of the wave field in 30 adjacent transversal slices with a 2×2×2 mm³ isotropic image resolution and eight time steps over the vibration period.

For the fiber position measurement, DTI data were acquired using a single-shot EPI sequence with 12 non-colinear directions. Tensor calculation and tractography along the CST were performed using the tools from the FMRIB Software Library (FSL).

Results: In Fig. 7, we show the MRI of the head as well as the positions of the X, Y, and Z displacement components on the top and bottom of the field of view. In Fig. 8, we show the results from DTI for an evaluation of the fiber pathways comprising the CST, and we show the results of applying the spatial-spectral filter to the MRE data along the CST fibers. In Fig. 9, we show the results of applying a sliding window spatial Fourier transform along two sample fibers for an evaluation of the local shear stiffness values, C_{44} and C_{55}, within the fiber's local reference frame. While estimates for
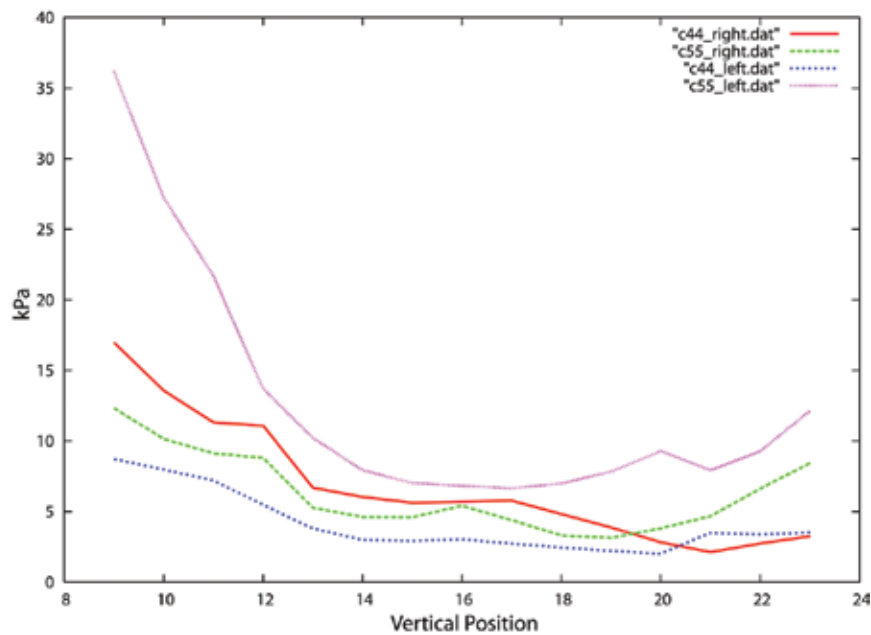
FIGURE 9
Stiffness values for elastic coefficients C_44 and C_55 within the right and left CST.

brain stiffness vary considerably in the literature, average values of around 2 kPa have been reported for the mean shear modulus within slices of healthy samples that include both grey and white matter. Here, the shear stiffness values along the white matter tracts appear to vary from around 2.5 to 10 kPa (i.e., shear wave velocities vary from 1.58 to 3.16 m/s) and are spatially dependent as we follow along the right and left CST from the bottom to the top of the head, while the compressional waves along the fibers have a much higher wave velocity. Future research will apply this approach to other brain structures and at different frequencies.

References
[1] R. Muthupillai, D.J. Lomas, P.J. Rossman, J.F. Greenleaf, A. Manduca, and R.L. Ehman, "Magnetic Resonance Elastography by Direct Visualization of Propagating Acoustic Strain Waves," *Science* **269**, 1854–1857 (1995).
[2] P.J. Basser, J. Mattiello, and D. Le Bihan, "MR Diffusion Tensor Spectroscopy and Imaging," *Biophys. J.* **66**, 259–267 (1994).
[3] A.J. Romano, P.B. Abraham, P.J. Rossman, J.A. Bucaro, and R.L. Ehman, "Determination and Analysis of Guided Wave Propagation Using Magnetic Resonance Elastography," *Magnetic Resonance in Medicine* **54**, 893–900 (2005).

AN/WLD-1 RMS(O) (2001) — NRL developed and transitioned this oceanographic variant of the Remote Minehunting System semi-submersible UUV by developing a swappable center section equipped with hydrographic survey sensors.

Atmospheric Science and Technology

Next-Generation Air–Ocean–Wave Coupled Ocean/Atmosphere Mesoscale Prediction System (COAMPS)

S. Chen,[1] T.J. Campbell,[2] S. Gaberšek,[3] H. Jin,[1] and R.M. Hodur[4]
[1]Marine Meteorology Division
[2]Oceanography Division
[3]University Corporation for Atmospheric Research
[4]SAIC, Monterey, California

Introduction: A team of NRL scientists from the Marine Meteorology and Oceanography Divisions has successfully transformed the one-way air–ocean Coupled Ocean/Atmosphere Mesoscale Prediction System (COAMPS®*) into a six-way fully coupled air–ocean–wave weather and marine forecasting system. This was accomplished using the state-of-the-art Earth System Modeling Framework (ESMF), making COAMPS the first limited area model to utilize ESMF in an effort to seamlessly couple multiple, individually skillful models into one flexible, coherent modeling system. The components used here consist of the COAMPS atmospheric model, the Navy Coastal Ocean Model (NCOM), two interchangeable wave models — Simulating WAves Nearshore (SWAN) and WAVEWATCH III — and a new air–sea coupler developed at NRL that surmounted many of the technical challenges that arose during the development of the coupled system. A mechanism was implemented in the air–sea coupler to support interoperable inter-exchange of two different wave models and different wave feedbacks to the ocean and atmosphere, a feature that enhances the capability of the coupled system to adapt new components. Additionally, special atmospheric, ocean, and wave hurricane observations were obtained to investigate and validate the sensitivity of hurricane intensity and track change in the forecast system due to various coupling processes.

Coupling Methods: A fully coupled air–sea–wave model can provide a natural mechanism for frequent two-way feedback between the air–ocean, air–wave, and ocean–wave components. Figure 1 shows the variety of model variables that are exchanged between each set of coupled components over the course of the coupled time-step. As illustrated in the figure, the atmospheric component provides a total of six ocean surface boundary forcing fields to the ocean component, while the ocean model returns a new sea surface temperature to the atmosphere that influences the next time-step prediction of the atmospheric surface fluxes

*COAMPS is a registered trademark of the Naval Research Laboratory.
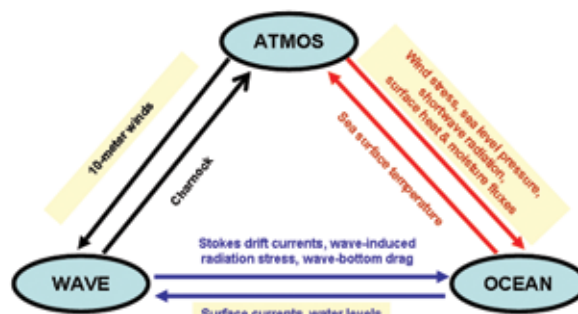
FIGURE 1
A schematic diagram of COAMPS six-way coupling between the atmospheric, ocean, and wave models and the fields that are exchanged between each pair of components.

and wind stress. The ocean component also provides the current and sea surface height to the wave component, while the atmospheric component impacts the waves through the wind-driven momentum drag. The feedback of the wave component to the ocean consists of 10 forcing terms, including the Stokes drift current, wave radiation stress gradients, wave-bottom current, and wave-bottom current radian frequency. The wave component feedback to the atmosphere consists of a nondimensional roughness length (Charnock number), which is related to the atmospheric momentum drag.

Hurricane Forecast Assessment: The prestorm ocean conditions, such as the warm or cold eddies along a hurricane track, influence the rapid intensity change of a hurricane. Additionally, a hurricane can induce a trailing ocean cold wake anomaly (up to several
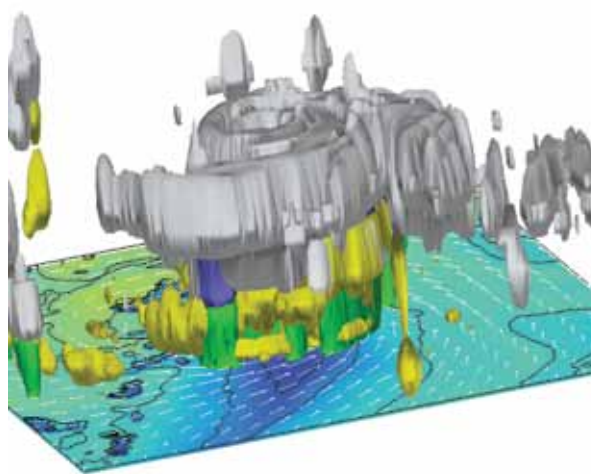
FIGURE 2
Six-way coupled COAMPS 48-h simulation of Hurricane Frances (2004). The figure shows the 0.1 kg/kg isosurface plots of cloud (yellow), ice (white), rain (green), and graupel (purple) mixing ratio. The color shading is the sea surface temperature with darker shade of blue depicting the cooling beneath the hurricane. The white arrows represent the 10-m wind (m/s). The view is from the southeast flank of the storm.

FIGURE 3
Comparisons of COAMPS simulated Hurricane Katrina (2005) significant wave height (m) without the currents forcing in the SWAN wave model (left panel) and the significant wave height difference between the run with the current and the run without the current (right panel). The red arrows are the surface currents. Note that the wave heights in the front right quadrant of the storm are reduced in this five-way coupled run. This is the result of currents being in the same direction of the surface wave packet propagation, which tends to increase the wave packet speed and decreases the wave heights.

degrees) that tends to form preferentially to the right of the storm track and can extend hundreds of kilometers to the rear of the storm, shown by our 48-h simulation in Fig. 2. This intriguing feature is important both for its immediate impact on the storm evolution as well as longer-term climatic impacts to changes in the ocean heat storage below the thermocline. To examine the impact of this feature on the tropical cyclone (TC) simulation in the model, the team performed a series of runs to evaluate the impact of coupling vs no coupling on two mature category 4 and 5 hurricanes, Katrina (2005) and Frances (2004). We compared the atmospheric model prediction of the hurricane track, intensity, and gale force wind radii; the ocean model prediction of the hurricane-induced cold ocean wake; and the surface wave model prediction of the significant wave height and period with the available observations. Among the most important findings are the following. First, two-way air–ocean coupling developed a cold ocean wake that acted to reduce the intensity of the simulated storm. This weakening was manifested by an increased asymmetry in the hurricane secondary circulation and expansion of the eye wall. Second, it was discovered that the horizontal advection of the near-surface cold ocean water contributed to the upper-ocean cooling and weakening of the hurricane as much as the vertical mixing and upwelling.[1] These new results show that the magnitude and size of the trailing ocean cold wake cannot be fully represented by coupling with simple one-dimensional mixed layer models only. Third, including the ocean current and water level forcing in the wave model reduced the hurricane-induced significant wave height bias in the front right quadrant of the storm (Fig. 3). This may have important implications for improving the maximum forecasted surge heights that

tend to be found in this quadrant of the storm. Finally, the 48-h intensity and track differences between the uncoupled and various coupled runs (one-to six-way coupling) were found to be as large as 18 m/s and 10 nautical miles, respectively. Further experiments are required to determine if this is typical for other tropical cyclones that form in other parts of the world as well.

Summary and Conclusions: Validation of the two-way coupling between the atmosphere and ocean only also showed forecast improvements in a variety of non-hurricane atmosphere and ocean phenomena.[2] With the new coupling capability in COAMPS, NRL scientists can now conduct a wider range of new research applications to further the understanding of the air–sea interaction processes that are of the utmost importance to the Navy.

References
[1] S. Chen, T.J. Campbell, H. Jin, S. Gaberšek, R.M. Hodur, and P. Martin, "Effect of Two-way Air–Sea Coupling in High and Low Wind Speed Regimes," *Mon. Wea. Rev.* **138**, 3579–3602 (2010).
[2] R.A. Allard, T.J. Campbell, R.J. Small, T.A. Smith, T.G. Jensen, S. Chen, J.A. Cummings, J.D. Doyle, X. Hong, and S.N. Carroll, "Validation Test Report for the Coupled Ocean Atmospheric Mesoscale Prediction System (COAMPS), Version 5," NRL/MR/7322--10-9283, Naval Research Laboratory, (2010).

New Ocean Wind Capability from Space

T.F. Lee,[1] M.H. Bettenhausen,[2] and J.D. Hawkins[1]
[1] *Marine Meteorology Division*
[2] *Remote Sensing Division*

Introduction: WindSat is a satellite-based polarimetric microwave radiometer designed and developed by the Naval Research Laboratory Remote Sensing Division and the Naval Center for Space Technology.[1] WindSat was launched in 2003 to demonstrate the capability of polarimetric microwave radiometry to measure the ocean surface wind vector from space. This demonstration has been highly successful, enabling WindSat data to be used operationally for weather forecasting (for example, to monitor tropical cyclone structure worldwide) and as input to numerical weather prediction models of the U.S. Navy, the U.S. National Oceanic and Atmospheric Administration (NOAA), and the United Kingdom Met Office.

The NRL WindSat ocean retrieval algorithm is an optimal estimation algorithm for retrieving the ocean surface wind vector and sea surface temperature from WindSat measurements.[2] The WindSat measurements represent a combination of microwave energy emitted and reflected from the Earth's surface and absorption and emission of the microwave energy as it propagates through the atmosphere. The algorithm also retrieves columnar atmospheric water vapor and columnar atmospheric cloud liquid water (CLW). We use a physically based forward model for the WindSat measurements that couples a one-layer atmospheric model with a sea surface emissivity model that accounts for wind-induced roughness and sea surface foam. The optimization algorithm adjusts the retrieved parameters to match the WindSat measurements. Near-real-time examples of WindSat products appear at http://www.nrl.navy.mil/WindSat/.

Forecasting Case Examples: Figure 4, which shows a cold front off the west coast of the U.S., illustrates the characteristic shift of winds from the southwest equatorward of a cold frontal band (white) to northwest poleward of the frontal band. Wind speeds (WS) throughout the image are generally from 20 to 30 kt with some higher speeds in the vicinity of the front. The convergence of winds along the front is, in part, what produces the upward motion responsible for the cloud band. Shades of gray indicate vertically integrated quantities of CLW from 0.0 (black) to 0.5 mm (white). White values without overplotted vectors indicate unavailable retrievals due to precipitation. Where black vectors are plotted on top of white, retrievals should be examined more closely for consistency. Similar retrievals are assimilated into numerical weather prediction models.

WindSat wind plots are used routinely by a variety of responsible agencies for routine reconnaissance of tropical cyclones. While heavy rain and clouds often prevent wind retrieval of the strongest winds near the central core of storms, useful wind information is still often observed in adjacent areas. Figure 5, which shows the WindSat vectors derived from Hurricane Earl, shows near-hurricane force winds of approximately 60 kt near the storm center in a large cloud-free (nearly black) region. While CLW amounts are too great for wind retrieval over most of the interior of the storm
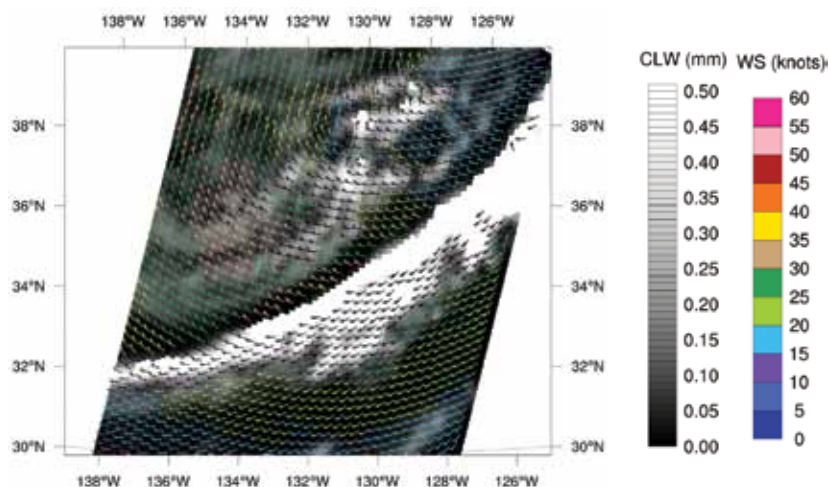
FIGURE 4
Frontal system off California, December 29, 2003. White indicates potential rain contamination of vector accuracy. Colored vectors show wind speed and direction; black vectors should be examined further for reliability.
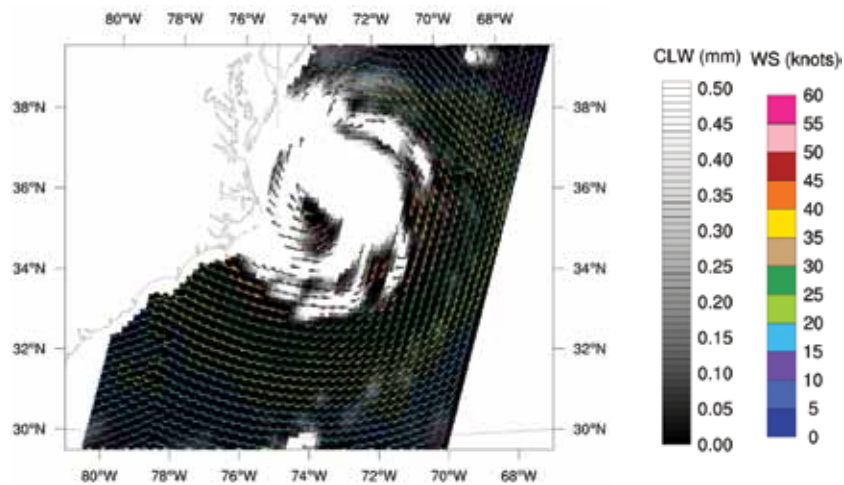
FIGURE 5
Hurricane Earl off the east coast of the United States, September 3, 2010. White indicates potential rain contamination of vector accuracy.
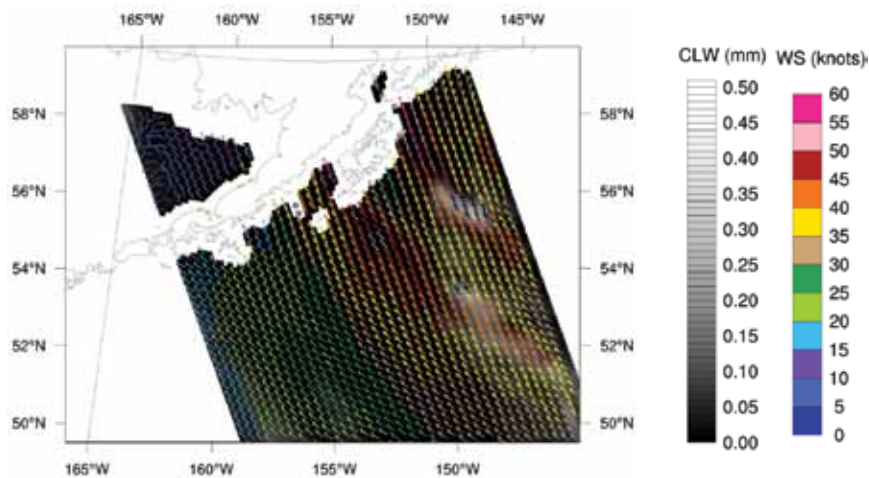
FIGURE 6
Gap winds south of Alaska, November 30, 2010.

(white without vectors), on the periphery of the storm where CLW is absent or reduced (black or gray), the vectors reveal a counterclockwise circulation. Remotely sensed winds from hurricane hunter airplane flights observed at nearly the same time show a strong correspondence to the winds observed by WindSat.

While WindSat cannot retrieve winds closer than 35 km from the coast, orographically induced wind systems can often be observed beyond this threshold and sometimes well out to sea (Fig. 6). High wind events south of Alaska often originate within coastal terrain gaps to produce accelerated low-level jets moving over the ocean. In Fig. 6, two major "gap winds" appear on either side of Kodiak Island (red and orange). Maximum wind speeds in each gap are about 55 kt from the north-northwest. "Safe harbor" conditions appear just south of Kodiak Island with winds at about 25 kt (green).

Conclusions: WindSat has pioneered an important new remote sensing technique for retrieving high quality winds over the world's oceans. Similar wind vector products have been available for about a decade from instruments known as scatterometers. They use an "active" strategy, whereby an onboard power supply releases periodic microwave pulses and processes the return from the ocean surface. Scatterometers have certain advantages over polarimetric instruments, including less sensitivity to precipitation and the capacity for retrievals closer to coastlines. However, the key advantage of polarimetric radiometers is that they can be used to retrieve CLW, atmospheric water vapor, and precipitation. All three are important for assessing the marine environment. In particular, CLW is crucial for assessing the accuracy of wind retrievals. Ideally, passive and active instruments can be used together to improve spatial and temporal wind vector coverage.

References

[1] P.W. Gaiser, K.M. St Germain, E.M. Twarog, G.A. Poe, W. Purdy, D. Richardson, W. Grossman, W.L. Jones, D. Spencer, G. Golba, J. Cleveland, L. Choy, R.M. Bevilacqua, and P.S. Chang, "The WindSat Spaceborne Polarimetric Microwave Radiometer: Sensor Description and Early Orbit Performance," *IEEE Trans. Geosci. Rem. Sens.* **42**, 2347–2361 (2004).

[2] M.H. Bettenhausen, C.K. Smith, R.M. Bevilacqua, N.-Y. Wang, P.W. Gaiser, and S. Cox, "A Nonlinear Optimization Algorithm for WindSat Wind Vector Retrievals," *IEEE Trans. Geosci. Rem. Sens.* **44**, 597–610 (2006).

■

Atmospheric Remote Sensing Aboard the International Space Station

S. Budzien and A. Stephan
Space Science Division

Introduction: In October 2009, the Remote Atmospheric and Ionospheric Detection System (RAIDS) experiment entered science operations investigating Earth's thermosphere and ionosphere from a vantage point on the International Space Station (ISS). Built jointly by NRL and The Aerospace Corporation, RAIDS is a suite of eight limb-viewing optical sensors for remote sensing of naturally occurring airglow across the spectrum from extreme-ultraviolet to near-infrared wavelengths (55 to 870 nm). The primary objective of the RAIDS mission is to provide the first global-scale temperature measurements of the lower thermosphere. Additionally, RAIDS is serving as a pathfinder experiment for atmospheric remote sensing aboard the ISS and providing practical insights for using the ISS as a platform for future Navy remote sensing missions.

Atmospheric Observations: The RAIDS experiment is focused on the transition layer from the coldest part of the atmosphere at the mesopause near 85 km up to the hottest regions of the thermosphere above 300 km. The importance of this region connecting lower-atmospheric phenomena to the edge of space and beyond has only recently been recognized. The impact to civilian and DoD systems is well known. Changes in the ionosphere affect operational systems such as GPS navigation, radar, and radio and satellite communication. Variability in thermospheric composition, density, and winds directly affects satellite drag and space debris tracking and influences the development, structure, and variability of the ionosphere. RAIDS is addressing the paucity of global temperature measurements that are needed to cohesively couple lower-atmosphere models and their upper-atmosphere counterparts into

a unified, high-accuracy space weather model that can forecast all these effects.

Airglow measured by RAIDS is produced by excitation of ambient atmospheric gas via solar radiation, charged particle precipitation, and chemical processes. Airglow measurements are interpreted using physical models of excitation and radiative transfer processes to reveal the composition, density, and temperature of the upper atmosphere. RAIDS derives thermospheric temperature from the spectral shape (color) of O_2 "atmospheric band" emission at 760 nm[1] with uncertainties nearing a few Kelvin (Fig. 7). RAIDS temperatures are in agreement with climatology estimated using the NRLMSISE-00 model.[2] In addition to this key result, RAIDS also has provided new data to enhance dayside ionospheric remote sensing techniques and to study the chemically and thermally important minor species nitric oxide.
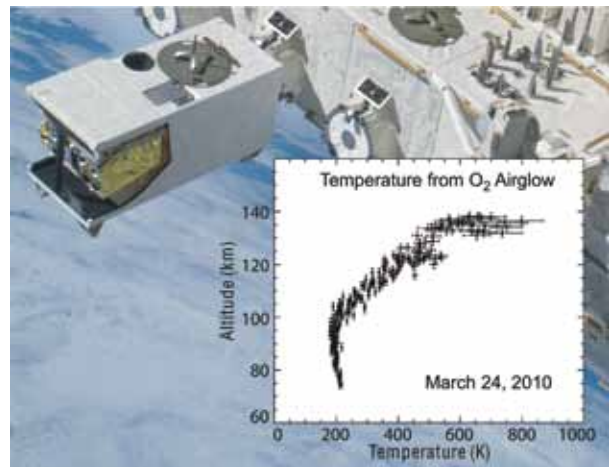
FIGURE 7
The gold-blanketed Remote Atmospheric and Ionospheric Detection System (RAIDS) experiment (top left) views the aft atmospheric limb from the open end of the HICO RAIDS Experiment Payload (HREP) aboard the International Space Station. The inset shows March 24, 2010, neutral temperatures derived from near-infrared O_2 atmospheric band emission. (Photo credit: NASA)

Mission: RAIDS and a companion experiment, NRL's Hyperspectral Imager for Coastal Ocean (HICO), comprise the HICO-RAIDS Experiment Payload (HREP) on the ISS. HREP is a collaborative venture involving the Space Science Division, the Remote Sensing Division, the Naval Center for Space Technology, and the Department of Defense Space Test Program (STP). HREP successfully demonstrated rapid, low-cost space payload development: it was designed, built, and integrated in-house at NRL facilities in only 2 years from design to delivery.

HREP is the first U.S. payload aboard the Japanese Experiment Module (JEM) Exposed Facility (EF).

On September 10, 2009, HREP was launched from Tanegashima, Japan, on the inaugural voyage of the H-IIB rocket and the H-II Transfer Vehicle (HTV), a Japanese unmanned resupply capsule for the ISS. After a week of flight maneuvers and tests, the HTV docked with the ISS. Astronauts used both the main ISS manipulator arm and a smaller arm on the JEM to transfer the modular payloads from the unpressurized section of the HTV to the JEM-EF. HREP was installed on September 24 (Fig. 8), and RAIDS entered science operations after 30 days of commissioning activities.

Using the ISS: The RAIDS team devised several strategies to maximize the science return from this unique platform. The 51.6° inclination and 340 km altitude of the ISS orbit required tailored atmospheric science objectives. Orbital precession enables observations over a range of local time and solar illumination conditions, but also requires brief monthly shutdowns as the orbital plane intersects the Sun. Extensive station structures near the field-of-regard scatter light that must be mitigated through good baffling of optical
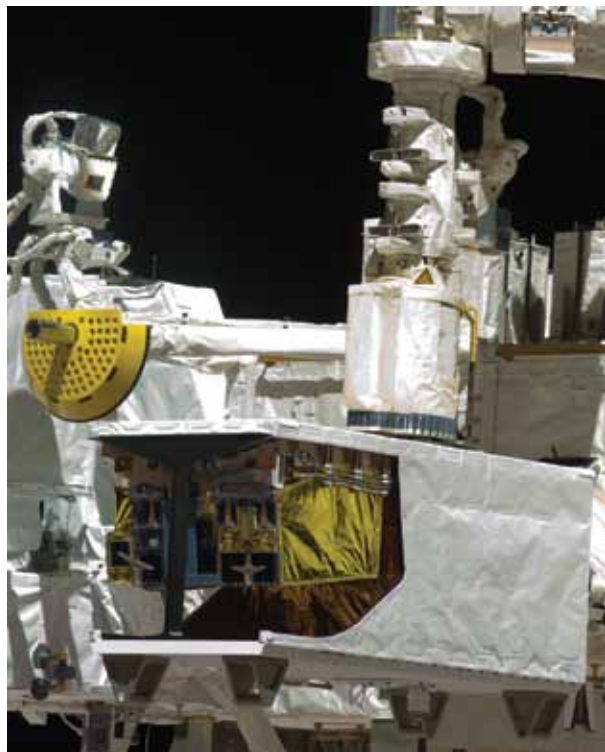
FIGURE 8
HREP (the open-ended white box) is attached to the remote manipulator arm (top) during installation onto the Japanese Experiment Module Exposed Facility. Installation and deinstallation are conducted entirely using robotic or unmanned space systems. (Photo credit: NASA)

sensors. Activities aboard the manned station, including construction work and attitude perturbations from

spacecraft dockings, occasionally disrupt observations. Small ISS pitch oscillations up to ±0.75° per orbit associated with solar array rotation posed a challenge for RAIDS limb measurements; NASA responded by improving the station's attitude stability. Finally, although manned environments are notoriously dirty for contamination-sensitive optical instruments, RAIDS sensors have not exhibited any unusual degradation.

The learning curve for developing effective mission operations was steep, as is expected for a pathfinder mission, but the RAIDS Team has met the challenge. RAIDS is functioning well and meeting its scientific objectives. The RAIDS baseline mission for 1 year could be extended up to 3 years, after which HREP will be removed from the JEM-EF and placed into an empty HTV for disposal by atmospheric reentry. By filling the gap in mid- and low-latitude temperature and composition measurements that exists in currently operating space missions, RAIDS and the ISS have combined to provide a unique, crucial dataset for studying this increasingly relevant region of the upper atmosphere.

References
[1] J.W. Heller, A.B. Christensen, J.H. Yee, and W.E. Sharp, "Mesospheric Temperature Inferred from Daytime Observation of the O_2 Atmospheric (0,0) Band System," *J. Geophys. Res.* **96**(A11), 19,499–19,505 (1991).
[2] J.M. Picone, A.E. Hedin, D.P. Drob, and A.C. Aikin, "NRLMSISE-00 Empirical Model of the Atmosphere: Statistical Comparisons and Scientific Issues," *J. Geophys. Res.* **107**(A12), 1468, (2003), doi:10.1029/2002JA009430.

◼

Geospace Climate Present and Future

J.T. Emmert
Space Science Division

Introduction: It has long been known that the near-Earth space environment responds strongly to variations in the Sun's photon, particle, and magnetic field output. More recently, it has become increasingly apparent that Earth's upper atmosphere and ionosphere are also intricately coupled to the underlying layers of the atmosphere, all the way down to the Earth's surface. It is now clear that a meaningful understanding of geospace behavior — including both climate and weather — cannot be attained except by considering the

atmosphere as a whole system that responds not only to direct solar influences, but also to internal variations and changes of both natural and anthropogenic origin. Research by NRL's Space Science Division is providing new insight into geospace climate and how it is evolving, including the atmospheric system's response to the unusual solar minimum of 2008. This research has significant implications for several applications, including policymaking to mitigate and reduce orbital debris.

Figure 9 depicts the typical structure and composition of Earth's atmosphere. The thermosphere is the operational environment of many satellites, and the
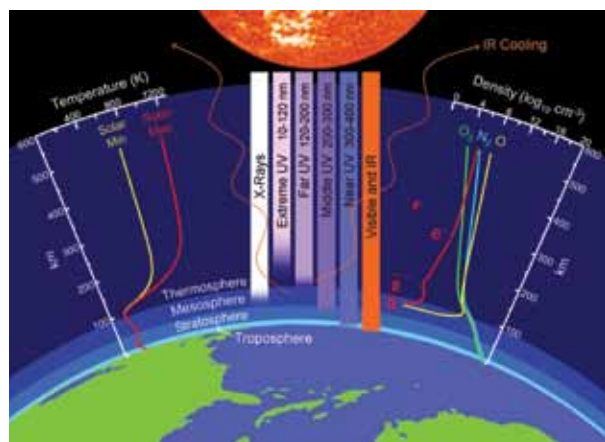
FIGURE 9

Thermal and compositional structure of Earth's atmosphere. The upper atmosphere, comprising the mesosphere, thermosphere, and embedded ionosphere, absorbs all incident solar radiation at wavelengths less than 200 nm. Most of that absorbed radiation is ultimately returned to space via infrared emissions. The plot on the left shows the typical resulting thermal structure of the atmosphere, as specified by the NRLM-SISE-00 empirical model, when the flux of solar radiation is at the minimum and maximum of its 11-year cycle. The plot on the right shows the density of nitrogen (N_2), oxygen (O_2), and monatomic oxygen (O), the three major neutral species in the upper atmosphere, along with the free electron (e^-) density (from the International Reference Ionosphere), which is equal to the combined density of the various ion species. The F, E, and D layers of the ionosphere are also indicated.

embedded ionosphere is an electric medium that fundamentally affects the propagation of radio-frequency communication and navigation signals. This region of the atmosphere is heated and ionized primarily via absorption of solar extreme ultraviolet (EUV) radiation; at high latitudes, energetic particles of solar origin and resistive dissipation of magnetospheric currents are also significant energy sources. Solar EUV irradiance increases by a factor of 2 from the minimum to maximum of an 11-year solar cycle, and the thermosphere responds by heating and expanding. The orbital drag experienced by satellites consequently varies drastically over a solar cycle, as illustrated in Fig. 10.
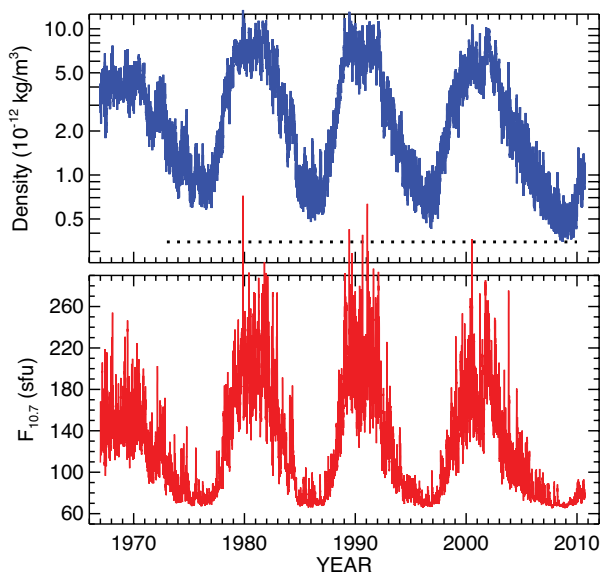
FIGURE 10

(Top) Global-average mass density, derived from the orbits of ~5000 objects, at an altitude of 400 km. The dotted horizontal line indicates the minimum overall density. (Bottom) The daily 10.7 cm solar radio flux ($F_{10.7}$) normalized to 1 AU, in solar flux units (sfu, 10^{-22} W m^{-2} Hz^{-1}). $F_{10.7}$ is a proxy for solar extreme ultraviolet irradiance.

Changing Geospace Climate: The same gases that have been implicated in lower atmospheric climate change also play important roles in the energy balance of the upper atmosphere. CO_2 is the primary cooling agent of the upper mesosphere and thermosphere (where, unlike in the troposphere, the atmosphere is too thin optically to trap infrared radiation emitted by CO_2). Anthropogenic increases in CO_2 propagate into the upper atmosphere, and there are strong theoretical grounds and experimental evidence[1,2] that these increases are causing the upper atmosphere to cool and contract. Some of the changes predicted to occur as a result of greenhouse gas increases have been detected in historical upper atmospheric data, and a coherent picture is beginning to emerge[2,3] (Fig. 11). NRL has contributed significantly to the study of geospace climate change by analyzing the orbital decay rates of thousands of low-Earth-orbit (LEO) objects covering the past 40 years; the results indicate that, after accounting for solar influences, thermospheric density at fixed heights has been decreasing at a rate of 2% to 5% per decade.[4]

There are also natural sources of geospace climate change. Long-term variations in the Sun's photon, particle, and magnetic field output will directly affect the structure and climate of the upper atmosphere. Secular changes in the geomagnetic field will further alter the distribution of plasma and the location and intensity of ionospheric currents. Because the state of the upper atmosphere responds strongly to solar drivers, both an-
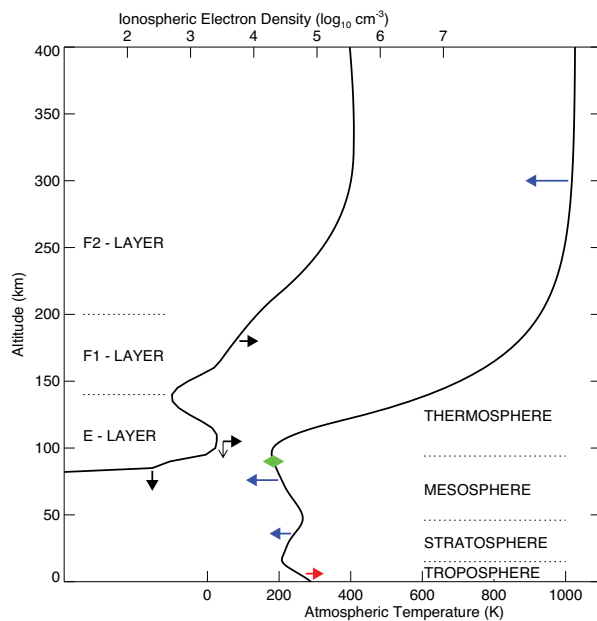
FIGURE 11
Qualitative summary of observed long-term trends in the atmosphere and ionosphere. Orbital drag studies at NRL and other institutions indicate a decrease in thermospheric temperature. A large body of research demonstrates temperature increases in the lower troposphere, decreases in the stratosphere and mesosphere, and no significant change near the mesopause (the boundary between the mesosphere and thermosphere). Electron densities in the E and F1 layers of the ionosphere have increased, and the heights of the E layer and the bottomside ionosphere have lowered. This qualitative picture is consistent with the predicted effects of CO_2 and O_3 changes in the atmosphere.

thropogenic and natural climate changes of terrestrial origin will, to varying degrees, depend on the phase of the solar cycle. Conversely, any terrestrial-driven climate change is expected to alter how the upper atmosphere responds to solar variations.

The exceptionally quiescent 2008 solar minimum, which had the greatest number of days without sunspots since the 1933 minimum, has provided a valuable opportunity to better understand this interplay between solar and lower atmospheric influences on geospace climate. An initial NRL study determined that thermospheric mass density was lower in 2008 than at any time since the beginning of the Space Age, and 30% lower than during the previous solar minimum[5] (see Fig. 10). The unusually quiet Sun can account for some of this reduction, as can record-high levels of atmospheric CO_2, but the state of the thermosphere during the past few years is still poorly understood and is an active research topic at NRL and other institutions. Besides contributing to the unusual behavior of the thermosphere, the quietness of the Sun has also facilitated discovery of previously unrecognized connections between the lower atmosphere and the space environ-

ment; in one such connection, dynamical events in the polar stratosphere can alter the electron content of the low-latitude ionosphere by up to 100%.[6]

Implications for Orbital Debris: The anthropogenic and natural evolution of geospace climate will have a profound effect on the LEO debris population because atmospheric drag is currently the only effective mechanism by which debris is removed from orbit. Of the 16,000 objects in the active satellite catalog (which only includes objects larger than 10 cm), 12,000 are debris or expended rocket bodies. The greatest density of debris is found between 500 and 1100 km altitude, where removal by atmospheric drag can take from 25 years to centuries. Recent studies have found that even without any new launches, the amount of debris in LEO will increase via collisional fragmentation faster than it is removed from orbit by atmospheric drag.[7] Active debris removal (ADR) strategies are therefore being explored by the international space community, but it is not clear how geospace climate change may affect these strategies. An initial study by researchers at the University of Southampton suggests that when potential long-term contraction of the thermosphere is taken into account, the effectiveness of ADR is dramatically reduced, thereby increasing the costs of achieving a stable debris population within the next hundred years.[8] In addition to long-term contraction, anomalous reductions in thermospheric density, such as occurred unexpectedly during the recent solar minimum, may also adversely affect efforts to control debris growth.

[Sponsored by ONR and NASA]

References
[1] R.G. Roble and R.E. Dickinson, "How Will Changes in Carbon Dioxide and Methane Modify the Mean Structure of the Mesosphere and Thermosphere?" *Geophys. Res. Lett.* **16**, 1441–1444 (1989).
[2] J. Laštovička, R.A. Akmaev, G. Beig, J. Bremer, J.T. Emmert, C. Jacobi, M.J. Jarvis, G. Nedoluha, Y.I. Portnyagin, and T. Ulich, "Emerging Pattern of Global Change in the Upper Atmosphere and Ionosphere," *Ann. Geophys.* **26**, 1255–1268 (2008).
[3] J. Laštovička, R.A. Akmaev, G. Beig, J. Bremer, and J.T. Emmert, "Global Change in the Upper Atmosphere," *Science* **314**, 1253–1254 (2006).
[4] J.T. Emmert, J.M. Picone, and R.R. Meier, "Thermospheric Global Average Density Trends, 1967–2007, Derived from Orbits of 5000 Near-Earth Objects," *Geophys. Res. Lett.* **35**, L05101 (2008), doi:10.1029/2007GL032809.
[5] J.T. Emmert, J.L. Lean, and J.M. Picone, "Record-Low Thermospheric Density during the 2008 Solar Minimum," *Geophys. Res. Lett.* **37**, L12102 (2010), doi:10.1029/2010GL043671.
[6] L.P. Goncharenko, A.J. Coster, J.L. Chau, and C.E. Valladares, "Impact of Sudden Stratospheric Warmings on Equatorial Ionization Anomaly," *J. Geophys. Res.* **115**, A00G07 (2010), doi:10.1029/2010JA015400.
[7] J.-C. Liou and N.L. Johnson, "Instability of the Present LEO Satellite Populations," *Adv. Space Res.* **41**, 1046–1053 (2008).

[8] H.G. Lewis, A. Saunders, G. Swinerd, and R. Newland, "Understanding the Consequences of a Long-Term Decline in Thermospheric Density on the Near-Earth Space Debris Environment," 6th IAGA/ICMA/CAWSES Workshop on Long-Term Changes and Trends in the Atmosphere, Boulder, Colorado, June 2010.

■

Chemical/Biochemical Research

Polaris (1955) — NRL participated extensively in the
conceptual planning and development of the submarine-
launched Polaris missile.

High-Durability Organosiloxane Nonskid Coatings

J. Martin, E. Lemieux, E.B. Iezzi, J. Tagert, J. Wegand, and P. Slebodnick
Chemistry Division

Introduction: The 2006 Cost of Corrosion Study issued by the Office of the Secretary of Defense (OSD) identified nonskid decking coatings as one of the Fleet's "top five" cost drivers. The Navy installs nearly 3.7 million square feet of the nonskid coatings at a cost of roughly $56.6 million per year. This is because the average life expectancy of traditional epoxy-based nonskid coating is at best 18 months.

The Office of Naval Research's (ONR) Future Naval Capability Program, together with NAVSEA's Capital Investment for Labor (CI-Labor) Program – Nonskid Initiative, aims to improve the state of the art of available nonskid coatings and materials. As the technical lead for ONR and NAVSEA, the Naval Research Laboratory is striving to extend the service life of Navy nonskid systems. This includes identifying or developing and testing next-generation non-epoxy alternatives for extended-durability flight and general deck performance, and addressing heat-resistant issues associated with current and future vertical launch aircraft requirements.

Currently, the Navy's traditional (MIL-PRF-24667) nonskid coatings are composed of an epoxy and an amine component, which are mixed together and applied over an anticorrosive deck primer. The coating is roll-applied to the deck using a phenolic roller to create a rough "peak and valley" profile, thereby providing a frictional surface that prevents the sliding or skidding of crew members, aircraft, storage containers, and machinery. To provide this aggressive profile, these coatings usually contain aluminum oxide or aluminum metal aggregate for general purposes areas (Type-G) or landing areas (Type-L), respectively. Typical MIL-PRF-24667 nonskid coatings are also modified with fillers (such as silicas, talc, and calcium carbonate) and thickening agents to yield a specified impact resistance and viscosity. Improper mixing of the two components, poor application, insufficient cleaning of the deck primer, outright lack of deck primer, as well as environmental/operating conditions, can all lead to premature or catastrophic failures, such as coating disbondment, corrosion seepage due to the cracks in the nonskid coating, and loss of slip resistance. Although the majority of these issues are examples of installer-related problems, the main problem with current nonskid technology is that the epoxy and amine components are not engineered to withstand the external environmental conditions that the U.S. Navy routinely encounters.

The epoxy component of traditional nonskid coatings is composed of aromatic epoxy resins, whereas the amine component is primarily composed of polyamine and/or amidoamine resins. Aromatic epoxy resins, which provide good hardness and chemical resistance, are notorious for degrading rapidly when exposed to external weathering conditions including UV radiation and oxygen. These resins are intended for use on internal structures, such as ballast tanks or floor primers, and are rarely used for the external coating of structures by the coating industry. As for the amine component, amidoamine resins contain chromophores that absorb external radiation and cause yellowing. The amide groups also impart high levels of hydrogen bonding, thereby increasing the level of solvent required to use the resin in a coating. Furthermore, polyamine and amidoamine resins can frequently cause "blushing," which is a reaction with CO_2 and water that creates an insoluble white film on the surface of the nonskid coatings.

Technology Description: Hybrid coating technology based on the incorporation of silicone-based resins with nonaromatic epoxy or amine chemistries can provide better performance characteristics than traditional coatings because silicone–oxygen bonds are much stronger than the carbon–carbon, carbon–hydrogen, or nitrogen–hydrogen bonds that are found in traditional nonskid coatings, not to mention the elimination of aromatic moieties that absorb UV radiation and easily degrade. This increased bond strength of siloxane groups leads to greater external durability because the silicone–oxygen bonds are already oxidized and do not absorb UV radiation, thereby extending the life of a coating and preventing the rapid chalking, fading, and cracking that occur with conventional nonskid formulations.

At the Naval Research Laboratory, we have recently formulated a novel siloxane-based nonskid coating (Fig. 1) that provides greater external durability, color retention, and chemical resistance than traditional

FIGURE 1
Close-up view of NRL's siloxane nonskid coating (rolled version).
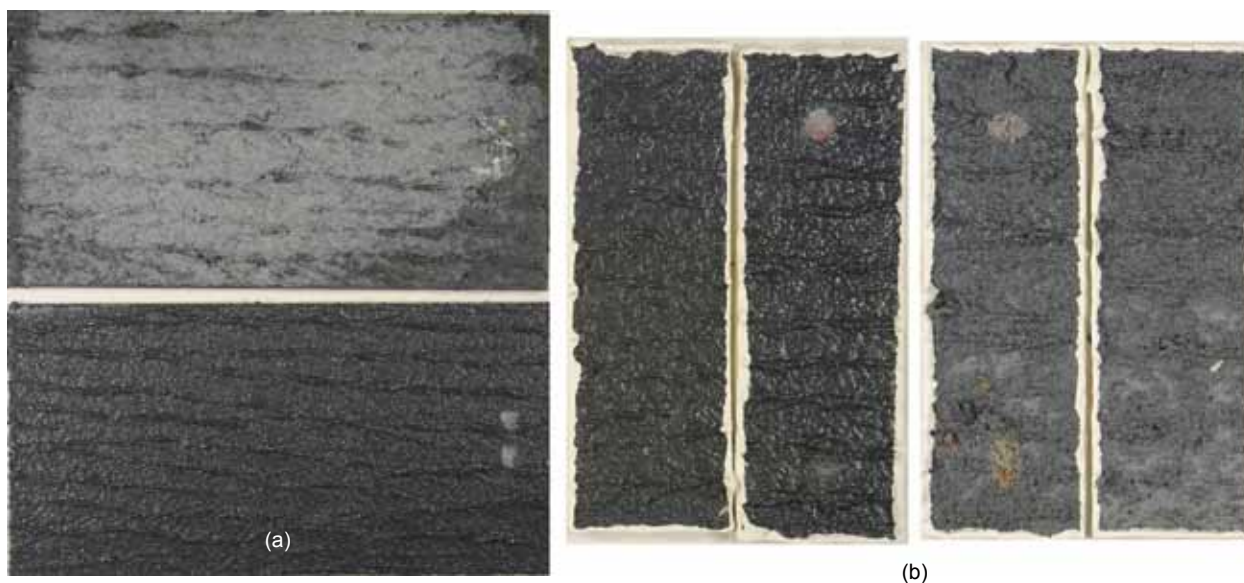
FIGURE 2
(a) NRL's siloxane nonskid (bottom) vs a commercial composition G epoxy (top) after 400 hours QUV-B exposure. (b) NRL's siloxane nonskid (left) vs a commercial epoxy (right) after 28 days of detergent immersion.

epoxy nonskid coatings. The newly developed coating can be applied over a primed surface or directly to clean and blasted steel, and applicators have the option of spraying or rolling the material. When subjected to numerous MIL-PRF-24667 tests, the siloxane nonskid coating greatly outperformed a traditional qualified nonskid epoxy coating, especially with regard to UV and chemical resistance (Fig. 2).

Technology Scale-Up and Demonstrations: To expedite technology transition to the Fleet, NRL is directly working with a Navy approved coatings supplier to produce production batches and work out system scale-up issues. The siloxane nonskid has been

FIGURE 3
NRL's siloxane nonskid (right) vs a commercial epoxy nonskid (left) after 6 months exposure on USS *Mason*. The commercial nonskid was dark blue when initially applied.

scaled-up to produce batches of over 160 gallons, thus allowing NRL to perform field demonstrations on several Norfolk, Virginia–based ships. For instance, the first trial occurred on USS *Ponce* in April 2010, where 50 gallons of siloxane nonskid was roll-applied on the 03 level – Aux Conn Station. Since then, both roll and spray trials have occurred on USS *Oak Hill* (May 2010), USS *Whidbey Island* (June 2010), USS *Mason* (June 2010), USS *Ramage* (August 2010), and USS *Cole* (December 2010). Figure 3 shows the siloxane nonskid adjacent to a traditional epoxy nonskid on the deck of USS *Mason*. One can easily see how after six months of exterior exposure, the traditional material has faded and begun to degrade, whereas the siloxane nonskid is color-fast and in nearly pristine condition.

Technology Cost and Product Characteristics: Currently, the cost of the siloxane nonskid is roughly $100 per gallon, or $500 for a 5 gallon kit (as supplied), whereas qualified Navy nonskid coatings range from $70 to $80 per gallon. However, it should be noted that this is not the final cost of the product, as price is based on manufactured volume and amount sold. When roll-applying the product, coverage is approximately 20 to 25 square feet per gallon. This number increases to approximately 45 square feet per gallon when spray application is used. It is anticipated that both application processes will be employed by the Fleet in the future; however, due to flight deck performance requirements, the roll application may be retained exclusively for aircraft carrier flight deck applications, whereas spray application may be employed for general traffic locations and rotary wing flight decks. It is anticipated that

the unit cost of the material will be significantly reduced as more material is specified for application in the Fleet when the product becomes approved for Navy use in the Qualified Product Database.

[Sponsored by ONR]

■

Advanced Trace Explosives Detection Testbed

S. Rose-Pehrsson,[1] R. Colton,[1] G. Collins,[1] B. Giordano,[1] D. Rogers,[1] M. Hammond,[1] C. Tamanaha,[1] C. Field,[1] M. Malito,[2] and R. Jeffries[2]
1Chemistry Division
2Nova Research, Inc.

Introduction: The Department of Defense (DoD) and the Department of Homeland Security (DHS) need improved explosives detection systems to protect personnel and platforms from attack from insurgents and terrorists both at home and abroad. Therefore, research is under way for the development of new materials and sensors for explosives vapor detection. However, uniform, reliable methods for evaluating new detection systems are limited, making assessment of the new products difficult. Drawing from much experience in hazardous chemical vapor generation and detection, the Naval Research Laboratory's Chemistry Division has developed a comprehensive testbed for trace explosives vapor generation and assessment of sensor technology.[1]

A multidisciplinary team of scientists and engineers from the Chemistry Division came together to design and construct the state-of-the-art trace explosives detection testbed, shown in Fig. 4, which facilitates the development and evaluation of advanced trace explosives detection technologies. The testbed is a fully automated

FIGURE 4
Advanced Trace Explosives Detection System Testbed with touch screen GUI.

system using NRL-developed custom software that is controlled by a touch screen graphical user interface (GUI). Six sample ports are available for individual or multiple, simultaneous testing of novel sensors and materials. The testbed consists of SilcoNert™-treated stainless steel gas lines, a custom mixer, and a dual distribution manifold (see Fig. 5) enclosed in a custom oven, which can operate at temperatures up to 150 °C. The dual manifold was designed to permit rapid switching
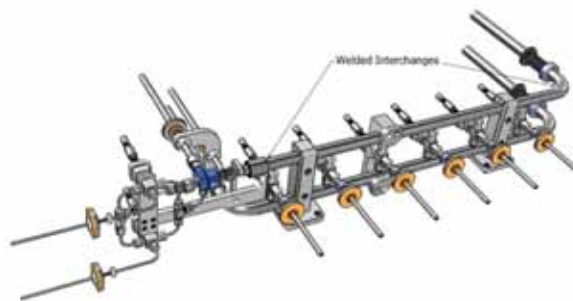
FIGURE 5
Dual manifold with six sample ports.

between clean air and the analyte sources, via computer-controlled actuators that drive custom feed-throughs to open and close all valves. All oven-enclosed components are bakeout-compatible, but the manifold may be easily exchanged with a duplicate manifold to prevent any possibility of cross contamination between different explosive analytes. The testbed employs a zero-grade air source with temperature and humidity control, and vapor generation systems for comprehensive testing of trace levels of explosives and potential interferents.

The touch screen interface allows a user to control and monitor all system components, enabling a wide variety of test conditions including different vapor concentrations, test mixtures, and test durations. Standard and custom test protocols are easily developed and implemented. The system was designed to enable the implementation of test protocols developed by any testbed-equipped laboratory, facilitating interagency sensor/material research collaborations and accelerating the validation of prototype commercial systems.

Custom sensor chambers, as shown in Fig. 6, were designed for evaluating materials and sensors. The Impactor Sample Chamber accommodates a variety of sensor types, directs the test vapor directly onto the sensor, and can be individually heated. An online verification system that uses a thermal desorption/gas chromatography/mass spectrometry/electron capture detector has also been incorporated into the testbed. The testbed was analytically characterized using both TNT and RDX for concentrations from parts per trillion (ppt) to parts per billion (ppb) in humid air from
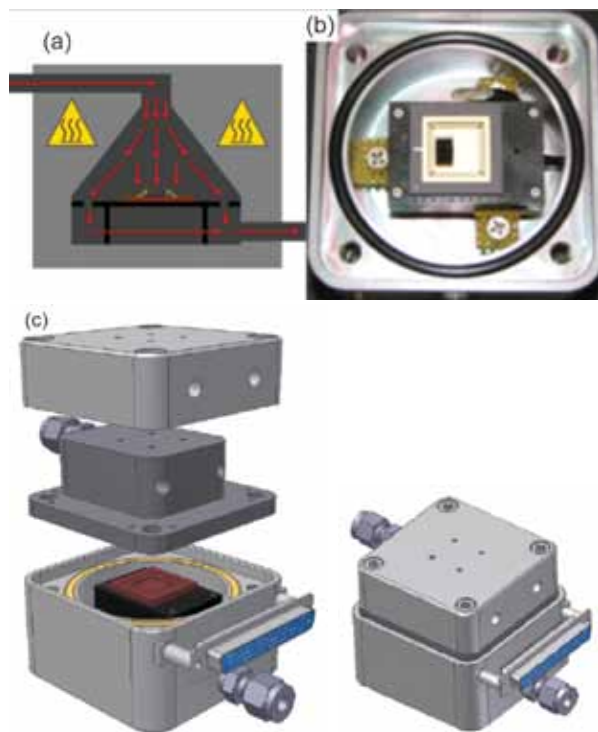
FIGURE 6
(a) Schematic of the Impactor Sample Chamber with the red arrows indicating the gas flow into the chamber, onto the sensor, and out to the exhaust. (b) A prototype sensor array mounted in a pin grid array and loaded into the Impactor Sample Chamber. Electrical connections to the device are made through the packaging and the zero insertion force (ZIF) socket (black). (c) Impactor Sample Chamber.

20% to 85% relative humidity (RH). Consistent results were observed at all six sample ports.

The NRL testbed is the only one of its kind in the world to provide quantitative results for explosive vapors over such a wide concentration range. NRL is using the testbed to evaluate sensor systems under development in the Chemistry Division. We expect to use the system to evaluate new materials and sensors being developed by DHS in the future. A second testbed was constructed and delivered to the Transportation Security Laboratory for evaluating new detection systems of interest to DHS. The concepts used for the DHS testbed were applied to the development of another testbed using large domes to provide uniform vapors over a large area for the evaluation of entire instruments or arrays of sensors. Both testbeds are now being expanded to include more threats and potential interferents. The Advanced Trace Explosives Detection System will allow DoD and DHS to assess technologies in a consistent manner, thus providing our troops and TSA personnel the best technologies to safeguard personnel and platforms.

Reference
[1] "NRL/DHS/TSL Advanced Trace Explosive Detection Testbed, Operations Manual," NRL/PU/6180--10-544, Naval Research Laboratory, September 2010.

■

Highly Conductive Molecular Wires for Electronic, Sensing, and Energy-Converting Devices

N. Lebedev,[1] S.A. Trammell,[1] S. Tsoi,[1] G.S. Kedziora,[2] I. Griva,[3] and J. Schnur[3]
[1]*Center for Bio/Molecular Science and Engineering*
[2]*High Performance Technologies*
[3]*George Mason University*

Introduction: The construction of highly efficient molecular electronic, sensing, and energy-converting devices requires a high rate of signal transduction between molecules and electrodes. One of the promising molecules in the construction of these devices is oligo(phenylene vinylene), OPV. This molecule can be considered as a graphene ribbon with an extremely narrow width approaching the single phenyl ring. The molecule has delocalized molecular orbitals and performs efficient electron transfer (ET) at various conditions. However, OPV has a relatively large highest-occupied-molecular orbital/lowest-unoccupied-molecular orbital (HOMO-LUMO) band gap with molecular orbitals located far from the electrode Fermi level and thus requires the application of high bias voltages for the generation of current. To achieve efficient ET between a molecule and an electrode at low bias voltages, one needs a molecule that has an electronic energy level near the electrode Fermi level.

A New Conductive Molecule with a Low Band Gap and a High Level of Electron Delocalization: To solve the problem, we synthesized a new molecule, oligo(phenylene vinylene) quinone, OPVQ, having OPV as the main component and a quinone with two oxygen atoms as an end group (Fig. 7). The molecule has a planar configuration allowing for efficient sp^2 hybridization and molecular orbital (MO) delocalization through the entire structure, and shows highly efficient conductivity at low biases in electrochemical and scanning tunneling microscopy (STM) measurements.[1,2]
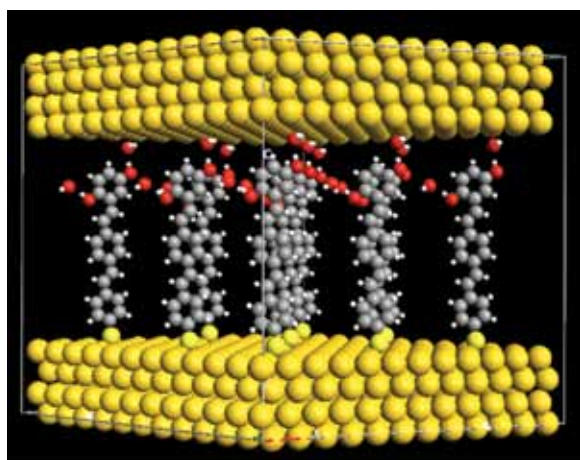
FIGURE 7
Model of the reduced and protonated form of OPVQH molecular wires including water between two gold electrodes.

The Narrow Transmission Band: The origin of the high conductivity of OPVQ lies in its molecular electronic structure and the electron transmission spectrum (ETS). The unique feature of OPVQ is the presence of a narrow transmission band near the gold electrode Fermi level (Fig. 8). This band has a Lorentzian shape and indicates extremely high rates of ET, 9.73e12 and 2.26e12 s^{-1}, to the left and right electrode, respectively.[3] The position of the band in the energy spectrum is very stable and only slightly shifts under either positive or negative bias without substantial changing of its width. In addition, no change in the band intensity under different bias voltages was observed.[3]

The Spatial Distribution of Electrostatic Potential: The discovered effect of the two oxygen atoms on the

molecular conductivity is due to the spatial distribution of electrostatic potential at the molecule–electrode junction (Fig. 9). At zero bias, the potential profile has two barriers of different width located between the sulfur atom and the carbon ring at one contact and between the quinone ring and the right electrode at the other contact. In addition, the profile shows that oxygen atoms generate a field in the surrounding molecule area that forms a local negative barrier, which prevents a uniform potential distribution in the space between the electrodes. Application of a small bias between electrodes (0.4 V, more negative at the left electrode) completely eliminates the potential barrier between the molecule and the left electrode and changes the spatial distribution of the electrostatic potential allowing for efficient ET to the molecule from the right electrode. Now the molecule is in equilibrium with the left electrode, and this electrode determines the potential of the molecule. Such distribution of the potential does not

FIGURE 8
Electron transmission spectra (a) and energy spectra (b) for Au|OPVQ Au (red) and Au|OPV Au (green) junctions.
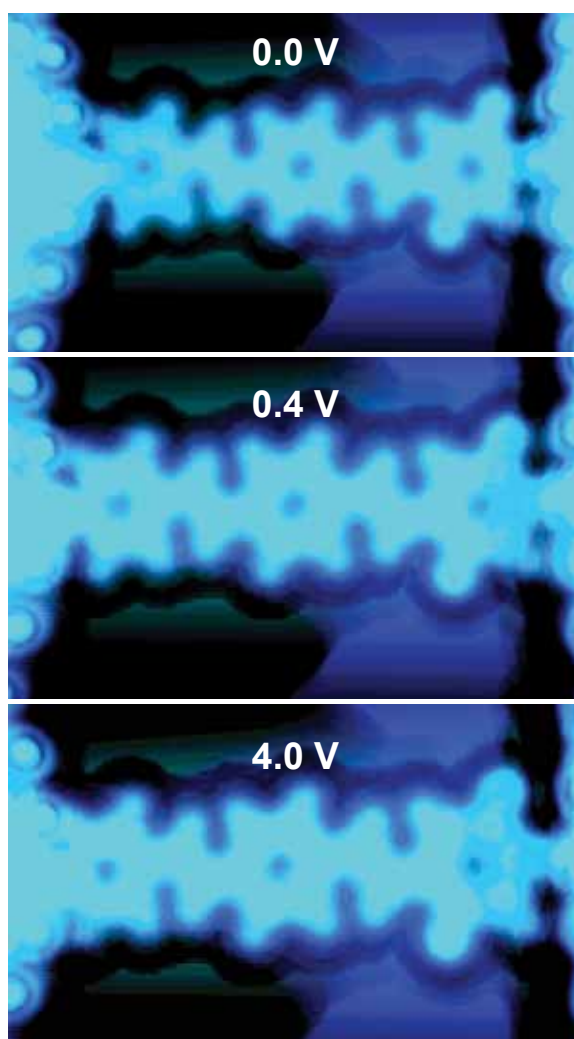
FIGURE 9
Real space effective potential for Au|OPVQ Au junction at biases = 0.0, 0.4, and 4.0 V (from top to bottom).
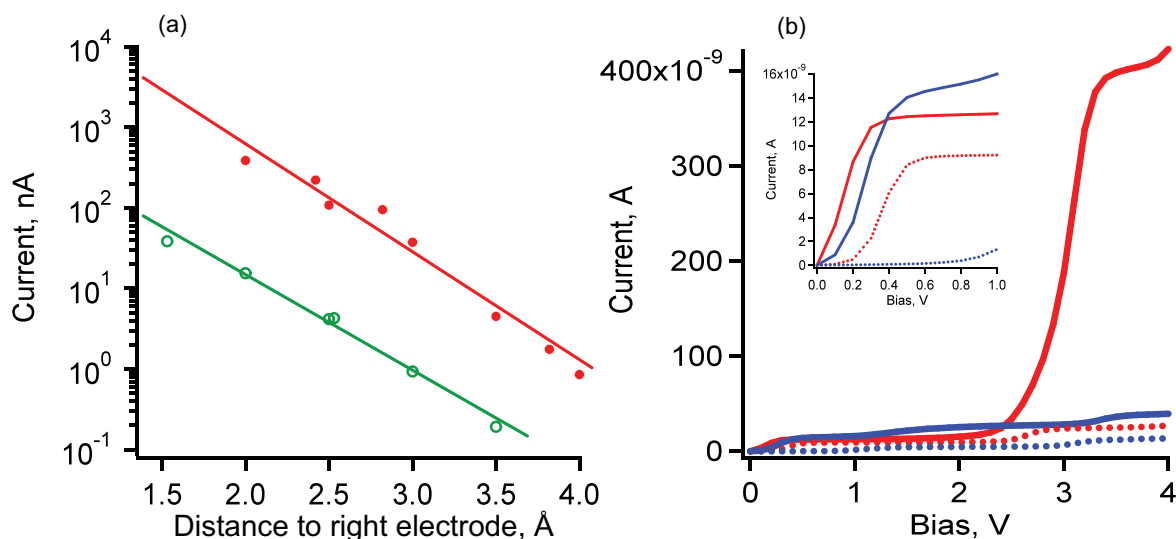
FIGURE 10
(a) Dependence of the current through Au|OPVQ Au (red) and Au|OPV Au junctions (green) on the distance between the molecule and the right electrode. Bias voltage = 0.4 V. Rings are the calculated data and the line is the linear fit. (b) I-V curves for the conductivity of OPVQ (red) and OPVQH (blue) between two gold electrodes in the absence (dashed) and presence (solid) of water. The distance between the electrodes is 25 Å. The current intensity at low biases is shown in the inset.

alter upon further increasing the bias. In addition, the potential profile shows the presence of a valley near one of the carbon atoms of the quinone ring that possibly specifies the main electron flow pathway through this carbon atom to the right electrode.

Distance Attenuation Factor: The tunneling through space is one of the most crucial factors determining the efficiency of molecular electronic devices. The current through OPVQ at increasing distances between the molecules and the electrode exponentially reduces with the decay attenuation factor $\beta = 2.69$ Å^{-1} (Fig. 10(a)). OPV shows the same slope and a similar distance attenuation factor, but the current is about 100 times lower. Extrapolation of the fitted curve to 1.4 Å distance between the OPVQ and the electrode (corresponding to a single carbon chemical bond) approaches the theoretical limit of molecular conductance (1 G$_0$). Thus, being chemically bound to both electrodes, the OPVQ should have a conductance close to the quantum limit.[3]

Electrochemical Conductance Switching: One of the most interesting features of the constructed molecule is the possibility of reverse-switching its molecular conductance by changing the electrochemical potential of the surrounding medium (electrochemical conductance switching).[2] Our electrochemical STM experiments show that the reduction-protonation of OPVQ is reversible and can be done many times without changing the conductance efficiency.[4] The electron transmission spectra show that the effect is due to appearance and disappearance of the narrow transmission band

around the Fermi level, which is typical for OPVQ, and is missing from OPVQH.

Long-Range Electron Transfer Through Water Molecules: Water molecules are a very important component in any chem/bio-sensing device.[5] The ET spectra of oxidized and reduced forms of OPVQ reveal that water molecules stabilize and improve conductivity through the narrow transmission band. In addition, the water molecules induce the formation of new strong transmission bands below the Fermi level leading to the appearance of additional p-type conductivity channels.[5] These effects of water lead to substantial changes in the I-V curves. For dry molecules at low source-drain biases (at about 0.4 V), the conductivity nearly turns off when the molecule is reduced-protonated (Fig. 10(b), inset). Instead, for wet devices at these biases, the reduced-protonated molecule has conductivity higher than the oxidized one. At biases between 3 and 4 V, when additional ET paths through water molecules become operational, the difference in conductivity for the wet configuration will be orders of magnitude (Fig. 10(b)). In addition to the increasing efficiency, the direct interaction of water molecules with OPVQ changes the pathway of ET, potentially allowing for its redirection.

Summary: Electron transfer at the organic–inorganic interface is a major roadblock in the construction of efficient chemical and biological sensing, soft optoelectronic, and energy-converting devices. We have shown that the problem can be overcome by the construction of innovative molecules with the efficient

electron delocalization and precise positioning of electron acceptor groups that allow for the efficient control of spatial charge distribution, and electron tunneling through space and solvent located between the molecule and the electrode. Our experimental and simulation results demonstrate that the conductance through the constructed molecules is highly efficient, coherent, and can achieve the theoretical limit of molecular conductance.

References

[1] S.A. Trammell, D.S. Seferos, M. Moore, D.A. Lowy, G.C. Bazan, J.G. Kushmerick, and N. Lebedev, "Rapid Proton-coupled Electron-transfer of Hydroquinone Through Phenylenevinylene Bridges," *Langmuir* **23**(2), 942–948 (2007), doi:10.1021/la061555w.

[2] S. Tsoi, I. Griva, S.A. Trammell, A.S. Blum, J.M. Schnur, and N. Lebedev, "Electrochemically Controlled Conductance Switching in a Single Molecule: Quinone-modified Oligo(phenylene vinylene)," *ACS Nano* **2**(6), 1289–1295 (2008).

[3] N. Lebedev, I. Griva, S.A. Trammell, G.S. Kedziora, L.M. Tender, and J. Schnur, "On the Role of Oxygen in the Formation of Electron Transmission Channels in Oligo(phenylene vinylene) Quinone Molecular Conductance," *J. Phys. Chem. C* **114**(28), 12341–12345 (2010), doi:10.1021/jp1031042.

[4] S. Tsoi, I. Griva, S.A. Trammell, G. Kedziora, J.M. Schnur, and N. Lebedev, "Observation of Two Discrete Conductivity States in Quinone-oligo(phenylene vinylene)," *Nanotechnology* **21**(8) (2010), doi:10.188/0957-4484/21/8/085704.

[5] N. Lebedev, I. Griva, G.S. Kedziora, A. Blom, and J.M. Schnur, "The Effect of Water on Electron Transfer Through Conductive Oligo(phenylene vinylene) Quinones," *J. Phys. Chem. C* **114**(51), 22710–22717 (2010), doi:10.1021/jp108868z.

■

Electronics and Electromagnetics

FLYRT (1993) — The FLYing Radar Target RF-distraction decoy flew at ship-like speeds following launch from a shipboard chaff launcher. The fiber optic gyroscope provided highly accurate angle rate data.

Full-Wave Characterization of Wavelength-Scaled Phased Arrays

R.W. Kindt
Radar Division

Introduction: Ultra-wideband antenna arrays achieve operation over bandwidths of 4:1 or more. These arrays are traditionally costly due to high element counts. Wavelength-scaled arrays (WSAs) have the same aperture size and bandwidth as traditional ultra-wideband arrays, but have significantly fewer elements. Using scaled elements of three different sizes, an 8:1 bandwidth WSA has fewer than 18% of the original element count. Due to the finite array complexity, powerful new computational tools based on the domain decomposition–finite element method (DD-FEM) with nonmatching grids have been developed to accurately model the WSA architecture. These simulation tools can model structures 1000 times more complex than previously possible. Prior to building expensive hardware, it is now possible to use full-wave characterization of phased array systems to very accurately predict and correct electromagnetic performance, thereby reducing implementation costs and significantly increasing the chance that hardware will operate as desired when deployed.

Full-Wave Simulation Tools: Phased array design typically begins with full-wave electromagnetic simulation tools that can predict exactly how electromagnetic structures perform. The finite element method (FEM) is a popular full-wave analysis technique for modeling electromagnetic structures such as antennas. Because full-wave tools like FEM are exact, they are computationally expensive, such that solving even electrically small objects (such as a single antenna) can require a significant amount of resources. Although modeling complete finite arrays has typically proven too difficult, future Navy platforms require accurate electromagnetic analysis of interference between many multifunction phased array apertures integrated into a common deck house. In order to improve the capacity of FEM for solving large multiscale electromagnetic problems such as this, researchers at NRL (in collaboration with the University of Massachusetts) have been working on domain decomposition techniques for FEM based on new Robin transmission conditions. This divide-and-conquer technique allows previously unsolvable problems (such as large finite phased arrays) to be split into smaller, easily solvable components that are coupled by these new boundary conditions. With this powerful technique, the domain decomposition–finite element method, a simpler, modular analysis approach is followed. With DD-FEM, rather than attempting to model large sections of Navy vessels with embedded phased array apertures as a single system of equations (which may not be computationally possible), modular components of the structure can be analyzed independently and then accurately coupled to each other, even if the grids at the interface between components do not match. While this research is ongoing, NRL has developed reliable in-house DD-FEM design tools that are currently being used to model electromagnetic interference and coupling (EMI/EMC) on ship platform configurations 1000 times more complex than previously possible.[1]

Wavelength-Scaled Arrays: The goal of the Office of Naval Research's Integrated Topside program is to reduce the proliferation of topside antennas and their associated mutual interference by integrating the many current separate antenna systems into a smaller set of wideband phased array apertures.[2] Because of excessive element counts combined with a high cost for electronics per array element, large wideband phased arrays can be prohibitively expensive. While the cost factor is somewhat offset by the fact that several antenna systems can be combined into a single aperture, in many cases the antennas being replaced are relatively inexpensive reflector-based systems. Because of the potential benefits in driving down the large number of onboard antennas and improving system flexibility, the Navy has considerable interest in reducing the cost of wideband phased array systems. Efforts to reduce the cost of phased arrays are mainly being directed at less expensive hardware. However, another approach currently being pursued at the Naval Research Laboratory is aimed at lowering cost by reducing total element count. The WSA architecture is being tested with this goal.[3] Based on the assumption that the multifunction aperture is oversampled at the low end of the frequency spectrum and has more than adequate aperture area to form beams at high frequencies, the wavelength-scaled array architecture uses elements of different scales to significantly alter the aperture layout to better match the required aperture utilization. Using scaled elements of three different sizes, an 8:1 bandwidth WSA has fewer than 18% of the original element count. Further, the subsequent aperture thinning results in additional space on the back side of the aperture, mitigating the need for ultra-miniaturized electronic packaging. Because of the asymmetry in the WSA aperture, the usual infinite-cell design tools cannot be employed to predict the performance of the array, and the large electrical size of the finite arrays means that analysis is beyond the capability of existing full-wave computational tools. To accurately predict the performance of the WSA, the structures must be evaluated using rigorous full-wave DD-FEM tools. Based on successful paper studies of
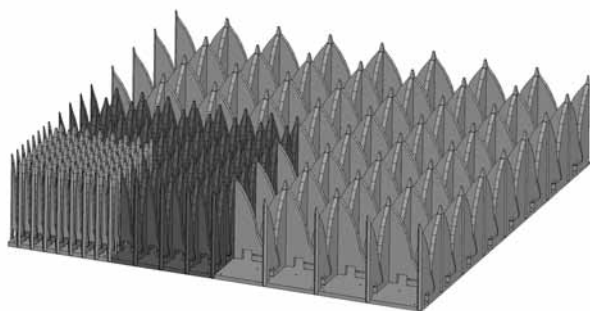
FIGURE 1
Model for a prototype 1–8 GHz wavelength-scaled array of flared notches; the array operates over an 8:1 bandwidth and uses three levels of element scaling to achieve a 6.4:1 reduction in element count.
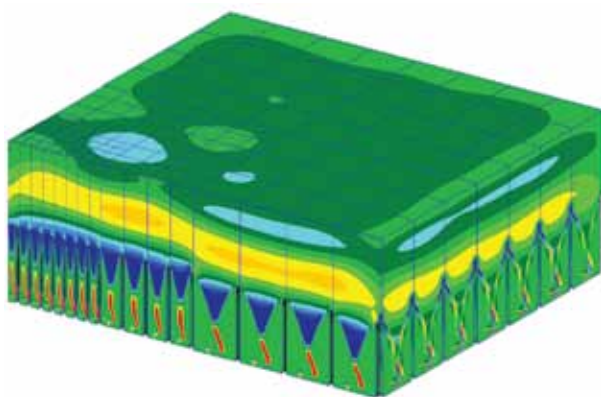
FIGURE 2
Full-wave electromagnetic simulation of the prototype WSA hardware. The complexity of the array structure is such that commercially available simulation tools are not powerful enough to perform the analysis. In-house modeling tools based on DD-FEM were developed to model complex array structures such as the WSA.
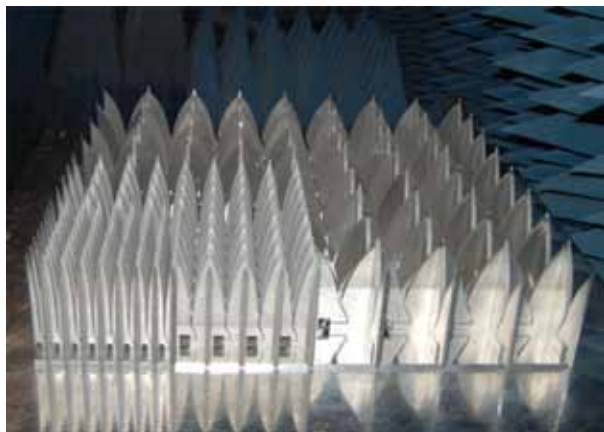
FIGURE 3
Actual prototype WSA hardware. Measurements of the prototype hardware compare favorably with full-wave electromagnetic simulations.

finite WSA architectures,[4] proof-of-concept hardware has been designed (Fig. 1), electromagnetically modeled (Fig. 2), built (Fig. 3), and tested, and NRL has applied for patents on this technology. For the initial prototype, flared-notch radiators were selected due to the combination of ultra-wide bandwidths and low VSWR levels.

[Sponsored by NRL and ONR]

References
[1] R.W. Kindt and M.N. Vouvakis, "Analysis of Wavelength-Scaled Array Architectures via Domain Decomposition Techniques for Finite Arrays," ICEAA '09 International Conference on Electromagnetics in Advanced Applications, Sept. 14–18, 2009, pp. 196–199.
[2] "InTop Program: U.S. Navy Develops Open RF Architecture for Future Platforms," *Defense Industry Daily*, March 2010, available at http://www.defenseindustrydaily.com/Navy-Awards-18-Contracts-for-RF-Communication-Technologies-for-Future-Platforms-05448/ (accessed May 18, 2010).
[3] R.W. Kindt and G. Tavik, "Wavelength-Scaled Ultra-Wide Bandwidth Multi-Function Phased Arrays," presented at 2010 IEEE International Conference on Wireless Information Technology and Systems, Honolulu, Hawaii, 2010.
[4] R.W. Kindt and M.N. Vouvakis, "Analysis of a Wavelength-Scaled Array (WSA) Architecture," *IEEE Trans. Antennas Propag.* **58**(9), 2866–2874 (2010).

Spectral Nulling of Radar Waveforms

T. Higgins and A. Shackelford
Radar Division

Introduction: The radio frequency (RF) spectrum available for radar operation is becoming increasingly crowded due to high demand for spectrum usage rights by the communications industry coupled with demand for wider bandwidths for radar applications. Consequently, techniques enabling radar systems to avoid interfering with other nearby narrowband RF systems are desired for future naval radars. Conceptually, a radar could, in real time, sense the RF environment in which it is operating, determine the frequency and bandwidth characteristics of other users, and adapt its transmitted waveform to avoid interference with other users of the spectrum.

The Radar Division has developed several techniques to achieve spectrally nulled radar waveforms using phase-only weighting techniques. Varying only the phase of the radar waveform (as opposed to amplitude and phase) is critical because it ensures that the adapted waveforms can be transmitted efficiently by standard saturated power amplifiers. In this article, we discuss experimental validation of these techniques for two different types of radar waveforms: stepped-frequency

(SF) waveforms and linear frequency modulation waveforms. In both cases, the spectral null is generated via a small phase perturbation of the radar waveform by a polyphase coded sequence.

Spectral Nulling Methods: Stepped-frequency waveforms transmit a burst of multiple narrowband pulses, each at a different center frequency, to synthesize wider bandwidth. The spectral null is generated by applying a unique phase coding to each pulse within the burst, creating the stepped-frequency polyphase code (SFPC) waveform.[1] To further improve performance, pulses with a center frequency near the desired spectral notch can be omitted. The second method of frequency nulling considered is applicable to linear frequency modulated (LFM) waveforms, which are commonly used in a variety of radar applications. The null is generated by modifying the phase of the LFM waveform via a phase-only weighting that has been optimized to produce a null at the desired location.[2]

Experimental Results: The SFPC and phase coded LFM (PC-LFM) waveforms are generated with a vector signal generator and recorded using a real-time spectrum analyzer for offline analysis. The thinned spectrum waveforms are compared to unperturbed waveforms to assess the performance of each approach.

The SFPC waveform is created from a burst of 10 pulses with a frequency step of 1 MHz, yielding a combined bandwidth of 10 MHz spanning from 3.5 to 3.51 GHz. The individual pulse width is 1 μs, resulting in a burst time of 10 μs. Two cases are examined: an in-band spectral null at 3.5015 GHz, and an out-of-band spectral null at 3.5115 GHz. For the first waveform, pulses two and three are removed due to their proximity to the desired spectral null. Figure 4(a) displays the results of the SFPC waveform as well as the original SF burst (with pulses two and three omitted). The spectral

notch is measured to be 48.5 dB below the original waveform. The case for the out-of-band null (3.5115 GHz) is shown in Fig. 4(b), where the depth of the notch relative to the original waveform is 25 dB.

The LFM waveform is created using the same parameters as the previous case: 10 MHz bandwidth and 10 μs pulse duration. A phase perturbation is applied to the waveform to produce a spectral notch at 3.5015 GHz. Figure 5 illustrates the performance of the PC-LFM waveform. The in-band null depth relative to the unperturbed LFM is 51 dB. The relative depth for the out-of-band-null is 32 dB, as seen in Fig. 5(b). Interestingly, the nulls are much narrower for the PC-LFM waveform than was observed for the SFPC waveform. This is due to the longer temporal extent of the phase coded sequence used to create the notch in the PC-LFM waveform. The phase-coded sequence for the SFPC waveform applied to each of the 10 pulses in the burst was only 1 μs long, whereas the coded sequence for the LFM was applied to the entire waveform (10 μs duration).

Radar Performance: The experimental results presented in the previous section are promising from the standpoint of interference mitigation. However, degradation in radar performance as a result of modifying the transmitted waveform must also be assessed for the techniques to be considered viable. As a metric, we compare the pulse-compressed output of the nulled waveforms relative to their unperturbed counterparts. The pulse compression outputs of the spectrally nulled waveforms (in-band nulls) shown in Figs. 4(a) and 5(a) are depicted in Figs. 6(a) and 6(b), respectively. The spectral nulling has almost no effect on the SFPC waveform, but the range sidelobes of the PC-LFM waveform are increased (as seen in Fig. 6(b)) relative to the LFM waveform. This slight degradation in performance may be acceptable in many radar applications.
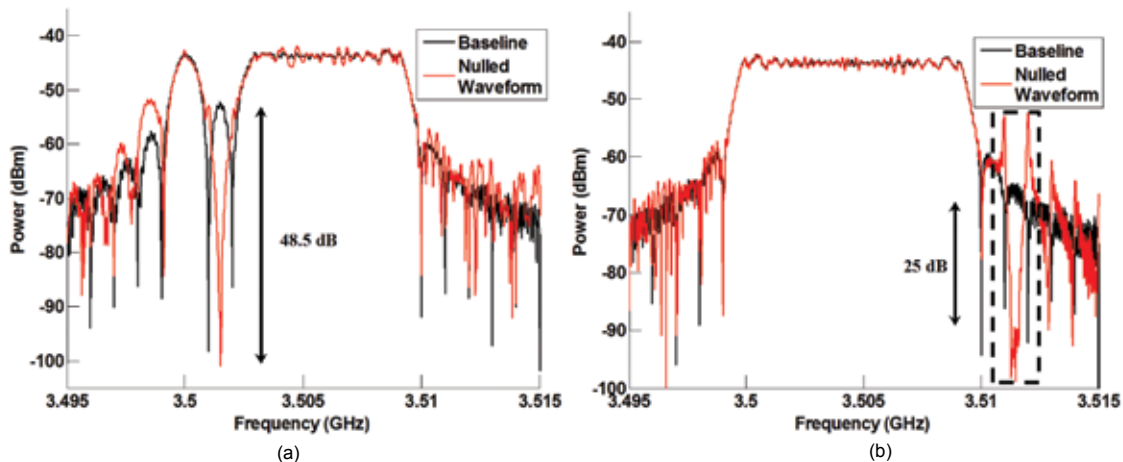
FIGURE 4
(a) Stepped-frequency polyphase code (SFPC) for an in-band spectral null at 3.5015 GHz. (b) SFPC with an out-of-band null at 3.5115 GHz.
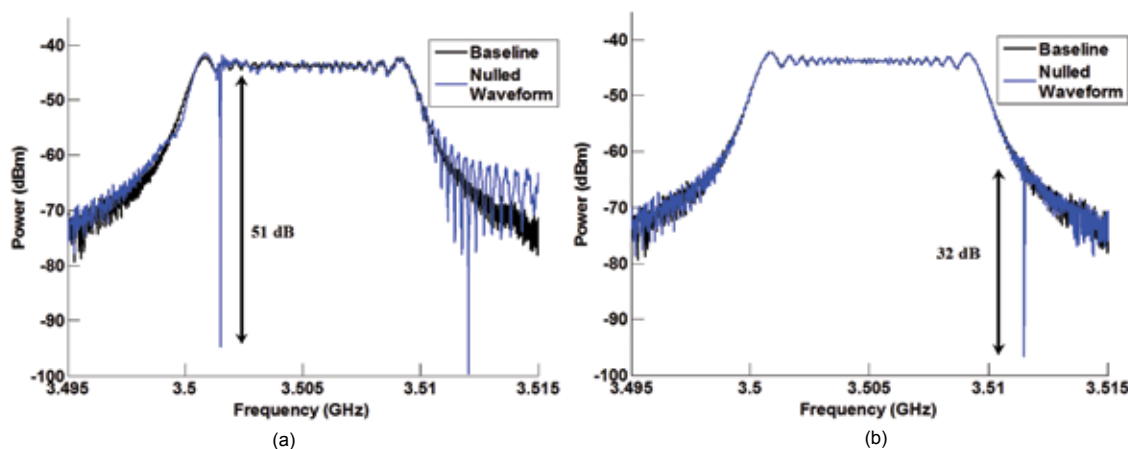
FIGURE 5

(a) The in-band spectral null at 3.5015 GHz generated using the phase-coded linear frequency modulation (PC-LFM) approach. (b) PC-LFM result for an out-of-band null at 3.5115 GHz.
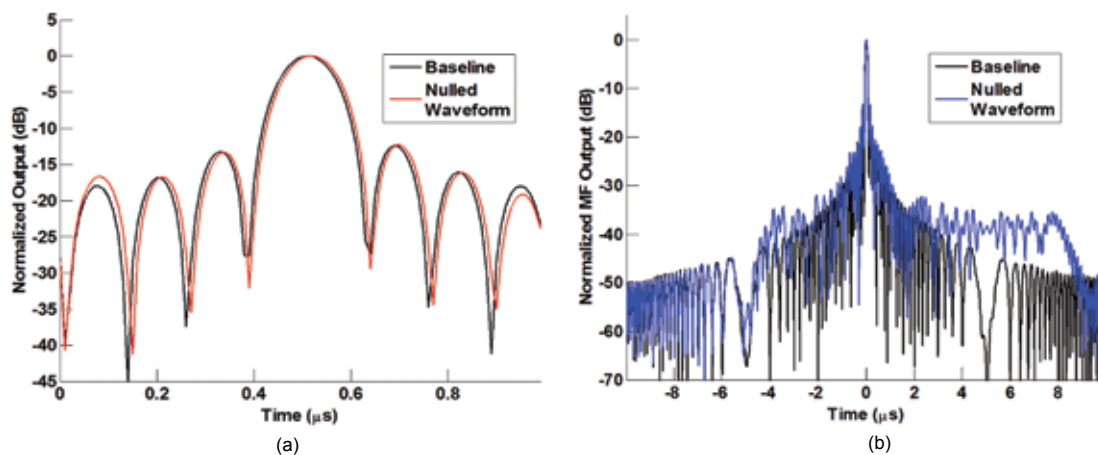
FIGURE 6

Radar pulse compression outputs for (a) the stepped-frequency polyphase-coded waveform and (b) phase-coded linear frequency modulation techniques.

Summary: Initial experimental verification of spectrally nulled radar waveforms has been presented. The next stage of this work is to transmit these waveforms through saturated power amplifiers, such as those commonly used in radar systems. These experiments will allow assessment of the impacts of nonlinearities in the power amplifiers on null depth and width. These and other characteristics of saturated power amplifiers may require further distortion of the radar waveform to achieve a sufficiently deep spectral null. Finally, tests will be conducted in the presence of narrowband communications signals to demonstrate radar/communication system spectral sharing.

[Sponsored by NRL]

References

[1] K. Gerlach, "Thinned Spectrum Ultrawideband Waveforms Using Stepped-Frequency Polyphase Codes," *IEEE Trans. Aerospace and Electron. Sys.* **34**(4), 1356–1361 (1998).
[2] K. Gerlach, M. Frey, M. Steiner, and A. Shackelford, "Spectral Nulling on Transmit via Adaptive Nonlinear FM Radar Wave-

forms," *IEEE Trans. Aerospace and Electron. Sys.*, accepted for publication.

■

Demonstration of Highly Efficient 4.5 kV Silicon Carbide Power Rectifiers for Ship Electrification

K. Hobart,[1] E. Imhoff,[1] F. Kub,[1] T. Duong,[2] A. Hefner,[2] S.-H. Rdu,[3] and D. Grider[3]
[1]*Electronics Science and Technology Division*
[2]*National Institute of Standards and Technology*
[3]*Cree, Inc.*

Introduction: The dramatic increase in shipboard electrical power due to demands of electric propulsion, weapons, and sensors requires associated innovations in power electronic components in order to address

size and weight of the associated power delivery systems. The present approach to increasing shipboard power capability is to increase the bus voltage. For example, on the LHD, LHA, and DDG platforms, the bus voltage has increased from 480 to 4160 V. The increase in bus voltage allows for significantly higher power distribution capability; however, the power electronics required to distribute and control the additional power adds undesirable weight and cabinet space to the ship. The recent interest in modernizing the DDG 51 class of ships will require substantial reductions in size and weight of power electronic systems to maintain a stable ship center of gravity. To address these challenges, NRL has developed new high voltage silicon carbide (SiC)-based power electronic components. SiC is a wide bandgap semiconductor with exceptional high voltage and high temperature capability with approximately 10 times higher critical electric field for breakdown than silicon (Si), the most common semiconductor. As demonstrated here, this high voltage and high temperature capability translates into SiC power electronic components that are far more efficient and reliable than their Si counterparts, allowing for more compact power conversion systems.

Silicon Carbide as the Alternative: Presently, the largest payoff for SiC component technology is to replace freewheeling rectifiers in power electronic circuits. The basic power electronic building block is the half-bridge, or phase leg, as each leg would drive a phase of the motor (Fig. 7). The upper and lower power transistors ("switches") are energized alternately "on" and "off" to produce a high frequency pulse width modulation (PWM) output to control the torque and rpm of a propulsion motor. The freewheeling recti-
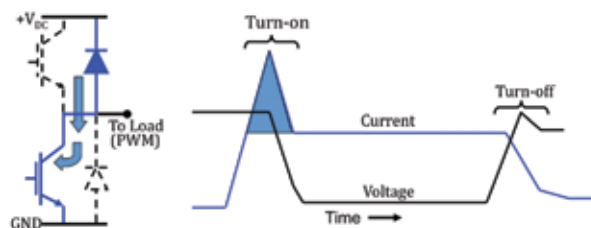
FIGURE 7
Schematic drawing of a half-bridge circuit (left) and current-voltage waveforms as seen across the lower (blue) switch (right). During turn-on, the upper diode discharges into the lower switch, producing a large current transient (as illustrated by large arrow).

fiers, or diodes, allow current to flow when the upper or lower switches are turned off to produce the correct output phase and magnitude of voltage and current while driving an inductive load. The primary inefficiencies in such a configuration arise from losses that occur during the switching transients, i.e., when the

current and voltage are simultaneously present across the switch. During the "turn-off," transient losses arise from the natural decay of charge carries in the transistor (in this case, an insulated gate bipolar transistor or IGBT), which produces a current "tail." The primary loss component during "turn-on" comes about from the discharge or reverse "recovery" of the opposing freewheeling diode. A great deal of charge is stored in the diode during the on-state and this charge, in the form of current, is conducted into the opposing IGBT during the off-state (Fig. 7). The result is a very high current spike that must be managed by switching the transistors more slowly, thereby increasing losses. Neglecting the current spike can result in catastrophic failure of the transistors. Replacing conventional Si "PiN" diodes with SiC Schottky barrier diodes is an accepted method of eliminating stored charge and the associated current spikes. SiC power rectifiers are available commercially at low voltages ($\leq$1700 V) and have been shown to be highly efficient as Si replacements. However, at high voltages critical to new and future Naval platforms, development is limited. To address this need, NRL led a team to fabricate and test the new SiC power rectifiers and perform the first comparisons to state-of-the-art high voltage Si rectifiers.

High Voltage Silicon Carbide Power Rectifier Development: The new SiC rectifiers are designed to match available high voltage Si components for a clear comparison. Commercially available Si IGBTs and diodes with ratings of 4.5 kV and 60 A were chosen for the demonstration. High voltage SiC junction barrier Schottky (JBS) rectifiers were fabricated at Cree, Inc. (Durham, NC). The rectifiers were characterized for both static and dynamic performance. Dynamic high power testing was performed through collaboration with the National Institute of Standards and Technology (NIST, Gaithersburg, MD). Figure 8(a) compares the high voltage standoff properties characterized by the reverse leakage current as a function of reverse voltage with increasing temperature. Due to its wider bandgap, the SiC rectifier can support the same voltage with less than a tenth of the active diode thickness and is less affected by increasing temperature. The forward conduction comparison (Fig. 8(b)) shows the forward current vs the forward voltage drop. Optimally, power rectifiers show an increase in the forward drop with increasing temperature to avoid thermal runaway and to allow paralleling of multiple diodes. Overall, the static characteristics demonstrate that SiC can be a direct replacement for equivalent Si parts.

Transient Characteristics: To quantify the benefit of SiC, the circuit shown by the blue components in Fig. 7 was constructed with an inductive load to simulate a propulsion motor, and the test results are summarized in Fig. 9. The reverse recovery current of the Si recti-

(a)

(b)
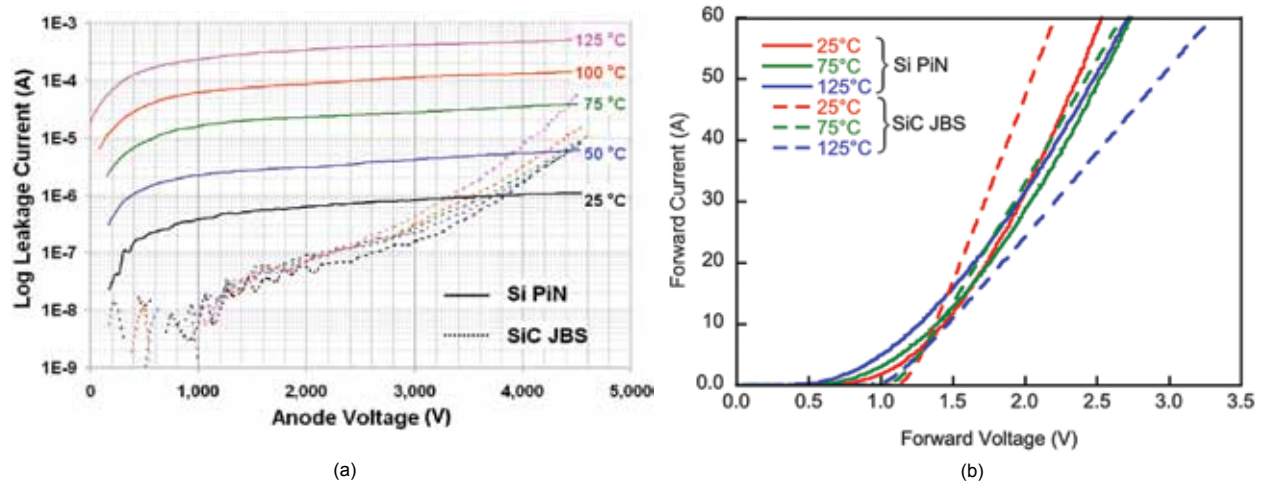
FIGURE 8
(a) Comparison of the reverse blocking characteristics of Si PiN (solid lines) and SiC Schottky (dashed line) rectifiers as a function of temperature. (b) Comparison of the forward conduction characteristics of Si PiN (solid lines) and SiC Schottky (dashed lines) diodes as a function of temperature.

(a)

(b)
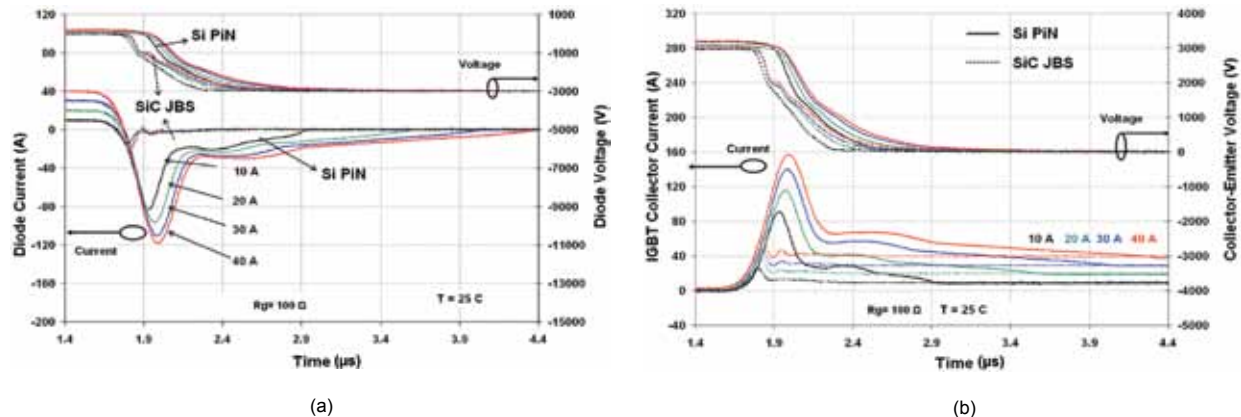
FIGURE 9
(a) Comparison of transient waveforms for Si (solid) and SiC (dashed) rectifiers under switching conditions of 3 kV and load currents varying from 10 to 40 A. The top traces are the voltage and the lower traces are the current waveforms. (b) Comparison of the impact of Si and SiC diode reverse recovery currents on switching transistor (IGBT) current waveforms. The current spike from the SiC rectifier is nearly negligible, while that of the Si rectifier is four to eight times the load current. The DC voltage was 3 kV and the load current varied from 10 to 40 A.

fier is observed to be highly dependent on the switching current compared to a negligible peak for the SiC diode (Fig. 9(a)). The key impact of the diode reverse recovery current can be seen in Fig. 9(b), which shows the current and voltage present at the IGBT. The diode current is essentially superimposed on the load current, producing a very large current spike in the IGBT. This current spike produces very large losses within the diode and IGBT that must be dissipated to the environment through the cooling system. Furthermore, the current spike impacts reliability of the switching transistors and can have negative effects downstream by stressing other components. Electromagnetic interference (EMI) is another concern, and measures taken to control EMI adversely affect system efficiency. Overall, the comparisons show that the SiC component can reduce switching losses by a factor of 4 and current

spike levels by nearly an order of magnitude.

Summary: In an apples-to-apples comparison, significant improvements have been demonstrated by replacing Si with SiC rectifiers in traditional phase leg architectures. Due to the superior properties of SiC, it is highly desirable to transition such components into the Fleet. This demonstration is a first and important step toward that realization.

Microfabrication of Next-Generation Millimeter-Wave Vacuum Electronic Amplifiers

C.D. Joye,[1] J.P. Calame,[1] K.T. Nguyen,[2] and B. Levush[1]
[1]Electronics Science and Technology Division
[2]Beam-Wave Research, Inc.

Introduction: Advanced vacuum electronic (VE) amplifiers capable of high continuous-wave (CW) output power and wide bandwidth are needed for such Naval applications as radar, ultra-high-data-rate communications, long-range imaging, and standoff spectroscopy. Operation at frequencies in the millimeter wavelength (mmW) and sub-mmW regimes is especially useful for these applications, and is practical because of reasonably low-loss atmospheric windows near 220 GHz, 670 GHz, 850 GHz, and 1 THz. The power levels achievable in VE devices are often orders of magnitude greater than comparable solid-state-based technologies owing to very high voltage operation and the spatially distributed nature of the energy conversion mechanisms, combined with high total current and all-metal construction. In particular, copper construction is preferred because copper exhibits low mmW losses and high thermal conductivity for high power handling, and is vacuum compatible. In order to keep VE devices compact, finely structured subwavelength copper features ("interaction circuits") are required to slow down the electromagnetic wave such that it can synchronize with a beam of electrons passing through the interaction circuit (Fig. 10). When the beam-wave coupling is significant, the power from the electron beam is transformed into electromagnetic energy, resulting in amplification. A major challenge at higher frequencies is fabricating the finely structured interaction circuits.
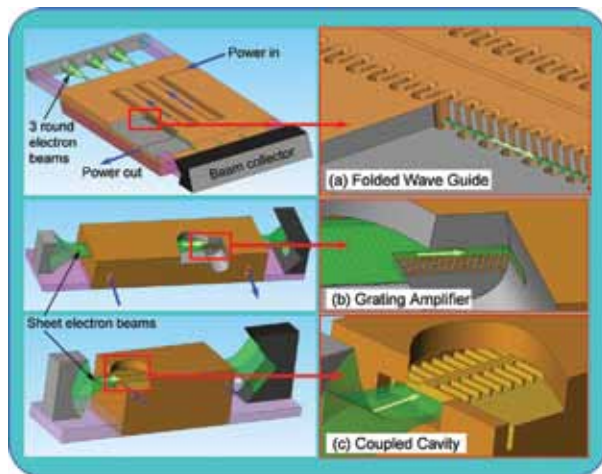
Microfabrication Solutions: Ultraviolet photolithography, combined with electroforming and molding (collectively known as UV-LIGA) is a low-cost microfabrication technique being developed as a replacement for the original and vastly more expensive X-ray LIGA techniques that required a synchrotron X-ray source. Using improved UV-LIGA techniques developed in-house, we recently demonstrated the ability to fabricate complete, all-copper grating circuits for 220 GHz VE amplifiers,[1] relying on three main steps (Fig. 11): First, on a copper substrate, we use the highly viscous SU-8 photoresist activated by UV light from a low-cost source to form microscopic features down as small as 10 μm; second, copper is electroformed to fill the volume around the SU-8; and last, the SU-8 is removed, leaving only finely structured copper behind. Our photoresist layers are usually in the range of 300 μm to 1 mm thick, far thicker than layers used in IC and transistor manufacturing. The SU-8 acts as a mold while copper is electroformed around it using pulse electroforming techniques in a sulfuric acid–based solution without any problematic grain-refining agents. The electroformed copper is also void-free to ensure vacuum compatibility and has been tested to survive over 900 °C for brazing. After electroforming, the surface is ground and polished, revealing the SU-8 buried in the copper. Since SU-8 is a highly crosslinked epoxy, it is notoriously difficult to remove chemically. We have developed a reliable molten salt method that completely removes SU-8 from high aspect ratio electroformed features, and have demonstrated high vertical aspect ratios in copper of over 15:1. Finally, the 220 GHz amplifier grating circuits were cold tested and characterized using vector network analysis over a very wide frequency range from 75 to 325 GHz. The results agreed with an analytic theory and also revealed that the grating circuits could prove useful as "brick wall" type filters for high-power antijamming applications at G-band and beyond.

The next phase of fabrication involves a game-changing ultra-wideband serpentine waveguide amplifier at 200 to 270 GHz using multiple electron beams to simultaneously achieve high power and wide bandwidth while lowering the intermodulation products.[2] Initial work on this device looks very promising (Fig. 12), and an electron gun and magnet system are being fabricated to construct a complete amplifier.

Summary: We have demonstrated in-house control over every aspect of the microfabrication process for mmW and sub-mmW amplifier circuits for devices

FIGURE 10
(Left) Several kinds of vacuum electron devices illustrating electron guns, beams, and collectors. For clarity, focusing magnets are not shown. (Right) Amplifier interaction circuits are shown in cutaway view.
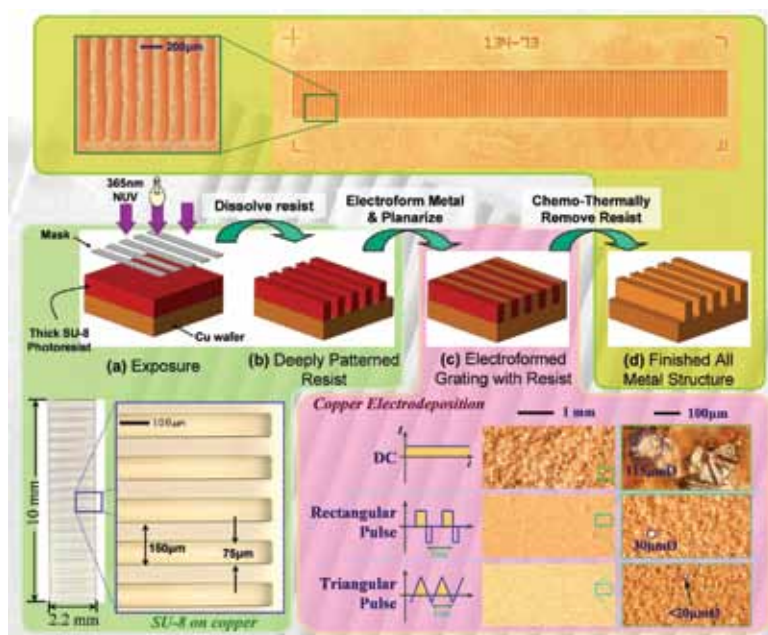
FIGURE 11
The UV-LIGA process. (a) SU-8 is deposited on a polished copper wafer and exposed with UV, (b) the unexposed SU-8 is removed, and (c) copper is electroformed up between the crosslinked SU-8 patterns. Pulsed copper electroforming produces grain sizes far smaller than DC. (d) Finally, the SU-8 is removed.
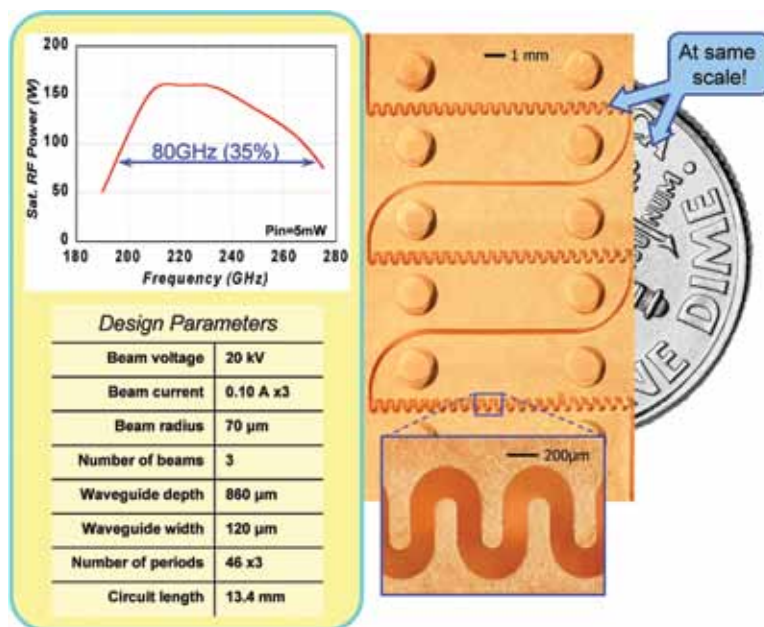
FIGURE 12
A very compact, ultra-wideband multiple-beam serpentine waveguide amplifier designed and fabricated at NRL using UV-LIGA techniques, predicted to generate over 100 W at 220 GHz.

predicted to produce record levels of CW output power. The techniques developed apply not only to VE devices, but also to miniaturized filters, couplers, antennas, and other components requiring high power capability and precise fabrication, and we are quickly expanding our fabrication capabilities to 670 GHz devices. These in-house techniques continue to produce high quality interaction circuits for the next generation of vacuum electron devices that will meet a variety of defense needs within the Navy.

[Sponsored by ONR]

References

[1] C.D. Joye, J.P. Calame, M. Garven, and B. Levush, "UV-LIGA Microfabrication of 220 GHz Sheet Beam Amplifier Gratings with SU-8 Photoresists," *J. Micromech/Microeng*, 125016, Dec. 2010.

[2] K. Nguyen, J. Pasour, E. Wright, D.K. Abe, L. Ludeking, D. Pershing, and B. Levush, "Linearity Performance of Multi-Stage TWT Amplifiers: Cascade vs. Series," Proc. 12th IEEE Int'l Vac. Elec. Conf., Bangalore, India, Feb. 21–24, 2011.

CMOS Integrated MEMS Resonators for RF and Chemical Sensing Applications

M.K. Zalalutdinov, J.W. Baldwin, and B.H. Houston
Acoustics Division

Introduction: In complementary metal oxide semiconductor (CMOS) devices integrated with micro-electromechanical systems (MEMS), the major role for the high spectral purity micromechanical resonators is to provide frequency selectivity — a feature that is crucial for radio frequency (RF) applications and that CMOS alone is lacking almost entirely. Devices like RF filters or frequency generators (clocks) that currently rely on bulky off-chip components (such as quartz crystals, surface acoustic wave (SAW) filters, and thin-film bulk acoustic resonators (FBAR)) will reduce their footprints by orders of magnitude and provide substantial power savings once the frequency determining element is implemented as an on-chip MEMS resonator.[1] "Radio-on-chip" is widely considered an essential milestone in CMOS-MEMS integration and is crucial for "smart dust" applications.[2] Even more important, novel types of RF signal processing that are based on nonlinear dynamics effects in the collective behavior of coupled oscillators are expected to emerge with the ability to fabricate large arrays of high quality factor resonators integrated with electronics.[3]

The challenges arise from the fact that the integration of the mechanical structures must be done without the risk of affecting the performance of the on-chip electronics. In practical terms, the rigidly defined sequence of operations in the CMOS fabrication process must go unaltered and the MEMS design frame in terms of structural materials is severely limited by a set combination of layers (with fixed thicknesses) that are included in a particular CMOS process flow. It is not uncommon for CMOS-MEMS designers to feel like they are trying to build a race car using the spare parts of a jet plane. Yet, to be viable, the resulting micromechanical resonator has to fit the required frequency range, demonstrate high quality factor Q, and provide low insertion loss (often expressed as motional resistance, R_m).[4] The last requirement is often the most challenging and most important since in RF MEMS devices, the incoming electrical signal is converted into mechanical motion of the resonator and then back into the electrical domain, and the efficiency of that double transduction is crucial.

In our research effort, we have developed a general design approach[5] that enables monolithic (on-chip) integration of high-Q RF MEMS resonators into a common type of CMOS process that features two polycrystalline silicon gate layers and field oxide isolation.[6] Using a commercially available CMOS process with minimum feature size 1.5 μm offered by ON Semiconductor (formerly AMI Semiconductor, accessible through MOSIS[7]), we have demonstrated fabrication and operation of polysilicon dome resonators with capacitive pick-up and arch bridge resonators with piezoresistive readout. Both domes and bridges are fabricated using the gate polysilicon as a structural material.

For the dome resonator, the vibrating structure (the dome itself) is comprised of the top polysilicon (poly2) layer only. In the post-CMOS fabrication process, a narrow gap (~100 nm) is created by dissolving inter-poly oxide (used as a sacrificial layer) that separates the suspended top poly2 layer shell from the anchored bottom poly1 layer (Fig. 13), forming a read-out capacitor. Shaping the suspended part as a shell (as opposed to a flat disc) is essential for maintaining the integrity of this ultra-narrow gap. The dome shape of the resonator is provided by placing a circular patch of the oxide isolation layer underneath the poly1 layer. The extra
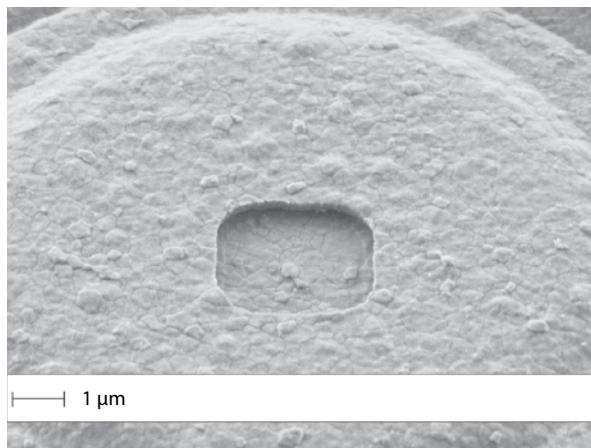
FIGURE 13
SEM image of polysilicon dome resonator. The poly2 shell is released by dissolving interpoly oxide through the irrigation hole (opening at the apex of the dome). The bottom polysilicon layer (poly1, visible through the irrigation hole) is covering a circular patch of field oxide conformally, defining the out-of plane curvature of the dome.

rigidity provided by the out-of-plane curvature of the dome makes the suspended structure robust and capable of withstanding forces that would be fatal for a flat plate. The mechanical-to-electrical transduction is accomplished by applying a DC bias voltage across that poly1–poly2 capacitor and by reading out the AC current induced by the modulation of the vacuum gap due to the mechanical motion of the top (poly2) shell. A scanning electron microscopy (SEM) image of the common-gate transimpedance amplifier placed next

to the dome resonator (Fig. 14) provides direct comparison for the relative size of the resonator and CMOS components. The fact that the footprint of the resonator is significantly smaller than even a single wire-bonding pad demonstrates how effective the monolithic CMOS-MEMS integration can be in microminiaturizing RF devices.

In contrast to the single-layer dome, an arch bridge resonator is designed as a laminar structure. The interpoly oxide is kept intact, providing a bond between a poly1 beam and a slightly wider poly2 cover band (Fig. 15), thus creating a bimorph structure. A rectangular field oxide patch located underneath the bridge is used as a sacrificial layer, which once dissolved sets the bridge free to vibrate. Out-of-plane vibrations of the laminated bridge are accompanied by cycles of compression and extension alternated between the top and bottom layers. Piezoresistive properties of polysilicon[8] make it possible to read out the resulting stress varia-

tions as a modulation of conductivity (induced by the mechanical motion) in either the bottom or the top polysilicon stripe. The other polysilicon layer, being electrically isolated by interpoly oxide, can be used for electrostatic or thermoelastic actuation.
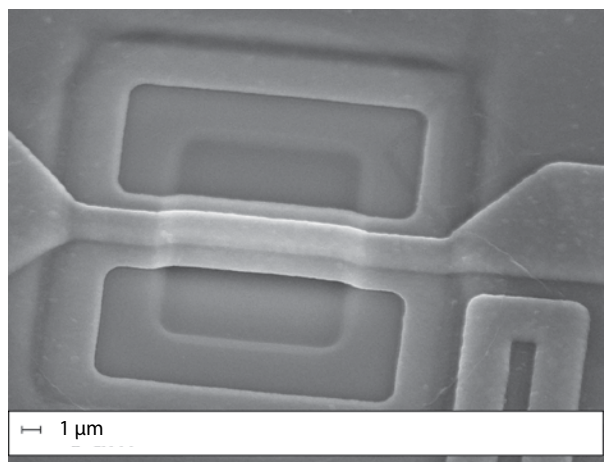
Rigid and robust arch bridges, unburdened by the vulnerabilities associated with ultra-narrow gaps, can find applications beyond RF signal processing. The small mass and high quality factor of the micromechanical arch bridge resonators provide sensitivity for added mass on the order of 1 femtogram. Featuring fully integrated readout and geared for mass production, such resonators can be used in chemical sensing, given that proper surface functionalization would provide specificity toward a particular analyte of interest.[9]

In conclusion, we have demonstrated monolithic integration of MEMS resonators into an unmodified, commercially available CMOS process. High quality factors up to Q ~ 8,000 for the domes and Q ~ 4,000 for arch bridge resonators (to be compared with Q ~ 20 for a conventional on-chip LC tank) in the frequency range 10 to 100 MHz open numerous applications in RF signal processing and chemical sensing. Low motional resistance R_m ~ 740 kOhm of the dome resonators represents almost an order of magnitude improvement compared to state-of-the-art CMOS-integrated MEMS resonators.[10] We are currently working on extending the frequency range for our RF MEMS resonators and refining the design for integration into cutting-edge, deep submicron CMOS processes.

FIGURE 15
SEM image of an arch bridge resonator. The laminated structure is comprised of a poly1 beam covered by a slightly wider poly2 stripe with a thin layer of interpoly oxide providing mechanical bonding between two poly layers, as well as electrical isolation.

References

[1] C.T.C. Nguyen, "MEMS Technology for Timing and Frequency Control," *IEEE Trans. Ultrasonics Ferroelectrics and Frequency Control* **54**(2), 251–270 (2007).

[2] J. Kahn, R. Katz, and K. Pister, "Emerging Challenges: Mobile Networking for "Smart Dust"," *J. Communications and Networks* **2**(3), 188–196 (2000).

[3] F. Hoppensteadt and E. Izhikevich, "Synchronization of MEMS Resonators and Mechanical Neurocomputing," *IEEE Trans. Circuits and Systems I — Fundamental Theory and Applications* **48**(2), 133–138 (2001); E.M. Izhikevich, *Dynamical Systems in Neuroscience* (The MIT Press, Cambridge, Mass., 2007).

[4] Y. Lin, S. Li, Z. Ren, and C. Nguyen, "Low Phase Noise Array-Composite Micromechanical Wine-Glass Disk Oscillator," in IEEE International Electron Devices Meeting 2005, Technical Digest, Washington, D.C., Dec. 5–7, 2005, pp. 278–281.

[5] M.K. Zalalutdinov, J.D. Cross, J.W. Baldwin, B.R. Ilic, W. Zhou, B.H. Houston, and J.M. Parpia, "CMOS-Integrated MEMS Resonators," *JMEMS* **19**(4), 807–815 (2010).

[6] P.E. Allen and D.R. Holberg, *CMOS Analog Circuit Design* (Oxford University Press, New York, 2002), p. 18.

[7] MOSIS (Metal Oxide Semiconductor Implementation Services), Fabrication Processes, available at http://www.mosis.com/products/fab/vendors/.

[8] N. Matsuzuka and T. Toriyama, "Analysis for Piezoresistive Property of Heavily-Doped Polysilicon with Upper and Lower Bounds," *J. Appl. Phys.* **108**, 064902 (2010).

[9] J. Baldwin, M. Zalalutdinov, B. Pate, M. Martin, and B. Houston, "Optically Defined Chemical Functualization of Silicon Nanomechanical Resonators for Mass Sensing," NANO '08. 8th IEEE Conference on Nanotechnology, Aug. 2008, pp. 139–142.

[10] J.L. Lopez, J. Verd, A. Uranga, J. Giner, G. Murillo, F. Torres, G. Abadal, and N. Barniol, "A CMOS-MEMS RF-Tunable Bandpass Filter Based on Two High-Q 22-MHz Polysilicon Clamped-Clamped Beam Resonators," *IEEE Electron Device Lett.* **30**(7), 718–720 (2009).

■

Software Reprogrammable Payload (SRP) Development

C.M. Huffine
Space Systems Development Department

Overview: The Software Reprogrammable Payload (SRP) is an open-architecture, government-owned reference design for a flexible, reconfigurable-while-in-operation software radio designed to meet current and future needs for Navy and Marine Corps missions. By using modern software radio technology based on leading-edge components used in the wireless industry, the payload can collect, process, and transmit a wide variety of signals, or utilize its processing elements for other tasks. Optimizing the application development process and location of processing between the field programmable gate array (FPGA) and the general-purpose processor (GPP) allows the system to achieve high reliability and throughput for a variety of applications while providing for application porting at lowered level-of-effort than previous software defined radio

(SDR) designs. Furthermore, suitably flexible hardware architecture provides for maximum access to a multitude of varied functions. Integrated with external components such as power amplifiers and antennas that may be indigenous on a particular platform, the SRP forms the core of a radio communications and intelligence-surveillance-reconnaissance (ISR) system. The initial development goal was to provide the USMC with robust, flexible, reconfigurable payload operation with their Shadow UAS (Figs. 16 and 17), starting with four applications: SINCGARS communications relay, bent-pipe UHF communications, UHF IP router for legacy tactical UHF radios, and automated identification system (AIS) as the "notional" SIGINT application.
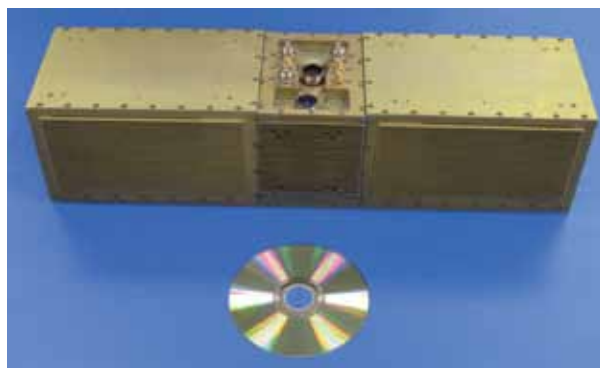
FIGURE 16
Form-factored prototype unit for USMC RQ-7B Shadow UAV.

FIGURE 17
USMC RQ-7B Shadow UAV. (Photo credit: marines.mil)

History: The genesis of the SRP development was as follow-on to previous efforts by the NRL Space Systems Development Department, including the JCIT and UCIM "system of systems" payloads, and other ISR and communications efforts. Recognizing the long timelines — often in excess of 10 years — to get new payloads into space, the concept of the reconfigurable, flexible payloads to help "future-proof" space has been pursued. While support for the space effort was strong, a "rudder redirect" occurred during a briefing to Navy

leadership, who articulated the fact that the more immediate need for SRP technology was UAS and aviation platforms. This advice directly supported our Division superintendent's vision: "Solve the Problem Once" — what can work for aviation can work well for ground, space, and undersea systems, too.

Thus, with excellent flag-level support from the USMC Deputy Commandant/Aviation and his technical project officers and the Office of Naval Research (ONR) Code 30, a 30-month development program began. The basic development and applications were finished on August 27, 2010, and now the SRP Team is proceeding with a series of preplanned product improvements (P3I) that cover a vast array of sensor applications as well as hardware improvement to increase the frequency range and overall utility. Expanding the applications to meet Marine Corps ground requirements and a vast array of Navy requirements is a logical progression and is currently under active development.

Key Development Attributes: The problems that the SRP is designed to solve, in some cases, are not yet defined. The SRP development model has been designed to be similar to what occurs in the open source software and hardware environment used today, as well as other government development environments of a similar nature. Thus, the development of hardware/software suites such as those based on the Google Android platform serve as a model that can be examined and optimized for our use. The needs of Android, for example, are similar to our needs — flexibility to port hardware to a wide variety of vendor and communications platform provider's hardware ensuring a common operating environment and the ability to maintain application compatibility and porting flexibility.

Fully recognizing that in an SDR system the key legacy of the development is literally the software is one of the most important factors to consider. Ensuring that expensive software becomes reusable, portable, and generic so that a wide range of hardware platforms can efficiently use it becomes paramount in ensuring the efficiency of the development process. Breaking down traditional barriers that intentionally or unintentionally develop due to organizational structures, funding streams, or other factors is also key. At NRL, crossing divisional boundaries to utilize the expertise of security engineers in the Information Technology Division or UAS engineers in the Tactical Electronic Warfare Division expands the SRP team to break down traditional barriers at NRL, just as the program seeks to do within industry. Lowering the cost of entry to develop SRP applications is a key effort — universities and small businesses should be on equal footing with large industry.

In recognizing that the software is the long-term investment that is being made, ensuring that the portability of the software is maximized protects the

government's investment. Maximizing portability by means of government-owned application programming interfaces (APIs) and software development kits (SDKs) lowers the cost of entry into designing and building software applications. Ensuring that applications developed are not encumbered with proprietary technologies that the government cannot use with government purpose rights needs to be carefully examined — those situations may lower the software value in the long term with only small short-term savings. The SRP development model allows the insertion of proprietary technologies at various places — if the Service sponsors deem that to be in their best interests.

Maintaining a rigorous systems-engineering process (SE) is a key developmental aspect. It can be tempting to bypass the process, particularly within the context of a spiral development, without the due diligence necessary of the SE. However, it is valid and necessary, particularly in cost-constrained programs, to tailor the SE effort in a way that provides the most efficient use of the team's knowledge and time. Finding the right mix between too little and too much documentation is a challenge. The SRP team's experience has shown that sufficient documentation, for example, during the design process, forces the engineer to more thoroughly think through the design and the ramifications to other subsystems, and provides other subsystem engineers who are participating in the peer review process enough insight into the design to add meaningful criticism. Too detailed documentation done too early will require expensive revisions to the as-built state down the line. In any case, detailed documentation is absolutely required for the boundaries — the places where external developers will utilize the SDK/APIs.

Finally, following decades of experience in designing end-to-end systems, the NRL Naval Center for Space Technology mantra of "test like you fly and fly like you test" is still relevant and necessary and cannot be overemphasized. Testing complex systems can be extremely expensive, particularly when it is done as an afterthought. Emphasizing testing and testability continuously and up front will reduce long-term schedule and costs. In modularized software systems, ensuring that those modules have built in regression testing suites that can be used also reduces the cost of the porting efforts when new hardware platforms become available.

Summary: The SRP provides a hardware and software platform to build upon for current and future requirements. The developmental program emphasized portability and reusability of the software elements and nonproprietary development of applications to ensure that the software, which is the majority of the system cost, has a life beyond a single hardware instantiation. Systems engineering discipline and a robust preplanned product improvement program keep the system and

software development moving forward for current and future requirements.

[Sponsored by ONR] ■

Octavia — Octavia is an MDS (Mobile/ Dexterous/Social) robot that uses an integrated sensor suite to perceive the world and cognitive models to interact with people.

Information Technology and Communications

Combined Aperture for Radio and Optical Communications for Deep Space Links

G.C. Gilbreath,[1] M.A. Rupar,[1] C.O. Font,[1] and R.C. Romeo[2]
[1]Information Technology Division
[2]Composite Mirror Applications, Inc.

Introduction: To save mass, reduce "wallplug" power, and potentially reduce complexity while increasing communications bandwidth, we consider the feasibility of using a shared aperture for radio frequency (RF) and optical communications. When constructed with composite materials and efficient coatings matched to the wavelengths of interest, we can expect at least an order of magnitude reduction in mass for the communications terminal, which will also enable the use of bandwidths that will support an increase of two orders of magnitude in data rate. NRL evaluated three antennas that could be converted into a dual-use antenna/telescope. We postulated the use of 36 GHz to 38 GHz in the K_a band and 1550 nm in the short wave infrared (SWIR). We compared placement of the secondary for either a shared aperture in the feed train or as part of a bent Cassegrain. The point designs enabled an engineering evaluation of feasibility. We considered adapting a 34-cm spiderless aluminum primary, a 38-cm silver-coated aluminum primary using a spider to hold the subreflector, and the 3-m primary used in the Mars Reconnaissance Orbiter mission. The three baseline structures are shown in Fig. 1.

Coatings: Before proceeding to the architecture itself, we considered coatings that can usefully reflect/transmit K_a while transmitting/reflecting SWIR wavelengths. Three likely candidates for common reflectance are aluminum, silver (to include coated silver), and gold. When considering reflectance at GHz frequencies, the key parameter is skin depth. The measure of reflectance is derived from this basic parameter and is usually estimated based on at least a factor of 2 multiplier. Since a typical thickness of a coating is on the order of 2 to 3 μm, conservative reflectance estimates between aluminum, silver, and gold are nearly equivalent (96.3% for aluminum, 95% for silver, and 95.4% for gold). The driver then becomes response in the SWIR. Equivalent reflectances in the SWIR are 97% for aluminum, 99.4% for silver, and 99% for gold. A coated silver coating may give the best response for a shared aperture. Bare metallic silver adheres weakly to glass and tarnishes when exposed to the atmosphere. The Denton FSS-99 coating, which is a SiO_2 coating, offers 99% reflectance in the infrared and slightly less in the GHz regime. Importantly, all three coatings have been space-qualified for different designs and some have been qualified on carbon reinforced fiber polymer (CFRP) composites.

Aperture/Feed Sharing: How to split the energy is a key question in the design of a shared RF-optical system. There are many ways to approach the problem. In our simple point design, we assume a shared aperture to illustrate use of coatings, unique shared aperture elements, and potential use of composites for the
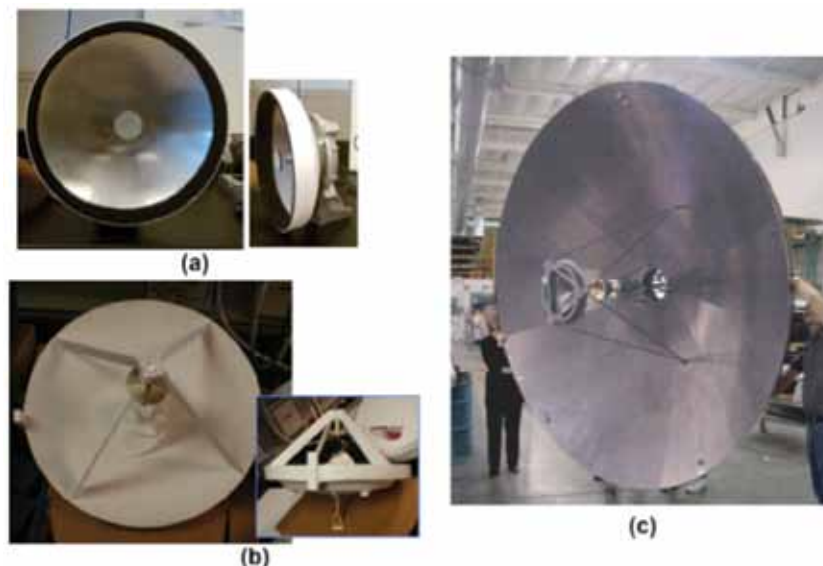
FIGURE 1
Basic structures considered for adaptation to E-O: (a) 34-cm spiderless K_a antenna; (b) 38-cm K_a antenna using spider-mounted subreflector; (c) Mars Reconnaissance Orbiter 3-m high-gain antenna (HGA) and its X-/K_a-band feed (Ref. 1).

structure. First, we assumed use of an antenna primary whose surface is covered with coated silver. This antenna structure now can serve as the telescope primary as well. The K_a energy is received by the antenna and the energy is directed to the subreflector located at the K_a focal point. The energy is reflected from the subreflector to the feed at the center of the antenna in a standard Cassegrain configuration. Similarly, the SWIR energy (1550 nm) is collected by the coated antenna, which we would now call the telescope. At this point, we have several choices. Among them, we can:

(1) Share a common feed aperture
(2) Bend the SWIR out of the feed train (bent SWIR Cassegrain)
(3) Bend the K_a out of the feed train (bent RF Cassegrain)

The shared aperture design is extensively described in literature and is not discussed here. We address the bent Cassegrain designs. In Fig. 2(a), the SWIR is bent from the common beam before the feed. It is directed to an off-axis optical collection path to direct the light to the detectors and electronics. The key element here is a dichroic element that can efficiently reflect 1550 nm and pass 34 to 36 GHz (K_a bands of choice). An alternative configuration is to pass the SWIR through to the optical feed at the center of the primary and bend the K_a energy via a wire mesh element. The mesh can successfully redirect the K_a and pass the SWIR. A G200 wire with 200 μm spacing will allow greater than 95% transmittance at 1550 nm and 99% reflectance at K_a. Although the SWIR efficiency may be impacted by diffraction and some obscuration, a more careful analysis will show that the impact will be on the order of 0.1 dB, if that. A more detailed sketch of this idea is shown in Fig. 2(b), which was offered by Composite Mirror Applications, Inc. as a point design for the concept.[1] Using a wire mesh as a beam dichroic does impose a polarization constraint on a design. That is, one polarization in the RF band is passed and the other is not. Therefore, to maximize efficiency, this must be taken into account when splitting the energy.

Composites: Reducing size, weight, and power (SWAP) of a host platform and its integrated payload is an overarching goal for space applications in particular. Reduction in mass can go a long way in the reduction of power requirements, which in turn further reduces weight and size. Composites, therefore, are of keen interest to the community. Thus, in addition to selection of an architecture where coatings and components are creatively integrated into an effective shared system, the use of composites for the structures themselves were considered. We specifically postulated the use of CFRP. This material has been used to manufacture telescopes and optical telescope assemblies for different architectures and for low-cost replicates. Off-axis aperture

(a)

D1/D2 < 35%

— Coating: Transparent to K_a Reflective at SWIR

— Composite

(b)

4" diameter gold wire grid with 10 micron spacing.

Wire Dichroic

K_a Band Diplexer
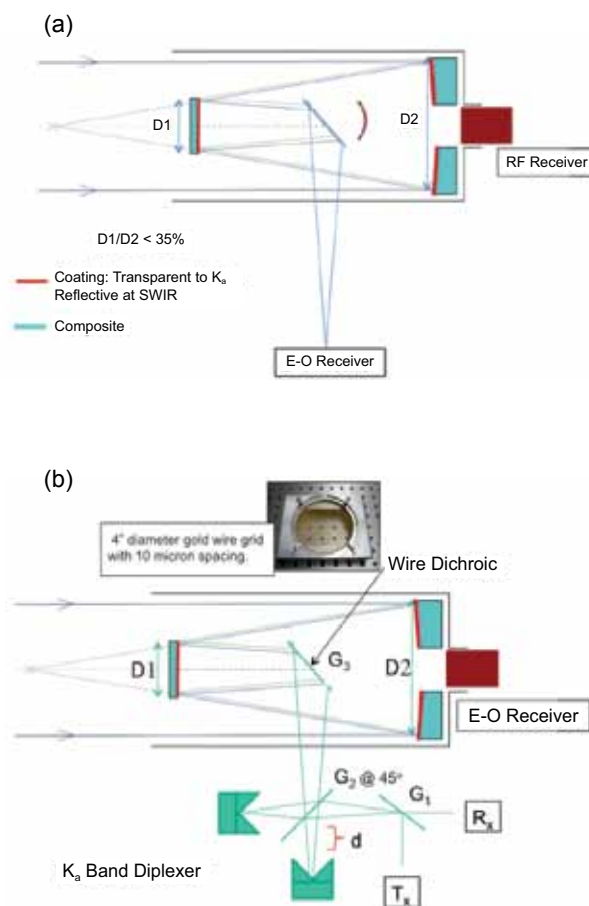
FIGURE 2

(a) Point design is shown to demonstrate how RF can be split from the energy train for a bent Cassegrain shared RF-SWIR aperture. The wire mesh in this case would transmit 1550 nm and pass K_a. (b) Point design is shown to demonstrate how E-O can be split from the energy train for a bent Cassegrain shared aperture. The dichroic in this case would reflect 1550 nm and pass both polarizations of K_a.

sharing, bent beams, and other possibilities will require a structure that is strong, lightweight, and lends itself to customized designs. CFRP can be constructed to roll and unroll for stowage and straightforward deployment. This latter feature is important for space applications.

The CFRP optics and optical train assemblies (OTAs) are at least an order of magnitude lighter than similar telescopes made using traditional glass with aluminum assemblies. CFRP structures are at least 50% lighter than their all-aluminum equivalents. Additionally, the stiffness-to-weight ratio of CFRP is about five times greater than that of steel, the Young's modulus similar, and the density much lower. Thus, stiff, lightweight structures are possible. In addition, the coefficient of thermal expansion for CFRP is very low at 1 to 2 ppm, roughly 20 times lower than for aluminum. For this reason, CFRP structures do not deform with

TABLE 1 — Densities Compared for Some Candidate Materials

Material	Areal Density kg/m²	Density kg/m³
Aluminum		2900
Silicon Carbide	32.0	3200
CFRP	5.5	1600
ULE Glass	10.0	2210
Zerodur Glass	45.0	2530

temperature changes. Also, the thermal conductivity of CFRP is similar to that of steel. This property, coupled with the lower mass of a CFRP structure, means that telescope components rapidly equilibrate to their surroundings, which reduces image distortion. Table 1 compares areal densities and volumetric densities for some candidate materials.

Candidate Implementation: When we combine coatings, composites, and unique shared apertures, we can eliminate one primary at a minimum. We further decrease mass by replacing the antenna/telescope assembly structure with composites and enable larger, lighter weight optical telescopes that can also support K_a radio transmissions. When applied to the 3-m high-gain antenna (HGA) used in the Mars Reconnaissance Orbiter, we can offer an efficient 3-m telescope at each end of a Mars–Earth orbiting link that can support the commensurate increase in data rates for both K_a and SWIR-based communications. Top-level link analysis suggests that the data throughput can be increased over baselined X-/K_a-band of 6 Mbps (near Earth) and 500 kbps (furthest from Earth) to multiple Gbps to ~300 Mbps using SWIR. Further efficiencies can be achieved with smart modems that would sense when the optical link is in play and put the RF link in hibernate mode to reduce power draws.[2] This scenario will result in a smaller power loading requirement, further reducing SWAP for the system. Pointing, acquisition, and tracking is assumed to be ideal for these trades. A more sophisticated treatment of the links can be found in Ref. 3.

Implications: The results of this study have been combined with the analyses of other national labs and are being considered by NASA for a Pre-Flight Phase A Study for future Deep Space Missions.

[Sponsored by NASA]

References
[1] G.C. Gilbreath, M.A. Rupar, C.O. Font, and R.C. Romeo, "Combined RF and EO Aperture Study," NRL Report to NASA, September 2010; NRL Formal Report in preparation.
[2] D.S. Kim, G.C. Gilbreath, J. Doffoh, C.O. Font, and M. Suite, "Hybrid Free-space Optical and Radio Frequency Switching," *Proc. SPIE* **7091**, 70910X–70910X-9 (2008).
[3] H. Hemmati, ed., *Near-Earth Laser Communications* (CRC Press, Boca Raton, Fla., 2009).

■

Goal-Driven Autonomy

D.W. Aha,[1] M. Molineaux,[2] and M. Klenk[3]
[1]*Information Technology Division*
[2]*Knexus Research Corporation*
[3]*Palo Alto Research Center*

Introduction: The Navy needs autonomous intelligent agents to help dominate the battlespace in several types of missions. For example, agents could reduce the amount of warfighter oversight required to operate unmanned vehicles, serve as proactive decision support assistants in C2 systems, and increase the realism of decision-making behaviors for simulated units in training and wargaming systems. However, current-generation agents are severely limited; they must be told how to behave in all situations that they will encounter, or be supervised continuously. Unfortunately, such knowledge engineering is impossible for their complex military environments, which are characterized by incomplete knowledge of the situation, dynamic situation updates, multiple adversaries, and stochastic agent actions. Thus, current agent deployments are highly constrained (e.g., they are programmed to withdraw and report to their operators when any unexpected situations occur).

To achieve full autonomy, agents should dynamically reason about what goals they should pursue to optimize mission performance measures. This will allow them to respond intelligently to unexpected situations as the battlespace situation evolves. We refer to this process as goal reasoning, and next describe our progress on defining a model for it, an agent implementation, and its evaluation.

Model: Figure 3 displays our novel computational model of goal reasoning, also called goal-directed

autonomy (GDA). GDA permits agents to select their goals throughout their deployment (under mission constraints). It extends the controller of the existing model for online planning, which envisions (1) a plan generator, (2) a controller that feeds the plan's actions to the environment, and (3) the environment itself, which uses a function to compute state updates from executing specific actions. A GDA agent monitors a
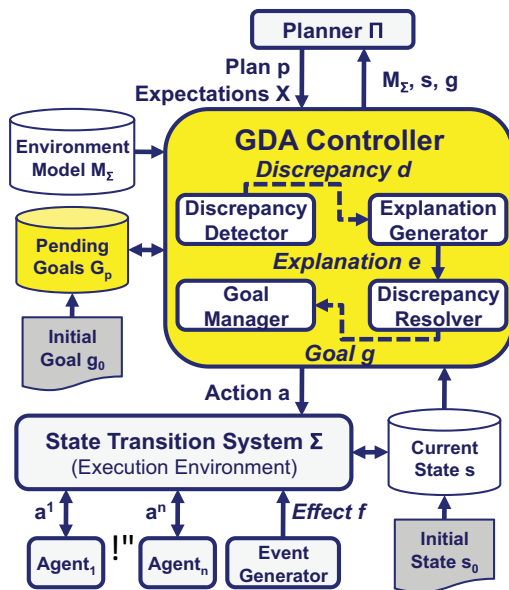
FIGURE 3
Conceptual model for goal-driven autonomy.

plan's execution, and continually compares the current and expected situations (or states). If a discrepancy is detected, then it will generate an explanation of its cause. This is given to a discrepancy resolution module, which may decide to formulate a new goal in response. Finally, a goal manager prioritizes and selects a set of (potentially new) goals to pursue, which are given to the planner to create new plans to execute.

GDA is a general model; many inferencing algorithms could be used for each GDA step. Below we describe one of our instantiations and its empirical investigation.

Implementation and Evaluation: Can the GDA model's additional complexity yield quantifiable benefits? Our hypothesis was that when scenarios produce states that require a GDA agent to change its goals to perform well, it should outperform agents that cannot change their goals. We assessed this by implementing this model in the ARTUE (Autonomous Response to Unexpected Events) agent and comparing its performance vs ablated versions in scenarios defined using complex simulation environments.[1] ARTUE is a simple GDA instantiation; it defines discrepancies as any differences between the expected and actual states, it uses

an augmented truth-maintenance system to generate explanations, a set of simple rules to trigger the formulation of goals with specified priorities, and always directs planning to the goal with the highest priority.

For some of our studies, we tested ARTUE using the Tactical Action Officer (TAO) Sandbox, which is a comprehensive littoral simulator used to train TAOs at the Surface Warfare Officers School. We modified the Sandbox such that ARTUE assumes the trainee's interactive role and controls a set of assets (e.g., ship, air, sensors) in antisubmarine and related mission scenarios. For example, the SubHunt scenario involves a search for an enemy submarine that has been spotted nearby. A ship is dispatched to locate and engage it. However, the submarine has been laying mines that can incapacitate the searching ship. As with each scenario, we defined a scenario-specific performance measure, in this case one whose value increases as a function of finding and destroying the submarine, as well as sweeping the mines. A non-GDA agent would ignore the mines because it would focus solely on its initial goal, whereas ARTUE would formulate a goal to sweep them. Table 2 displays our results for ARTUE and its ablations (i.e., which perform no GDA steps, only discrepancy detection, or only the first two steps,

TABLE 2 — Mean Performance Scores for the
TAO Sandbox Scenarios

N = 25	Scouting	Iceberg	SubHunt
PLAN1	0.33	0.35	0.35
REPLAN	0.40	0.48	0.48
EXPLAIN	0.58	0.64	0.74
ARTUE	0.74	0.73	0.98

respectively). Analysis reveals significant performance differences between ARTUE and its ablations for all these scenarios.

Discussion: Our evaluations on the TAO Sandbox and other simulators involving multiple GDA agents have been encouraging.[2] However, many open research issues exist. For example, ARTUE requires a set of rules for triggering goal formulation during discrepancy resolution. We recently extended ARTUE to interactively acquire these rules and will soon study methods for automatically identifying events of interest to discrepancy detection. In an upcoming project, we will transition extensions of ARTUE for use in ICODES, a deployed system for ship cargo loading/unloading. Future plans also include examining its utility for controlling unmanned systems in complex maritime environments.

[Sponsored by NRL]

References

[1] M. Molineaux, M. Klenk, and D.W. Aha, "Goal-Driven Autonomy in a Navy Strategy Simulation," Proceedings of the Twenty-Fourth AAAI Conference on Artificial Intelligence, Atlanta, GA, July 11-15, 2010, pp. 1548–1554.

[2] H. Muñoz-Avila, U. Jaidee, D.W. Aha, and E. Carter, "Goal Driven Autonomy with Case-based Reasoning," Proceedings of the Eighteenth International Conference on Case-Based Reasoning, Alessandria, Italy, pp. 228–241 (Springer, Berlin, 2010).

■

Managing Multiple Radio Communications Channels

C. Wasylyshyn
Information Technology Division

Introduction: It is expected that future Naval forces will be defined by their agility and their capacity for coping with highly dynamic environments.[1] Decision-making in the Combat Information Center (CIC) of the future is exactly such an environment. The individual Naval watchstander might be responsible for the concurrent monitoring of numerous radio communications channels, along with actively monitoring and responding to events on multiple visual displays. Such attentionally demanding environments have motivated various human–computer interaction (HCI) solutions to help warfighters deal with the vast number of information sources needing to be monitored in order to perform their duties successfully.

Monitoring Multiple Communications Channels: Unlike reading, in which the information input rate can be controlled by one's eye movements, comprehension of speech is often dependent on a transient acoustic signal whose input rate is largely controlled by the speaker, not the listener. The information input rate, thus, is determined by the environment, and previous information is often not reviewable. In order to comprehend auditory information effectively, input must be analyzed, segmented, and processed for structure and meaning, all of which must occur even as new auditory information continues to arrive. When auditory input is rapid, listeners have even less time to carry out these integrative processes, and successful comprehension requires greater cognitive effort on the part of the watchstander.

This project addresses a critical consideration when designing HCI solutions in auditory display research: the limitations in watchstanders' abilities to attend to multiple, active communications channels. Instead of presenting messages that must be monitored in parallel, as is the current state of affairs in the CIC, listeners hear messages that are serialized and acceler-

ated in order to facilitate better comprehension. In addition, this project explores the role of natural biases in human attention toward certain categories of information during the listening process. Building an effective system of synthetically accelerated voice communications requires the integration of insights from multiple disciplines including signal processing, cognitive psychology, and linguistics. Each of these disciplines has made and will continue to make contributions to the design and execution of our experiments.

Experimental Design: An auditory test bed was created with communications messages that were synthetically accelerated using a patented NRL speech-rate compression algorithm[2] known as pitch-synchronous segmentation (PSS). PSS retains the fundamental frequency of speech signals and preserves a high degree of intelligibility by representing speech as a combination of individual pitch waveforms that do not destructively interfere with one another. The PSS algorithm was used to construct synthetically accelerated communications messages for our experiments at rates ranging in 15% increments from 50% to 140% faster than normal.

The communications messages, themselves, were also structured to enhance comprehension. Based on theories of attention and memory,[3] the human attentional capacity is thought to be optimized for detecting relevant changes in the environment, or in this case, the communications message. These changes serve as natural cues to encode and later remember pertinent information. We, therefore, presented auditory information in a way that approximates how listeners more naturally perceive it, that is, by varying the number of natural cues contained in the message. It was expected that comprehension of messages that contained more of these natural cues would be better than comprehension of messages that contained fewer.

In order to assess the effectiveness of our design, we tested for training effects and practice effects when listening to accelerated speech, and examined whether the number of natural cues included in the messages would influence comprehension.

Results: Comprehension of auditory messages was compared at normal speed and at seven accelerated speech rates. Figure 4 shows data from one group assigned to a training condition compared to another group assigned to a condition where accelerated speech messages were presented in a random fashion. As can be seen in Fig. 4, overall comprehension for both groups declined as speech rate increased. Training was effective at slower accelerated speech rates (50% and 65% faster than normal). The optimum acceleration rate for comprehension, or the fastest rate at which speech can be presented so that performance does not
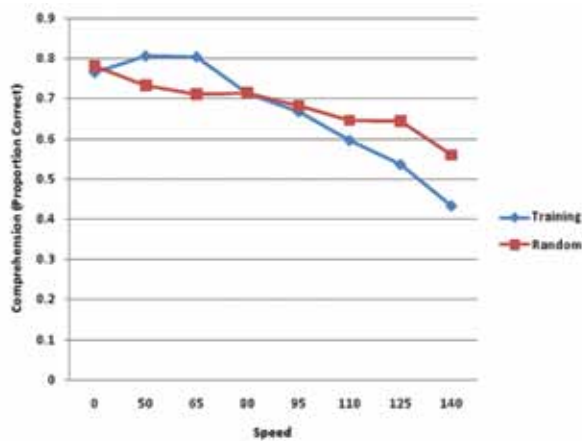
FIGURE 4
Comprehension (proportion correct) as a function of speed for the training and random presentation conditions. Note that 0 indicates normal speed speech; 50 to 140 denote % speed faster than normal.

differ from that at a normal rate, was 65% faster than normal. However, practice did not aid comprehension. That is, there was no systematic improvement shown after listening to multiple auditory messages presented at the same accelerated speech rate. Listeners simply adapted quickly when listening to accelerated speech. Structuring messages to contain more natural cues did enhance listeners' comprehension of information stated in the messages. This relationship is shown in Fig. 5.
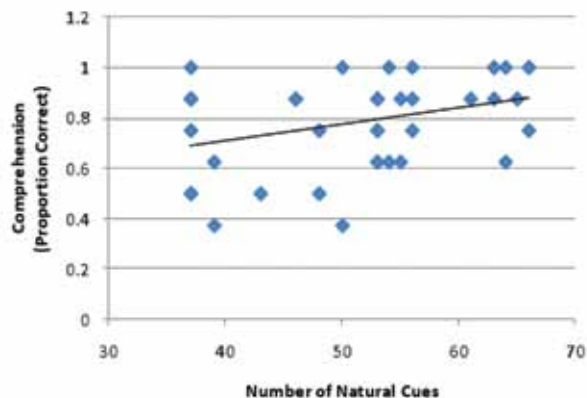
FIGURE 5
The relationship between comprehension (proportion correct) and the number of natural cues presented in the communications messages.

Summary: This research effort integrates several disciplines, including signal processing, cognitive psychology, and linguistics, in order to design a radio communications protocol that is minimally taxing to the watchstander and that will maximize the probability of message retention and understanding.

References
[1] V. Clark, "Sea Power 21 Series - Part I: Projecting Decisive Joint Capabilities," *Naval Institute Proceedings Magazine* **128** (October 2002).
[2] G.S. Kang and L.J. Fransen, "Speech Analysis and Synthesis Based on Pitch-Synchronous Segmentation of the Speech Waveform," NRL/FR/5550--94-9743, Naval Research Laboratory, Washington, DC, 1994.
[3] J.M. Zacks and B. Tversky, "Event Structure in Perception and Conception," *Psychological Bulletin* **127**, 3–21 (2001).

■

Clutter Avoidance in Complex Geospatial Displays

M.C. Lohrenz[1] and M.R. Beck[2]
[1]*Marine Geosciences Division*
[2]*Louisiana State University*

Introduction: Clutter is a known problem in complex geospatial displays and can impact visual search and target detection performance. Set size (the number of distractors, i.e., features competing with the target for attention) and crowding (the amount of visual noise near the target) can predict search efficiency in displays with relatively simple features. However, set size and crowding can be difficult to measure in very complex displays.[1]

The authors recently introduced a measure of display clutter called the color-clustering clutter (C3) model, which correlates highly with subjective clutter ratings.[2] C3 measures clutter as a function of color density and saliency. Color density is determined by clustering all pixels in an image by location and color and calculating, for each cluster, the number of clustered pixels divided by the cluster area. Higher density implies lower clutter, because similarly colored pixels are packed more closely together, giving an impression of less complexity. Saliency is calculated as the difference in color between each cluster and all adjacent clusters. High saliency in a region with low density predicts the greatest clutter (see Ref. 2 for more details about C3).

Beck et al.[1] demonstrated that at least two interacting measures of clutter (using C3) are needed to (1) predict target detection performance (measured as response time) and (2) model limitations on attention during visual search of complex displays. These two measures are global clutter (the average clutter of the entire display) and local clutter (the clutter immediately surrounding the target). The authors found that, in

complex geospatial displays, global clutter can represent set size, and local clutter can represent crowding, both of which impact the limits on attention during visual search.

In an effort to better understand the effects of clutter on visual search and target detection performance, the authors examined search strategies by tracking the pattern of eye movements. They found that people tend to start searching in less cluttered areas and progress to more cluttered areas as needed to find a target.[3] The authors designed a follow-on experiment to test and validate that claim, the results of which are published here.

Method: Forty-two undergraduates from the Louisiana State University (LSU) participated for course credit. Stimuli were cropped sections (740 × 580 pixels) of digital aeronautical charts. Thirty-six charts were selected such that their global C3 values were equally spaced from the least-cluttered chart (#1, C3 = 0.95) to the most-cluttered chart (#36, C3 = 9.29). Two versions of each chart were created: one with a target in a relatively low local-clutter area of the chart, and the other with a target in a relatively high local-clutter area. In each case, the target was a single-bump obstacle symbol (17 × 16 pixels) randomly overlaid on the charts.

Charts were presented on a 19-in. CRT monitor. Subjects rested their heads in a chin rest 40 cm from the screen. An EyeLink II (SR Research Ltd.) eye tracker presented the stimuli in random order and recorded key presses and eye movement data, including saccades and fixations. A saccade is detected when eye movement velocity is more than 30 degrees per second, and a fixation is detected when eye movement velocity is below this threshold. Subjects fixated on a dot in the center of the screen and pressed a key to begin. For each trial, a chart was presented, and subjects found the target as quickly as possible, pressing a button to indicate they had found it.

A fixation was considered to be on the target if it was within 36 pixels (2° visual angle) of the target. Otherwise, the fixation was said to be on some other, non-target feature. Local C3 values were calculated for 60 × 60 pixel sections of the charts centered on each non-target fixation, excluding the initial center-point fixation for each trial and all fixations after the subject found the target.

Results: Figure 6 (top) presents normalized C3 clutter (relative to global clutter) for non-target fixations, averaged by fixation index (where #1 is the first fixation in a given trial) across all subjects and all charts. The average number of fixations per trial was 50.2, and the median was 19.5, ranging from 1 to 403. Fixation #1 is excluded, since it was constrained to be

at the center of the display. The average local clutter of fixated regions first drops sharply (R = –0.97; R^2 = 0.94) from fixations #2 through #4, as subjects direct their attention away from the center point. Figure 6 (bottom) shows that the locations of these first few fixations are strongly influenced by the central starting point.

After fixation #4, however, the average clutter of fixated regions steadily increases, suggesting subjects tend to move from less cluttered regions of the display to progressively more cluttered regions until finding the target (Fig. 6, top). The last fixation index included in the analysis is fixation #24 because there were fewer than 50% of participants with fixation indexes higher than 24. The correlation between average fixation clutter and fixation index for fixations #4 through #24 is 0.93 (R^2 = 0.87). These findings are consistent with (and stronger than) those from Lohrenz and Beck.[3]

Average Normalized C3 over Time

Average distance from center, by fixation index
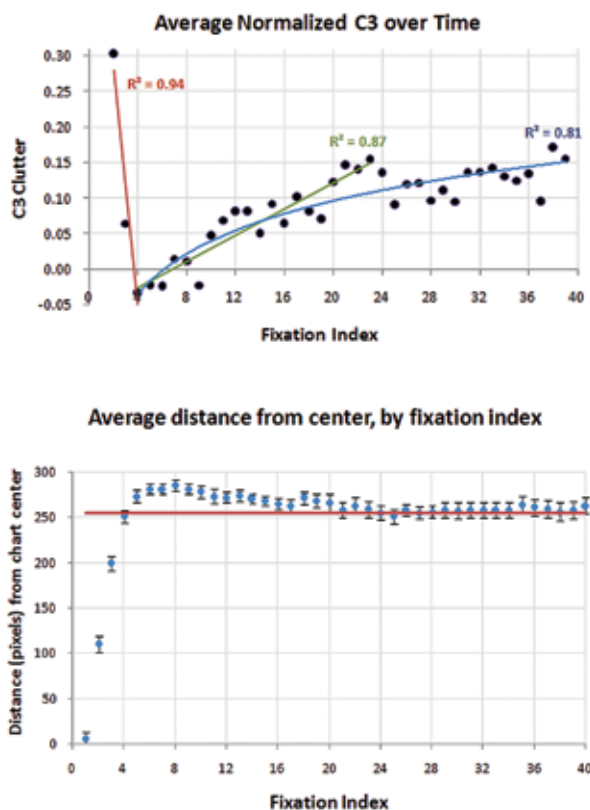
FIGURE 6

Top: The local clutter value for fixated regions of the chart (averaged by fixation index) drops sharply at the beginning of trials (fixations #2 through #4), then gradually increases as the search proceeds. The effect tapers off as fewer participants are left in a trial. Fixation #24 is the last fixation index for which at least 50% of participants fixated, on average. Bottom: The distance of fixations from the center of the chart (averaged by fixation index, across all subjects and charts) shows that the locations of the first four fixations of each trial are strongly influenced by the central starting point. The maximum possible distance from the center of the chart to a fixation (i.e., in a chart corner) is 470 pixels. Error bars represent 2 standard errors of the mean.

Examination of eye movements during this search task also reveals that participants were using a "coarse-to-fine" search strategy in charts of all levels of clutter; as search progresses, the duration of fixations increases, while saccade distance (between adjacent fixations) decreases (Fig. 7). This "coarse-to-fine" search strategy is not necessarily the most efficient. The authors found that participants using a global attention strategy (fewer and longer fixations) from the start of a trial found the target faster, especially in the high local-clutter condition (Fig. 8). However, this strategy was not typically seen until later in a trial (Fig. 7).
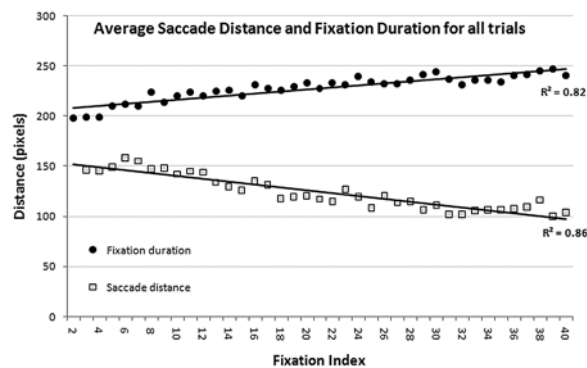
FIGURE 7
Participants used a "coarse-to-fine" search strategy in charts of all levels of clutter; as search progressed, the duration of each fixation increased and the distance between fixations decreased.
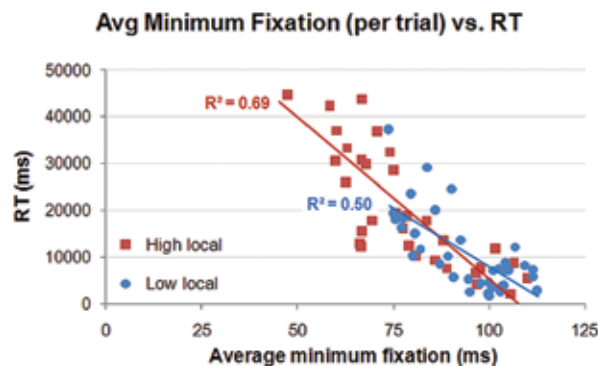
FIGURE 8
Participants with longer minimum fixations found the target faster, suggesting that a global attention strategy (longer and fewer fixations) was more efficient, especially in the more difficult high local-clutter condition.

Conclusions: This report describes several visual search strategies observed in participants during a target detection task with complex aeronautical charts. Participants tended to initially seek out less cluttered regions of the chart to begin their search, only searching in more cluttered regions if needed to find the target. These results validate earlier experiments.[3]

Likewise, at the start of trials, participants tended to use shorter fixations and longer saccades (i.e., quickly refocusing attention to different parts of the chart), and gradually transitioned to longer fixations with shorter saccades as the trial progressed. This is not the most efficient search strategy, however, since participants who tended to use fewer and longer fixations throughout a trial found the target faster. This suggests that it might be possible to train people to be more efficient searchers by training their patterns of eye movements.

References
[1] M.R. Beck, M.C. Lohrenz, and J.G. Trafton, "Measuring Search Efficiency in Complex Visual Search Tasks: Global and Local Clutter," *Journal of Experimental Psychology: Applied* **16**(3), 238–250 (2010).
[2] M.C. Lohrenz, J.G. Trafton, M.R. Beck, and M.L. Gendron, "A Model of Clutter for Complex, Multivariate, Geospatial Displays," *Human Factors* **51**(1), 90–101 (2009).
[3] M.C. Lohrenz and M.R. Beck, "Evidence of Clutter Avoidance in Complex Scenes," Proceedings of the Human Factors and Ergonomics Society 54th Annual Meeting, San Francisco, CA, September 2010, pp. 1355–1359.

Materials Science and Technology

FREND (2008) — NRL developed and ground-demonstrated guidance and control algorithms to allow a robotic servicing vehicle to autonomously rendezvous and dock with satellites not pre-designed for docking. The demonstration was completed in a realistic spaceflight environment under full autonomy with no human-in-the-loop assistance.

Laser Printed MEMS and Electronic Devices

A.J. Birnbaum,[1] H. Kim,[1] R.C.Y. Auyeung,[1]
N.A. Charipar,[1] K.M. Metkus,[2] S.A. Mathews,[1]
and A. Piqué[1]
[1]*Materials Science and Technology Division*
[2]*NOVA Research, Inc.*

Introduction: The vast majority of devices and structures fabricated at the micro-scale and nanometer scale rely on the use of lithographic methods developed decades ago for the microelectronics industry. These methods, while ideal for batch, wafer-based manufacturing, suffer from significant limitations due to material incompatibilities (temperature and chemical resistance), the inability to fabricate based upon nonplanar or curved architectures, and overall process inflexibility.

Interest in digital printing techniques for generating patterns or structures nonlithographically continues to grow. Nonlithographic processes offer relatively low cost, the potential for scalability, inherent flexibility, compatibility with low temperature, and compatibility with nonplanar substrates. Through one such technique, the laser decal transfer (LDT) process developed at NRL, we have demonstrated the fabrication of a range of micron-scale components and devices; these include as-deposited, free-standing structures for sensing/actuation without the use of sacrificial release layers; 3D interconnects; cavity sealing membranes; and multilayered polymer/metal capacitors.

Free-Standing Structures: Traditional lithographic techniques almost always rely on removing (etching) sacrificial layers in order to generate free-standing features such as micro-cantilevers for sensing/actuating applications. This etching process represents three to four additional steps in fabrication, as well as the loss in sacrificial material. Using NRL's LDT process in conjunction with specially developed high-viscosity nanocomposites, we have been able to directly print free-standing beams[1] and membranes[2] in an as-deposited manner — that is, without the need for any sacrificial materials or release processes. We have rigorously characterized both the dynamic response of these structures via laser vibrometry, and the mechanical properties via nanoindentation and finite element simulation. Figure 1 shows a schematic of the process and two examples of free-standing components we have produced and characterized.

Electronic Devices: Printed electronics have received a great deal of interest in recent years due to their compatibility with low-cost, high-throughput

manufacturing techniques such as roll-to-roll processing. The ability to print electronics on nonplanar surfaces is also extremely attractive for DoD-relevant applications and Navy platforms, such as conformal antennae on the wings of an unmanned aerial vehicle (UAV). We have demonstrated the ability to print many types of structures such as 3D interconnects[3] and microscale capacitors[4] via the LDT process. These are shown in Fig. 2. Printing interconnects in a noncontact manner provides the potential for significantly reducing the space required by traditional wire bonding techniques and therefore allows more devices to be embedded within a given area. Furthermore, single laser pulse printing of multilayered laminate structures allows for extremely efficient placement of devices in an "on-demand" fashion. These two abilities applied in tandem serve as key elements for the nonlithographic fabrication of entire circuits.

Finally, in addition to the techniques detailed above, we are developing direct-write processes for printing over large areas in a parallel fashion. Figure 3 shows a laser-printed pattern made by integrating a digital micromirror device (DMD) into our present laser direct-write setup.[5] It is seen that this advancement allows us to dynamically alter the desired pattern to be printed "on the fly." It also shows that instead of having to, for example, build up the "R" one pixel at a time, the entire letter or even word "NRL" can be printed simultaneously from a single laser pulse. This capability is unique to laser printing since no other direct-write technique is capable of printing reconfigurable 3D pixels, or voxels, and represents a significant advance in throughput.

Moving Forward: In order to integrate microscale devices and components into existing nonplanar architectures and with nontraditional materials, it is necessary to move beyond the lithographic, wafer-based paradigm. The laser printing methods developed at NRL provide the pathway for providing nonlithographic solutions for small-scale device fabrication without suffering from the drawbacks and limitations of its lithographic counterparts. Furthermore, these laser printing processes lend themselves to being developed for low-cost, high-throughput manufacturing techniques which can prove invaluable for enhancing Navy-relevant technologies.

References
[1] A.J. Birnbaum, R.C.Auyeung, K.J. Wahl, M. Zalalutdinov, A.R. Laracuente, and A. Piqué, "Laser Printed Micron-Scale Free Standing Laminate Composites: Process and Properties," *Journal of Applied Physics* **108**, 083526 (2010), doi:10.1063/1.3492708.
[2] A.J. Birnbaum, M. Zalalutdinov, K.J. Wahl, and A. Piqué, "Fabrication and Response of Laser-Printed Cavity-Sealing
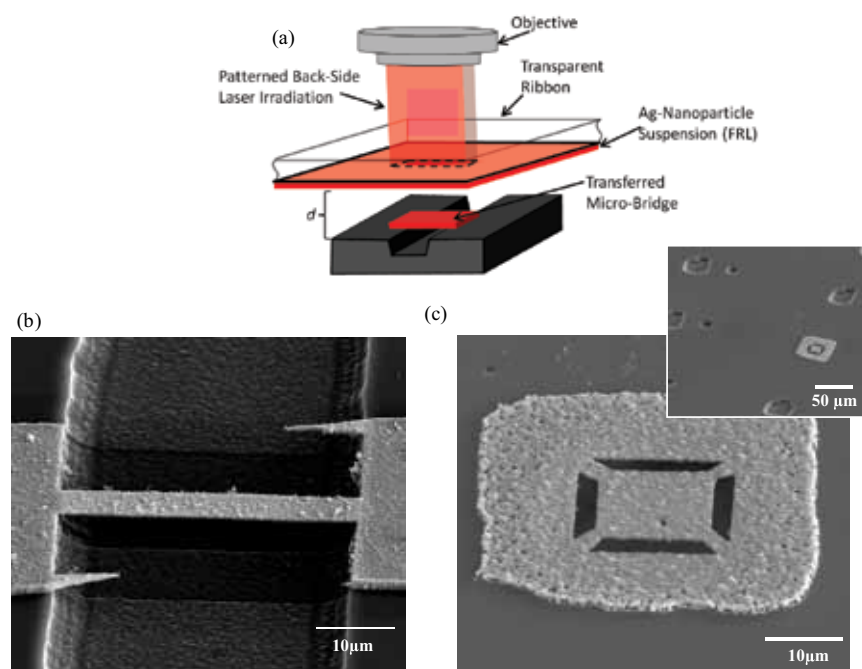
FIGURE 1
(a) Schematic of the laser decal transfer process over a prefabricated microchannel. (b) Electron micrograph of a laser-printed micro-bridge over a prepatterned Si channel. (c) Electron micrograph of a suspended, cavity-sealing membrane that has been milled with a focused ion beam for use as a bolometer. Inset is a low-magnification view of the suspended structure and uncovered cavities.
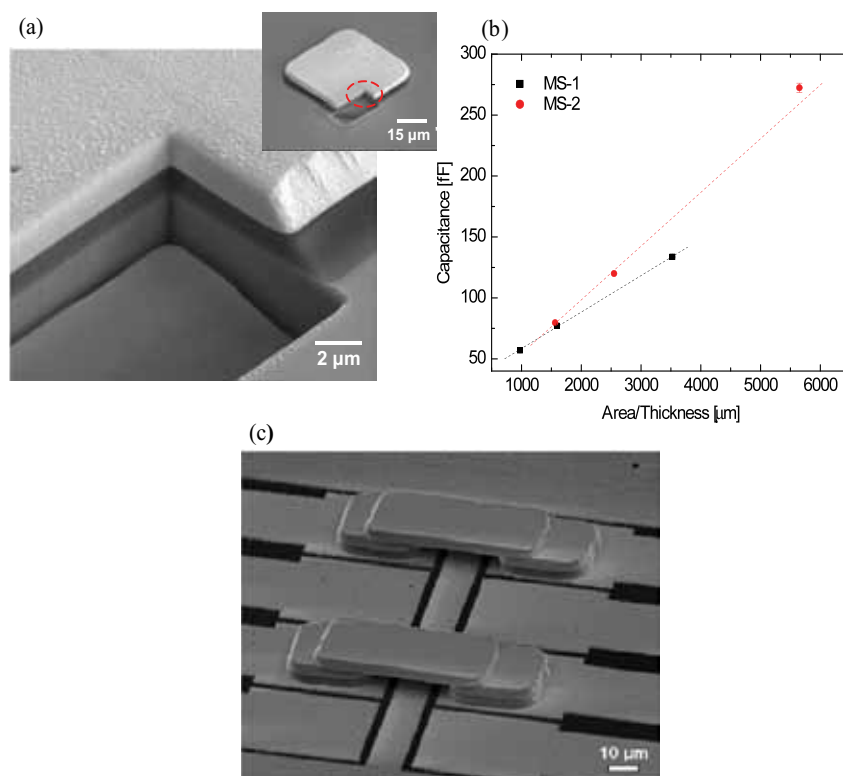
FIGURE 2
(a) Electron micrograph of a cross section of a multilayered Ag/polymer stacked hetero-structure capacitor; inset: low-magnification SEM of individual transfer. (b) Capacitance measurements on two different Ag/polymer combinations (MS-1 and MS-2). (c) Electron micrograph of free-standing laser-printed 3D interconnects.
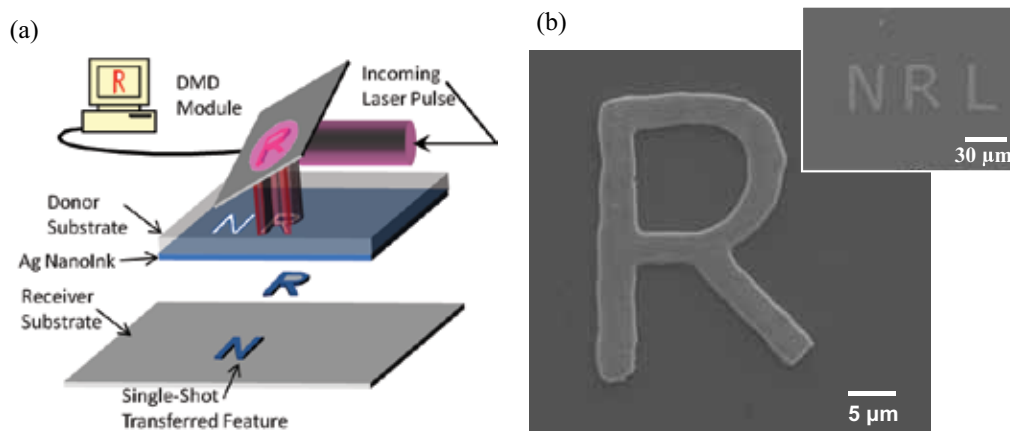
FIGURE 3
(a) Schematic of laser printing technique with integrated digital micromirror device. (b) Electron micrograph of parallel laser printed pattern demonstrating quality and resolution of current setup; inset: low-magnification image.

Membranes," *Journal of Microelectromechanical Systems* **20**(2), 436–440 (2010), doi:10.1109/JMEMS.2011.2105251.

[3] J. Wang, R.C.Y. Auyeung, H. Kim, N.A. Charipar, and A. Piqué, "Three-Dimensional Printing of Interconnects by Laser Direct-Write of Silver Nanopastes," *Advanced Materials* **22**, 4462–4466 (2010), doi:10.1002/adma.201001729.

[4] A.J. Birnbaum, H. Kim, N.A. Charipar, and A. Piqué, "Laser Printing of Multi-Layered Polymer/Metal Heterostructures for Electronic and MEMS Devices," *Applied Physics A* **99**, 711–716 (2010), doi:10.1007/s00339-010-5743-8.

[5] R.C.Y. Auyeung, H. Kim, N.A. Charipar, A.J. Birnbaum, S.A. Mathews, and A. Piqué, "Laser Forward Transfer Based on a Spatial Light Modulator," *Applied Physics A: Materials Science and Processing* **102**, 21–26 (2010), doi:10.1007/s00339-010-6054-9.

■

Microstructural Evolution During Friction Stir Welding of Titanium

R.W. Fonda and K.E. Knipling
Materials Science and Technology Division

Introduction: Friction stir welding (FSW) has become an important joining technique for aluminum alloys, and promises many benefits in the joining of other alloys. In FSW, a rotating, nonconsumable tool is plunged into and traversed along the joint line of a softer material, generating frictional and deformation-induced heating that softens the surrounding material without melting it, allowing the two sides of the solid metal to be "stirred" together. Since no melting is involved, many problems normally associated with conventional welding are reduced or eliminated.[1]

The microstructural evolution occurring during FSW of titanium alloys can be very complex. The rotating tool introduces shear deformation into the surrounding material, and the heat generated during welding can transform the hexagonal low-temperature α phase to a cubic high-temperature β phase, which reverts back to the α phase during cooling. The heat of welding can also induce grain growth and deformation recovery within the welded regions.

The Friction Stir Weld: The weld examined in this study was fabricated in a 12.7 mm (0.5 in.) thick plate of Ti-5111, a near-α titanium alloy with a composition of Ti-5Al-1Sn-1Zr-1V-0.8Mo (in wt %) developed for superior toughness and corrosion resistance in marine applications. The weld was prepared with a simple tool with a truncated conical shape and a narrow shoulder.[2] The original baseplate (BP) microstructure consists of large (~5 mm) prior β grains containing colonies of parallel α laths. By comparison, the weld stir zone (SZ) adjacent to the tool and in the deposited weld consists of fine (~10–20 μm diameter) equiaxed prior β grains containing different orientations of much finer α laths. This microstructure indicates that the peak temperature in the SZ was sufficiently high to fully transform the BP material to β during welding. Separating the BP from the SZ is a relatively narrow (~500 μm wide) thermomechanically affected zone (TMAZ). The objective of this study is to understand the microstructural evolution that occurs across this narrow TMAZ.

Microstructural Evolution Across the TMAZ: Since the deformation introduced by the rotating tool is mostly confined to the two-dimensional plane of the plate, the microstructural evolution is best revealed by sectioning the weld terminus in plan-view at the mid-thickness of the baseplate (see Fig. 4(a)). Various regions around the tool exit hole and in the deposited
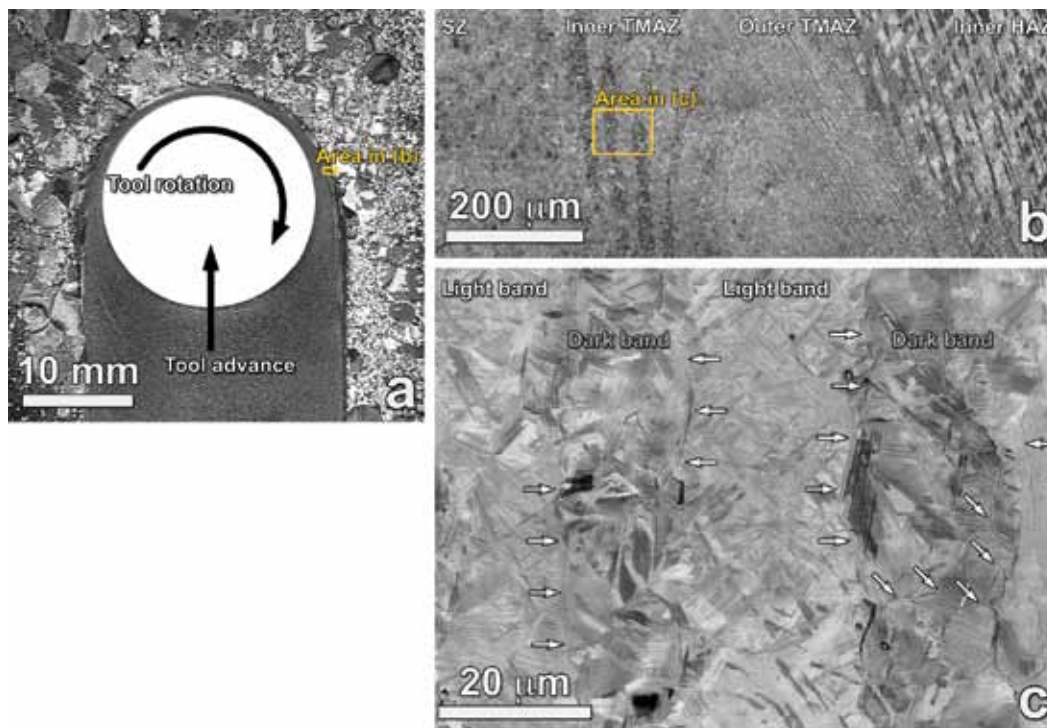
FIGURE 4
(a) Optical micrograph of the mid-thickness weld terminus, and backscattered electron micrographs (b) across the transition region and (c) of the microstructural characteristics of the bands.
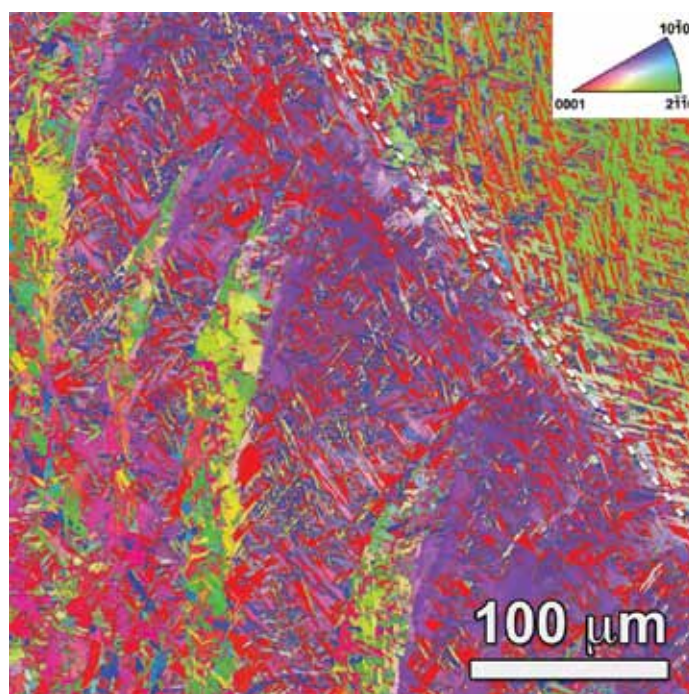
FIGURE 5
Orientation map showing the microstructural evolution across the TMAZ.
Colors represent the orientations shown in the inset.

weld were examined, but this discussion focuses on a single region (shown in Figs. 4(b) and 5) that best illustrates the evolutionary processes. In the outer portions of the TMAZ, the shear deformation produced by the rotating tool effects a gradual rotation of the grains. Concurrently, the heat generated during welding partially transforms this region to β, resulting in refined α lath variants (Fig. 4(b)) and new α lath orientations (Fig. 5) that are all related to the original β phase orientation. An abrupt ~10° rotation (dotted line in Fig. 5) in the middle of this region aligns the α phase close-packed directions along the shear direction imposed by the rotating tool.

The inner TMAZ has a banded appearance. Detailed analysis of the bands reveals that the light/purple bands (see Figs. 4(c) and 5) have a microstructure with multiple refined α lath orientations and no prior β grain boundaries, similar to that observed in the outer

the tool, the high temperatures fully transform the material to β, which is readily deformed by the rotating tool. Further from the tool, where the material is only partially transformed to β, there is a gradient of microstructures (and thus flow strengths) resulting from the thermal gradient across this region. Due to this incomplete transformation, deformation of this region is more difficult. Some limited deformation can be achieved through a fragmentation of the microstructure into blocks that individually rotate, establishing a discontinuous lattice rotation in the middle of the TMAZ. This will produce micro-shear bands between the blocks to satisfy the local geometric constraints (Fig. 6(b)). Within the rotated blocks of partially transformed material, continued deformation is constrained by the remaining primary α so that little further rotation occurs along the length of those blocks. However, the localized deformation within the micro-
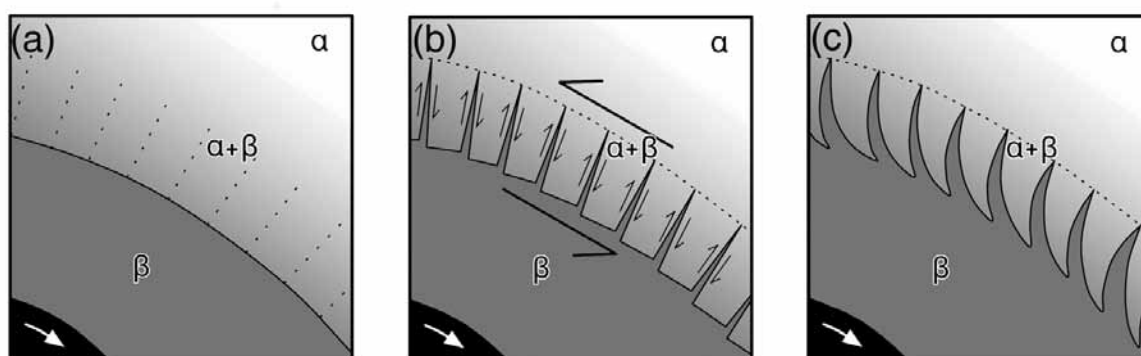
FIGURE 6
Schematic of the microstructural evolution during FSW of Ti-5111.

TMAZ. The only significant differences between the inner TMAZ and outer TMAZ are the 10° rotation between them and the larger fraction of refined α laths in the inner TMAZ, indicating a more complete transformation to β before cooling. Thus, these bands are a continuous extension of the original microstructure observed in the BP and outer TMAZ. Alternatively, the dark/green bands have a microstructure of very small (~10 μm diameter) prior β grains containing fine, parallel α laths. The α phase delineating both the prior β grain boundaries (diagonal arrows in Fig. 4(c)) and the interband boundaries (horizontal arrows) demonstrates that this dark/green band completely transformed to β during welding. It is interesting to note that, despite the close proximity of these two bands, the light/purple bands maintain a similar orientation along their length while the dark/green bands exhibit extensive (~110°) rotations along their length.

Proposed Mechanism: The mechanism proposed to explain the observed microstructural features and their evolution is summarized in Fig. 6. In the SZ near

shear bands will locally raise the temperature and may fully transform the material in the shear bands to the high-temperature β phase, making it susceptible to extensive (>90°) shear-induced rotations due to the lower flow stress of the β phase. These shear bands expand in width as they experience higher temperatures near the tool, and their microstructure extends continuously into the SZ microstructure near the tool (Fig. 6(c)).

The continuous evolution of these two bands from a common original orientation indicates that the microstructure observed in both bands, as well as in the SZ near the tool, evolved directly from the BP microstructure through a continuous process of transformation, deformation, and recovery.

References
[1] R.S. Mishra and Z.Y. Ma, "Friction Stir Welding and Processing," *Mater. Sci. Eng. R* **50**(1–2), 1–78 (2005).
[2] K.E. Knipling and R.W. Fonda, "Texture Development in the Stir Zone of Near-α Titanium Friction Stir Welds," *Scripta Mater.* **60**(12), 1097–1100 (2009).

Advanced Dielectric Composites with Templated Microstructure through Freeze Casting

E.P. Gorzkowski and M.-J. Pan
Materials Science and Technology Division

Background: The fabrication of composite dielectric materials to combine the functionalities of constituents in one structure is often limited to very simple configurations, such as randomly distributed particles in a continuous matrix. This is largely due to the lack of an appropriate technique to control the particle assembly process to achieve complex configurations efficiently. In this study, we utilized a freeze casting technique to create a lamellar microstructure with ice as a template. The objective is to fabricate ceramic-polymer composites with a dielectric constant at least ten times higher than that of the conventional random mixture approach. This was achieved by arranging the two phases in an electrically parallel configuration to obtain extremely high permittivity.

The Freeze Casting Process: High permittivity ceramic powder is mixed with dispersant, binder, plasticizer, and water to form an aqueous slurry. The slurry is placed in a mold and frozen unidirectionally in a controlled temperature gradient. This is accomplished by placing the mold between two copper rods that are cooled with liquid nitrogen and controlled by band heaters as can be seen in Fig. 7. During freezing, the ice platelet growth front repels ceramic particles to form the interleaving ice/ceramic layered microstructure (Fig. 8). Subsequent freeze drying causes the ice to sublime, thus leaving the desired lamellar ceramic structure. This then may be sintered to improve its mechanical strength or other functionalities. Finally, the lamellar structure is infiltrated with a polymer material to form the desired ceramic-polymer composite.
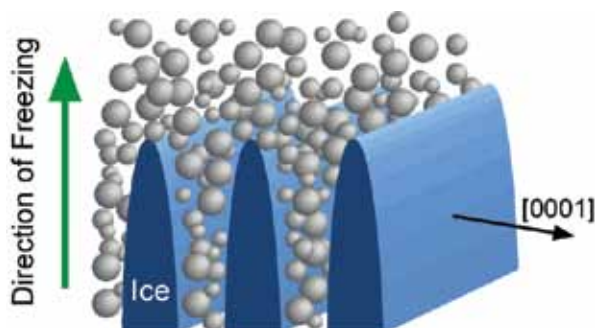
FIGURE 8
Schematic of directional freezing process.

Microstructure: A typical lamellar microstructure produced by the freeze casting approach is shown in Fig. 9. The platelet thickness is determined by the freezing rate and ceramic volume fraction. In general, the higher the freezing rate, the thinner the platelets and smaller the spacing. Our experimental data showed that, on a log–log scale, the slope of the platelet thickness versus ice growth velocity plot is –0.5, which is consistent with theoretical predictions.[1] The thickness also increases with the ceramic volume fraction up to 60 vol %, beyond which the microstructure breaks down due to insufficient water to push the ceramic out of solution, resulting in dendritic growth.

FIGURE 7
Directional freezing apparatus.
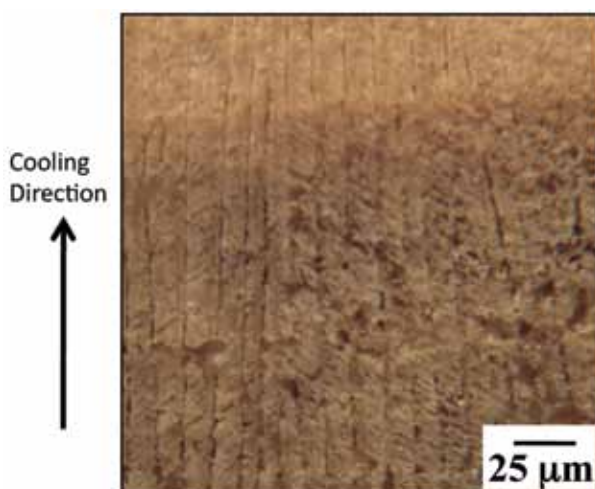
FIGURE 9
Light optical microscopy (LOM) image of a typical lamellar microstructure produced from the freeze casting process.

Properties and Applications: The resulting dielectric constant (K) is at least one order of magnitude higher than that of a conventional random mixture, as shown in Fig. 10. The maximum K achieved using barium titanate powder (BT) at 35 vol % is approximately 800, compared to 70 in a random mixture. When PMN-PT (lead magnesium titanate–lead titanate) powder is used, the maximum K increases to 2000 (versus 20 for random). The dramatic increase in freeze-cast samples is due to the connectivity/percolation in the ceramic phase. We showed that there is a linear relationship between the composite dielectric constant and the ceramic volume fraction, and the K approaches the rule-of-mixture prediction (Fig. 11). An unexpected advantage of the dielectric composite is the graceful failure mode. While conventional ceramic capacitors fail catastrophically, our composite self-clears after a breakdown event. That is, it maintains the capability to sustain high voltage loading — a highly desirable characteristic in high K dielectrics. The benign failure mode is attributed to the local clearing of electrode material near the breakdown spot.

The composite also exhibits excellent piezoelectric properties. The piezoelectric coefficient of a 35 vol % lead zirconate titanate (PZT-5A)–epoxy composite was ~250 pC/N, comparable to that of monolithic PZT-5A. Moreover, the 2-2 connectivity of the phases, flexibility in tailoring platelet spacing, and ease of fabrication make the composite a good choice for high-frequency transducer applications. In collaboration with the University of Southern California, a 58 MHz medical transducer for high-resolution imaging was demonstrated successfully.[2]
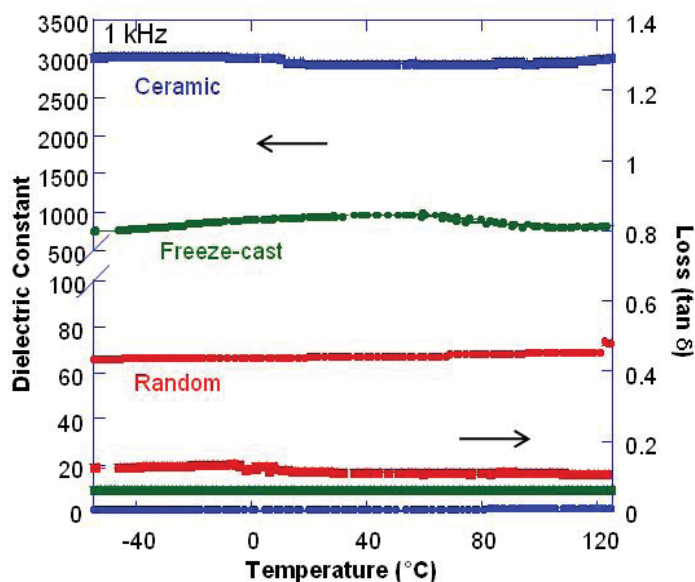
FIGURE 10
Comparison of dielectric constant vs temperature data for 35 vol % barium titanate samples created with different processes.
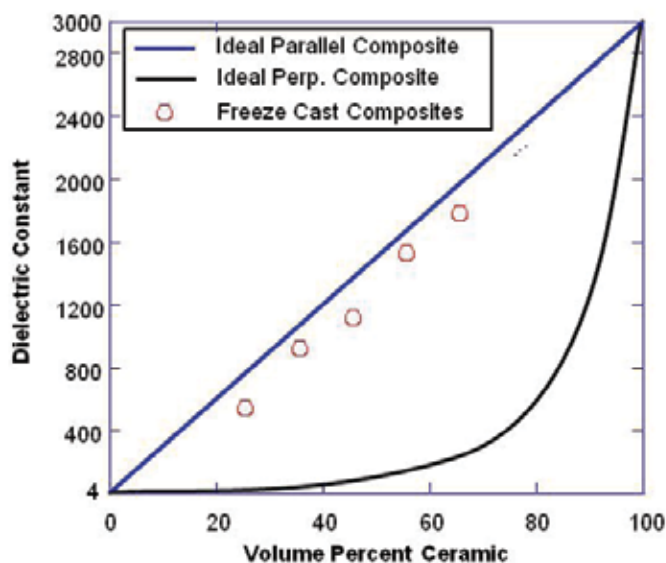
FIGURE 11
Dielectric constant vs volume percent ceramic.

Continuous Casting: The technique is being adapted to a continuous casting process on a tape caster. The major hurdle to such a process transition is the freeze drying of ice, which requires high vacuum that is difficult, if not impossible, to achieve in a continuous process. Consequently, we switched to camphene as the freeze medium, as it exhibits low melting temperature (45 °C) and readily sublimes at atmospheric pressure and room temperature. The corresponding adjustment of slurry formulation was accomplished successfully. Although the resulting microstructure is not as anisotropic as in the aqueous case, the connectivity of the ceramic phase still leads to respectable permittivity.

Summary: This study demonstrated the feasibility, utility, and flexibility of the freeze casting technique for fabricating ceramic-polymer composites. By controlling the freezing of a ceramic slurry, one introduces aligned templates to achieve the desired composite microstructure. The correlation between processing condition, microstructure, and properties was established quantitatively. Most notable, the dielectric constant can be two orders of magnitude higher than that of a random mixture. In addition, the composite's merit as the active element in a high-frequency medical transducer was also demonstrated. The current research focus is to shift the water-based process to a camphene-based process for continuous processing to facilitate future transitions.

[Sponsored by NRL]

References

[1] H. Zhang, I. Hussain, M. Brust, M.F. Butler, S.P. Rannard, and A.I. Cooper, "Aligned Two- and Three-dimensional Structures by Directional Freezing of Polymers and Nanoparticles," *Nat. Mater.* **4**(10), 787–793 (2005).

[2] B.P. Zhu, Q.F. Zhou, C.H. Hu, K.K. Shung, E.P. Gorzkowski, and M.J. Pan, "Novel Lead Zirconate Titanate Composite via Freezing Technology for High Frequency Transducer Applications," *J. of Advanced Dielectrics*, **1**(1), 85-89 (2011).

■

Novel Air Purification Materials

B.J. White,[1] B.J. Melde,[1] G.W. Peterson,[2] and B.J. Schindler[3]
[1]*Center for Bio/Molecular Science and Engineering*
[2]*Edgewood Chemical Biological Center*
[3]*Science Applications International Corporation*

Inhalation Threats: In 2009, the TIC/TIM Task Force released a document focused on toxic industrial chemicals and materials (TICs and TIMs) that pose a threat to the lungs and eyes of deployed troops.[1] The list of compounds is prioritized based on toxic hazard and the likelihood of an encounter. Compounds such as ammonia, sulfur dioxide, nitric acid, and cyanogen chloride are identified in the set of priority inhalation hazards. Traditional air purification materials employed by the military rely on porous carbons. Activated carbon, or activated charcoal, is utilized in a wide range of purification applications including some that are commonly encountered. Home water filtration, for example, relies on a carbon-filled cartridge. Through modification of these types of carbon materials, a number of functional moieties can be combined with the high surface area and adsorptive properties to provide air purification materials with improved characteristics or novel function. Efforts directed at improving the performance of carbon materials in air purification applications, including designing additional capacity for the priority TIC/TIM targets, are under way. Simultaneous efforts seek to provide alternatives to these materials. The effort described here falls into the latter category.

Novel Reactive Purification Materials: Our efforts in developing air purification materials have focused on mesoporous organosilicas which are materials that combine organic groups with inorganic silica components to produce sorbents with the properties of both. The materials are rugged and stable, withstanding temperatures of at least 200 °C and exposure to a wide range of chemical conditions. Organosilicate materials are synthesized as shown in Fig. 12. The resulting sorbents consist of particles that have large (~1 μm) pores with small pores (~5 nm) in their walls. The small pores provide the desired high surface area; the larger pores offer reduced resistance to flow and increased connectivity throughout the structure.

The organosilicate materials are the scaffold into which functional moieties are incorporated. One of the major classes of functionalities under consideration is porphyrins. Porphyrins strongly absorb visible light and fluoresce intensely (Fig. 13). They are also well-established electro- and photocatalysts. When compared to proteins and microorganisms, porphyrins are much less sensitive to variations in conditions such as pH and have been shown to withstand temperatures above 150 °C. Modifications to the structure of the porphyrins can be used to alter their binding and catalytic characteristics (Fig. 13). In the novel materials under development for air purification, porphyrins are covalently immobilized within the organosilicate scaffold, providing a high concentration of functional moieties in a low density material.[2]

Removal of Contaminants: Targets under consideration for these studies are ammonia, phosgene,
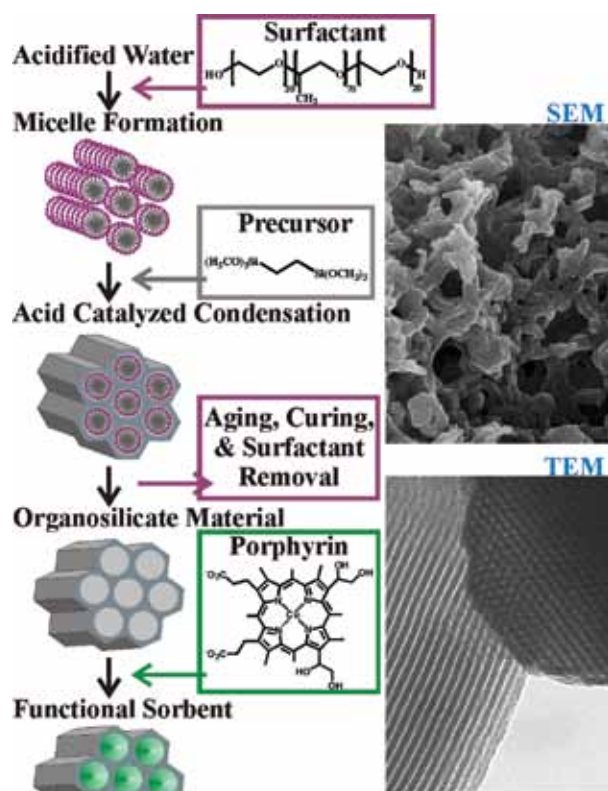
FIGURE 12
Synthesis and Morphology. Conditions are established to produce the formation of organized groups of surfactant molecules called micelles. Siloxane precursors, which have alternating organic and silicate groups, are then added to the solution. The surfactant micelles act as a template during condensation of precursors; the organized pore system (7.8 nm pores) is retained when the surfactant is removed. This is seen in the transmission electron microscopy (TEM) image. Phase separation during condensation leads to the formation of large features (~1 μm) in addition to the mesopores. These pores can be seen in the scanning electron microscopy (SEM) image. Porphyrins are grafted onto the surface of the organo-silicate materials following synthesis to provide a functional sorbent.

cyanogen chloride, sulfur dioxide, octane, and nitric oxide. Both the spectrophotometric response and the performance of the materials in micro-breakthrough experiments are being evaluated (Fig. 14). A single organosilicate scaffold has been combined with four different porphyrins at a range of loading levels and with varying metal ion incorporation. Using these materials variants, the potential of the porphyrin-embedded organosilicates has been demonstrated, and improved ammonia removal over a control material has been shown. We have also shown that phosgene removal is based on a reactive process rather than a physisorption mechanism. Using a copper porphyrin, the removal of two grams of phosgene per gram of sorbent has been demonstrated in less than five minutes, and repeated

exposure cycles show no decrease in performance. Removal of other targets can be enhanced through the use of functional groups. Primary amine groups, for example, increase the capacity for cyanogen chloride removal, and isocyanate groups increase the capacity for octane removal.

Applications: This reactive sorbent technology is being developed with a view toward offering enhanced protective capabilities in next-generation gas masks. The approach taken can, however, be applied to a wider range of air purification applications, such as the removal of formaldehyde from the air systems of buildings. Formaldehyde is one of the common off-gassing products from traditional adhesives and paints. The materials also offer a broader range of applicability
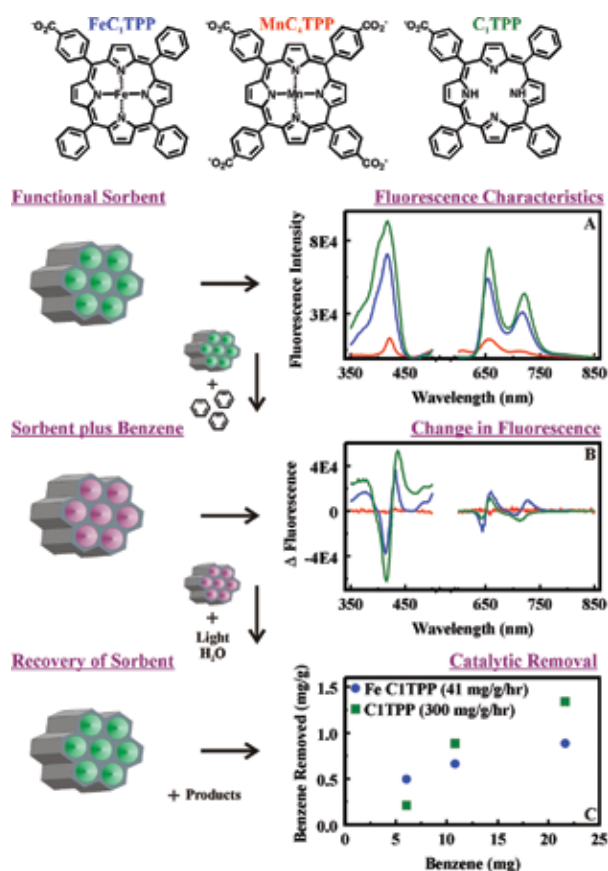
FIGURE 13
Porphyrins: Structure and Function. The structures of three representative porphyrins are presented: iron 5-mono(4-carboxyphenyl)-10, 15, 20-triphenyl porphine (FeC$_1$TPP, blue); manganese meso-tetra(4-carboxyphenyl) porphine (MnC$_4$TPP, red); and 5-mono(4-carboxyphenyl)-10, 15, 20-triphenyl porphine (C$_1$TPP, green). Incorporation of porphyrins into an organosilicate material yields sorbents with unique fluorescence characteristics (A), and changes in those characteristics upon target exposure also vary between materials (B). Alteration of the porphyrin structure impacts catalytic activity as shown here for the photoconversion of benzene (C).

Interaction of ammonia and CuDIXEG

Ammonia Breakthrough

BPL = 1.82 mol/kg

CuDIXEG = 4.89 mol/kg

Fluorescence Response

Pre-exposure
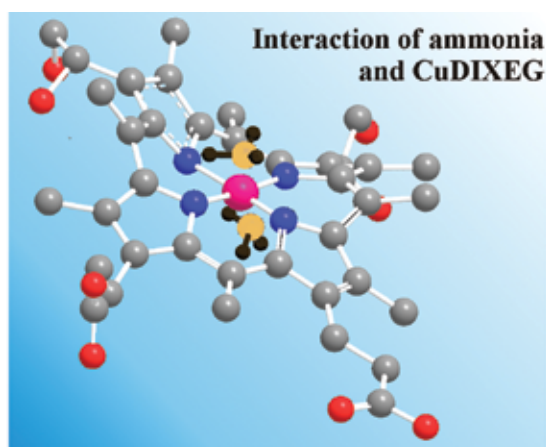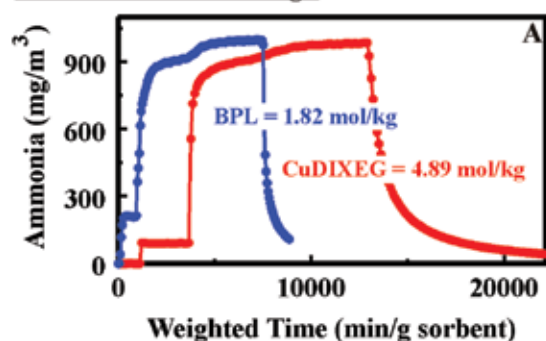
Post-exposure
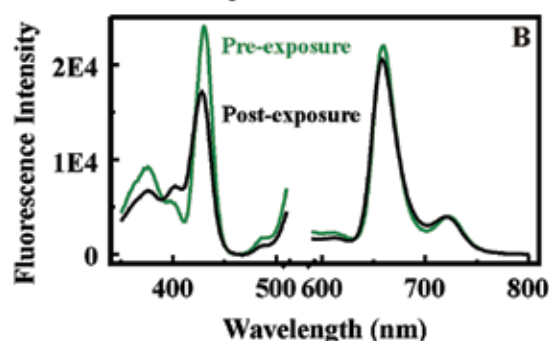
FIGURE 14

Sorbent Performance. Materials were evaluated as powders in a micro-breakthrough apparatus. The system uses a small sorbent sample packed into a tube, and target is delivered as a gas stream. The stream is continuously monitored for target breakthrough by infrared spectroscopy. (A) The porphyrin-embedded organosilicate sorbent (red) removed more ammonia than the BPL carbon control material (blue, functionalized with zinc and triethylene diamine, TEDA). (B) The fluorescence response to ammonia exposure for a porphyrin-embedded sorbent is also apparent when the fluorescence of the material before (green) and after (black) exposure are compared.

through the tunable nature of both the functional moiety and the organosilicate scaffold. Compounds such as traditional nerve agents and pesticides can be targeted through careful design of the organosilicate and selection of the porphyrin catalyst. These types of materials offer the potential for self-decontaminating fabrics and

surfaces. The novel sorbents also have potential relevance to sensing applications that utilize absorbance or fluorescence detection mechanisms. Overall, the materials and approaches described here are intended to provide enhanced capabilities in personal protective equipment for use by the warfighter and in chemically resistant coatings for use on military equipment.

References
[1] Toxic Industrial Chemical/Toxic Industrial Material Task Force, "TIC/TIM Task Force Prioritization & Application Recommendations," Joint Program Executive Office for Chemical and Biological Defense, http://www.dodsbir.net/sitis/view_pdf.asp?id=REF CBD11_107 FINAL TIC TIM Task Force 060109.pdf, Feb. 2009.
[2] B.J. Johnson, B.J. Melde, C. Thomas, A.P. Malanoski, I.A. Leska, P.T. Charles, D.A. Parrish, and J.R. Deschamps, "Fluorescent Silicate Materials for the Detection of Paraoxon," *Sensors* **10**(3), 2315–2331 (2010), doi:10.3390/s100302315.

Clementine (1994) — NRL built and operated the first spacecraft known to conduct autonomous operations scheduling. The Spacecraft Command Language (SCL) became a widely used standard for automating spacecraft.

Powered by Rust™

J.W. Long, M.B. Sassin, and D.R. Rolison
Chemistry Division

Making Rust Useful: The cost, country of origin, and environmental impact of state-of-the-art materials that store energy in batteries and electrochemical capacitors (ECs) propel the ongoing search for charge-storage materials beyond the oxides of nickel, cobalt, or ruthenium. By applying the design concept of "multi-functional electrode nanoarchitectures," pioneered by NRL's Advanced Electrochemical Materials Section,[1] we transform an otherwise uninteresting battery material, iron oxide (FeO*x*) — also known as rust — into a battery- and EC-relevant form in which the oxide is painted as a nanometers-thick coating on the walls of a sponge-like, conductive scaffold.

The Right Kind of Electrode Architecture: To incorporate FeO*x* as nanoscale rust into electrode nanoarchitectures, we have developed a low-cost, solution-based deposition process predicated on the redox reaction between aqueous potassium ferrate (K_2FeO_4, a strong oxidant) and the electron-rich surfaces of ultraporous carbon-based scaffolds (Fig. 1, top).[2] Our scaffold of choice is carbon-fiber-paper-supported carbon nanofoam, which offers us an ideal platform to design high-performance electrode architectures with such inherent and important attributes as high specific surface area (300–500 $m^2 g^{-1}$), high electrical conductivity (20–40 S cm^{-1}), through-connected networks of size-tunable pores (nanometers to micrometers), and synthetic scalability in length and width (~100 cm^2) as well as thickness (70–300 μm).

These device-ready carbon substrates have macroscale form factors that present challenges to achieving homogeneous coatings because the internal surfaces are non-line-of-sight and accessed by tortuous and size-disperse pore networks. We identified solution conditions to self-limit the reaction of ferrate at carbon, resulting in conformal deposits of FeO*x* nanoribbons (10–20 nm thick) that permeate the macroscopic thickness of the nanofoam substrate (up to 150 μm), while leaving the 3D plumbing of the carbon nanofoam intact (Fig. 1, bottom center).[2] The direct reaction of the ferrate precursor and carbon surface also ensures intimate physical and electrical association between the FeO*x* and the underlying carbon nanoarchitecture (Fig. 1, bottom right), which ultimately supports electrochemical performance and stability under challenging operating conditions. Characterization of the resulting materials by X-ray absorption spectroscopy confirms that the form of iron oxide produced by the ferrate–carbon reaction is a hydrated Fe(III)-oxide and a close relative of rust.

Enhanced Power with Well-Wired Rust: Bulk forms of FeO*x* perform poorly as electrode materials because of modest electronic and ionic conductivity, but when distributed as a nanoscale coating on a 3D conductor, such as carbon nanofoam, FeO*x* exhibits
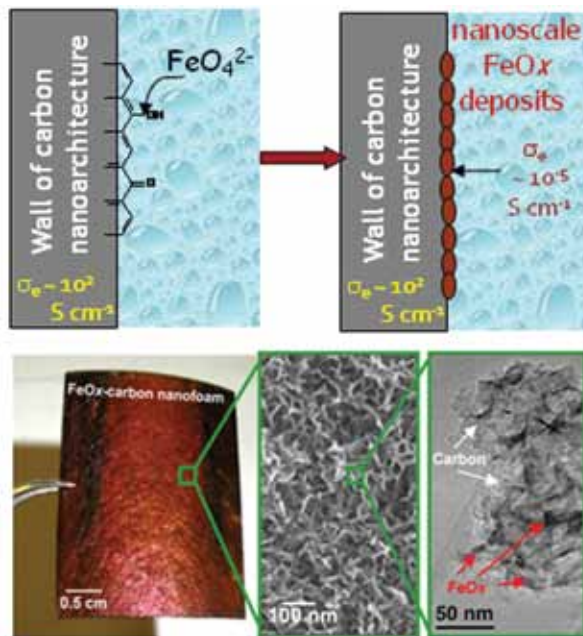
FIGURE 1
Schematic of FeO*x* deposition process (top); optical image (bottom left), scanning electron micrograph (bottom center), and transmission electron micrograph (bottom right) of an FeO*x*−carbon nanofoam.

high charge-storage capacity and rapid charge–discharge characteristics. Preliminary electrochemical measurements in mild aqueous electrolytes (e.g., 2.5 M Li_2SO_4) demonstrate that the addition of the FeO*x* coating, even at modest oxide mass loadings (~30 wt %), significantly increases the total mass- (3×), volume- (7×), and area-normalized (7×) capacitance of the carbon nanofoam (Fig. 2). The larger enhancement in the volume- and area-normalized capacitance results from the multifunctional electrode architecture design, because painting the walls of the nanofoam with FeO*x* does not increase the volume or geometric footprint of the electrode. The additional capacitance provided by the rust paint (~340 F per gram of FeO*x*) is due to the reversible electrochemical toggling of the Fe oxidation state between 3.0 and 2.7 (Fig. 2) and is threefold higher than previously reported for iron oxides tested under similar electrochemical conditions.[2] By designing the electrode as a multifunctional architecture we maximize the charge-storage utilization of the FeO*x* coating, while also projecting the ultrathin coating in three dimensions to achieve technologically relevant footprint-normalized metrics (2D: mF cm^{-2} vs 3D: F cm^{-2}).
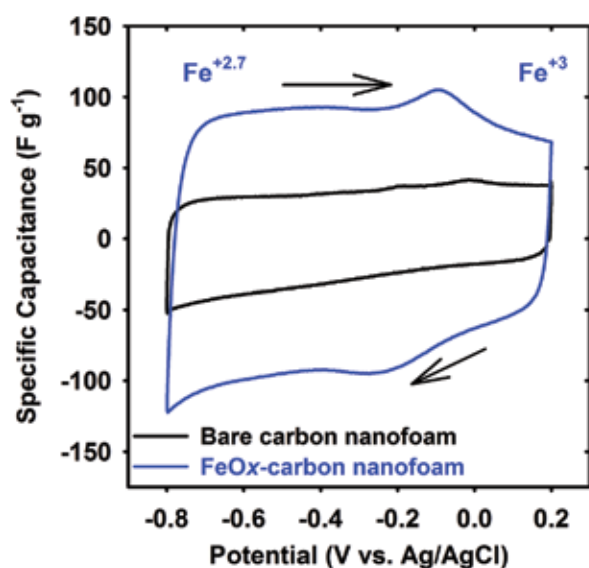
FIGURE 2
Specific capacitance vs potential for bare carbon nanofoam (black curve) and an FeOx–carbon nanofoam (blue curve) in 2.5 M Li$_2$SO$_4$ at 5 mV s^{-1}.

FIGURE 3
Schematic of an aqueous asymmetric EC cell with a MnOx–carbon nanofoam positive electrode and an FeOx–carbon nanofoam negative electrode (top left); optical image of prototype MnOx(+) | | FeOx(−) EC cell (top right); galvanostatic charge–discharge curves of a MnOx(+) | | FeOx(−) EC pouch cell between 0.2 and 1.8 V (bottom).

Devices and Batteries: Prototype asymmetric EC devices with FeOx–carbon as the negative electrode and analogously designed MnOx–carbon[3] as the positive electrode sustain operating cell voltages of ~2 V in mild aqueous electrolytes. The increased operating voltage beyond the thermodynamic window of H$_2$O (~1.2 V) is due to the poor hydrogen-evolution kinetics at the FeOx negative electrode (Fig. 3). Adding the extra energy of a wider voltage window to the enhanced charge-storage capabilities of the metal oxide–painted carbon nanofoams results in cell-level specific capacitances of >30 F g^{-1} and an energy density of 13.5 W h kg^{-1}; ECs composed of powder-composite electrode structures of MnOx and FeOx deliver only 7 W h kg^{-1}. The energy density of the EC prototype MnOx(+) | | FeOx(−) can be extracted within tens of seconds, revealing that the multifunctional electrode architecture enables enhancements in capacity and energy density while maintaining the high-rate capabilities characteristic of the underlying carbon nanofoam substrate. More recently, we demonstrated that the applications of these rust-painted structures extend beyond ECs to serve as high-performance anode materials for Li-ion batteries.

Summary: Next-generation ECs and batteries that incorporate these advanced electrode structures should bridge the current performance gap between the high energy density of batteries and the high power density of ECs. We can now design power sources that deliver energy over mission-relevant time scales as well as deliver on-demand burst-power in a single device.

This next generation of energy-storage devices will support such critical military and consumer applications as telecommunications, bridge/backup power, and hybrid-electric vehicles.

[Sponsored by ONR]

References
[1] D.R. Rolison, J.W. Long, J.C. Lytle, A.E. Fischer, C.P. Rhodes, M.E. Bourg, and A.M. Lubers, "Multifunctional 3D Nanoarchitectures for Energy Storage and Conversion," *Chem. Soc. Rev.* **38**, 226–252 (2009).
[2] M.B. Sassin, A.N. Mansour, K.A. Pettigrew, D.R. Rolison, and J.W. Long, "Electroless Deposition of Conformal Nanoscale Iron Oxide on Carbon Nanoarchitectures for Electrochemical Charge Storage," *ACS Nano* **4**, 4505–4514 (2010).
[3] A.E. Fischer, K.A. Pettigrew, D.R. Rolison, and J.W. Long, "Incorporation of Homogeneous, Nanoscale MnO$_2$ within Ultraporous Carbon Structures via Self-Limiting Electroless Deposition: Implications for Electrochemical Capacitors," *Nano Lett.* **7**, 281–286 (2007). ∎

Anomalously Large Linear Magnetoresistance Effects in Graphene

A.L. Friedman[1] and P.M. Campbell[2]
[1]*National Research Council Postdoctoral Associate*
[2]*Electronics Science and Technology Division*

Introduction: In the 1960s, it was discovered that interesting galvanometric behavior could result from the

addition of small inhomogeneities in device materials.[1] Specifically, Abrikosov developed a model for quantum linear magnetoresistance (LMR) in which a system confined to the "extreme quantum limit" at low temperature as a result of inhomogeneities that are small compared to the device size will exhibit a large, non-saturating LMR as opposed to the usual quadratic and then low-field saturating magnetoresistance (MR) of most conductors.[2] However, LMR is only now garnering attention because of the recent discovery of several narrow bandgap semiconductors with the high mobilities required of the Abrikosov model. Recent research has shown that there are classical analogues to quantum LMR.[3] By incorporating highly conductive impurities in devices in the form of metallic shunts,[4] these classical models predict that an even larger linear MR (called extraordinary magnetoresistance, or EMR) can be achieved. Graphene is a hexagonally ordered monolayer of carbon atoms that, due to its zero bandgap, high room-temperature mobility, and zero effective mass, provides the perfect platform for the realization of room-temperature LMR and EMR devices. These devices show much promise for future use as magnetic sensors and in memory device applications.

Quantum Linear Magnetoresistance: Despite predictions, LMR has yet to be observed in graphene devices because the large-amplitude Shubnikov–de Haas oscillations (SdHO) and quantum Hall effect observed in clean, homogeneous exfoliated graphene (the current experimental standard) overwhelm and obscure any linear dependence. However, epitaxially grown multilayer graphene devices on the carbon face of SiC can allow LMR observation because of their disorder. Raman spectroscopy (Fig. 4(d)) finds two types of inhomogeneity in the devices: (1) a variation of film thickness across the device with an average of 16 ± 3 nm and (2) a graphene grain size of ~1.5 μm, which is much smaller than the device length (~125 μm). Despite these inhomogeneities, research has shown that in multilayer epitaxially grown graphene, layers are essentially noninteracting and conduction properties are similar to those of single-monolayer graphene. Figure 4(a) shows quantum LMR from 2.2 K
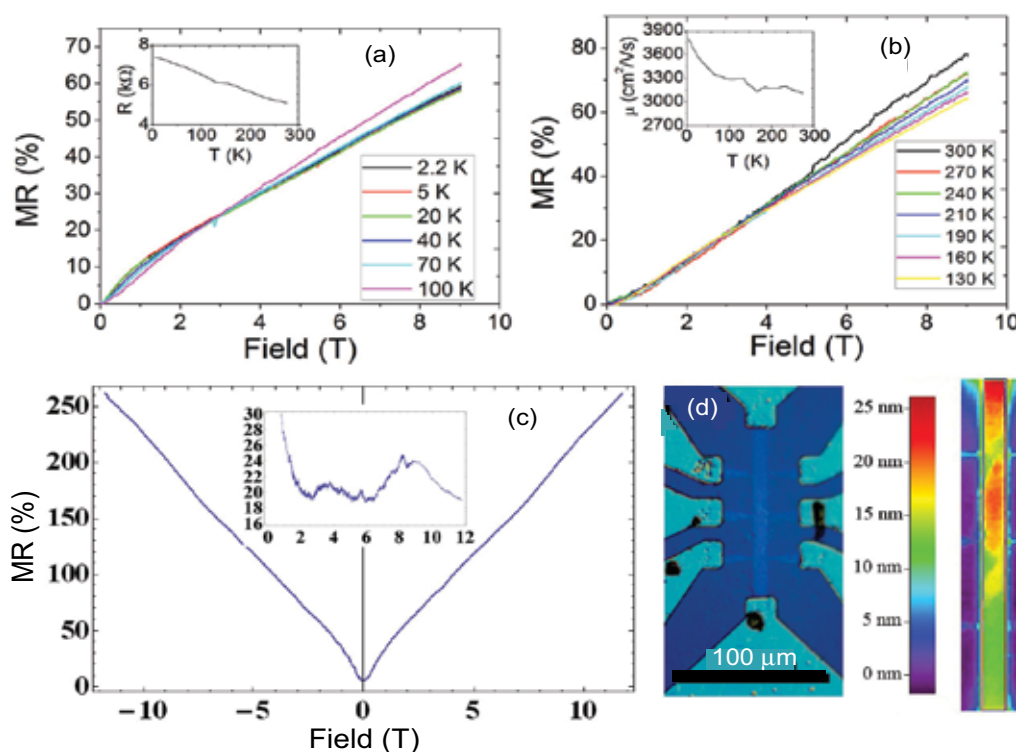
FIGURE 4
(a) Quantum LMR from 2.2 K to 100 K. The inset shows the resistance as a function of temperature. (b) Quantum LMR from 130 K to 300 K. The inset shows the mobility as a function of temperature. (c) Large MR value (250% at 12 T) obtained from a quantum LMR sample at 4.2 K. The inset shows the Shubnikov–de Haas oscillations at 4.2 K. (d) Nomarski image (left) showing the LMR device and corresponding Raman spectroscopy map (right) indicating inhomogeneities in the device necessary for the unmasking of the LMR behavior.
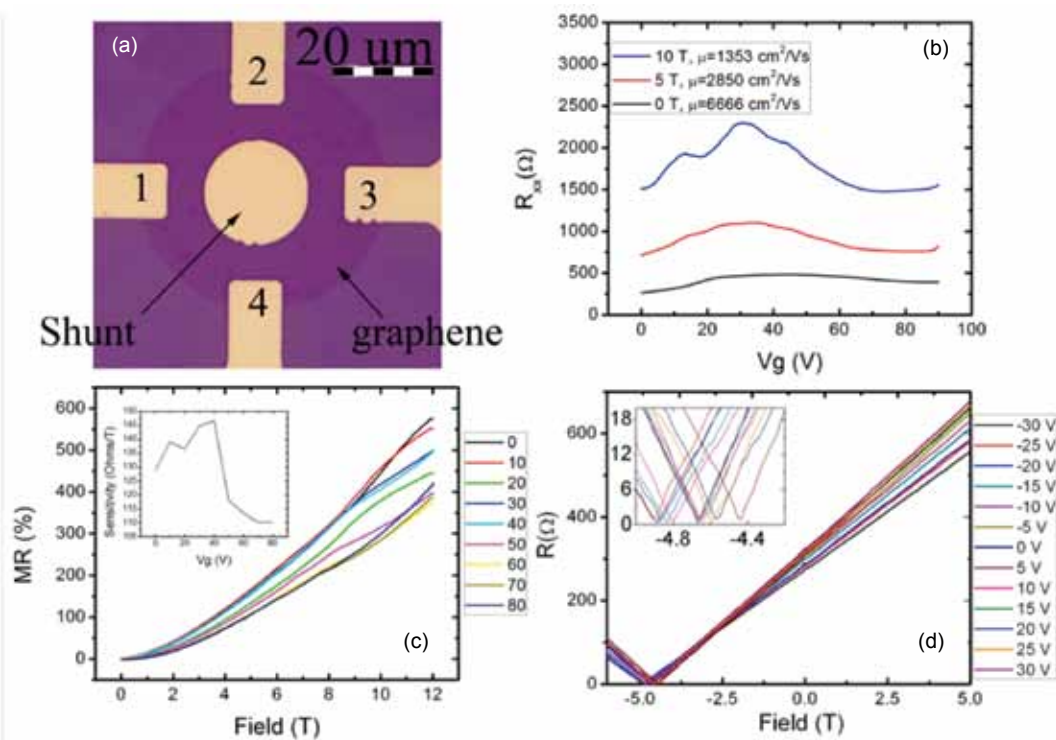
FIGURE 5
(a) Shunted graphene van der Pauw disk device. (b) Resistance vs gate voltage for several applied magnetic fields. (c) MR vs field for a variety of gate voltages. The inset shows the sensitivity as a function of gate voltage, which corresponds to the Dirac point. (d) Resistance vs field at a variety of gate voltages for the device operated in the Hall measurement configuration.

to 100 K. The behavior of the device changes very little over this temperature range. Figure 4(b) shows quantum LMR from 130 K to 300 K. To date, this is the only reported observation of room temperature quantum LMR. The insets of Figs. 4(a) and (b) show the resistance and the mobility, respectively, of the device as a function of temperature. It is precisely because of the small change in resistance and mobility as the temperature increases, along with graphene's zero effective mass, that the conditions for quantum LMR are satisfied even at room temperature. Figure 4(c) shows quantum LMR at 4.2 K in a sample in which the MR reached ~250% at 12 T. The small SdHO shown in the inset of Fig. 4(c) were extracted from the data and further attest to the quantum nature of the effect.

Extraordinary Magnetoresistance: Figure 5(a) shows an optical image of a shunted graphene device grown by chemical vapor deposition. Based on the calculated components of the conductivity tensor, in zero magnetic field, the current will flow through the shunt, while in a magnetic field, the current will tend to flow around the shunt and redistribute in the graphene film. The larger the magnetic field, the more current

flows through the graphene and not the shunt. This translates to an enhancement in the MR. EMR devices exploit geometric changes in devices to maximize MR signal. Therefore, the MR can be further maximized by changing the size of the shunt and the contact measurement configuration. Figure 5(b) shows a graph of resistance vs gate voltage at different magnetic fields. At zero field, the curve is relatively featureless. The mobility is very high as most of the current flows through the shunt. As the field increases, a Dirac point becomes evident and the mobility decreases, eventually to saturate at the mobility of the graphene film, as more current flows around the shunt and redistributes in the graphene. Hall oscillations become visible at 10 T. Figure 5(c) shows the MR of the device with the current (10 µA) passed between electrodes 1 and 4, and voltage measured between electrodes 2 and 3 at 4.2 K. The measured MR of ~600% at 12 T is the highest MR measured thus far in graphene. The inset of Fig. 5(c) shows the sensitivity of the device, which corresponds to the Dirac point. Figure 5(d) shows resistance measured in the Hall configuration (current passed between electrodes 1 and 3 and voltage measured between electrodes 2 and 4). The devices show a gate-tunable

minimum in MR instead of the usual zero MR at zero field, which is most likely caused by chemical dopants remaining from processing that are trapped beneath the shunt. This suggests that with controlled chemical doping, we can choose the position of this minimum and can exploit it for device purposes.

Conclusions: As the search for applications for graphene continues — particularly applications that do not require a bandgap or atomic-scale chemical modification — devices that make simple use of graphene's innate properties will become more important. The large, linear MR in both LMR and EMR can be used in a variety of applications including read-heads and magnetic sensors. Graphene is also easily scalable without compromising any of its inherent characteristics, which is an important difference over the narrow-gap semiconductors currently used in EMR device applications. We measure a signal-to-noise ratio of ~30 dB at 1 GHz and 50 mT, which makes these devices slightly better than similar devices made of narrow-gap semiconductors. With further optimization of materials and device design, these devices will likely offer sensitivities significantly better than the current state of the art.

[Sponsored by NRL]

References

[1] C. Herring, "Effect of Random Inhomogeneities on Electrical and Galvanomagnetic Measurements," *Journal of Applied Physics* **31**, 1939–1953 (1960).

[2] A. Abrikosov, "Galvanometric Phenomena in Metals in the Quantum Limit," *Sov. Phys. JTEP* **29**, 746 (1969).

[3] M.M. Parish and P.B. Littlewood, "Non-Saturating Magnetoresistance in Heavily Disordered Semiconductors," *Nature* **426**, 162–165 (2003).

[4] S.A. Solin, Tineke Thio, D.R. Hines, and J.J. Heremans, "Enhanced Room-Temperature Geometric Magnetoresistance in Inhomogeneous Narrow-Gap Semiconductors," *Science* **289**, 1530–1532 (2000).

■

Ocean Science and Technology

Vanguard (1958) — Vanguard I proved that solar cells could be used for several years to power satellite radio transmitters. Vanguard's solar cells operated for about 7 years, while conventional batteries powering another onboard transmitter lasted only 20 days.

Mixture Theory Model of Vortex Sand Ripple Dynamics

A.M. Penko and J. Calantoni
Marine Geosciences Division

Introduction: Our lack of understanding of the evolution of seabed roughness (e.g., sand ripples) in sandy coastal regions inhibits our ability to accurately forecast waves and currents and ultimately large-scale morphodynamics. Most wave and circulation models input a constant bottom roughness value (i.e., friction factor) or fixed bed profile that parameterizes the effects of seabed roughness, ignoring any temporal or spatial response of the bed to changing wave and sediment conditions. However, seabed roughness length scales may span three orders of magnitude (e.g., from grain-scale variations to sand ripples), causing significant differences in boundary layer turbulence, wave energy dissipation, coastal circulation, and sediment transport. The constant evolution of the seabed also has significant implications for naval operations (e.g., ocean acoustics, mine hunting missions, littoral navigation).

All bathymetric change ultimately results from sediment entrainment and deposition occurring at the fluid-sediment interface inside the wave bottom boundary layer (WBBL). Despite the apparent accessibility of the phenomena, highly turbulent, sediment-laden flow remains poorly understood and difficult to quantify mainly because of our failure to understand the fundamental interaction forces driving sediment transport. However, with recent advances in high performance computing, it is now possible to perform highly resolved simulations of fluid-sediment dynamics in the WBBL that accurately model the evolution of seabed roughness for sandy substrates. The high-resolution model described here (SedMix3D) is based on mixture theory. Although the approach is well known and understood for industrial and biological applications, it has never before been applied to coastal sediment dynamics.

Mixture Theory Model: Mixture theory treats a fluid-sediment mixture as a single continuum with effective properties that parameterize the fluid-sediment and sediment-sediment interactions (e.g., hindered settling, particle pressure, and diffusion). SedMix3D predicts the time-dependent sediment concentration and three-component velocity field under varying wave conditions. The bulk mixture parameters (e.g., density and viscosity) are dependent on the local sediment concentration of the fluid-sediment mixture. Grid spacing is on the order of a sediment diameter and time steps are nearly four orders of magnitude less

than the smallest turbulent fluid temporal scale. Using the Message-Passing Interface (MPI) for parallelization, SedMix3D may be run on up to 512 processors on high performance computing (HPC) architectures. The development and optimization of SedMix3D and the analysis presented here have utilized over 1.5 million CPU hours and over 5 TB of storage space provided by the DoD High Performance Computing and Modernization Program during the past two years.
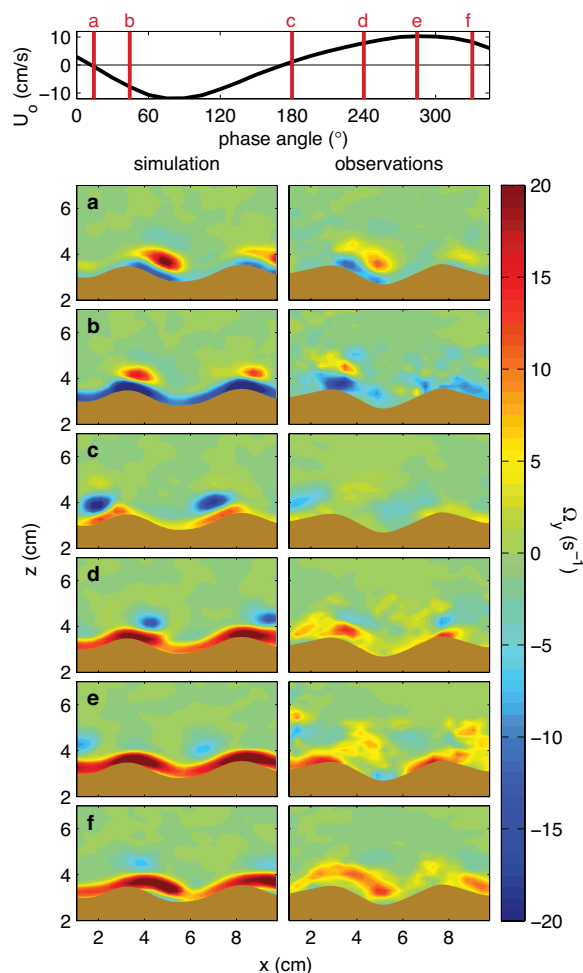
FIGURE 1
Ensemble-averaged model and observed vorticity fields, Ω_y (s^{-1}), at six phase locations of a wave are plotted in the contoured panels. The top graphic is a plot of the ensemble-averaged free stream wave velocity where the red lines indicate phase location of panels a through f. Flow is initially directed to the left (onshore). Positive (red) contours in panels a through f indicate clockwise rotation. A time-average of the simulated (left) and observed (right) bed profile is contoured in brown for reference. The model predicts the location, size, and rotational direction of the vortices for all phases shown. The shape of the vortex structure, including the vortex tails (the area of vorticity connecting the ejected vortex to the generation point, as in panels a and f) predicted by the model is also in good agreement with the observations.

Model Validation: Simulated vorticity fields, swirling strength, and mean horizontal and vertical velocities were recently compared to particle image velocimetry (PIV) data obtained from a free surface laboratory flume. Comparisons of time-varying vorticity and bulk flow statistics to laboratory measurements show the model in excellent agreement with observations. The modeled and observed ensemble-averaged vorticity fields are plotted in Fig. 1. The results of the comparisons show that SedMix3D does provide an accurate representation of turbulent flow over ripples for the conditions represented by the experiments. Additionally, SedMix3D has been found to predict sand ripple geometries (i.e., ripple height and wavelength) under a range of flow conditions typically found in the laboratory and also simulates the transition from one ripple state to another.[1] SedMix3D is a powerful research tool that may now be used to better understand the currently unknown effects of sand ripples.

Research Applications: SedMix3D provides details of small-scale sand ripple dynamics and may be used to understand presently unknown phenomena including (1) the effects of suspended sediment concentration on turbulence modulation, (2) the dynamics of ripple transitions from 2D to 3D (and back to 2D) under changing forcing conditions, and (3) the role of terminations and bifurcations on ripple migration and growth rates. These processes are important in determining the quantity of wave energy dissipated by seabed roughness. SedMix3D allows for the quantification of the effects of seabed morphology on the generation and dissipation of boundary layer turbulence. Recently, simulations of flow over a bifurcated ripple (two parallel ripples connected by a diagonal ripple between them) produced a substantial increase in the production of boundary layer turbulence when compared to the same simulation without the bifurcation. The excess turbulence significantly increased the boundary layer thickness (Fig. 2).

Summary: Ultimately, all process-based models for nearshore bathymetric evolution are limited by shortcomings in fundamental knowledge of multiphase boundary layer physics. SedMix3D provides an unprecedented level of detail for the study of fluid-sediment interactions that is impossible to obtain with available measuring technologies in the field or laboratory. Our current lack of detailed knowledge of vorticity dynamics and the transport of sediment over rippled beds hinders our ability to fully understand the mechanics and effects of bedform morphology. Therefore, it is necessary to determine the correlation between three-dimensional bedform morphology, turbulence, and boundary layer shear stress to understand the complex

bottom boundary layer processes occurring over rippled seabeds. Understanding of these complex physical processes will eventually improve military operations, such as oceanographic forecasting and mine warfare, as well as have societal benefits, such as improving the design of coastal structures and prolonging the effects of coastal restoration.
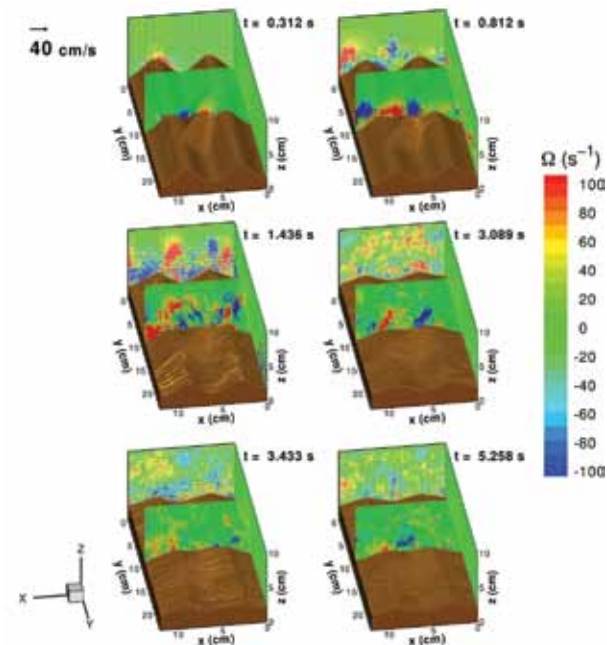
FIGURE 2
Shown are six snapshots from a bifurcated ripple simulation. The bifurcated ripple is at a 45° angle to the two parallel ripples. The flow direction is perpendicular to the ripples (in the x-direction). Contours of y-vorticity (Ω_y) are plotted in the planes bisecting the ripples (x-z planes). Contours of x-vorticity (Ω_x) are plotted in the plane parallel to the ripples (y-z plane). During the initial spin-up, the flow circulates over the bifurcation, transporting sediment into the termination areas. The bifurcation is almost completely eroded after three wave periods. Here, the boundary layer extends to the top of the simulation domain, which is more than double the boundary layer thickness over non-bifurcated ripples.

Reference
[1] A.M. Penko, D.N. Slinn, and J. Calantoni, "Model for Mixture Theory Simulation of Vortex Sand Ripple Dynamics," *Journal of Waterway, Port, Coastal, and Ocean Engineering* **137**(5), 225 (2011), doi:10.1061/(ASCE)WW.1943-5460.0000084.

High-Performance ISR Exploitation with the Geospatial Hub

E.Z. Ioup, J.T. Sample, and B.Y. Lin
Marine Geosciences Division

Introduction: Over the last several years, the military has seen an expansion in the diversity and quality of intelligence, surveillance, and reconnaissance (ISR) products available to the warfighter. Advances in remote sensing mean that raw intelligence products now include data from a diverse set of field-deployable sensors. Improvements in computing hardware allow for significantly more real-time analysis of this data. These changes require that the high volumes of data being produced by multiple diverse sensor and analysis systems be managed and disseminated in the field. NRL's Geospatial Hub (GHub) is a field-deployable Common Information Space (CIS) designed as a high-performance solution to managing these DoD sensor and intelligence products.

Data Management: The GHub CIS is the core of the GHub architecture and is designed to manage and disseminate a diverse collection of ISR products. These include imagery, vector products, Powerpoint and Word documents, sensor detections, moving object tracks, analysis products, etc. The data management capability of the GHub CIS supports storing and indexing data products. Data is versioned to allow tracking of changes and prevent data loss. A common set of metadata is stored with the data including description, classification, geographic area, temporal extent, etc. Both the data itself and the common set of metadata are indexed to allow users to efficiently search for and discover relevant data products.

The GHub provides a Web interface to allow users to browse or search for data, both textually or geographically. They may also upload or download data products. A key feature of the GHub is its ability to customize the Web interface to the data being viewed. For example, the Web page for a collection of ISR imagery will provide previews of each image.

As an alternative to the Web interface, the GHub CISView provides a custom 3D map-based interface to the GHub CIS (see Fig. 3). It supports previewing data on a map overlaid with high-resolution DoD imagery and charts. The CISView is designed for real-time visualization of live streaming of data as it arrives in the GHub CIS. It also supports querying the GHub CIS for older data in support of forensic analysis.

Net-Centric Interfaces: The GHub supports full net-centric access to its data and services. Every core function provided by the GHub is made available through a full Web service Application Programming Interface (API). External sensor and analysis systems

FIGURE 3
The GHub CISView streaming real-time ISR data, a combination of sensors and human reporting, from the GHub CIS.

automatically download and upload data through the API, without any human involvement. By using the Web service API, ISR data may be added and retrieved from the GHub at a high rate, supporting real-time analysis and visualization operations.

The GHub also provides a suite of geospatial Web services. These services, which are standardized by the Open Geospatial Consortium (OGC), allow geospatial data stored in the GHub to be used by a wide variety of geospatial clients. Common tools such as Google Earth, ArcMap, and FalconView may all retrieve data using these services.

Synchronization: The GHub is designed to support fielded military users. To address the need for fielded users to have access to up-to-date geospatial data, the GHub includes an enterprise-level synchronization capability. A field-deployed GHub synchronizes data to a fixed-site GHub system located at a reachback cell. The fixed-site GHub contains the master copy of all the data used by all of its connected field-deployed GHub systems. The field-deployed GHub subscribes to data on the fixed-site GHub. Whenever that data is updated, the field-deployed GHub automatically downloads it. Similarly, when data is uploaded to a field GHub, it automatically publishes to the fixed-site GHub for further distribution.

Field locations often have low bandwidth or intermittent network connections. As a result, the GHub synchronization process was designed to be resilient to these network problems. In fact, the GHub synchronization capability has been successfully tested over tactical mesh networks with intermittent connectivity, low bandwidth, and high latency. Using GHub synchronization, users never have to monitor long-distance data transfers to ensure they complete successfully; the GHub manages these automatically.

Conclusion: The GHub has served as the central data repository of the ISR architecture in a number of field exercises. The ISR architectures tested in these exercises included a large number of diverse sensor and analysis systems. By providing a standardized means of disseminating and discovering data, the GHub made it possible for these diverse systems to work together. The result was both a speedup in the ISR to Command and Control dataflow and an improvement in intelligence products available to commanders.

Underwater Applications of Compressive Sensing

G.F. Edelmann and C.F. Gaumond
Acoustics Division

Introduction: Recently, it has been shown that it is possible to exactly reconstruct a sparse signal with fewer linear measurements than would be expected from traditional sampling theory.[1] This novel and unexpected method, termed compressive sensing, is an optimization problem with a constraint that is expressed with different norms, such as l_1 or the absolute value. By solving a convex optimization problem, exact recovery of the partially sampled signal is possible. The required sampling is neither complete (e.g., Nyquist theorem) nor equally spaced. The only caveats are that the unknown signal must be sparse in some sense and we must choose the correct basis functions to represent the signal.

In this paper we demonstrate compressive sensing by applying it to a problem in underwater acoustics: the detection of a quiet ship signature, where the spectral lines are sparse in frequency space. Ship signatures are dominated by tonal lines generated by ship gearing, engine, or propellor rotation and so are candidates for compressive sensing. Despite low signal-to-noise ratio (SNR), ocean variability, and poorly sampled measurements, this technique was able to extract a ship signature in measured at-sea data. The demonstration of robustness to measured oceanic noise and to imperfect single component signal model shows that this technique has great promise for other underdetermined inversion problems in the underwater environment.

Methodology: Compressive sensing is a relatively new technique for solving inverse problems.[2] Inverse problems arise in several underwater acoustics applications, for example, detecting frequency lines in a time domain signal. This problem can be viewed as inverting time samples into frequency components. The typical approach using Fourier transforms implements algebraically the formalism of integral equations, treating the signals as vectors, with a distance defined in terms of root squared magnitude. This definition of a distance is similar to that of vectors in Euclidean space, where the distance is the square root of x squared plus y squared.

Compressive sensing, however, is based on the l_1 norm, which defines distance as the the sum of the absolute values of the differences of each component direction. The distance is the sum of the absolute value of x plus the absolute value of y. This mathematical approach has been used extensively in various applications, such as business and the "minimum salesman

route problem." The l_1 norm describes the distance traveled by a taxi cab in a city with streets laid out in a rectangular grid. However, this approach is rarely used in physical sciences.

Recently, techniques using l_1 have been applied to problems closely associated with wireless communications and image compression.[3] NRL is currently applying l_1 techniques to problems in underwater acoustics, such as signal detection, array processing, and array design, as well as in other areas such as radar.

Measured Ship Signature: Figure 4 shows an example of compressive sensing of at-sea data measured on an acoustic hydrophone in a towed array during the MAPEX 2000 experiment.[4] A spectrogram of 14 seconds of typical data is shown in the top left panel of Fig. 4. The lower portion of the frequency spectrum contains chirps used for the geoacoustic experiment. After band-pass filtering, the resulting 4096 point time series is shown in the top right panel. The signal is then subsampled to just 409 points. Compressive sensing of the at-sea data is shown in the lower panels of Fig. 4. These results are remarkable. First, the technique is robust to ocean noise and variability. Second, the tone is modulated during the period, yet compressive sensing produced the center frequency. The conclusion is that the sparsity constraints successfully minimize detections in the frequency domain.
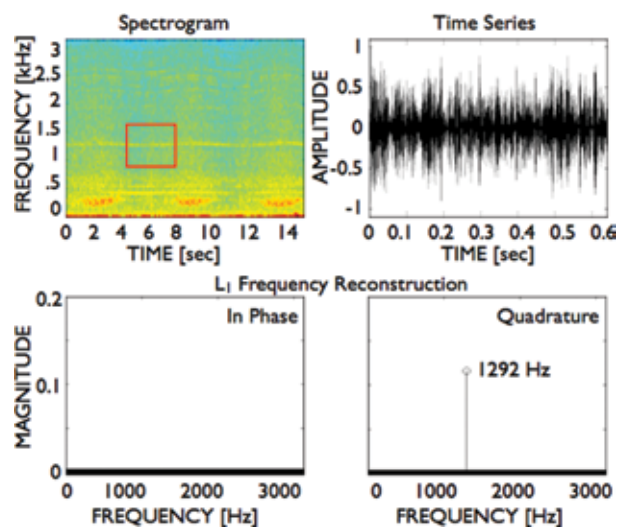
FIGURE 4
Compressive sensing of the at-sea data. The ship's signature is detected and extracted even in the presence of noise and variability.

It is difficult to produce probability of detection and false alarm rates as a function of SNR for a towed array because the ship radiation and the background noise remain fairly constant in strength. To avoid adding numerically generated white noise, the SNR was controlled by changing the size of the passband; the

effective SNR was varied from –3 to 5.5 dB. The left panels of Fig. 5 show the time series and frequency domain of the tightly band-passed modulated signal in red and the noisy bandwidth in blue. In the right panels, the probability of detection and false alarm rate are shown in the solid boxes for the at-sea data. The faint gray background lines show the numerically simulated results to guide the eye on expected performance over a larger SNR regime.
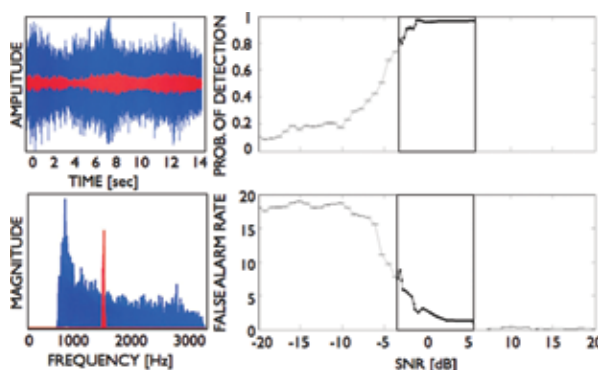
FIGURE 5
Probability of detection and false alarm rate vs signal-to-noise ratio. Even down to –3 dB SNR, the at-sea results (solid boxes) show that compressive sensing can reliably detect ship signatures.

Summary: We are adding to the U.S. expertise in anti-submarine warfare (ASW) and supporting disciplines to improve national capabilities to detect, locate, and identify targets at sea. This paper shows, for the first time, the application of compressive sensing to an ASW problem of interest. Despite low SNR, ocean variability, and poorly sampled measurements, the technique was able to extract a ship signature in measured at-sea data. The demonstration of robustness to measured oceanic noise and to imperfect single component signal model shows that this technique has great promise for other underdetermined inversion problems in undersea warfare.

[Sponsored by ONR]

References
[1] E. Candès, J. Romberg, and T. Tao, "Robust Uncertainty Principles: Exact Signal Reconstruction from Highly Incomplete Frequency Information," *IEEE Trans. Inf. Theory* **52**(2), 489–509 (2006).
[2] http://www.acm.caltech.edu/l1magic (accessed Sept. 2010).
[3] S. Boyd and L. Vanderberghe, *Convex Optimization* (Cambridge University Press, Cambridge, 2004).
[4] M.R. Fallat, P.L. Nielsen, and M.Siderius, "The Characterization of a Range-Dependent Environment Using Towed Horizontal Array Data from the MAPEX 2000 Experiment," SACLANTCEN Report SM-402 (2002).

GRACE (2002) — A joint project with academic and corporate partners, GRACE was an autonomous robot system entered in the 2002 AAAI Robot Challenge. GRACE acted autonomously to travel, without a map, from the front floor of a convention center to the registration desk by interacting with people and reading signs, then registered, made its way to an assigned location, presented a talk, and answered questions about itself.

High Efficiency Ceramic Lasers

J.S. Sanghera, W. Kim, C. Baker, G. Villalobos, J. Frantz,
L.B. Shaw, A. Lutz, and I. Aggarwal
Optical Sciences Division

The Problem: Lightweight and compact high power lasers will facilitate integration of directed energy weapons systems on board tactical platforms without compromising mobility (Fig. 1). Solid-state crystal lasers would be ideal for these applications. Single-crystal yttrium aluminum garnet (YAG) has been the workhorse of solid-state crystal lasers, whereby doping YAG with about 1% to 2% of rare earth ions (e.g., Yb^{3+}

FIGURE 1
Schematic representation of terrestrial and airborne platforms with high energy laser systems.

or Nd^{3+}) has led to lasing at a wavelength of ~1 μm. However, scaling to very high laser powers with good beam quality in YAG is limited by its thermal conductivity and the sudden drop in thermal conductivity with increasing dopant concentration. An additional problem is the poor dopant solubility in YAG, which leads to non-uniform dopant concentration, a big problem at high dopant concentrations. A better solution is to use materials with better dopant solubility and higher thermal conductivity, such as the sesquioxide Lu_2O_3. In fact, the thermal conductivity for Lu_2O_3 remains relatively constant with increasing dopant concentration due to the similarity of the phonon energy of the dopant and the host. However, single-crystal Lu_2O_3 is difficult to make by traditional high-temperature crystal growing from the melt, due its very high melting temperature of 2400 °C. This leads to crucible reactions, volatilization, chemical inhomogeneity, lattice strain, defects, and cracks, which therefore limit the size of the crystal to the millimeter scale. These small sizes are not suitable for making high power lasers. Therefore, alternative methods are needed to make suitable-sized solid-state laser materials.

The Solution: The polycrystalline ceramic process is a method that can mitigate the problems associated with growing single crystals from their melts at high temperature. This process uses high-purity, submicron powder that is densified at only two-thirds of the melt temperature using vacuum sintering or hot pressing. The small size of the powder makes it very accommodating to lattice strain and so it is easy to dope with high levels of rare earth ions. Also, the product is a polycrystalline material, typified by grains and grain boundaries. The grains, which are single crystals, can range in size from a few microns to several tens of microns. As their size is small, they can also accommodate higher rar earth ion dopant concentration, with any additional lattice strain being accommodated by the grain boundaries. If the grain boundaries are clean, i.e., without impurities, then the polycrystalline ceramic will be transparent and with high optical quality. This process is readily scalable to large sizes and conformal shapes. A further advantage is that ceramics are tougher and stronger than their crystalline counterparts and so they possess a higher threshold for thermal shock, thereby enabling higher laser output power.

Experimental Details and Results: We have developed wet chemistry processes to make submicron $Yb^{3+}:Lu_2O_3$ powder that has a particle size of approximately 100 nm, surface area of 33 m^2/g and less than 1 ppm impurity content. The powder is uniformly doped with tailored amounts of the dopant Yb^{3+}. Hot pressing this fine, non-agglomerated powder at ~1600 °C for a couple of hours under a load of ~5,000 psi

FIGURE 2
A polished 1-in.-diameter transparent 10% Yb^{3+} doped Lu_2O_3 ceramic sample.

yields a partially transparent ceramic with >99% density. Subsequent hot isostatic pressing (HIP) at ~1600 °C using an argon gas pressure of 30,000 psi completes the process by increasing the density to 100% and providing full transparency. Figure 2 shows a polished 1-in.-diameter transparent 10% Yb^{3+} doped Lu_2O_3 ceramic sample that exhibits excellent optical quality. Pumping this sample with a diode laser operating at 975 nm leads to lasing with more than 16 W output power at 1080 nm and a slope efficiency of 74% (Fig. 3). This result represents the highest output power and highest efficiency obtained from Lu_2O_3 ceramics. What makes this result even more remarkable is the high doping concentration of 10% Yb^{3+}. This technology, along with several patents, has been licensed to industry. The domestic availability of transparent rare-earth-doped Lu_2O_3 ceramics will enable fabrication of ceramic laser materials for power scaling and implementation in highly efficient and compact directed energy weapons systems.
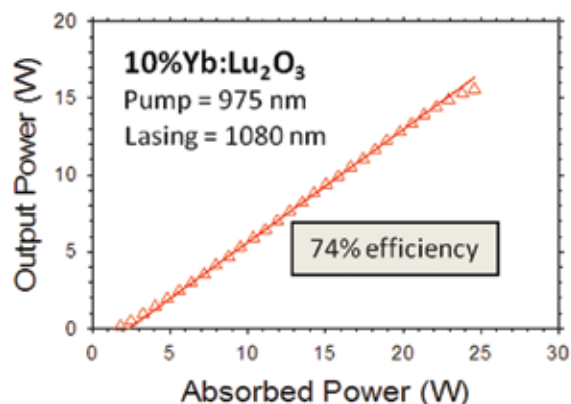
FIGURE 3
Output laser power at 1080 nm vs absorbed pump laser power at 975 nm.

Aerosol Agent Detection Using Spectroscopic Characterization

V. Sivaprakasam,[1] J. Czege,[2] M. Currie,[1] J. Lou,[2] and J. Eversole[1]
[1]Optical Sciences Division
[2]Global Defense Technology & Systems, Inc.

Introduction: Detection of chemical and biological agents that would most likely be dispersed as aerosols has become a critical component of modern defense capability. Under a Defense Threat Reduction Agency (DTRA) supported program, the NRL Optical Sciences Division has recently developed advanced ambient air monitoring and aerosol classification technologies based on laser interrogation and spectroscopy. These optical characterization measurements are performed on individual aerosol particles entrained in a continuous air stream as they move past the sensor focal volume at rates up to 10,000 per second. Multiple laser beams at several wavelengths are used to interrogate the particles. Six beams are generated by one continuous-wave visible wavelength diode laser and collectively provide position and velocity information of the aerosol particles. Subsequently, each particle is illuminated with one or two pulsed ultraviolet (UV) lasers. If the particle is composed of biological material, the UV lasers will excite characteristic fluorescence. These UV laser-induced fluorescence (UV-LIF) signals from discrete spectral channels are recorded, as are the elastic scattering intensities. Up to 14 optical measurements may be obtained from each particle. These data values are used to differentiate and classify the particles into potential-threat or non-threat categories.

Spectral Discrimination: Figure 4 shows a scatter plot survey of UV-LIF particle signatures from eight separate populations with different compositions as described in the legend and elsewhere.[1] The data shown are the sum of the emission intensities from multiple channels for the two indicated excitation wavelengths. The aerosol particles shown here are approximately one micron in diameter, and each point on the plot represents a single particle. One can easily see that significant discrimination is obtained for four broad categories of different materials, including those relevant to biological agents. However, the spread in these particle data includes variation in instrument optical collection efficiency and laser illumination of the particle depending on its location in the sensor focal volume. To improve discrimination, we have implemented a new laser beam design to reduce variability due to particle position.

Instrument Design: The basic optical design has been previously published,[1] and contains greater detail than can be accommodated here. The original design uses a single separate continuous-wave laser beam as a "trigger" to indicate the presence of an aerosol particle entering the instrument, and cue the firing of pulsed UV lasers. Most recently, this trigger beam has been split into a set of six spatially structured beams that provide data on the specific position and velocity of each particle. This arrangement, referred to as
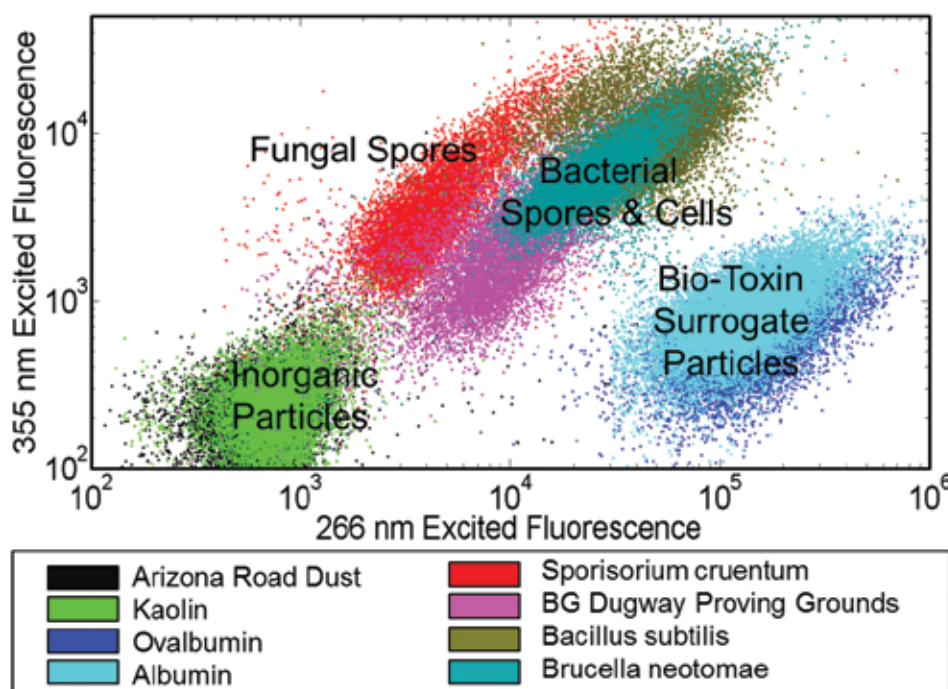
FIGURE 4

An illustration of the separation observed in measured UV-LIF emission intensities in two spectral channels from lab-generated populations of aerosol particles representing four broad groups: inorganic ambient background particles, fungal spores, bacterial particles (spores or cells), and bio-toxin surrogates (proteins). The eight specific example compositions are color-coded in the legend.

a structured trigger beam (STB),[2] provides the ability to reduce the spread of the fluorescence and elastic scattering data used to characterize the particle. By knowing the precise particle location, the instrument response function due to spatially dependent laser beam intensity profiles and optical collection efficiency can be normalized. Figure 5 shows the precision mask (a) used to generate six spatially distinct STB laser beams, and a typical oscilloscope trace (b) of a particle passing through these beams (lower, blue trace). The particle position and velocity is coded into the relative positions of these six pulses generated by the particle passing through each beam. Figure 5(c) shows typical x-y-z trajectories for an ensemble of particles calculated from the STB data, while Fig. 5(d) shows the (parabolic) distribution of flow velocities for the same particles as a function of their position (x-y) in the flow cross section. Finally, the effectiveness of the STB positional data to normalize fluorescence intensities can be seen by comparing Fig. 5(e) to Fig. 5(f). Figure 5(e) shows a histogram of un-normalized (raw) fluorescence pulse heights, while Fig. 5(f) shows the same data normalized for spatial position instrument response. The result clearly shows the presence of three distinct test populations of fluorescent particles that were previously completely obscured.

Future Directions: In the past year, we have also developed customized UV laser light sources that offer certain advantages, such as greater energy efficiency, over the commercially available laser systems employed so far (e.g., 266 and 355 nm wavelength lasers). Figure 6(a) shows a photograph of an NRL-developed, mode-locked fiber laser that provides high-intensity pulses (<500 fs in duration) at a 41 MHz repetition rate.[3] The photograph shows the coiled optical fiber laser (as bright purple) as well as its second harmonic converted light (as green). The fiber laser pulse intensities are sufficiently high that two-photon absorption can be used to effectively produce fluorescence. The scatter plot in Fig. 6(b) shows UV fluorescence intensities in two spectral bands from three different populations of aerosol particles excited by green laser light. These data are the first published[3] observations of emission due to multiphoton absorption from bacterial aerosol particles.

[Sponsored by DTRA]

References

[1] V. Sivaprakasam, A. Huston, C. Scotto, and J. Eversole, "Multiple UV Wavelength Excitation and Fluorescence of Bioaerosols," *Opt. Express* **12**, 4457–4466 (2004); V. Sivaprakasam, H.-B. Lin, A.L. Huston, and J.D. Eversole, "Spectral Characterization of Biological Aerosol Particles Using Two-Wavelength Excited Laser-Induced Fluorescence and Elastic Scattering Measurements," *Optics Express* **19**(7), 6191–6208 (2011).

[2] W.D. Herzog, S.M. Tysk, D.W. Tardiff, G.C. Cappiello, J.M. Jong, T.H. Jeys, R.H. Hoffeld, A. Sanchez, and V. Daneu, "Measurement of Aerosol Particle Trajectories Using a Structured Laser Beam," *Appl. Opt.* **46**, 3150–3155 (2007).
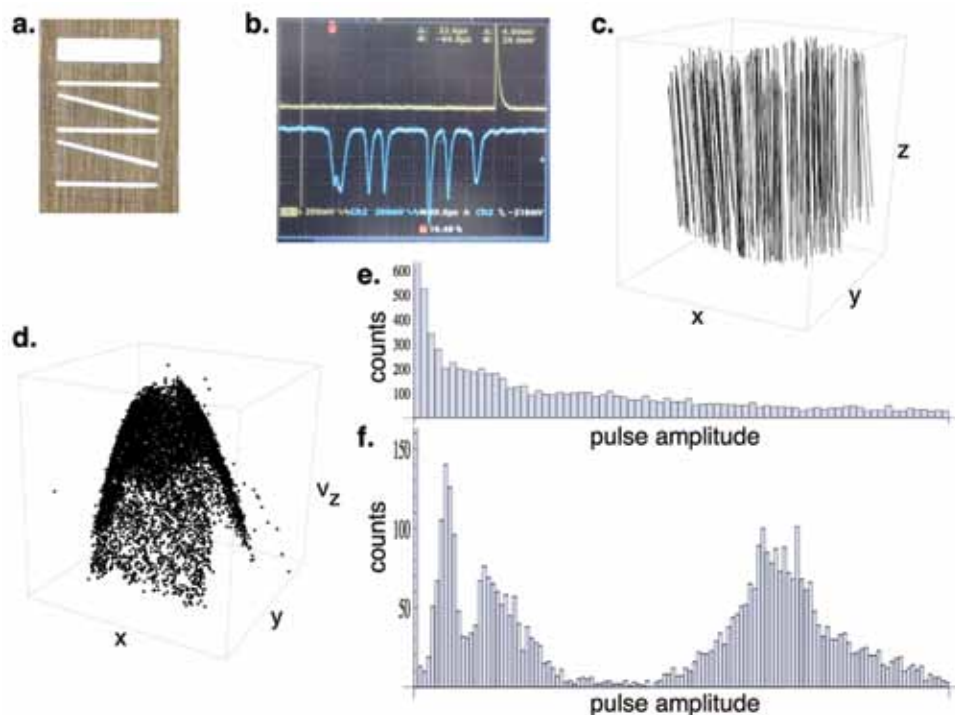
FIGURE 5
Different aspects of the structured trigger beam (STB) are shown, starting with: (a) the high-precision mask used to generate the six beams, (b) a typical oscilloscope trace (blue trace) showing the six-pulse signature as a particle passes through each of the beams, (c) a three-dimensional representation of particle trajectories for an ensemble of particles created from STB data, (d) the corresponding velocity (v_z) profile from that particle ensemble, (e) uncorrected LIF pulse height data from test particles, and (f) the same LIF data as in (e), corrected now using the STB data, and revealing the presence of three distinct fluorescent populations.
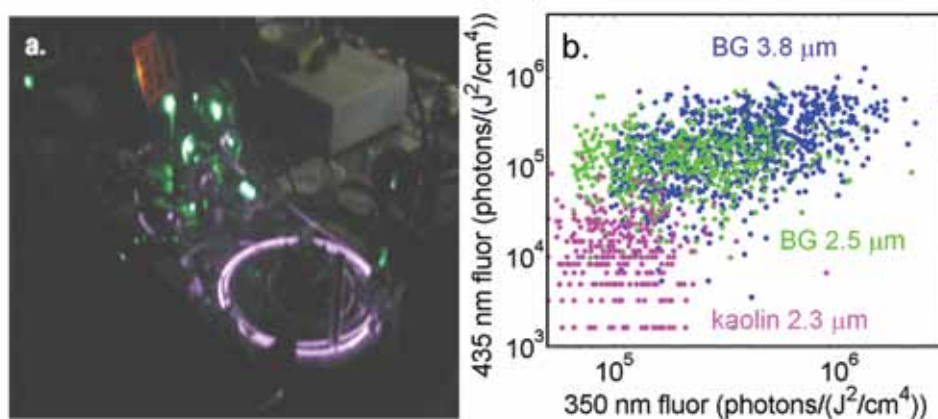
FIGURE 6
(a) A photograph of a unique, mode-locked fiber laser developed to provide a continuous train of short (<500 fs) pulses of light for aerosol particle interrogation. The laser fundamental wavelength can be either doubled to 526 nm (green) or quadrupled to 263 nm (UV) very efficiently.
(b) Because of its high peak power, two-photon absorption of the laser green light results in UV fluorescence from aerosol particles of bacterial spores (BG clusters of 2.5 and 3.8 µm diameters) compared to nonfluorescent mineral particles (kaolin) of similar size as shown in this scatter plot.

[3] J.W. Lou, M. Currie, V. Sivaprakasam, and J.D. Eversole, "Green and Ultraviolet Pulse Generation with a Compact, Fiber Laser, Chirped-Pulse Amplification System for Aerosol Fluorescence Measurements," *Rev. Sci. Instrum.* **81**(10), 103107 (2010); V. Sivaprakasam, J. Lou, M. Currie, and J.D. Eversole, "Two-Photon Excited Fluorescence from Biological Aerosol Particles," *JQSRT* **112**(10), 1511–1517 (2011).

■

Angel Fire/Blue Devil Sensors for Wide-Area ISR and Persistent Surveillance

J.N. Lee, M.R. Kruer, D.C. Linne von Berg, J.G. Howard, B. Daniel, and P. Lebow
Optical Sciences Division

Introduction: The Applied Optics Branch has been developing technology for use in a broad range of tactical and wide-area surveillance systems. These systems include high-resolution, high-framing-rate, panchromatic, and hyperspectral imaging systems in the visible through infrared spectral regions, on platforms ranging from low-altitude small UAVs to high-altitude standoff aircraft. Recently, a dual-band wide-area persistent surveillance sensor system (DB-WAPSS) has been developed, flight-tested, and transitioned. The DP-WAPSS IR subsystem uses a 16.7-megapixel mid-wave infrared (MWIR) focal plane array (FPA; 4096 × 4096 pixel, 15-µm pixel pitch, sensitive from 3.5 to 5.1 µm wavelength) to provide the largest presently available day/night IR coverage in addition to increased resolution performance at lower altitudes. The visible subsystem is a large-format 59-megapixel camera that can operate at high frame rates. Both imaging subsystems are incorporated into a step-stare gimbal, the CA-247 from Goodrich ISR Corporation, that can increase coverage by creating a mosaic of images, i.e., trading update rate against area coverage. The DB-WAPSS/CA-247 system has been demonstrated to a Technology Readiness Level (TRL)-7 level of maturity, showing direct application to existing and developing wide-area persistent surveillance airborne platforms used by U.S. Navy, U.S. Marine Corps, U.S. Air Force, and U.S. Army. Seven sensors were developed for the Marine Corps' Angel Fire program, each sensor showing high-level, reproducible performance; these sensors have since transitioned to other Services' applications, in particular the Air Force's Blue Devil program. We describe key subsystem breakthroughs and resultant system performance.

Focal Plane Array and Sensor Development: Major challenges for focal planes for framing-camera applications are maximizing the number of pixels per array and simultaneously maximizing the array frame rate. Silicon FPAs for the visible/near-IR (VNIR) spectral band are commercially available in sizes of several tens of millions of pixels. However, these commercially available FPAs are not yet available at frame rates above 1 to 2 per second and with electronic shuttering, which is needed for long-duration, persistent surveillance applications. The sizes of IR FPAs for day and night usage significantly lag behind sizes available in the VNIR. Progress in large IR FPAs has been made primarily in the MWIR band. Prior to DB-WAPSS, the largest IR FPA available was the 4-megapixel MWIR array, developed by NRL and L3 Communications, Cincinnati Electronics, Inc. (L3 CE), used on the Navy's SHARP system and for early persistent surveillance demonstrations.[1] Use of a reticulating process by L3 CE on the SHARP FPA design allowed scaling up in size from a 4-megapixel, 25-µm pixel pitch to a 16-megapixel, 15-µm pitch FPA on an only modestly larger die size than for the SHARP FPA. Further scale-up to 64 megapixels should be possible and is presently being explored.

The IR FPA is integrated into an IR Imaging Module (IRIM) that produces the high-speed output data. Non-uniformity corrections (NUC) and bad pixel replacement are calculated within the IRIM and applied in real time. The IRIM is preloaded with two preset integration times that correspond directly to two operating temperature ranges. The temperature ranges are operator selectable and can be used for either change in climate or change between day and night operation. The image data is output over four 14-bit CameraLink data ports, which are then converted by a multiplexer into two gigabit Ethernet outputs for interface convenience.

The VNIR capability of the DB-WAPSS 59/16 is provided by a ruggedized 59-megapixel CMOS camera, the V59M, produced by Teledyne Imaging Sensors. The camera produces a square-format of 7680 × 7680 pixels, and images at almost 10 frames per second (fps) with an electronic global shutter. The camera's high quality EO lens matches the same 22.8° field of view as the MWIR channel. The V59 output is also CameraLink, with possible conversion into multichannel gigabit Ethernet.

The IRIM and the V59 are integrated into a single unit and installed into a stabilized CA-247 gimbal. The sensor may be operated in IR, visible, or simultaneous EO/IR modes, gaining the benefits of fused multiband image products. Figure 7 shows the DB-WAPSS-59/16 sensor. The central rectangular box contains the IRIM, which uses the 16.7-megapixel MWIR FPA and the V59M camera with the 59-megapixel FPA. Large drive motors power both the roll and azimuth axes in the DB-WAPSS 59/16, allowing the sensor to slew quickly in large steps to commanded positions. The sensor is
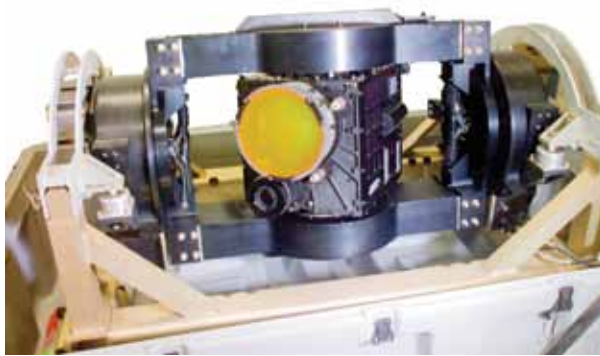
FIGURE 7
DB-WAPSS 59/16 camera. IR optics shown with yellow protective cover. VNIR optics below and to the left of the IR optics.

capable of stepping a 2 × 2 pattern of images in less than a second, maintaining a high degree of stabilization during frame exposures, and covering a total field of regard of approximately 36° on each side. The sensor is 40 in. long and has a rotational "keep-out" diameter (including sway space) of 24.75 in. If step-stare is not used, the imaging unit can frame faster than the 4-fps limit set by the stepping motors.

The sensor is designed to operate in harsh military environments on either manned or unmanned platforms. System mean-time-between-failure (MTBF) is estimated at greater than 2800 hours using MIL-HD-BK-217.

Test and Evaluation: Seven 16.7-megapixel IRIM units were produced for Blue Devil DB-WAPSS sensors. Measured IRIM characteristics for five IRIMs are summarized in Table 1.

TABLE 1 — Measured IRIM Characteristics

Parameter	Average of 5 Units
Operability	99.0%
Max Power during Cool Down (W)	175.42
SS Power Operating at Temp. (W)	59
Weight (lb)	28

Sensor imaging performance was validated during factory test by measuring the system relative edge response (RER) and calculating the associated system modulation transfer function (MTF). Measured response has matched very closely with predicted performance from modeling. The production sensors

have produced system RERs from 0.63 to 0.68, resulting in average system MTF values from 33% to 35% at the Nyquist frequency (33.3 lines/mm). Imagery captured during NRL flight tests show image quality commensurate with system MTF values in this range (Fig. 8).

Processing DB-WAPSS Sensor Data: DB-WAPSS sensor data were processed using NRL's "Blackjack" software suite designed for persistent surveillance applications. This software suite is based on the common open-architecture, standards-based design that NRL has used on many ISR data exploitation and fusion stations.[2] Blackjack satisfies two key processing requirements for DB-WAPSS: (a) processing at the full dynamic range of the raw camera outputs — 14-bits for

FIGURE 8
DB-WAPSS daytime MWIR flight imagery (June 9, 2009). Inset images show (top) a resolution target, and (bottom) vehicles in a magnified view of the parking area.

the IRIM and 12-bits for the V59M, and (b) real-time processing and display for image formation and for target detection, identification, and tracking — without sacrificing full-dynamic range processing.

IR data from NRL flight tests have been processed to demonstrate the sensor's detection capability and its ability to detect subtle changes in revisited scenes and in tracking moving vehicles from an orbiting aircraft. The sensor's image stream, motion-video at 4 fps, was used to obtain the tracking results shown in Fig. 9. The imagery was of sufficient quality to implement an NRL motion-tracking algorithm that can reliably initiate and maintain tracks of moving targets under stressful conditions. The tracking algorithms executed on the processing system reliably reject false track initiations caused by parallax, and provide capability to track through temporary obscurations and momentary stoppage of movement. The high-quality MWIR image data complement the performance of the tracking system.

Summary: An advanced dual-band step-stare sensor using a 16.7-megapixel MWIR and a 59-megapixel

FIGURE 9
Top: Track initiations, indicated by green markers. Bottom: Track generation for three vehicles, T:1, T:2, and T:3.

visible array has been developed, and seven copies of the sensor constructed and tested for the Marine Corps' Angel Fire program and transitioned to the Air Force's Blue Devil program. Test results from these sensors demonstrated the reproducibility of the mechanical, data-handling, and high-quality MWIR-imaging performance. Airborne flights demonstrated a TRL-7 level of maturity. The quality of the MWIR data, together with NRL's real-time, standards-based processing, enables effective day/night change-detection and tracking performance.

References
1 J.N. Lee, J.G. Howard, M.R. Kruer, D.C. Linne von Berg, M. Colbert, S. Frawley, and M. Schicker, "Infrared Airborne Pod for Wide Area Day-Night Persistent Surveillance," invited presentation, 2005 National Military Sensing Symposium (MSS), Orlando, FL, Nov. 15, 2005.
2 D. Linne von Berg, J.N. Lee, M. Kruer, M.D. Duncan, F.M. Olchowski, E. Allman, and G. Howard, "Airborne Net Centric Multi-INT Sensor Control, Display, Fusion, and Exploitation Systems," presented at Airborne Intelligence, Surveillance, Reconnaissance (ISR) Systems and Applications, SPIE Defense and Security Symposium, Orlando, FL, April 13, 2004, and published in *Proc. SPIE* **5409**, 111–119 (2004).

Remote Sensing

Remote-Controlled Pontoon Plane (1924) — NRL developed the control system for the first U.S. flight of a radio-controlled pilotless aircraft. Remotely controlled from the ground, the N-9 float plane took off from the Potomac River, followed a triangular course, executed glides and climbs, and landed on the river.

Adaptive Velocity Estimation System

W. Chen and R. Mied
Remote Sensing Division

Introduction: Knowledge of the velocity field in littoral waters is crucial to specifying the battlespace and is important in oceanographic studies as well. In many areas, however, direct measurement of surface velocity requires a large amount of in situ data from ships or current meters, which may not possible if the region is denied or otherwise inaccessible. Instead, successive spaceborne or airborne images are being used more extensively to extract surface velocity information in oceans, rivers, and littoral areas.

The general topic of velocity estimation from an image sequence is a well-known inverse problem in computer vision, geosciences, and remote sensing. It has been of fundamental interest in many diverse fields such as velocity estimation from large and small displacements, object tracking, advanced video editing, and deriving surface currents for ocean dynamics studies.

Almost all existing velocity estimation models and algorithms assume that the image intensity recorded from different physical sensors obeys a conservation equation for tracer, heat, or optical flow in space and time. The inverse problem was believed to be underconstrained, however, because the two unknown velocity components must be derived from this single conservation equation at each of these pixel points. To solve the underconstrained problem for the intensity conservation equation from an image sequence, different models or frameworks with additional constraints have been reported in literature.

Adaptive Velocity Estimation System: Our strategy[1,2] converts the underconstrained system to an overconstrained one by modeling the velocity field as a set of tiles or blocks. Within each block, the velocity is specified as a binomial or B-spline. By collectively constraining the set to obey the above conservation equation in a least-squares sense, we derive a global optimal solution (GOS) for the velocity field. We can adjust the tile (block) size to control the degree of the overconstrained system and its robustness to noise. To obtain higher accuracy in velocity estimation, especially in larger scale displacement motion, a temporal integral form of the conservation constraint equation (the nonlinear inverse model) has been created to replace a differential form of the equation (the linear inverse model).

In addition, we have proven that this inverse problem for motion determination is generally not underconstrained based on an innovative approach.

The motion fields are identified by the velocity field and displacement field. In general, the velocity determination is an ill-posed problem, because the information about the path and rate is lost after a temporal sampling. However, the problem of the displacement field determination is well-posed because the initial and final configurations of a textured moving particle can be physically determined and observed by an image sequence. A fully constrained nonlinear system of equations combing the Displacement Vector Invariant (DVI) equation is presented without any approximation and imposing additional constraint and assumption. An adaptive framework for resolving the displacement or average velocity field has been developed.

NRL's Adaptive Velocity Estimation System (AVES) has been developed based on these fully constrained nonlinear systems of equations, velocity field modeling, GOS strategies, Gauss–Newton and Levenberg–Marguardt methods, an algorithm of the progressive relaxation of the pyramid constraint, and adaptive frameworks.

Demonstration: We test the performance of the new inverse model and algorithms by experimental results synthesized from a numerical simulation[1] and actual thermal images. The synthetic tracer (i.e., the two background images in Figs. 1(a) and 1(b)) in a square box with dimension L = 50 km has been deformed by an initial velocity distribution and is significantly different from its original tracer field. The average benchmark velocity vectors for t = 18 h and 20 h as given by the numerical simulation are shown in Fig. 1(a). For comparison, the velocity field estimated by the AVES from the tracer fields at 18 h and 20 h is shown in Fig. 1(b). Average values of angular and magnitude measures of error[2] are applied to evaluate the performance of the velocity estimations, as shown in Fig. 2.

Finally, we demonstrate the utility of AVES by deriving a velocity map from actual satellite-borne NOAA Advanced Very High Resolution Radiometer (AVHRR) images taken in the New York Bight, east of the New Jersey coast and south of Long Island, New York, on May 25, 2007 (Fig. 3(b)). For a comparison, a measured velocity array by the Coastal Ocean Dynamics Application Radar (CODAR) is shown in Fig. 3(a).

Summary: The inverse problem of velocity estimation from an image sequence had been considered as an underconstrained problem for several decades. Previous models for solving the inverse problem have done so by imposing unphysical constraints, which yields sparse and often inaccurate velocity fields.

The inverse problem for displacement or average velocity determination based on two successive frames has been proven to be fully constrained without any
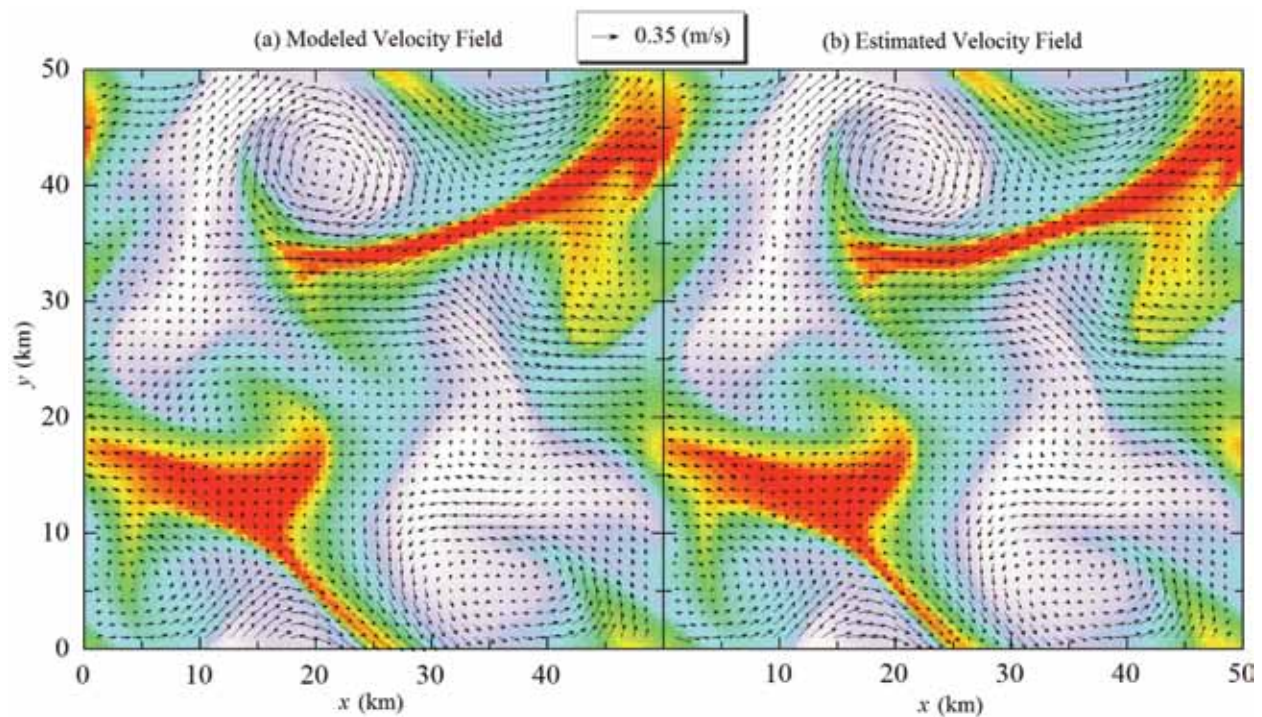
FIGURE 1
Velocity fields: (a) Velocity field generated by averaging numerical model results at times t_1 = 18 h and t_2 = 20 h; (b) Velocity field estimated by the AVES between times t_1 = 18 h and t_2 = 20 h. The background images shown in (a) and (b) are the tracer fields at t_1 = 18 h and t_2 = 20 h, respectively.
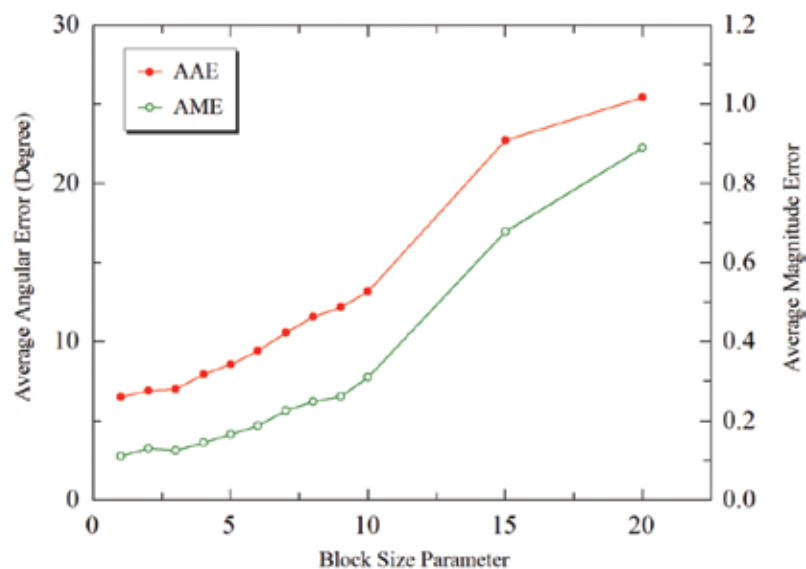
FIGURE 2
Quantitative measurements of average angular and magnitude errors (AAE and AME) vs block size parameter for the AVES estimator with ocean simulation model data are plotted.

(a) CODAR Velocity Field (7:00 to 11:00)   (b) Estimated Velocity Field (7:21 to 10:46)
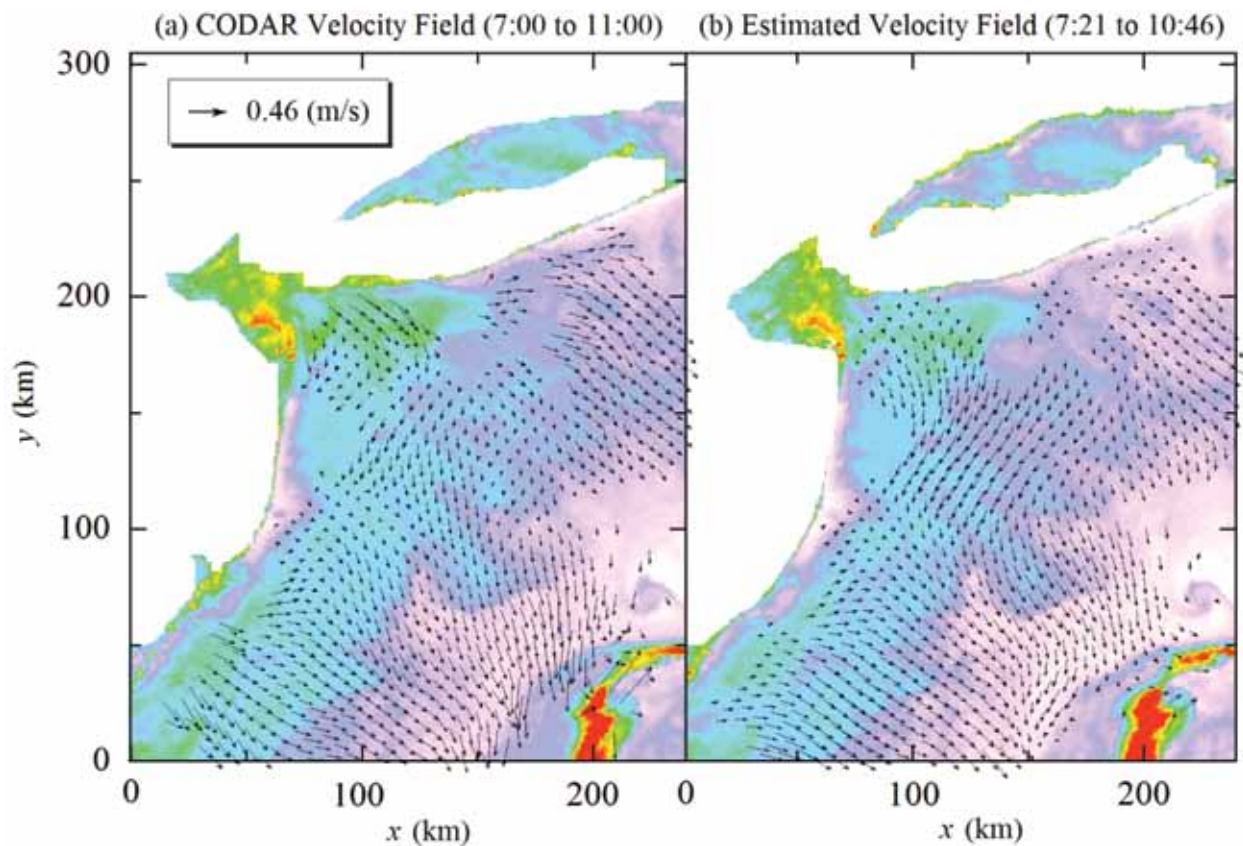
FIGURE 3
The velocity vectors are superimposed on the AVHRR image pair at time 7:21 and 10:46 UT on May 25, 2007 (false-color representation). (a) Average of the CODAR velocity field from 7:00 to 11:00 (the background image at t_1 = 7:21 UT). (b) Estimated velocity field obtained from the AVES (the background image at t_2 = 10:46 UT).

additional unphysical constraints. The Remote Sensing Division has developed the powerful AVES to retrieve velocities from image sequences based on this fully constrained system. NRL's AVES is an integration of models, methodologies, and state-of-the-art techniques. It is suited for motion field estimation from visible-band, thermal, or hyperspectral image sequences with complicated coastal land boundaries in ocean/river dynamics studies. The AVES framework has a wide variety of applications in both computer vision and remote sensing fields.

[Sponsored by ONR]

References
[1] W. Chen, R.P. Mied, and C.Y. Shen, "Near-Surface Ocean Velocity from Infrared Images: Global Optimal Solution to an Inverse Model," *J. Geophys. Res.* **113**, C10003 (2008), doi:10.1029/2008JC004747.
[2] W. Chen, "A Global Optimal Solution with Higher Order Continuity for the Estimation of Surface Velocity from Infrared Images," *IEEE Trans. Geosci. Rem. Sens.* **48**(4), 1931–1939 (2010).

Coupling Satellite Imagery and Hydrodynamic Modeling To Map Coastal Hypoxia

R.W. Gould, Jr.,[1] M.D. Lewis,[1] R.D. Smith,[2]
D.-S. Ko,[1] and J.D. Lehrter[3]
[1]*Oceanography Division*
[2]*Jacobs Advanced Systems Group*
[3]*U.S. Environmental Protection Agency*

Introduction: The frequency, extent, and severity of coastal hypoxic events are increasing worldwide due to increasing eutrophication. Hypoxia occurs when dissolved oxygen levels in the water column drop below 2 mg/l, and these low oxygen levels can potentially impact local fisheries and benthic organisms, with important ecological and economic consequences. A "dead zone" off the coast of Louisiana forms every summer and is the second largest hypoxic zone in the world (only the Baltic Sea hypoxic zone is larger). It is generally thought that agricultural fertilization upstream and runoff delivered via the Mississippi-Atchafalaya river

basin leads to the increased nutrient loading on the Continental Shelf, stimulating a phytoplankton bloom. As the bloom stimulated by this nutrient-rich discharge of the Mississippi and Atchafalaya Rivers sinks and decays, oxygen levels near the bottom become depleted. In addition to the bloom decay, water column stratification is also a required condition for hypoxia development, to prevent mixing with surrounding oxygen-replete waters.

TABLE 1 — Size of Coastal Louisiana Hypoxic Zone, as Determined by Mid-Summer Ship Surveys[1]

Year	Hypoxia Size (km²)
1998	12,400
1999	19,750
2000	4,000
2001	20,720
2002	22,000
2003	8,560
2004	15,040
2005	11,840
2006	17,280
2007	20,500
2008	20,720
2009	8,000
2010	20,000

Ship-based surveys have been conducted each summer since 1985 by the Louisiana Universities Marine Consortium (LUMCON) to map the spatial extent of the bottom hypoxic waters (Table 1); this measurement represents the officially reported size of the hypoxic zone.[1] Ten other cruises covering the Louisiana shelf from 2002 to 2009 by the U.S. Environmental Protection Agency (EPA) provided additional physical oceanographic data. There is currently a national mandate to decrease the size of the hypoxic zone to 5,000 km² by 2015, mostly by a proposed 40% reduction in annual nitrogen discharge into the Gulf of Mexico. A monitoring program is required to assess whether these goals are being met. However, ship sampling is expensive and is not spatially or temporally synoptic. Our goal is to develop a technique to more effectively map coastal hypoxia.

Can We Combine Surface Satellite Imagery and 3D Hydrodynamic Modeling To Map the Spatial Extent of Bottom-Water Hypoxia? To answer this question, NRL first collected, processed, and archived a 13-year time series of satellite ocean color imagery covering the northern Gulf of Mexico from 1998 to 2010. All imagery was processed using the NRL automated satellite processing system (APS) to derive water optical properties.[2] APS is a complete end-to-end system

that includes sensor calibration, atmospheric correction (with near-infrared correction for coastal waters), and bio-optical inversion. APS incorporates the latest NASA algorithms, as well as NRL algorithms tailored for Navy-specific products. We then applied an optical water mass classification (OWMC) system developed at NRL to the imagery to characterize the absolute and relative surface optical conditions.[3] Using this satellite climatology, we extracted optical properties at hypoxic locations (delineated by the mid-summer ship surveys) for each year to develop frequency distributions to characterize expected optical conditions of hypoxic waters.

As mentioned, water column stratification is also required for hypoxia development. A real-time ocean nowcast/forecast system (ONFS) has been developed at NRL.[4] The NRL ONFS provides short-term forecasts of ocean current, temperature, salinity, density, and sea level variation including tides. It is based on the Navy Coastal Ocean Model (NCOM) hydrodynamic model, but has additional components such as data assimilation for sea surface height (SSH) and sea surface temperature (SST) and improved forcing with actual river discharge data. A nested model with 2-km horizontal resolution and 40 vertical layers has been implemented in the northern Gulf of Mexico, and we use the surface-to-bottom vertical density gradient derived from this model as our stratification index. Based on the in situ and model data, we estimated a minimum stratification threshold required for hypoxia development.

To determine likely hypoxic areas in an image, we compare the observed satellite-derived optical properties (absolute and relative water composition) to the expected conditions (from the optical climatology). We couple this with the model-derived stratification index and the bathymetry in a four-tiered testing approach to provide a spatial estimate of possible hypoxic areas. A pixel is flagged as potentially hypoxic if all four of the following criteria are satisfied:

(1) the relative optical properties match the historical hypoxic properties in at least 8 years and occur at least 500 times (i.e., in at least 500 pixels over the 10 years);

(2) the absolute optical properties match the historical hypoxic properties in at least 8 years and occur at least 500 times;

(3) the water depth is shallower than 50 m;

(4) the surface-to-bottom density difference from the model is greater than 1.5 kg/m³ (i.e., the water column is stratified).

The premise is that by comparing current optical conditions to those observed during past hypoxic events, we can "predict" where hypoxia is most likely to occur. Figure 4 shows a schematic of the process.
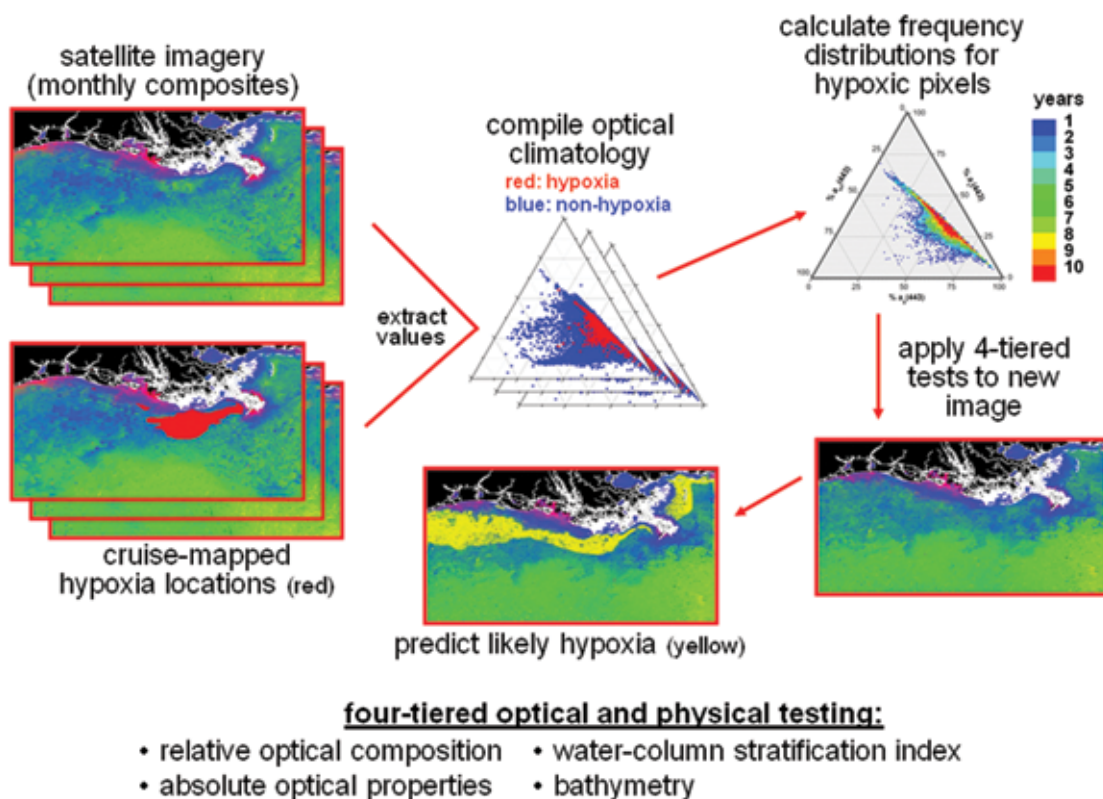
FIGURE 4
Schematic illustration showing the steps involved in the estimation of hypoxic locations, using a combination of satellite ocean color imagery and hydrodynamic modeling. A four-tiered test based on both the optical and physical properties of the water is applied; if all four criteria are met, an image pixel is flagged as hypoxic.

Validation: To validate the approach, we can compare the cruise-mapped and the satellite-estimated hypoxia regions. Figure 5 shows example results for one year (2006). Following extraction of the optical values from the 2006 satellite OWMC image, comparisons were made with the past hypoxia optical conditions as prescribed by the frequency plots. The four-tiered test described above, coupling the optical and physical conditions, was then applied; the intersection of the resulting four regions determined the final prediction (red and yellow pixels in Fig. 5). Note the close correspondence between the estimated and observed hypoxic regions. Why can we successfully use surface optical imagery to represent a bottom hypoxic process? We believe that the success of this approach is due to the causative linkage between the bottom hypoxia and the prior surface phytoplankton bloom, which can be detected by satellite.

Impact: Our research has led to the development of a novel approach that combines satellite ocean color imagery and hydrodynamic modeling to estimate both the size and location of coastal hypoxia. This approach can be used to augment ship surveys and delineate areas of expected hypoxia in near-real time, reducing costs and providing coastal managers with a new monitoring and predictive tool. In addition, this approach can be extended to a variety of other applications, such as mapping, tracking, and forecasting of harmful algal blooms and other coastal processes that impact both Navy and civilian operations.

References
[1] Louisiana Universities Marine Consortium. "Hypoxia in the Northern Gulf of Mexico," http://www.gulfhypoxia.net, 2009.
[2] P. Martinolich and T. Scardino. "Automated Processing System User's Guide Version 3.8," Naval Research Laboratory, Washington, D.C., http://www7333.nrlssc.navy.mil/docs/aps_v3.8/html/user/aps/aps.html (2009).
[3] R.W. Gould, Jr., and R.A. Arnone, "Optical Water Mass Classification for Ocean Color Imagery," in *Proceedings: Second International Conference, Current Problems in Optics of Natural Waters*, I. Levin and G. Gilbert, eds., St. Petersburg, Russia, 2003.
[4] D.S. Ko, P.J. Martin, C.D. Rowley, and R.H. Preller, "A Real-Time Coastal Ocean Prediction Experiment for MREA04," *J. Marine Systems* **69**, 17–28 (2008), doi:10.1016/j.jmarsys.2007.02.022. ■
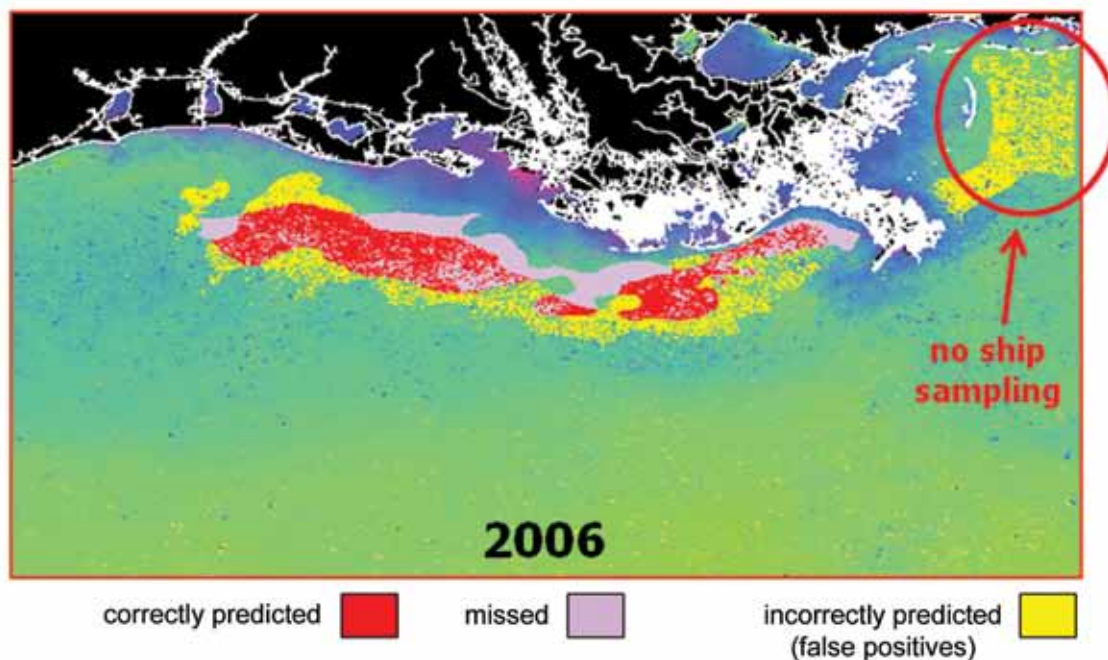
FIGURE 5
Estimated hypoxic locations for coastal Louisiana in 2006, compared to observed hypoxia locations as determined by the mid-summer cruise. Red pixels indicate correctly predicted locations using our approach, pink pixels indicate "missed" locations (i.e., the cruise survey observed hypoxia but our approach failed to highlight these areas as hypoxic), and yellow pixels indicate "false positives" (i.e., our approach indicated likely hypoxia but the cruise sampling did not observe hypoxia). Note the large area of yellow pixels east of the Mississippi River delta. These are better described as "uncharacterized" rather than "false positives" because this region was not sampled by any of the mid-summer surveys. However, some work has indicated that this area experiences sporadic hypoxia, and our approach also indicates that hypoxia is likely there. Plans are under way for future sampling in that area.

MIS Sensor Program Endures Turbulent Year

R.H. Towsley[1] and P.W. Gaiser[2]
[1] *Spacecraft Engineering Department*
[2] *Remote Sensing Division*

MIS Progress: The imaging of the Earth's surface and the sounding of the atmosphere using passive sensing of microwave and millimeter-wave frequencies has become a critical piece of Earth observations. Measurements in the 6 to 184 GHz frequency range provide information and insight into soil moisture, sea surface winds, atmospheric temperature, atmospheric moisture, sea surface temperature, water vapor, and precipitation. The Microwave Imager/Sounder (MIS) will be the first instrument to measure across all of these frequencies with a single sensor. Figures 6 through 8 depict its planned deployment aboard the spacecraft.

The MIS combines the capability of an imaging microwave radiometer, a lower and upper atmosphere micro/millimeter-wave sounder, and a polarimetric radiometer. Using algorithms developed in conjunc-

tion with the flight hardware and software, sensed data will be processed to produce microwave imagery and other specialized meteorological and oceanographic products. These products will be disseminated to users worldwide by the DoD in the form of raw data records (RDRs), temperature data records (TDRs), sensor data records (SDRs), and environmental data records (EDRs). To provide this unique capability for our nation, the Naval Center for Space Technology's Spacecraft Engineering Department has teamed with the Remote Sensing Division to develop an operational sensor for the Defense Weather Satellite System. The Electronics Science and Technology Division is providing their expertise to support the program's sounding channels.

From WindSat to MIS: In 2003, the NRL-built WindSat instrument was launched aboard the Coriolis Mission spacecraft. The National Polar-orbiting Operational Environmental Satellite System (NPOESS) Integrated Program Office (IPO) and the United States Navy jointly sponsored the WindSat sensor. To build WindSat, NRL put together a science and engineering team drawn from the Spacecraft Engineering Department and the Remote Sensing Division.
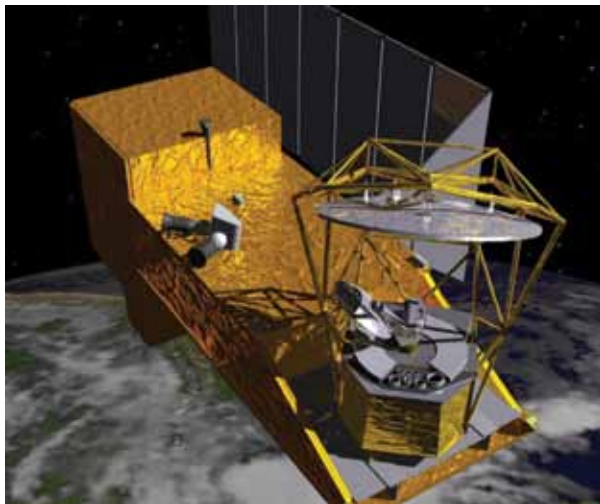
FIGURE 6
Microwave Imager/Sounder depicted on the spacecraft bus.
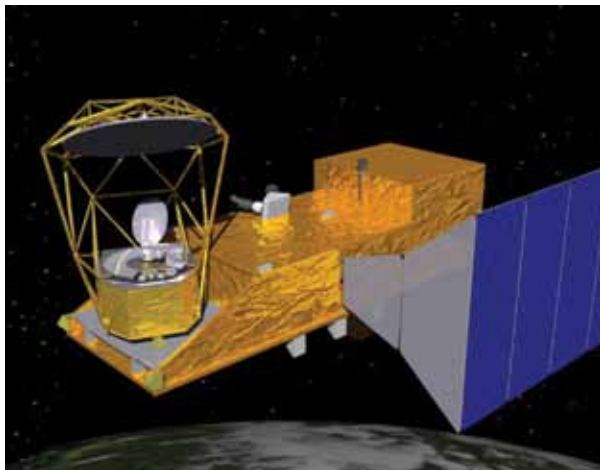
FIGURE 7
Microwave Imager/Sounder depicted on the spacecraft bus (view 2).
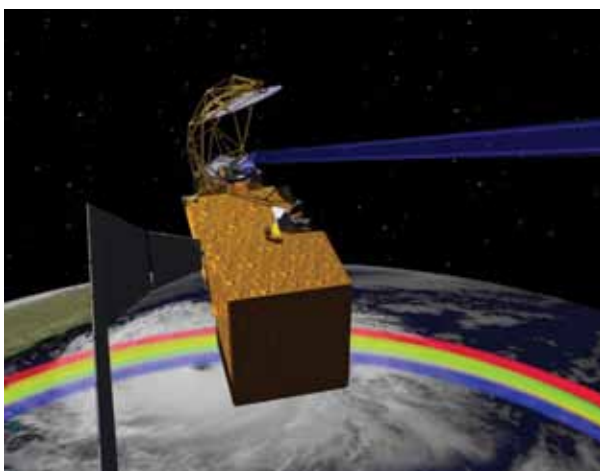
FIGURE 8
Microwave Imager/Sounder showing cold sky scene (for calibration) and operational sensor sweep.

The WindSat sensor brought together the long national heritage of Scanning Multichannel Microwave Radiometers from Seasat and Nimbus-7 through the Special Sensor Microwave Imager with advances in polarimetric science to create the first conical scanning polarimetric microwave radiometer. More than 8 years later, the "operational leave behind" capability of an on-orbit WindSat continues to provide data to military and civilian users.

The NPOESS IPO competitively selected NRL to build MIS because of the Laboratory's demonstrated experience and knowledge. In July 2008, the NPOESS IPO tendered an Economy Act order to NRL's Naval Center for Space Technology to design, develop, build, and transition to industry production a conical scanning polarimetric microwave radiometer based on the highly successful WindSat project. The 41-channel MIS instrument would be an operational sensor and would include an atmospheric sounding capability.

This MIS Program team completed a successful System Requirements Design Review (SRDR) in May 2009. On November 24, 2009, the MIS Program completed its Integrated Baseline Review (IBR), which validated the technical scope of work, verified the program's budget and schedule as articulated in the Performance Measurement Baseline (PMB), and assessed program risk. Upon exiting the review, the program sponsor and Program Manager mutually agreed to the executability of the program. A successful IBR is a significant milestone for the Earned Value Management (EVM) process for program cost and schedule oversight.

From NPOESS to DMSG: In February 2010, the President directed the dissolution of the Tri-Agency managed NPOESS. The dissolution of NPOESS returned to the Defense Meteorological System Group (DMSG) the responsibility for the space-based satisfaction of military weather-forecasting, storm-tracking, and climate-monitoring requirements per a March 17, 2010, Acquisition Decision Memorandum (ADM). DMSG is managed by the Space and Missile Systems Center (SMC) at Los Angeles Air Force Base, California.

On April 8, 2010, the MIS program successfully completed its Preliminary Design Review (PDR) for the 41-channel MIS on the NPOESS spacecraft bus. The MIS PDR was the second in a series of event-driven Systems Engineering Technical Review (SETR) milestones that are rigorously adjudicated by independent technical experts and review teams. The PDR validated the preliminary design performance meets the requirements and also verifies necessary technical processes and documentation. The NPOESS IPO approved the MIS Program to proceed to the Complete Design Phase.

Since PDR and during sponsor transition, the MIS Program continued to perform design, development, and risk reduction for both 23- and 43-channel conically scanning microwave radiometer options, based heavily on the NPOESS MIS. On November 1, 2010, management of the MIS Program was officially transferred from the NPOESS IPO to the Defense Weather Satellite Systems (DWSS) System Program Office (SPO).

During the sponsor transition analysis of alternatives (AOA), the transition of the MIS technology to industrial production was eliminated. The MIS sensor will be the microwave remote sensing instrument of record for the future Major Defense Acquisition Program (MDAP) Defense Weather Satellite System. DWSS has asked NRL to produce two MIS instruments. The NRL-built MIS will be used operationally from 2018 through 2028.

[Sponsored by NRL and DWSS]

■

Simulation, Computing, and Modeling

Analyte 2000 Fiber Optic Biosensor (1998) — As payload on the Swallow UAV, NRL's biosensor provided one of the first demonstrations of the identification of aerosolized bacteria by a sensor flown on a remotely piloted plane, with data transmitted to a ground station.

Vision-Based Recovery of Unmanned Aerial Vehicles

A.D. Kahn
Tactical Electronic Warfare Division

Introduction: A key requirement for performing reconnaissance missions using small unmanned aerial vehicles (UAVs) from a ship is the ability to automatically recover the air vehicle on board the ship. The automatic landing system must be simple to use, not add additional hardware to the air vehicle, and have a minimal footprint to the operation of the ship.

Current systems used for automatic landing of UAVs on board ships require the installation of large and/or expensive equipment on the air vehicle.[1-3] Some of these systems present a logistics challenge due to their large footprint on board ships.

The system in this program addresses these issues by leveraging the existing reconnaissance payload consisting of a video camera and transmitter, along with the existing UAV autopilot and data link. On the ship, in addition to the UAV operator terminal and hardware, is a laptop computer and recovery target with optical markers. Figure 1 presents the recovery system concept.
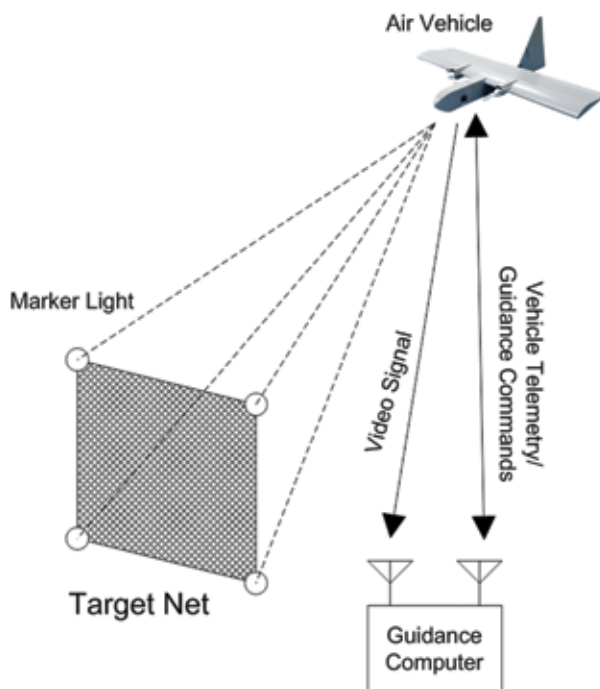
FIGURE 1
Vision-based automatic recovery system diagram.

System Development: The development of the vision-based automatic landing system began with the creation of a simulation environment. The simula-

tor models the behavior of the vehicle, autopilot, and data link, and generates a synthetic camera view. The simulation tool was useful in the invention and evaluation of the vision and guidance algorithms. In addition to computer simulation, a series of static real-world experiments were performed to validate the robustness of the machine vision algorithms in various lighting environments.

Flight experiments were conducted to evaluate the closed-loop performance of the prototype automatic landing system. The experiments were performed against a stationary optical landing target. The landing target was a square of 1.8 m per side with high-intensity lights at the corners. The vehicle was flown at a speed of approximately 18 m/s. With a camera resolution of 640×480 pixels and field of view of about 40 degrees, which is similar to that of cameras used on UAVs in current operation with the Fleet, the system can detect the landing target at a range of approximately 121 m. At this closure speed and range, the system has about 7 seconds to maneuver the vehicle into a collision path with the landing target. During the flight experiments, eight fully automatic approaches were performed, with the computer acquiring and tracking the target six times. Based on recorded video from the UAV, the vehicle would have hit the target on four attempts. This was estimated as the vehicle was told to automatically wave-off the approach at a range of 36.5 m from the target. This was done because the target was made of 2 by 4 lumber instead of a net. Figure 2 is a photograph of the UAV automatically approaching the target during one of these runs.

FIGURE 2
UAV in automatic approach to the simulated recovery target.

Conclusion: The new automatic recovery technology uses the existing hardware sensor package already present in many small tactical UAVs. The data from

these sensors are fused using a ship-based computer that generates steering commands for the vehicle to perform. This system has a significantly smaller footprint on board ship in comparison to other existing landing systems. Manpower requirements and logistics are reduced because the system performs recoveries fully automatically, and no additional expensive hardware is needed on board the air vehicle. A simulator was developed to evaluate the machine vision and guidance algorithms. A prototype system has been successfully flight tested.

References
[1] Sierra Nevada Corporation, "UCARS-V2: UAV Common Automatic Recovery System – Version 2 for Shipboard Operations," product brochure, 2006.
[2] The Insitu Group, Inc., "Unmanned System: Launch and Retrieval," http://www.insitu.com/launch_and_retrieval, 2010.
[3] RUAG, "Ranger UAV System," product brochure, 2006.

■

Simulating Natural Gas Explosions in Semiconfined Geometries

D.A. Kessler, V.N. Gamezo, and E.S. Oran
Laboratory for Computational Physics and Fluid Dynamics

Introduction: Detonations are violent, supersonic, high-pressure reaction waves that can develop during an explosion and cause severe damage. In the most powerful explosions, detonations can be initiated directly by strong shock waves. Under certain conditions, however, detonations can arise spontaneously from weak explosions or even from simple sparks.

This latter process, called the deflagration-to-detonation transition (DDT), takes place in two stages.[1] In the first stage, the relatively slow initial flame accelerates and becomes a fast, turbulent flame ("deflagration") that moves at nearly the speed of sound into the unburned but combustible gas. This can occur in semiconfined areas where the flow caused by thermal expansion of the burning gases acts like a piston to accelerate the flame. Flow instabilities and other interactions with the surrounding environment stretch and distort the flame and cause it to release energy more and more quickly. Eventually, pressure builds up in front of the flame and causes a high-pressure shock

wave to form. In the second stage of the DDT process, this shock wave collides with physical obstructions or disturbances in the flow, heating and compressing small pockets of gas just ahead of the flame. The compressed gas in these "hot spots" can then ignite and produce a detonation.

In the past, this DDT process has been studied for simple, highly reactive fuels, such as hydrogen, acetylene, and ethylene. Now, we are working toward understanding the conditions necessary for DDT to occur in natural gas, an important but less reactive fuel that can be found in mine tunnels, access corridors on a ship, power-generation plants, fuel-storage facilities, and many other military and industrial settings. The loss of lives and property in several recent coal mine explosions in the United States and abroad have highlighted the need for an improved understanding of how and why detonations can form in natural gas explosions.

Model Development: Simulating an explosion requires specifying a model for the release of energy by chemical reactions in addition to solving the typical fluid flow equations. Detailed chemical models often involve hundreds of reactions. In a large, multidimensional simulation, computing each of these reactions would be too time-consuming. To make such computations feasible, we instead approximate the energy release from these hundreds of reactions with a single global reaction. This one-step model cannot exactly reproduce all properties of flames and detonations in natural gas–air mixtures, but we can calibrate it so that it gives reasonable approximations of the key length and time scales involved at the different stages of DDT, namely the speed, thickness, and temperature of flames and the speed and thickness of detonations in these mixtures.

Flame Acceleration and DDT in Semiconfined Channels: The calibrated reaction model is used with the usual fluid flow equations to simulate flame acceleration and DDT in a two-dimensional, semiconfined channel. The system we simulate, a diagram of which is shown in Fig. 3(a), is a simplified model of an experimental system that was used to study DDT in mixtures of methane (the primary fuel in natural gas) and air.[2] The physical obstructions arranged periodically in the channel help to more quickly accelerate the flame. A time progression of the temperature fields in the lower half of a 17.4 cm wide channel with obstructions blocking 30% of the cross-sectional area of the channel (blockage ratio of 0.3) is shown in Figs. 3(b-i). Both stages of the DDT process are shown. After being ignited by a weak spark, a flame travels from the closed (left) end of the channel toward the outflow. In the process, it becomes distorted and speeds up considerably.
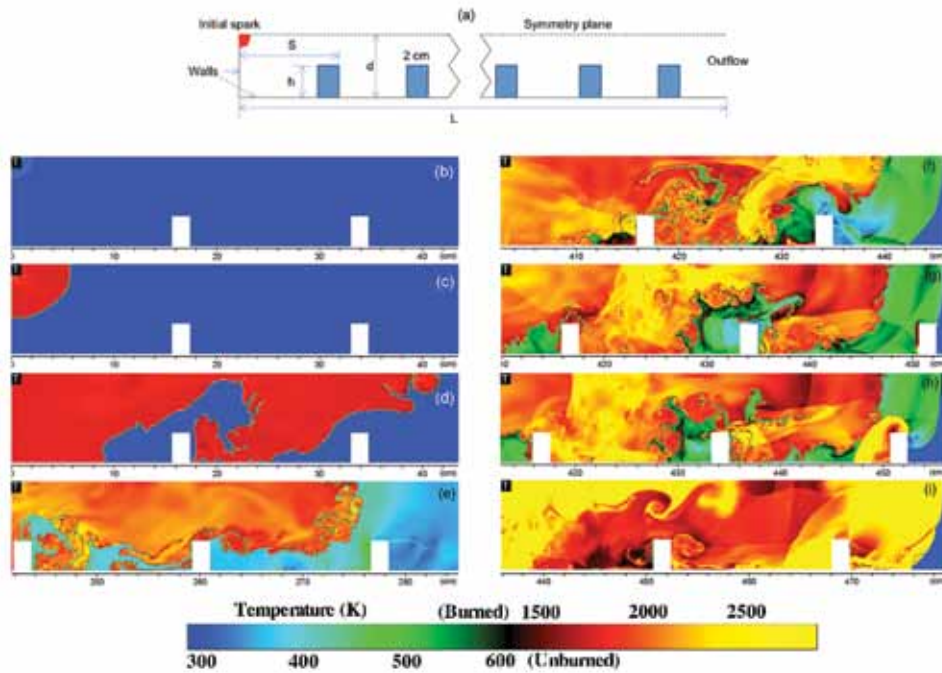
FIGURE 3
(a) Two-dimensional model geometry of a semiconfined space used in the simulations. Obstacles (blue rectangles) are spaced uniformly throughout the channels. We assume the channel is perfectly symmetric and simulate only the bottom half. In this simulation, d = 8.7 cm, h = 2.61 cm, L = 11.8 m, and S = 17.4 cm. (b-i) Temperature maps in the lower half of the channel near the leading edge of the reaction front showing (b) flame ignition by a weak spark, (c) laminar flame propagation, (d) flame stretching caused by thermal expansion and flame wrinkling, (e) pressure buildup in front of a deflagration, (f) shock wave formation, (g) hot spot formation after collision of a shock with an obstacle, (h) detonation initiation, and (i) detonation propagation.
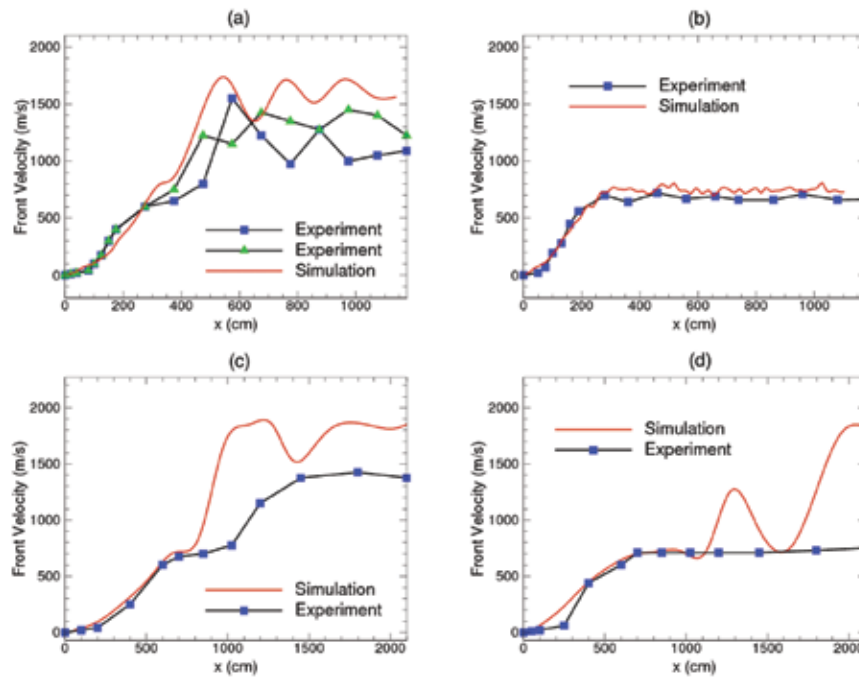
FIGURE 4
Velocity of the leading edge of the reaction front as a function of its position in the system calculated using the reaction model (red lines) and measured in experiments (blue and green symbols) for systems (a) 17.4 cm wide with blockage ratio 0.3, (b) 17.4 cm wide with blockage ratio 0.6, (c) 52 cm wide with blockage ratio 0.3, and (d) 52 cm wide with blockage ratio 0.6.

The shock wave that forms ahead of the flame collides with the solid obstacles, and the hot spot created by the collision shown in Fig. 3(g) ignites a detonation (see the figure caption and Ref. 3 for more complete descriptions). In Fig. 4(a), we compare the average velocity of the leading edge of the reaction zone in this simulation to several experimental measurements taken in a 17.4 cm diameter tube with the same blockage ratio. The results of three other simulations in channels of various sizes and blockage ratios are also compared to similar experiments in Figs. 4(b-d). The results calculated using the simple reaction model qualitatively, and in many cases quantitatively, match the experiments.

Summary and Future Directions: The innovation in this work is the development of a fast, reliable model for simulating DDT in natural gas–air mixtures that we have validated with existing experimental data. The speed of these calculations gives us the ability to simulate larger and more complex systems. We are currently working to understand how the DDT process scales to larger systems similar to those used in experiments conducted by the National Institute for Occupational Safety and Health (NIOSH)[4] and are finding that methane still detonates, in large systems, with concentrations lower than previously thought possible.

[Sponsored by NIOSH and NRL]

References
[1] E.S. Oran and V.N. Gamezo, "Origins of the Deflagration-to-Detonation Transition in Gas-Phase Combustion," *Combustion and Flame* **148**, 4–47 (2007).
[2] M. Kuznetsov et al., "DDT in Methane-Air Mixtures," *Shock Waves* **12**, 215–220 (2002).
[3] D.A. Kessler, V.N. Gamezo, and E.S. Oran, "Simulations of Flame Acceleration and Deflagration-to-Detonation Transitions in Methane-Air Systems," *Combustion and Flame* **157**, 2063–2077 (2010).
[4] R.K. Zipf, Jr., V.N. Gamezo, M.J. Sapko, W.P. Marchewka, K.M. Mohamed, E.S. Oran, D.A. Kessler, E.S. Weiss, J.D. Addis, F.A. Karnack, and D.D. Sellers, "Methane-Air Detonation Experiments at NIOSH Lake Lynn Laboratory," *Proceedings of the Eighth International Symposium on Hazards, Prevention, and Mitigation of Industrial Explosions*, Yokohama, Japan, Sept. 5–10, 2010.

■

Using Noise to Reveal Properties of Nonlinear Dynamical Systems: Making Noise Work for You

I.B. Schwartz,[1] L. Billings,[2] and M. Dykman[3]
[1] *Plasma Physics Division*
[2] *Montclair State University*
[3] *Michigan State University*

Introduction: In systems far from equilibrium, noise is found to play an increasingly important role in understanding the dynamics. Many of the systems we have studied, including delay coupled lasers,[1] adaptive networks,[2] and epidemic spread in finite populations,[3,4] are all modeled in the presence of noise. As sensing devices become smaller, or as the number of particles in populations gets smaller, new metastable states may be created, leading to novel observed dynamics.

For very small noise, it is known the system will remain close to an equilibrium state for very long times. However, if the system is nonlinear, sufficiently large noise will cause the system to leave its local attracting state, and explore other parts of phase space. In particular, it may find other distinct states, which may or may not be stable. If the dynamical system has more than one attracting state, noise may cause the dynamics to switch between states. A physical example of a system having more than one attractor is that of a micromechanical oscillator, shown in Fig. 5(a). It has a potential similar to that schematically drawn in Fig. 5(b), which is a generic picture of a bistable potential. It is clear that each attracting state is separated from the other by a barrier height of the potential, and in the case of
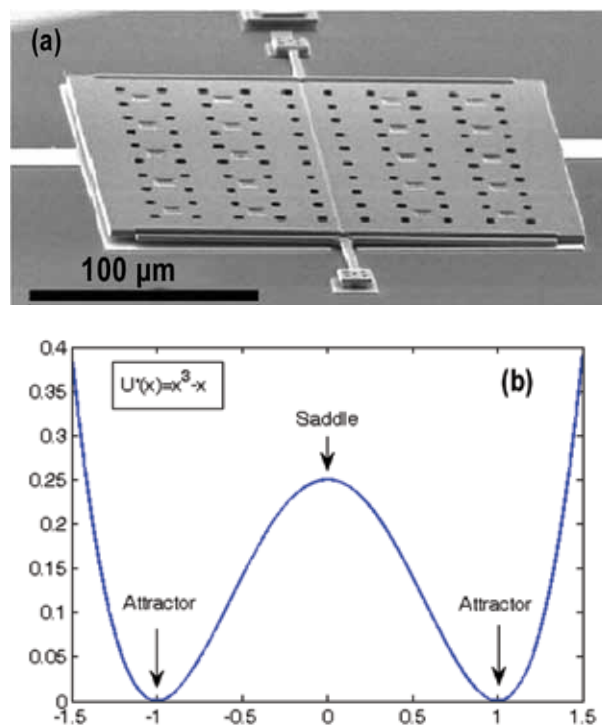
FIGURE 5
(a) An image of a micro-torsional oscillator. There are two stable states and hysteresis under suitable driving conditions. For details, see Ref. 8. (b) A schematic of a scalar potential possessing bistability. The two attracting states, located at the minima, are separated by an unstable object, such as a saddle. Deterministically, the trajectories go to one of the two attracting states, and remain there. However, if noise is added to the system, the trajectory may switch from one attractor to another.

Bistability

Extinction
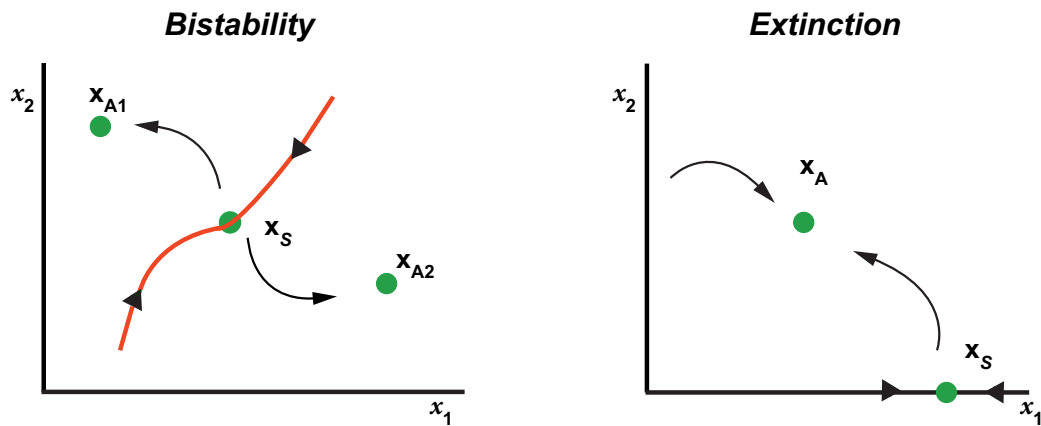
FIGURE 6
Phase portraits of two examples of changing states. (Left) The topology of a switching process. The stable manifold of a saddle divides the phase space between two attractors, forming a basin boundary. The stable manifold is a barrier that must be crossed in order to switch from one state to another. (Right) The topology of an extinction process. There exists a unique attracting state and an unstable extinct, which is a saddle. Noise drives the process to extinction by overcoming the unstable force of the extinct state.

Gaussian thermal noise, the exponent of the switching rate between attractors is proportional to the barrier height. The left graph in Fig. 6 depicts the phase space topology of the bistability in two dimensions. There is a saddle separating the two attracting states. The stable manifold acts as a basin boundary separating the basins of attraction between the two attractors. The noise must overcome the basin boundary to switch states.

On the other hand, if the system consists of a finite number of particles, such as a chemical reaction or population, noise may cause one or more of the species

to approach zero, i.e., the species goes extinct. Generic epidemic models typically have one attracting endemic state and one extinct state. The extinct state is typically a saddle; the topology of this type of system is given in the right graph of Fig. 6. For extinction to occur, noise again must overcome an unstable barrier to approach the extinct state.

An example of probability to extinction is shown in Fig. 7(a). In this finite population epidemic model, there is one attracting state and one unstable extinct state. However, due to random interactions between
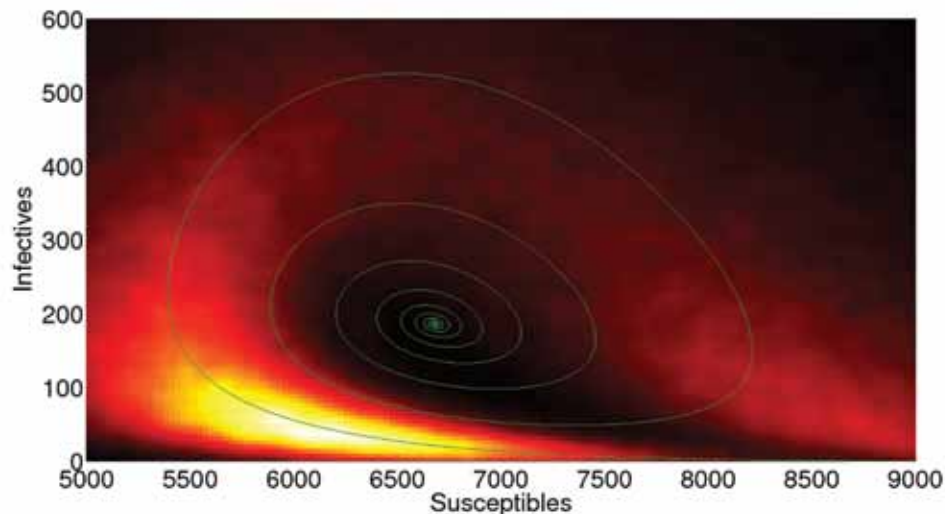
FIGURE 7(a)
An example of an extinction event in an epidemic model in a finite population of individuals. The population consists of infectious and susceptible individuals. Colors indicate the probability density (lighter corresponding to higher probability) for 20,000 stochastic realizations. The results were computed using Monte Carlo simulations. (Figure made by Simone Bianco, currently with the University of California at San Francisco.)
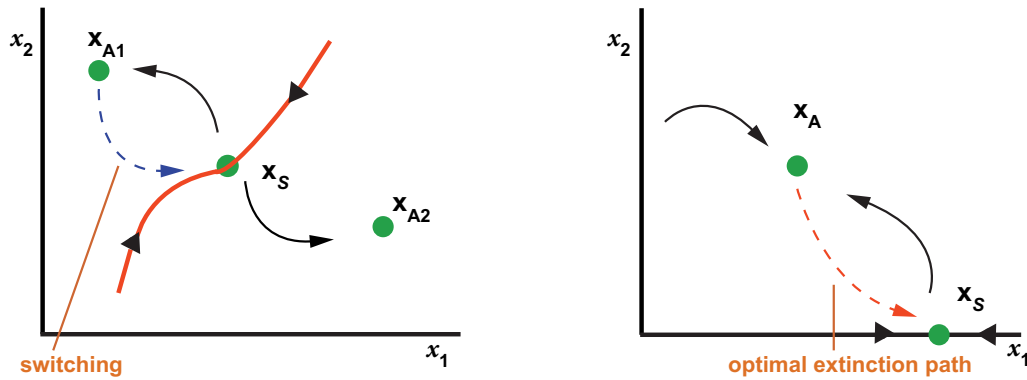
FIGURE 7(b)
A schematic of optimal paths for switching and extinction. (Left) The path to switch in a bistable situation. (Right) The optimal path to an extinct state. In both cases, noise is the driving force causing the system to overcome unstable directions of a saddle to either switch, as in the left panel, or go extinct.

particles, internal noise causes the system to overcome the instability of the extinct state, and one component vanishes.

One important point in understanding the probability of switching or extinction is that there exist many paths which generate a probability distribution of the events. One interesting question that may be asked is which paths optimize the probability of switching events, or extinctions? In particular, how do these paths arise as noise-driven events, and how do they depend on parameters of the system? The answers to these questions may be addressed by considering certain parameter regions. The graphs in Fig. 7(b) show possible optimal paths for switching and extinction, and the graph in Fig. 7(a) shows the actual optimal path for an epidemic model going from the endemic state to the extinct state where the number of infectious individuals (y-axis) approaches zero. For the rest of this article, we concentrate on quantifying switching rates in non-Gaussian noise situations near bifurcations. This is used to actually quantify parameters and noise characteristics in general sensing devices. References 5 through 7 provide the general theory in generic models as well as in stochastic models with multiple time scales.

Quantifying Switching Rates Near Instabilities:
One aspect of nonlinear systems in noisy environments is that the rates of switching depend on a parameter that controls the number of states in the systems. In particular, when a system undergoes changes in stability or in the number of observed states in a system, it is said to undergo a bifurcation. Parameters ranges near bifurcations are important in that they control the rate at which the dynamics proceeds. In particular, the relevant components are slowed down in this range, and as a result of weak stability, noise-induced fluctuations are comparatively large. They ultimately lead to switching of the system from the stable state. Close to a bifurcation point, the switching rate becomes measurable even

where far from this point it is exceedingly small for a given noise level. The high sensitivity of the rate to the system parameters has been broadly used to determine parameters of many high quality sensing devices such as Josephson junctions and Josephson junction-based systems, nanomagnets, mechanical nanoresonators, and recently in quantum measurements. (Reference 5 provides a list of references to specific devices.)

The analysis of switching conventionally relies on the assumption that the underlying noise is Gaussian. Then the switching exponent Q, i.e., the exponent in the expression for the switching rate, $W \cong \exp(-Q)$, displays a power law dependence on the distance to the bifurcation point in the parameter space, η. That is, $Q = \eta^\epsilon$. Recently, there has been much interest in large fluctuations and switching induced by non-Gaussian noise. Such switching can be used to determine the noise statistics. However, the features of the switching rate near bifurcation points have not been explored. Yet, one may expect that the dependence of the switching exponent will differ from that for a Gaussian noise and will be very sensitive to the noise statistics. Indeed, we have found that there exists a non-power-law behavior when non-Gaussian noise is considered.

Non-Gaussian Noise-Induced Switching: We consider noise-induced switching in two different generic bifurcations: a saddle-node bifurcation and a pitchfork bifurcation. In both cases, we consider a Langevin problem where the potential function is a scalar, and the non-Gaussian noise source is Poisson, having amplitude *g* and mean frequency *v*. Figure 8 shows examples of two potential functions that characterize the saddle-node and pitchfork bifurcations. Several curves are plotted to illustrate the dependence on the bifurcation parameter for each bifurcation.

To predict what scaling law behavior occurs, we theoretically find the exponent of the switching rate. The exponent of the switching rate is given by classical
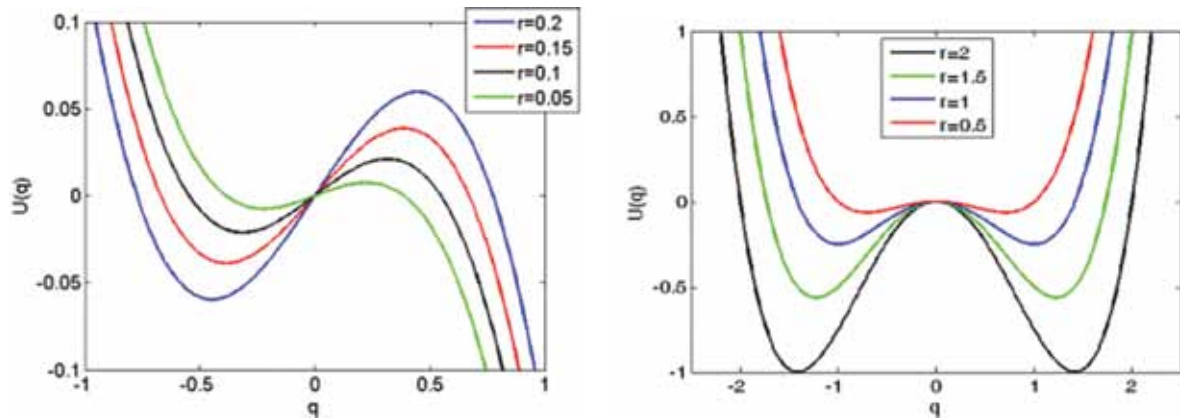
FIGURE 8
Potential functions for different bifurcation values of *r* in *U(q)*. The left panel is the potential for a saddle node bifurcation, while the right panel is that of a pitchfork bifurcation.
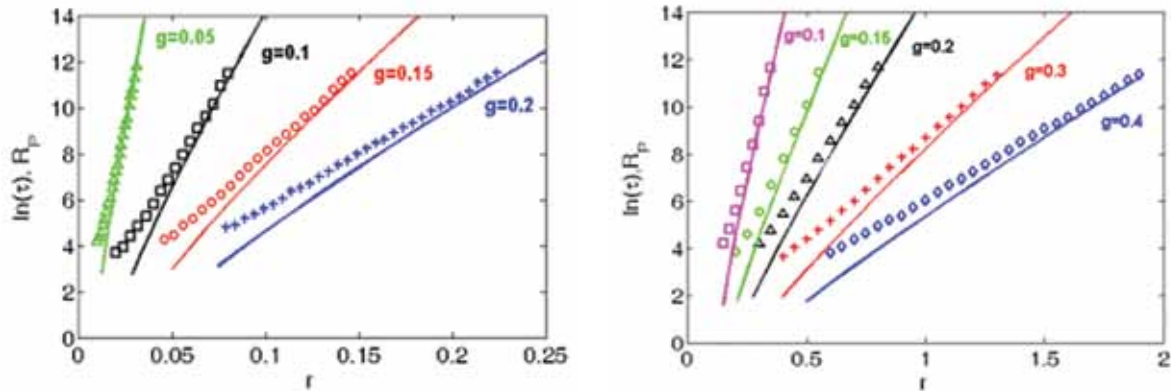
FIGURE 9
Switching exponents comparing numerical Monte Carlo simulations (symbols) vs theoretical predictions (solid curves). Poisson noise is characterized by amplitude *g* and mean frequency *v*. Pulses were only positive; i.e., pulses were one-sided. Saddle-node results are in the left panel and pitchfork results in the right panel.

analogue of the action, which is defined as the path integral from one state to the saddle. The trajectory of the path comes from an associated Hamiltonian, and may be computed from the derived equations of motion.

The interesting fact about computing the path for switching rates in a stochastic problem is that the optimal path maximizing the switching rate is determined by a deterministic conservative system. This system is twice the dimension of the original deterministic model. The extra dimensions model the noise as an effective force on the system, which drives the dynamics across the barrier. (See Fig. 7(a) for an optimal path example.)

The non-power-law behavior is predicted for both bifurcations in Ref. 5, and theory is compared with simulation in Fig. 9. Clearly, the power law dependence no longer exists due to a logarithmic correction. For Poisson noise, the change in sensor measurement characteristics is considerable, even for small noise amplitudes, *g*.

Conclusions: Many devices used as sensors, such as photonics and mesoscale devices, are driven by non-Gaussian noise sources. Here, we briefly reviewed new theoretical machinery that can characterize the physical parameters of a device by examining the scaling laws associated with switching rates. In contrast to power law behavior that is observed for Gaussian noise, non-Gaussian noise leads to non-power-law behavior. In the case of Poisson noise found in many devices, we find different logarithmic corrections in the two bifurcation scenarios. Thus, accurate measurements of switching rates may also determine the type of instability in the device, as well as where the bifurcation points are located.

Elsewhere, we have also considered the mixing between Gaussian and non-Gaussian sources.[5] It turned out that even a weak additional Gaussian noise becomes the major cause of switching sufficiently close to the bifurcation point. A qualitative and quantitative description of the crossover from Poisson- to Gaussian-

noise-controlled switching and of the bifurcation distance dependence of the switching exponent is in full agreement with numerical simulations.

[Sponsored by ONR]

References
[1] A.L. Franz, R. Roy, L.B. Shaw, and I.B. Schwartz, "Effect of Multiple Time Delays on Intensity Fluctuation Dynamics in Fiber Ring Lasers," *Phys. Rev. E* **78**(1), 016208 (2008).
[2] L.B. Shaw and I.B. Schwartz, "Enhanced Vaccine Control of Epidemics in Adaptive Networks," *Phys. Rev. E* **81**(4), 046120 (2010).
[3] I.B. Schwartz, L. Billings, M. Dykman, and A. Landsman, "Predicting Extinction Rates in Stochastic Epidemic Models," *J. Statistical Mechanics: Theory and Experiment* **2009**(1), P01005 (2009).
[4] E. Forgoston, S. Bianco, L.B. Shaw, and I.B. Schwartz, "Maximal Sensitive Dependence and the Optimal Path to Epidemic Extinction," *Bull. Mathematical Biol.*, **73**(3), 495–514 (2011).
[5] L. Billings, I.B. Schwartz, M. McCrary, A.N. Korotkov, and M.I. Dykman, "Switching Exponent Scaling near Bifurcation Points for Non-Gaussian Noise," *Phys. Rev. Lett.* **104**(14), 140601 (2010).
[6] E. Forgoston and I.B. Schwartz, "Escape Rates in a Stochastic Environment with Multiple Scales," *Siam J. Appl. Dynamic. Sys.* **8**(3), 119–1217 (2009).
[7] L. Billings, M.I. Dykman, and I.B. Schwartz, "Thermally Activated Switching in the Presence of Non-Gaussian Noise," *Phys. Rev. E* **78**(5), 051122 (2008).
[8] H.B. Chan, M.I. Dykman, and C. Stambaugh, "Paths for Fluctuation Induced Switching," *Phys. Rev. Lett.* **100**, 130602 (2008).

■

Space Research and Satellite Technology

GRAB (1960) — The Galactic Radiation and Background satellite was America's first electronic intelligence (ELINT) satellite. GRAB's ELINT antennas collected each pulse of a Soviet radar signal in a specified bandwidth, and a larger and separate turnstile antenna transponded a corresponding signal to NRL receiving and control huts.

Plasma Bubbles in the Post-Sunset Ionosphere

J.D. Huba,[1] G. Joyce,[2] and J. Krall[1]

[1] *Plasma Physics Division*

[2] *Icarus Research, Inc.*

Introduction: Post-sunset ionospheric irregularities in the equatorial F region were first observed by Booker and Wells[1] using high-frequency radio transmitters (ionosondes). This phenomenon has become known as equatorial spread F (ESF). During ESF, the equatorial ionosphere becomes unstable because of a Rayleigh–Taylor-like instability: large-scale (tens of km) electron density "bubbles" can develop and rise to high altitudes (1000 km or greater at times). Understanding and modeling ESF is important because of its impact on space weather: it causes radio wave scintillation that degrades communication and navigation systems. In fact, it is the focus of the Air Force Communication/Navigation Outage Forecasting System (C/NOFS) mission.

A major problem in self-consistently modeling equatorial plasma bubbles is capturing bubble dynamics on scale lengths of less than approximately 10 km within the context of the global ionosphere with scale lengths of approximately 1000s of km. This is critical because the day-to-day variability of ESF is controlled (in part) by the prereversal enhancement (PRE) of the eastward electric field. The PRE in turn is controlled by the thermospheric neutral wind through a global dynamo mechanism.

To meet the Navy's need to specify the disturbed ionospheric environment, we have developed a new, three-dimensional code of the low- to mid-latitude ionosphere that self-consistently models the onset and evolution of post-sunset, large-scale plasma bubbles in the equatorial ionosphere.

Results: Our initial effort to model equatorial plasma bubbles was based on a modified version of SAMI3, dubbed SAMI3/ESF.[2] SAMI3 is a comprehensive, 3D, first-principles physics model of the ionosphere developed at NRL; it is based on the NRL 2D model SAMI2.[3] To achieve the high resolution (less than approximately 10 km) needed in the longitudinal (zonal) direction, we simulated a narrow "wedge" of the ionosphere in the post-sunset period. The angular width of the wedge was 4° (approximately 500 km), and the spatial resolution was approximately 5 km.

Although the plasma dynamics of the bubble was "decoupled" from the global electrodynamics of the ionosphere, we were able to model the 3D dynamics of equatorial bubble evolution for the first time. Figure 1 presents typical results from SAMI3/ESF simulations. This figure shows a 3D graphic of the electron density (left panel) and electron temperature (right panel). The large blue isosurface in the left panel is the rising plasma bubble associated with ESF. In the right panel, the blue isosurface shows the cooling of the electrons inside the bubble; the red isosurface shows the heating of the electrons by collisional coupling with the ions and by thermal conduction at higher altitudes. Subsequently we have used SAMI3/ESF to explain compositional anomalies, enhanced airglow, and "plasma blobs" associated with bubble development.

To overcome the limitation of SAMI3/ESF to a narrow longitudinal region of the ionosphere, we improved SAMI3 to self-consistently solve for the neutral wind-driven dynamo electric field as well as the gravity-driv-
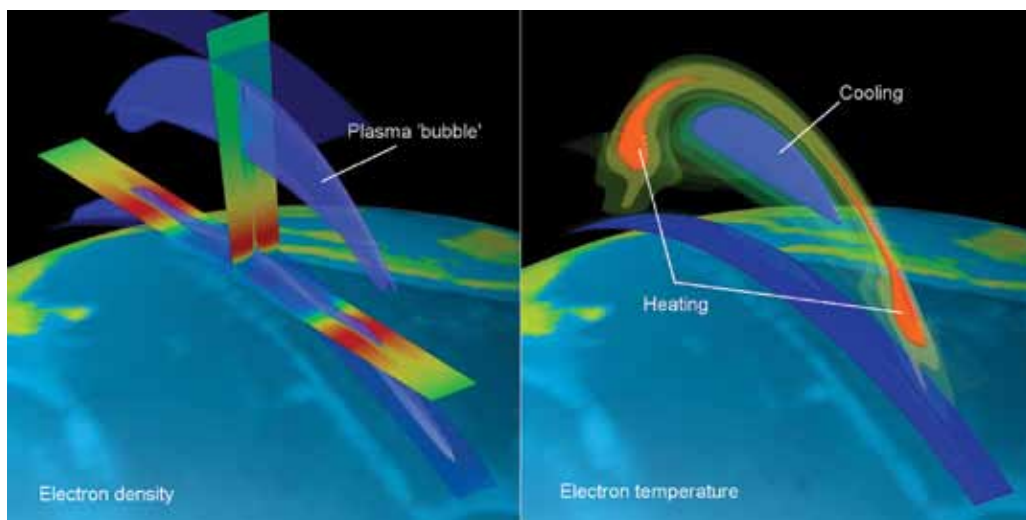
FIGURE 1
SAMI3/ESF simulation of an equatorial plasma bubble: electron density (left) and electron temperature (right).

en electric field associated with plasma bubbles.[4] The latter is achieved by incorporating a high-resolution longitudinal grid in the pre- to post-sunset sector (i.e., 1630 MLT to 2230 MLT; MLT = magnetic local time). The minimum resolution in this region is $\Delta\varphi = 0.0625°$ (i.e., a spatial scale $\Delta x \sim 7$ km). Such high resolution in a global ionosphere model is unprecedented.

Initial results from the new version of SAMI3 are shown in Fig. 2. In this figure, we show color-coded contours of the electron density in the equatorial plane. The view is looking down on the Earth above the North Pole; the Sun is to the left, dawn is at the top and dusk is at the bottom. The ionosphere builds after sunrise, achieves a maximum density in the afternoon, and starts to decay after sunset. In this simulation, a 5% electron density perturbation is imposed in the F region (at 318 km) at magnetic local times 1700, 1720, 1740, 1800, and 1820. Note that sunset is at 1800 MLT, which is at the bottom of the figure. These perturbations convect into the post-sunset sector and initiate large-scale plasma bubbles (the dark blue tilted structures in the lower, right portion of the figure). These results are consistent with observational data.
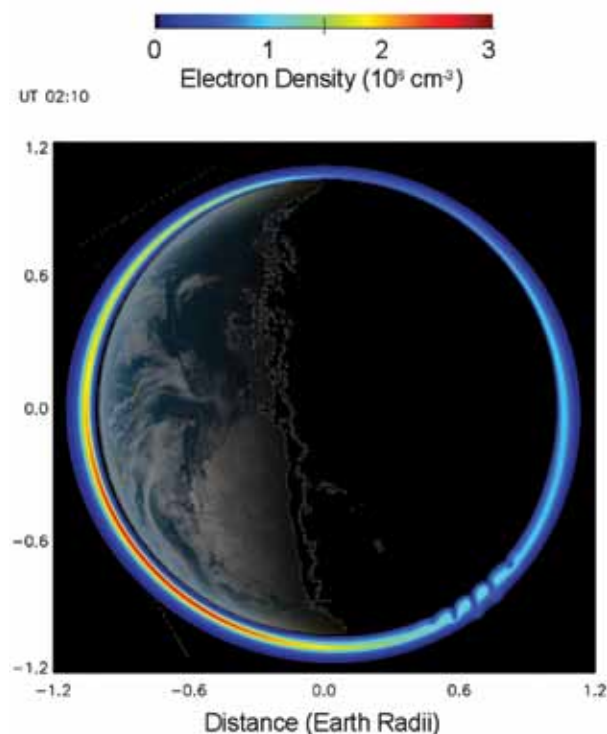
FIGURE 2
SAMI3 simulation equatorial plasma bubbles on a global scale.

Future Research: The upgraded version of SAMI3 represents a unique resource to investigate the physics of equatorial spread F. One vexing question concerning ESF is, what processes control the day-to-day vari-

ability of ESF? We will be able to address this question by investigating the impact of background ionospheric conditions on ESF bubble development (e.g., different neutral wind models, F10.7, PRE), as well as "seed" mechanisms such as gravity waves and velocity shear. To achieve closure, we will compare model results to data (e.g., radar measurements, optical observations, in situ satellite data) to assess the validity of the model results to explain ESF day-to-day variability.

[Sponsored by ONR]

References
[1] H.G. Booker and H.G. Wells, "Scattering of Radio Waves in the F-region of the Ionosphere," *Terr. Mag. Atmos. Elec.* **43**, 249–256 (1938).
[2] J.D. Huba, G. Joyce, and J. Krall, "Three-dimensional Equatorial Spread F Modeling," *Geophys. Res. Lett.* **35**, L10102 (2008), doi:10.1029/2008GL033509.
[3] J.D. Huba, G. Joyce, and J.A. Fedder, "Sami2 is Another Model of the Ionosphere (SAMI2): A New Low-Latitude Ionosphere Model," *J. Geophys. Res.* **105**, 23,035 (2000).
[4] J.D. Huba and G. Joyce, "Global Modeling of Equatorial Plasma Bubbles," *Geophys. Res. Lett.* **37**, L17104 (2010), doi:10.1029/2010GL044281.

The WISPR Instrument on the Solar Probe Plus Satellite

R.A. Howard, A. Vourlidas, S. Plunkett, and C. Korendyke
Space Science Division

Introduction: Our Sun is 150×10^6 km away from Earth. This distance is called an astronomical unit (AU). All of our knowledge about the Sun originates from remote sensing instruments from the distance of the Earth or beyond and from in situ measurements of the solar wind, which is a constantly varying and very low-density plasma flowing out from the Sun. The closest that man has ever gone to the Sun is about 0.30 AU, which is the minimum distance of the planet Mercury in its orbit about the Sun.

The Sun itself is responsible for much of the variable nature of the solar wind, but there is a lot of interaction as the wind travels out to the vicinity of Earth's orbit where most of the in situ observations have been made. How much of the variability that is seen at Earth is due to the source or due to the transport is an open issue. Even more important are a number of questions and assumptions about the near-Sun environment that have been lingering for 50 years, such as the following: What heats the corona? Are waves depositing energy in the corona, and if so, what type of wave? Or perhaps the energy comes from small coronal explosions, called

flares, driven by magnetic reconfigurations or some other mechanism? What accelerates the solar wind? What are the near-Sun plasma properties (particle density, magnetic field)? Does the solar wind come out in tubes that spread out? What is the thickness of the various plasma surfaces?

The National Aeronautics and Space Administration (NASA) is implementing a new mission to go close to the Sun in an encounter mode to answer these questions. Such an encounter mission was originally proposed in 1958 and has been proposed again several times since, but closely approaching the Sun demands new technology, particularly for heat rejection. The new NASA mission, Solar Probe Plus (SP+), will be launched in July 2018. NRL has been selected by NASA to provide the only imager for the mission. Our instrument, the Wide Field Imager for Solar PRobe Plus (WISPR), will image the solar corona in white light. At its closest approach, SP+ will pass within about 5×10^6 km from the solar limb.

The Spacecraft: The spacecraft is a challenge to design: the spacecraft and instruments must be maintained at a relatively constant temperature, while the input energy flux onto the spacecraft increases to 510 times the value in Earth orbit. The Johns Hopkins University Applied Physics Laboratory (APL) is responsible for the SP+ spacecraft, shown in Fig. 3. Most of the instruments will sit behind the shadow of the thermal protection shield (TPS). The solar arrays generate electricity by converting the photons into electrical energy, but when the SP+ gets close to the Sun, the arrays must be stowed. Otherwise, the spacecraft is a normal 3-axis stabilized design. A high-gain antenna provides high-speed downlink when the spacecraft is more than 0.25 AU from the Sun. Low-gain antennas provide command uplink and "health and status" downlink during solar encounters.
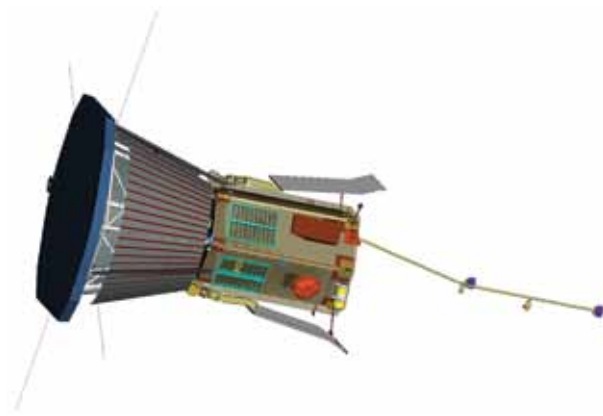
FIGURE 3
Solar Probe Plus spacecraft concept. The thermal protection shield is the hexagonal shaped plate at the top of the spacecraft and is always pointed at the Sun. It is fabricated with carbon-carbon sheets coated with a ceramic.

The Mission Profile: The SP+ will be put into an elliptic orbit using gravitational assists by flying close to the planet Venus to modify the orbit trajectory. Only three months after launch, the first perihelion of 35 R_{sun} (1 R_{sun} is 696,000 km) is reached, and subsequent gravitational assists (a total of seven) lead to a minimum perihelion of 9.5 R_{sun} about 6.4 years (2025) after launch. The instruments will make observations for about 20 days (±10 around each orbit perihelion). An orbit is about 90 to 100 days depending upon the perihelion. Figure 4 shows the distance profile as a function of time after launch.
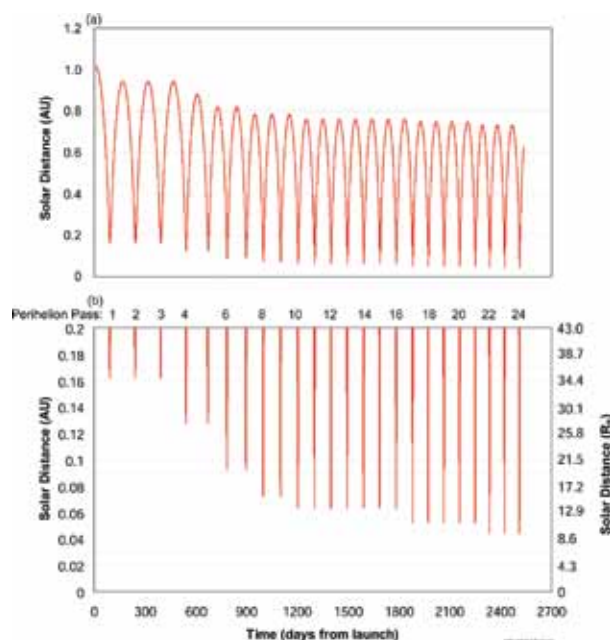
FIGURE 4
Solar distance profile of SP+. The upper plot shows both perihelion and aphelion, and the lower plot zooms in on the perihelion interval. The changes in the perihelion distances occur after each of the gravity assists resulting from the fly-bys of Venus.

The WISPR Instrument: WISPR images the solar corona with a 105° wide field of view, which corresponds to about 17 R_{sun}, at the minimum perihelion distance of 9.5 R_{sun}. The instrument observes in the visible and records the photospheric light scattered by the electrons within solar wind structures. This is very similar to the coronagraphs that NRL has flown on LASCO and SECCHI, but with much higher spatial resolution. As the spacecraft flies through the coronal density structures, they are first seen far away and then close up. Their substructure will be resolved to finer scales as they approach the spacecraft. At the same time, their scattering efficiency increases, making them easier to detect compared to solar wind structures further afield. This transition from remote sensing to local sensing will provide unprecedented observations of the

small-scale density fluctuations. The fast motion will also enable tomographic reconstructions from multiple viewpoints rather than just the two we have from the STEREO mission. If a coronal mass ejection (CME) occurs during the perihelion passage, SP+ will provide definitive measurements of the density and magnetic field ahead of and inside of the CME. WISPR will make the first observations of the dust-free region around the Sun, which has been a difficult, if not impossible, observation to make from 1 AU. Dust is the source of the zodiacal light or F-corona, but the dust evaporates as it nears the Sun. The distance at which the evaporation occurs depends on the particular material within the dust, which we expect to cause a slight inflection in the slope of the brightness curves.

WISPR will also search for density turbulence by taking images at a fast rate. Turbulence is a byproduct of wave heating. We will be able to explore the degree of turbulence in the near-Sun environment for various types of coronal structures beyond the local region around the spacecraft and to compare with the in situ measurements of magnetic and velocity turbulence.

The instrument, shown in Fig. 5, is a simple wide angle telescope, but with the complexity of rejecting the disk light by more than ten orders of magnitude to see the faint corona light. Our coronagraphic experience on the STEREO mission as well as previous missions carries over to this mission. Several new problems are presented and must be addressed. Both the dust and radiation environments will be greatly enhanced. The glass for the optics must survive impact of dust moving at a relative velocity of ~200 km/s and must be radiation hard. We must also replace the charge-coupled-device (CCD) sensors we have used previously with a new Advanced Pixel Sensor (APS) that is more immune to radiation damage. The APS opens up the new science

regime of turbulence studies from an imager because it allows fast readouts of selected regions of the detector. It accommodates variable exposure times across the field, which allows us to obtain high sensitivity across the full field of view despite the greater than 10^6 variation in the coronal signal.

Summary: The SP+ mission is an exciting mission with the promise of providing measurements of fundamental importance in solving some of the major outstanding problems of solar physics. The Space Science Divison–provided WISPR instrument, the only imager on board, plays a fundamental role in the success of this mission. WISPR will provide the first close-up images of the solar wind, coronal mass ejections, and possibly sungrazer comets. It will finally verify whether a dust-free zone exists in the inner corona. The WISPR images and density spectra link the remote sensing observations of the solar corona (from other platforms) and the in situ measurements from the SP+ payload, thus ensuring that the long-standing secrets of the solar wind will finally be revealed.

[Sponsored by NASA]

∎

Solar Active Regions – The Sources of Space Weather

G.A. Doschek and H.P. Warren
Space Science Division

The Magnetic Sun and Solar Activity: In visible light, the Sun appears as a near-constant light source that varies significantly in brightness only over time-scales of millions of years. The Sun in visible light is a relatively normal and not too interesting star compared with the zoo of astronomical objects such as supernova explosions and black holes. However, when solar radiation other than visible light is examined, the story changes dramatically. Two-thirds of the way from the Sun's core to its surface, convection of the solar gas begins and a magnetic dynamo is generated. Magnetic fields contain energy, and the fields disrupt the flow of radiative energy from the Sun's core to its surface, producing cool regions called sunspots. The magnetic fields near the sunspots are strong and, together with surrounding weaker fields, turn the Sun into an enormous magnetic object with an extremely complicated magnetic structure (see Fig. 6).

By processes not yet understood, the gas above the Sun's surface is heated by this magnetic field to temperatures ranging from 10,000 K to between 3 and 4 million degrees, creating a vast atmosphere that flows outward (the solar wind) past the Earth to the very
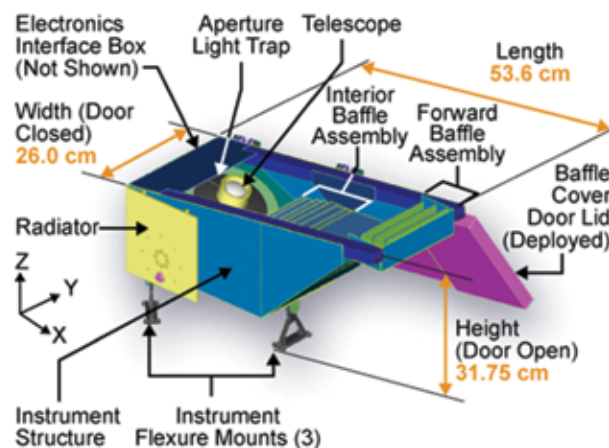
FIGURE 5
The WISPR instrument uses forward and interior baffles to reject unwanted scattered light from the Sun and the spacecraft. The concepts are derived from a significant heritage of coronagraphic instruments.
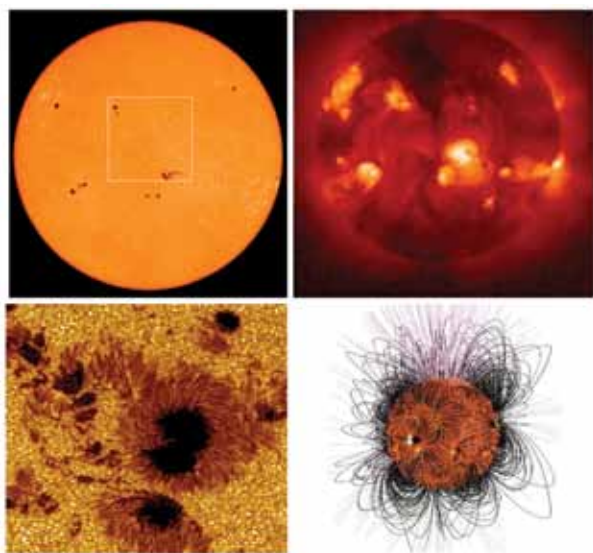
FIGURE 6
Upper left: visible light image of the Sun showing sunspots. Upper right: image of the Sun in X-rays showing hot bright regions above sunspots. Lower left: a sunspot up close showing surrounding convective "granules." Lower right: the Sun's magnetic field extending up into the solar atmosphere.

edge of the solar system, where it plows into the interstellar medium. The ultraviolet (UV), extreme-ultraviolet (EUV), and X-rays from the Sun are enormously variable, and sometimes the magnetic fields twist and annihilate themselves (by a process called magnetic reconnection), converting their energy into titanic explosions called flares and coronal mass ejections (CMEs). Flares reach temperatures of 30 million degrees and more, and a CME can send a billion tons of matter moving towards Earth at a million miles an hour. The X-ray–UV radiation and energetic particles in these eruptions create hazards to DoD assets in space, forming a local space weather that must be predictable in order to protect those assets.

The hottest regions of the Sun's atmosphere, and the regions in which flares and CMEs occur, are located over sunspots and are called active regions because they are seething infernos of transient eruptions and explosions. The gas in active regions is confined to magnetic lines of force and appears as giant plumes and loops. Understanding the heating in these linear structures is critical for understanding the flares and CMEs that are initiated in active regions.

Understanding Solar Activity at NRL: At NRL there is a sophisticated space-based remote sensing program working towards understanding the causes of active region heating with extensive support from NRL/ONR and NASA. One of our instruments is an Extreme-ultraviolet Imaging Spectrometer (EIS) flown on a Japanese spacecraft called Hinode. This instru-

ment is an international collaboration involving the U.S., the UK, Norway, and Japan. A spectrometer breaks light down into its component wavelengths (colors). Different elements such as iron emit radiation at discrete wavelengths ("spectral lines") depending on how many electrons are present around the atom's nucleus, and this depends on the temperature. EIS detects these spectral lines, and from atomic physics we can decipher the information they contain. Thus, EIS is a remote sensing thermometer, and by comparing the spectral lines of the same and different elements, it can also function as a barometer, a chemical composition analyzer, and, perhaps best of all, measure the speeds and turbulence in the gas within and above the active regions.

Heating and Dynamics of the Solar Atmosphere: With the unprecedented diagnostic information provided by EIS, we are finally beginning to understand the characteristics of the physical processes that actually heat the loops,[1] and as the current solar cycle proceeds to solar maximum, we hope to apply our techniques to understanding flares and mass ejections. For example, we find that the cores of active regions contain very hot loops with temperatures of 3 to 4 million degrees, while the outer parts of active regions contain "warm" loops with temperatures of about 1.4 million degrees. Figure 7 shows an active region as it appears in spectral lines formed at different temperatures. We find that the hot core loops appear to be steadily heated, while the warm loops are transiently heated. We are linking the heating characteristics of loops to the magnetic field structure of the active region, thus advancing our understanding of how magnetic energy is converted to gas heating.

Another interesting result concerns the length of time it takes the warm loops to cool. From intensity light curves and density measurements made with EIS, we now know that the warm active region loops contain unresolved magnetic structures that are somehow heated and cooled coherently. The density measurements imply that the loops should have much shorter lifetimes than observed. We can explain the observed lifetimes with a model that sequentially heats unresolved magnetic threads in the loops. However, the temperature evolution of the loops indicates that the sequential heating is not in complete agreement with the idea that the heating is caused by very tiny flares, called nanoflares, that is currently a popular model.

Finally, at the edges of active regions we find extended outflow regions (see Fig. 8) with plasma flowing outward at speeds ranging from 50 to 200 km/s.[2] We feel that at least some of this outflowing plasma reaches the heliosphere and could form part of the slow solar wind. EIS is revealing new and exciting results from
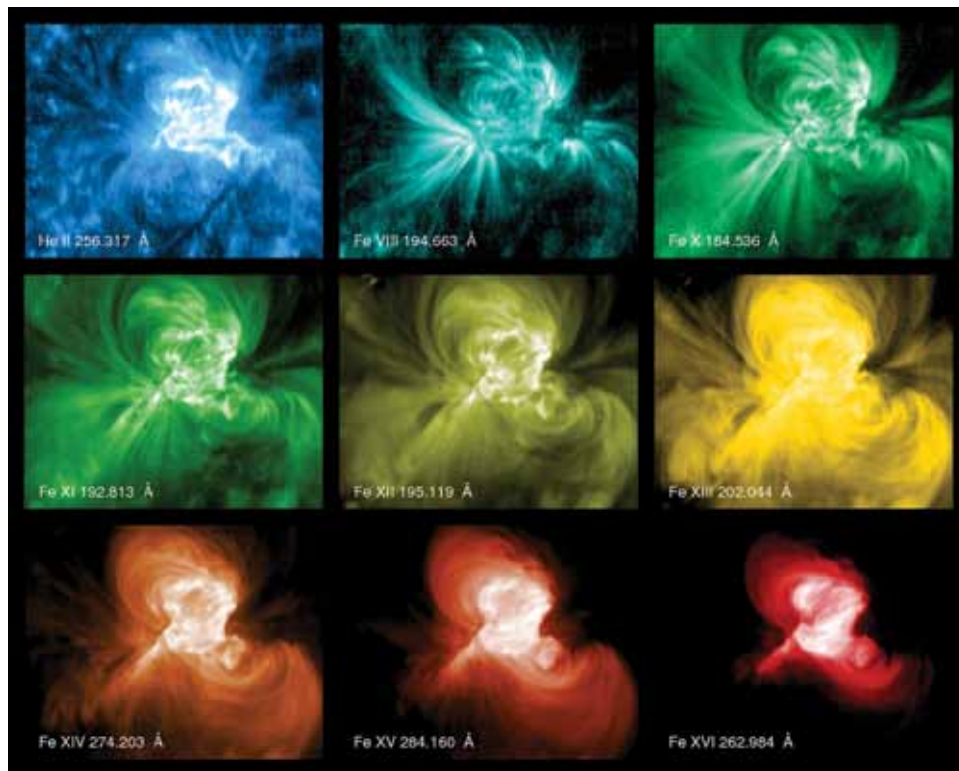
FIGURE 7
An active region as it appears in spectral lines of helium and iron formed at temperatures ranging from about 100,000 degrees (upper left) to 3–4 million degrees (lower right). Images from Hinode/EIS.
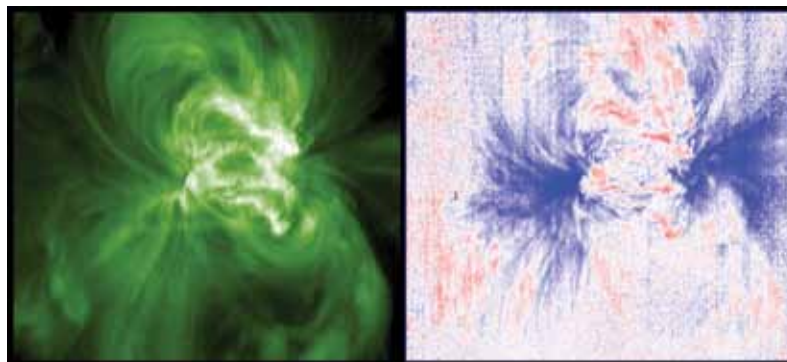
FIGURE 8
Left: An active region image in a spectral line of Fe XII formed at about 1.4 million degrees. Right: a Doppler map showing gas flow in the active region towards us (blue) and away from us (red). White emission corresponds to no velocity along our line of sight. Images from Hinode/EIS.

active regions, taking us closer to understanding how active regions are heated and produce transient phenomena. This brings us closer to realizing a predictive space weather capability based on the actual physics that produces space weather.

[Sponsored by NRL and ONR]

References
[1] H.P. Warren, D.M. Kim, A.M. DeGiorgi, and I. Ugarte-Urra, "Modeling Evolving Coronal Loops with Observations from STEREO, Hinode, and TRACE," *Astrophys. J.* **713**, 1095–1107 (2010).
[2] P. Bryans, P.R. Young, and G.A. Doschek, "Multiple Component Outflows in an Active Region Observed with the EUV Imaging Spectrometer on Hinode," *Astrophys. J.* **715**, 1012–1020 (2010).

Testing Spacecraft Atomic Clocks

F.M. Vannicola, R.L. Beard, J.D. White, K.L. Senior, A.J. Kubik, and D.C. Wilson
Space Systems Development Department

Introduction: NRL is conducting the third in a series of Global Positioning System (GPS) atomic frequency standard life tests in the NRL Precision Clock Evaluation Facility (PCEF). The PCEF is one of the major facilities within the Naval Center for Space Technology and an overview is provided in the *2008 NRL Major Facilities* book. Figure 9 is a block diagram of the PCEF. The PCEF was originally developed to evaluate high precision atomic clocks for the GPS concept program (Block I). The facility was expanded for dedicated space clock evaluation conducted for operational system development and deployment. The space atomic clocks' progress is evaluated, and the clocks are qualified and acceptance-tested for space flight using the facility's assets. Testing performed includes long- and short-term performance evaluation and environmental testing (including shock and vibration). Investigations of on-orbit anomalies are performed within the PCEF

in an attempt to duplicate and understand similar effects in space-qualified hardware under controlled conditions. The ability to evaluate and test highly precise atomic clocks, especially in a space environment, requires unique facilities, precise time and frequency references, and precise instrumentation not available elsewhere.

Background: The first extended life test conducted at NRL was on the GPS Block IIR Rubidium Atomic Frequency Standard (RAFS), which began in 1997 and lasted more than seven years.[1] Each Block IIR satellite contains three RAFS units. That life test began about one year before any of the RAFS were used in orbit. For the GPS Block IIF program, each satellite will contain one Digital Cesium Beam Frequency Standard (DCBFS) manufactured by Symmetricom, and two Rubidium Frequency Standards (RFS) built by PerkinElmer Optoelectronics. Life testing of two DCBFS flight production units began in August 2004 and has been on hold since October 2006 due to DCBFS production parts availability problems; however, these tests will resume in FY 2011. The third life test, which involves two production RFS units, has run continuously since August 22, 2008. The Block IIF life test is being con-
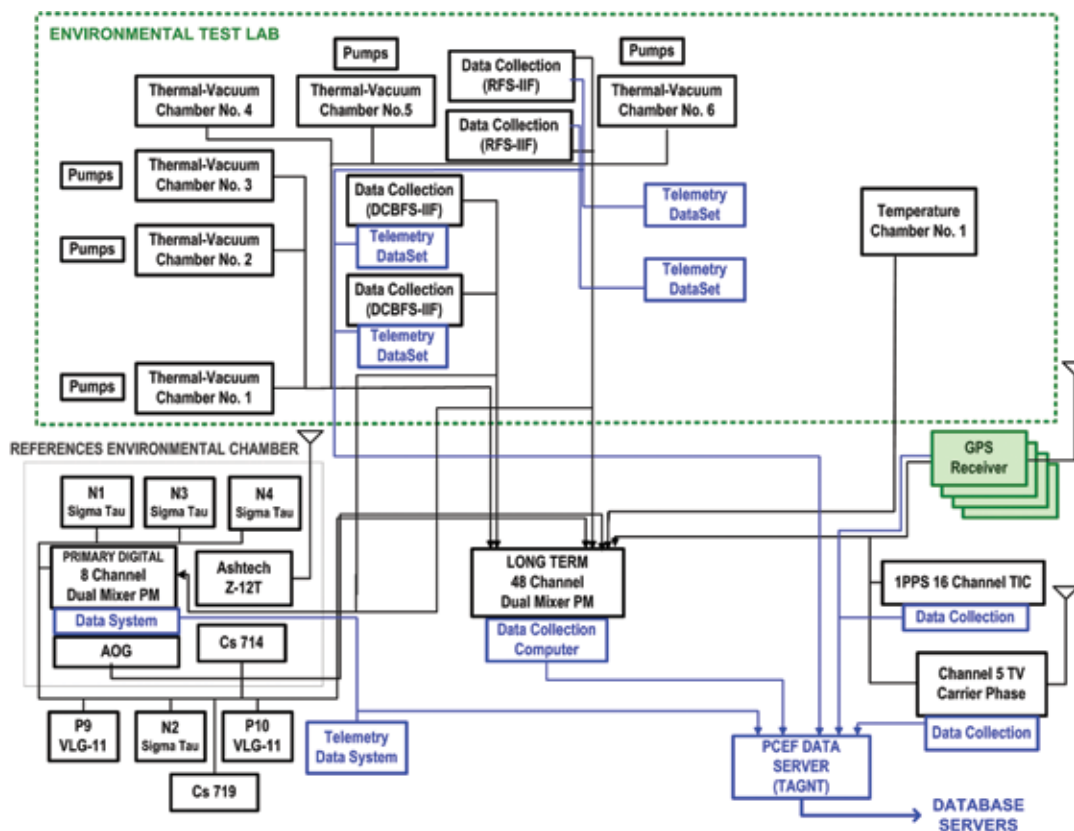
FIGURE 9
The NRL PCEF consists of the Time and Frequency References, Precision Clock Signal Measurement Systems, Environmental Testing Laboratory, Data Systems and Server, and GPS Receiver Laboratory.

ducted in conjunction with the GPS Directorate, GPS Block IIF Prime Contractor, Boeing, and the atomic frequency standards manufacturers, and is scheduled to run for a minimum of 3 years.[2] With the launch of the first GPS Block IIF satellite on May 28, 2010, NRL gained the unique ability to compare the ground clock performance with the clocks on-orbit. The frequency stability performance requirement for the GPS Block IIF clocks is 6×10^{-14} at one day.

Life Test Configurations: The life test principal objectives are accomplished by evaluating each Block IIF flight unit under continuous operation in a simulated space-like environment, thus replicating their operation in the GPS spacecraft as closely as possible. Separate thermal vacuum chambers whose mounting baseplates are independently temperature controlled house each of the units (Fig. 10). Figure 11 is a schematic diagram of the RFS life test configuration, which is similar to the DCBFS setup.

FIGURE 10
One of the closed vacuum chambers and equipment racks containing the data collection and monitoring systems.

FIGURE 11
RFS life test configuration and list of clock telemetry and PCEF environmental monitors.

DCBFS Anomalies/Performance: The DCBFS life test quickly uncovered a defect in the high voltage power supplies used for the ion pump and electron multiplier functions in the clocks. The first unit failed approximately 100 days into the test and after repair failed again 21 days into operation. The other unit had a continuous run of 591 days before it too experienced the same failure. The power supply problem was thoroughly researched and the flight units were modified to prevent future failures. No other anomalies were found.

RFS Anomalies/Performance: There have been no failures associated with either RFS unit; however, both units have experienced a combined total of 10 frequency steps, which were also seen during the RAFS life test and on-orbit. The steps experienced have ranged between -3.5×10^{-14} and $+7 \times 10^{-14}$. Neither clock is exhibiting a pattern to these steps. On two occasions there was an apparent correlation between the telemetry and the frequency steps. Clocks of this type have a tendency to experience frequency jumps, and specific causes have yet to be determined.

Temperature Testing: In an attempt to replicate the temperature changes experienced on board a GPS satellite, temperature cycling of one RFS unit was performed using the $\pm$ 3.5 °C peak-to-peak 12-hour cycle requirement from the clock specification. Effects were seen throughout the clock parameters, and the most notable, as expected, are in the baseplate thermal controller and the various ovens. Additional testing is required to determine a temperature coefficient.

Relevance: The NRL PCEF is a unique facility that provides the ability to perform extended life tests in order to establish a baseline for on-orbit clock performance and to identify potential risks in the flight test units. After 2 years of continuous operation, the two RFS life test units are performing well and display excellent stability. Despite the anomalies experienced in the two DCBFS life test units, their stabilities performed within design limits. With the launch of the first Block IIF satellite, the on-orbit performance of both the DCBFS and RFS clocks is within specification.

[Sponsored by the GPS Directorate]

References

[1] R. Beard, J. Buisson, F. Danzy, M. Largay, and J. White, "GPS Block IIR Rubidium Frequency Standard Life Test Results," in Proceedings of the 2002 IEEE International Frequency Control Symposium, May 29–31, 2002, New Orleans, Louisiana, pp. 449–504 (2002).

[2] F. Vannicola, R. Beard, J. White, K. Senior, A. Kubik, and D. Wilson, "GPS Block IIF Rubidium Frequency Life Test," in Proceedings of the Institute of Navigation Global Navigation Satellite System Conference, September 21-24, 2010, Portland, Oregon, pp. 812–819 (2010).

Unmanned Free-Swimming Submersibe (UFSS) (1979) — NRL developed a long-range autonomous submersible to demonstrate (1) autonomy obtained by an OMEGA navigator and a preprogrammed command and control microcomputer, and (2) high endurance (25 hr at 5 kt) attained with a low-drag hull and inexpensive battery energy source.

Programs for Professional Development

PROGRAMS FOR NRL EMPLOYEES

The Human Resources Office supports and provides traditional and alternative methods of training for employees. NRL employees are encouraged to develop their skills and enhance their job performance so they can meet the future needs of NRL and achieve their own goals for growth.

One common study procedure is for employees to work full time at the Laboratory while taking job-related courses at universities and schools local to their job site. The training ranges from a single course to undergraduate, graduate, and postgraduate course work. Tuition for training is paid by NRL. The formal programs offered by NRL are described here.

GRADUATE PROGRAMS

The **Advanced Graduate Research Program** (formerly the Sabbatical Study Program, which began in 1964) enables selected professional employees to devote full time to research or pursue work in their own or a related field for up to one year at an institution or research facility of their choice without the loss of regular salary, leave, or fringe benefits. NRL pays all travel and moving expenses for the employee. Criteria for eligibility include professional stature consistent with the applicant's opportunities and experience, a satisfactory program of study, and acceptance by the facility selected by the applicant. The program is open to employees who have completed six years of Federal Service, four of which have been at NRL.

The **Edison Memorial Graduate Training Program** enables employees to pursue graduate studies in their fields at local universities. Participants in this program work 24 hours each workweek and pursue their studies during the other 16 hours. The criteria for eligibility include a minimum of one year of service at NRL, a bachelor's or master's degree in an appropriate field, and professional standing in keeping with the candidate's opportunities and experience.

To be eligible for the **Select Graduate Training Program**, employees must have a Bachelor's degree in an appropriate field and must have demonstrated ability and aptitude for advanced training. Students accepted into this program devote three academic semesters to graduate study. While attending school, they receive one-half of their salary and benefits, and NRL pays for tuition and travel expenses.

The **Naval Postgraduate School (NPS)**, located in Monterey, California, provides graduate programs to enhance the technical preparation of Naval officers and civilian employees who serve the Navy in the fields of science, engineering, operations analysis, and management. NRL employees desiring to pursue graduate studies at NPS may apply for a maximum of six quarters away from NRL, with thesis work accomplished at NRL. Participants continue to receive full pay and benefits during the period of study. NRL also pays for tuition and travel expenses.

In addition to NRL and university offerings, application may be made to a number of noteworthy programs and fellowships. Examples of such opportunities are the **Capitol Hill Workshops**, the **Legislative Fellowship (LEGIS) program**, the **Federal Executive Institute (FEI)**, and the **Executive Leadership Program for Mid-Level Employees**. These and other programs are announced from time to time, as schedules are published.

CONTINUING EDUCATION

Undergraduate and graduate courses offered at local colleges and universities may be subsidized by NRL for employees interested in improving their skills and keeping abreast of current developments in their fields.

NRL offers **short courses** to all employees in a number of fields of interest including administrative subjects, and supervisory and management techniques. Laboratory employees may also attend these courses at nongovernment facilities.

For further information on any of the above Graduate and Continuing Education programs, contact the Workforce Development and Management Branch (Code 1840) at (202) 404-8314 or via email at Training@hro.nrl.navy.mil.

The **Scientist-to-Sea Program (STSP)** provides opportunities for Navy R&D laboratory/center personnel to go to sea to gain first-hand insight into operational factors affecting system design, performance, and operations on a variety of ships. NRL is a participant of this Office of Naval Research (ONR) program. Contact (202) 767-7627.

PROFESSIONAL DEVELOPMENT

NRL has several programs, professional society chapters, and informal clubs that enhance the professional growth of employees. Some of these are listed below.

The **Counseling & Referral Service (C/RS)** helps employees improve job performance through counseling designed to resolve problems that may adversely affect job performance. Such problems may include family and/or work-related stress, relationship difficulties,

behavioral, emotional, or substance abuse problems. C/RS provides confidential assessment, short-term counseling, training workshops, and referral to additional resources in the community. Contact (202) 767-6857.

The NRL **Women in Science and Engineering (WISE) Network** was formed in 1997 through the merger of the NRL chapter of WISE and the Women in Science and Technology Network. Luncheon meetings and seminars are held to discuss scientific research areas, career opportunities, and career-building strategies. The group also sponsors projects to promote the professional success of the NRL S&T community and improve the NRL working environment. Membership is open to all S&T professionals. Contact (202) 404-4389.

Sigma Xi, The Scientific Research Society, encourages and acknowledges original investigation in pure and applied science. It is an honor society for research scientists. Individuals who have demonstrated the ability to perform original research are elected to membership in local chapters. The NRL Edison Chapter, comprising approximately 200 members, recognizes original research by presenting annual awards in pure and applied science to two outstanding NRL staff members per year. In addition, an award seeking to reward rising stars in the lab is presented annually through the Young Investigator Award. The chapter also sponsors several lectures per year at NRL on a wide range of topics of general interest to the scientific and DoD community. These lectures are delivered by scientists from all over the world. The highlight of the Sigma Xi Lecture Series is the Edison Memorial Lecture, which traditionally is given by a internationally distinguished scientist. Contact (202) 767-2007.

The **NRL Mentor Program** was established to provide an innovative approach to professional and career training and an environment for personal and professional growth. It is open to permanent NRL employees in all job series and at all sites. Mentees are matched with successful, experienced colleagues having more technical and/or managerial experience who can provide them with the knowledge and skills needed to maximize their contribution to the success of their immediate organization, to NRL, to the Navy, and to their chosen career fields. The ultimate goal of the program is to increase job productivity, creativity, and satisfaction through better communication, understanding, and training. NRL Instruction 12400.1B provides policy and procedures for the program. Contact (202) 404-8314 or Training@hro.nrl.navy.mil.

Employees interested in developing effective self-expression, listening, thinking, and leadership potential are invited to join the Forum Club, a chapter of **Toastmasters International**. Members of this club possess diverse career backgrounds and talents and to learn to communicate not by rules but by practice in an atmosphere of understanding and helpful fellowship. NRL's Commanding Officer and Director of Research endorse Toastmasters. Contact (202) 404-4670.

EQUAL EMPLOYMENT OPPORTUNITY (EEO) PROGRAMS

Equal employment opportunity (EEO) is a fundamental NRL policy for all employees regardless of race, color, national origin, sex, religion, age, sexual orientation, or disability. The NRL EEO Office is a service organization whose major functions include counseling employees in an effort to resolve employee/management conflicts, processing formal discrimination complaints, providing EEO training, and managing NRL's affirmative employment recruitment program. The NRL EEO Office is also responsible for sponsoring special-emphasis programs to promote awareness and increase sensitivity and appreciation of the issues or the history relating to females, individuals with disabilities, and minorities. Contact the NRL Deputy EEO Officer at (202) 767-2486 for additional information on any of their programs or services.

OTHER ACTIVITIES

The award-winning **Community Outreach Program** directed by the NRL Public Affairs Office fosters programs that benefit students and other community citizens. Volunteer employees assist with and judge science fairs, give lectures, provide science demonstrations and student tours of NRL, and serve as tutors, mentors, coaches, and classroom resource teachers. The program sponsors student tours of NRL and an annual holiday party for neighborhood children in December. Through the program, NRL has active partnerships with three District of Columbia public schools. Contact (202) 767-2541.

Other programs that enhance the development of NRL employees include sports groups, Toastmasters, and the **Amateur Radio Club**. The **NRL Fitness Center** at NRL-DC, managed by Naval Support Activity Washington Morale, Welfare and Recreation (NSAW-MWR), houses a fitness room with treadmills, bikes, ellipticals, step mills, and a full strength circuit; a gymnasium for basketball, volleyball, and other activities; and full locker rooms. The Fitness Center is free to NRL employees and contractors. NRL employees are also eligible to participate in all NSAW MWR activities held on Joint Base Anacostia–Bolling and Washington Navy Yard, less than five miles away. The **NRL Showboaters Theatre**, organized in 1974, is "in the dark." Visit www.nrl.navy.mil/showboaters/Past_Productions.php for pictures from past productions such as Annie Get Your Gun, Gigi, and Hello Dolly. Contact (202) 404-4998 for Play Reader's meetings at NRL.

PROGRAMS FOR NON-NRL EMPLOYEES

Several programs have been established for non-NRL professionals. These programs encourage and support the participation of visiting scientists and engineers in research of interest to the Laboratory. Some of the programs may serve as stepping-stones to federal careers in science and technology. Their objective is to enhance the quality of the Laboratory's research activities through working associations and interchanges with highly capable scientists and engineers and to provide opportunities for outside scientists and engineers to work in the Navy laboratory environment. Along with enhancing the Laboratory's research, these programs acquaint participants with Navy capabilities and concerns and provide a path to full-time employment.

RECENT Ph.D., FACULTY MEMBER, AND COLLEGE GRADUATE PROGRAMS

The **National Research Council (NRC) Cooperative Research Associateship Program** selects associates who conduct research at NRL in their chosen fields in collaboration with NRL scientists and engineers. Appointments are for one year (renewable for a second and possible third year).

The **NRL/ASEE Postdoctoral Fellowship Program**, administered by the American Society for Engineering Education (ASEE), aims to increase the involvement of highly trained scientists and engineers in disciplines necessary to meet the evolving needs of naval technology. Appointments are for one year (renewable for a second and possible third year).

The **Naval Research Enterprise Intern Program (NREIP)** is a ten-week program involving NROTC colleges/universities and their affiliates. The Office of Naval Research (ONR) offers summer appointments at Navy laboratories to current sophomores, juniors, seniors, and graduate students from participating schools. Application is online at www.asee.org/nreip through the American Society for Engineering Education. Electronic applications are sent for evaluation to the point of contact at the Navy laboratory identified by the applicant. Students are provided a stipend of $7,500 (undergraduates) or $10,000 (graduate students).

The American Society for Engineering Education also administers the **Navy/ASEE Summer Faculty Research and Sabbatical Leave Program** for university faculty members to work for ten weeks (or longer, for those eligible for sabbatical leave) with professional peers in participating Navy laboratories on research of mutual interest.

The **NRL/United States Naval Academy (USNA) Cooperative Program for Scientific Interchange** allows faculty members of the U.S. Naval Academy to participate in NRL research. This collaboration benefits the Academy by providing the opportunity for USNA faculty members to work on research of a more practical or applied nature. In turn, NRL's research program is strengthened by the available scientific and engineering expertise of the USNA faculty.

The **National Defense Science and Engineering Graduate Fellowship Program** helps U.S. citizens obtain advanced training in disciplines of science and engineering critical to the U.S. Navy. The three-year program awards fellowships to recent outstanding graduates to support their study and research leading to doctoral degrees in specified disciplines such as electrical engineering, computer sciences, material sciences, applied physics, and ocean engineering. Award recipients are encouraged to continue their study and research in a Navy laboratory during the summer.

For further information about the above six programs, contact (202) 404-7450.

PROFESSIONAL APPOINTMENTS

Faculty Member Appointments use the special skills and abilities of faculty members for short periods to fill positions of a scientific, engineering, professional, or analytical nature at NRL.

Consultants and experts are employed because they are outstanding in their fields of specialization or because they possess ability of a rare nature and could not normally be employed as regular civil servants.

Intergovernmental Personnel Act Appointments temporarily assign personnel from state or local governments or educational institutions to the Federal Government (or vice versa) to improve public services rendered by all levels of government.

COLLEGE AND HIGH SCHOOL STUDENT PROGRAMS

The student programs are tailored to high school, undergraduate, and graduate students to provide employment opportunities and work experience in naval research. These programs are designed to attract applicants for student and full professional employment in fields such as engineering, physics, mathematics, and computer sciences. The student employment programs are designed to help students and educational institutions gain a better understanding of NRL's research, its challenges, and its opportunities. To participate in these programs, the student must be continuously enrolled in school on at least a half-time basis at a qualifying educational institution.

The **Student Career Experience Program (SCEP)** employs students in study-related occupations. The program is conducted in accordance with a planned schedule and a working agreement among NRL, the educational institution, and the student. Primary focus is on the pursuit of undergraduate and graduate degrees in engineering, computer science, or the physical sciences. Applications are accepted year-round.

The **Student Temporary Employment Program (STEP)** is a one year temporary employment program that may be renewed. This program enables students to earn a salary while continuing their studies and offers them valuable work experience. They must be continuously enrolled in school on at least a half-time basis at a qualifying educational institution. Applications are accepted year-round.

The **Summer Employment Program (SEP)** employs students for the summer that are enrolled in a qualifying educational institution on at least a half-time basis studying paraprofessional and technician position in engineering, physical sciences, computer sciences, and mathematics. Applications are due the 2nd Friday in February.

The **Student Volunteer Program** helps students gain valuable experience by allowing them to voluntarily perform educationally related work at NRL. Applications are accepted year-round.

For additional information on these student programs, contact (202) 767-8313.

For high school students, the **DoD Science & Engineering Apprenticeship Program (SEAP)** offers students grades 9–12 the opportunity to serve for eight weeks to participate in research at a Department of Navy laboratory during the summer. Under the direction of a mentor, students gain a better understanding of research and the science and engineering career fields. Criteria for eligibility are based on academic background, research interests, scientific and engineering skills and knowledge, and a recommendation from a high school official. For additional information, contact 202-767-6736 or SEAP@hro.nrl.navy.mil.

NRL EMPLOYMENT OPPORTUNITIES

for Highly Innovative, Motivated, and Creative Professionals

NRL offers a wide variety of challenging S&T positions that involve skills from basic and applied research to equipment development. The nature of the research and development conducted at NRL requires professionals with experience. Typically there is a continuing need for electronics, mechanical, aerospace, and materials engineers, metallurgists, computer scientists, and oceanographers with bachelor's and/or advanced degrees and physical and computer scientists with Ph.D. degrees.

■ **Biologists.** Biologists conduct research in areas that include biosensor development, tissue engineering, molecular biology, genetic engineering, proteomics, and environmental monitoring.

■ **Chemists.** Chemists are recruited to work in the areas of combustion, polymer science, bioengineering and molecular engineering, surface science, materials synthesis, nanostructures, corrosion, fiber optics, electro-optics, microelectronics, electron device technology, and laser physics.

■ **Electronics Engineers and Computer Scientists.** These employees may work in the areas of communications systems, electromagnetic scattering, electronics instrumentation, electronic warfare systems, radio frequency/microwave/millimeter-wave/infrared technology, radar systems, laser physics technology, radio-wave propagation, electron device technology, spacecraft design, artificial intelligence, information processing, signal processing, plasma physics, vacuum science, microelectronics, electro-optics, fiber optics, solid-state physics, software engineering, computer design/architecture, ocean acoustics, stress analysis, and expert systems.

■ **Materials Scientists/Engineers.** These employees are recruited to work on materials, microstructure characterization, electronic ceramics, solid-state physics, fiber optics, electro-optics, microelectronics, fracture mechanics, vacuum science, laser physics and joining technology, and radio frequency/microwave/millimeter-wave/infrared technology.

■ **Mechanical and Aerospace Engineers.** These employees may work in areas of spacecraft design, remote sensing, propulsion, experimental and computational fluid mechanics, experimental structural mechanics, solid mechanics, elastic/plastic fracture mechanics, materials, finite-element methods, nondestructive evaluation, characterization of fracture resistance of structural alloys, combustion, CAD/CAM, and multifunctional material response.

■ **Oceanographers, Meteorologists, and Marine Geophysicists.** These employees work in the areas of ocean and atmospheric dynamics, air–sea interaction, upper-ocean dynamics, oceanographic bio-optical modeling, oceanic and atmospheric numerical modeling and prediction, data assimilation and data fusion, retrieval and application of remote sensing data, benthic processes, aerogeophysics, marine sedimentary processes, advanced mapping techniques, atmospheric physics, and remote sensing. Oceanographers and marine geophysicists are located in Washington, DC, and at the Stennis Space Center, Bay St. Louis, Mississippi. Meteorologists are located in Washington, DC, and Monterey, California.

■ **Physicists.** Physics graduates may concentrate on such fields as materials, solid-state physics, fiber optics, electro-optics, microelectronics, vacuum science, plasma physics, fluid mechanics, signal processing, ocean acoustics, information processing, artificial intelligence, electron device technology, radio-wave propagation, laser physics, ultraviolet/X-ray/gamma-ray technology, electronic warfare, electromagnetic interaction, communications systems, radio frequency/microwave/millimeter-wave/infrared technology, computational physics, radio and high-energy astronomy, solar physics, and space physics.

For more information and current vacancy listings,
visit http://hroffice.nrl.navy.mil/

General Information

Laboratory for Autonomous Systems Research (2012) —
NRL opened the LASR to become a nerve center for autonomous
systems research for the Navy and Marine Corps.

TECHNICAL OUTPUT

The Navy continues to be a leader in initiating new developments and applying these advancements to military requirements. The primary method of informing the scientific and engineering community of the advances made at NRL is through the Laboratory's technical output — reports, articles in scientific journals, contributions to books, papers presented to scientific societies and topical conferences, patents, and inventions.

The figures for calendar year 2010 presented below represent the output of NRL facilities in Washington, D.C.; Bay St. Louis, Mississippi; and Monterey, California.

In addition to the output listed, NRL scientists made more than 2181 oral presentations during 2010.

Type of Contribution	Unclassified	Classified	Total
Articles in periodicals, chapters in books, and papers in published proceedings	1472*	0	1472*
NRL Formal Reports	6	6	12
NRL Memorandum Reports	67	8	75
Books	2	0	2
Patents granted	92		92
Statutory Invention Registrations (SIRs)	0		0

*This is a provisional total based on information available to the Ruth H. Hooker Research Library on April 2, 2012. Additional publications carrying a 2010 publication date are anticipated. Total includes refereed and non-refereed publications.

KEY PERSONNEL

Code	Office	Phone Number
	EXECUTIVE DIRECTORATE	
1000	Commanding Officer	767-3403
1000.1	Inspector General	767-3621
1001	Director of Research	767-3301
1001.1	Executive Assistant for the Director of Research	767-2445
1002	Chief Staff Officer	767-3621
1004	Head, Technology Transfer Office	767-3083
1006	Head, Office of Program Administration and Policy Development	767-3091
1008	Office of Counsel	767-2244
1030	Public Affairs Officer	767-2541
1100	Director, Institute for Nanoscience	767-3261
1200	Head, Command Support Division	767-3621
1220	Head, Information Assurance and Communications Security	767-0793
1400	Head, Military Support Division	767-2273
1600	Commander, Scientific Development Squadron One	301-342-3751
1700	Director, Laboratory for Autonomous Systems Research	767-2684
1800	Director, Human Resources Office	767-3421
1830	Deputy EEO Officer	767-5264
3005	Deputy for Small Business	767-6263
3540	Head, Safety Branch	767-2232
	BUSINESS OPERATIONS DIRECTORATE	
3000	Comptroller/Associate Director of Research	767-2371
3200	Head, Contracting Division	767-5227
3300	Head, Financial Management Division	767-3405
3400	Head, Supply and Information Services Division	767-3446
3500	Director, Research and Development Services Division	404-4054
	SYSTEMS DIRECTORATE	
5000	Associate Director of Research	767-3425
5300	Superintendent, Radar Division	404-2700
5500	Superintendent, Information Technology Division/ NRL Chief Information Officer*	767-2903
5600	Superintendent, Optical Sciences Division	767-7375
5700	Superintendent, Tactical Electronic Warfare Division	767-6278
	MATERIALS SCIENCE AND COMPONENT TECHNOLOGY DIRECTORATE	
6000	Associate Director of Research	767-3566
6100	Superintendent, Chemistry Division	767-3026
6300	Superintendent, Materials Science and Technology Division	767-2926
6400	Director, Laboratory for Computational Physics and Fluid Dynamics	767-3055
6700	Superintendent, Plasma Physics Division	767-2723
6800	Superintendent, Electronics Science and Technology Division	767-3693
6900	Director, Center for Bio/Molecular Science and Engineering	404-6000
	OCEAN AND ATMOSPHERIC SCIENCE AND TECHNOLOGY DIRECTORATE	
7000	Associate Director of Research	404-8690
7100	Superintendent, Acoustics Division	767-3482
7200	Superintendent, Remote Sensing Division	767-3391
7300	Superintendent, Oceanography Division	228-688-4670
7400	Superintendent, Marine Geosciences Division	228-688-4650
7500	Superintendent, Marine Meteorology Division	831-656-4721
7600	Superintendent, Space Science Division	767-6343
	NAVAL CENTER FOR SPACE TECHNOLOGY	
8000	Director	767-6547
8100	Superintendent, Space Systems Development Department	767-0410
8200	Superintendent, Spacecraft Engineering Department	404-3727

---

*Additional Duty

CONTRIBUTIONS BY DIVISIONS, LABORATORIES, AND DEPARTMENTS

SUBJECT INDEX

AUTHOR INDEX

NAVAL RESEARCH LABORATORY

4555 Overlook Ave., SW • Washington, DC 20375-5320

LOCATION OF NRL IN THE CAPITAL AREA

NAVAL RESEARCH LABORATORY

Quick Reference Telephone Numbers

	NRL Washington	NRL- SSC	NRL- Monterey	NRL CBD	NRL VXS-1 Patuxent River
Hotline	(202) 767-6543	(202) 767-6543	(202) 767-6543	(202) 767-6543	(202) 767-6543
Personnel Locator	(202) 767-3200	(228) 688-3390	(831) 656-4763	(410) 257-4000	(301) 342-3751
DSN	297- or 754-	828	878	—	342
Direct-in-Dialing	767- or 404-	688	656	257	342
Public Affairs	(202) 767-2541	(228) 688-5328	(202) 767-2541	—	(202) 767-2541

Additional telephone numbers are listed on page 255.

General information on the research described in this *NRL Review* can be obtained from the Public Affairs Office, Code 1030, (202) 767-2541. Information concerning Technology Transfer is available from the Technology Transfer Office, Code 1004, (202) 767-7230. Sources of information on the various educational programs at NRL are listed in the *NRL Review* chapter entitled "Programs for Professional Development."

For additional information about NRL, the *NRL Fact Book* lists the organizations and key personnel for each division. It contains information about Laboratory funding, programs, and field sites. The *Fact Book* can be obtained from the Technical Information Services Branch, Code 3430, (202) 404-4963. The web-based *NRL Major Facilities* publication, which describes each NRL facility in detail, can be accessed at http://www.nrl.navy.mil.

NRL REVIEW STAFF

www.nrl.navy.mil

2011 NRL REVIEW